

Understanding and Preventing the Degradation of Silicon as a Lithium Ion Battery Anode

Nis-Julian Hendrik Kneusels

Gonville & Caius College

A thesis submitted for the degree of

Doctor of Philosophy (PhD)

August 2019



UNIVERSITY OF
CAMBRIDGE



Declaration

I hereby declare that this dissertation with the title “Understanding and Preventing the Degradation of Silicon as a Lithium Ion Battery Anode” is the result of my own work that has been carried out between October 2015 and August 2019 in the Department of Chemistry at the University of Cambridge. Results that were obtained in collaboration are declared in the text and/or the acknowledgments. None of the work has been submitted for a degree or diploma or other qualification at the University of Cambridge or any other University or similar institution. The work does not exceed the prescribed word limit by the Degree Committee of 60 000 words.

Nis-Julian H. Kneusels

Cambridge, August 2019

Abstract – “Understanding and Preventing the Degradation of Silicon as a Lithium Ion Battery Anode”

Nis-Julian Kneusels

Silicon anodes are of great interest for lithium ion batteries (LIBs) due to their promising high gravimetric capacity compared to conventional carbon anodes. However, the immense volume expansion and continuous solid-electrolyte interphase (SEI) formation during operation hinder stable long-term cycling. This thesis aims to identify factors that drive the degradation of the silicon anode and propose strategies to overcome it using electrolyte additives and poly(phosphazenes) as artificial SEIs.

Chapter 1 outlines the need for LIBs and their functionality and introduces silicon as an anode material and the chemistry of (poly)phosphazenes. Chapter 2 describes the relevant techniques such as scanning electron microscopy (SEM), galvanostatic cycling, etc. and their application for this work.

Chapter 3 addresses the degradation of the silicon anode using thin-films of the material, as the application of nanosized silicon anodes yields reasonable electrochemical performance. Previous studies have analysed a wide range of thin-films using varying techniques, however, no clear view of the degradation processes involved can be concluded. Thin-film electrodes are created by magnetron sputtering and thoroughly tested. Electrochemical cycling demonstrates the impact of the anodes thickness and substrate structure and varying cycling conditions suggest ideal parameters to improve the performance. The electrodes undergo distinct morphological changes during operation which are identified by electron microscopy-SEM and compared to data from electrochemical cycling. In Chapter 4, the impact of the electrolyte additives fluoroethylene carbonate (FEC) and vinylene carbonate (VC) on the thin-film electrode is investigated, suggesting the formation of a mechanically robust SEI. Electrochemical experiments and electron microscopy give an insight into both structural and chemical differences that arise from the addition of the individual electrolyte additives.

Chapter 5 introduces poly(phosphazene) coatings to stabilise the silicon thin-film anode and increase its performance. The design of an artificial SEI based on mechanically and chemically flexible poly(phosphazenes) is demonstrated and greatly increases the cycle life of the thin-film electrode. These inorganic-organic hybrid polymers are synthesised from simple starting materials, allowing the functionalisation with various organic side-groups to tune their properties. The polymer synthesis and deposition of thin polymer films are described in detail and the film morphologies observed before and after electrochemical cycling are presented.

Stabilisation of the anode with a polyether-substituted poly(phosphazene) is further improved by introducing trifluoroethoxide side-groups. The coatings provide mechanical and chemical stability depending on its functionalisation. Chapter 6 shows proof-of-principle studies of phosphazene surface-grafting on to silicon summarised as ongoing work. Results indicate that very thin poly(phosphazene) layers can be engineered.

All results are summarised in Chapter 7, drawing conclusions on the impact of this work in the field and its implications on future work.

Acknowledgements

My sincerest thanks go to Prof Clare Grey and Prof Dominic Wright for assigning me this challenging project and their trust in me, time and guidance and for supporting me in every situation throughout the past four years. I feel honoured to have been pursuing my PhD studies as a member of their groups. I want to further thank the U.S. Department of Energy, the Royal Society and the Cambridge Trust for funding my research.

I want to thank all members of Team Silicon for their fruitful scientific discussions and collaborations on such a challenging subject. Thanks to Dr Zachary Ruff, for the help with coatings and electron microscopy and coatings and Ben Smith for his help in showing the true beauty of electrochemical cycling data. Thank you, Dr Yanting Jin, for being a constant help from the first day of the project, sharing your know-how on the topic with me and keeping me engaged in collaborations. And thank you, Dr Robert Weatherup, for making large parts of this thesis possible through your expertise and helping me in every aspect, being an encouragement and inspiration. I wish to thank everyone in the Grey and Wright groups, as well as all other co-workers from the third floor, for making every day at work a pleasure. Thank you for helping me feel at home in lab 301 and the fun times in- and outside the lab. I would like to thank Joe Gregory and Cassius Clark for their hard work during their projects and wish them all the best for their future. I want to especially thank Kellie Jenkinson for her patience and constant support with microscopy and life in general. Thank you, Rajesh Jethwa, for being an amazing colleague, it was a pleasure working with you and thank you for teaching me some proper English.

Further I would like to thank Heather Greer, for her help with SEM, John Walmsley for his help with the FIB SEM, the staff at the Harwell XPS facility for XPS measurements and all the staff at the Department of Chemistry being happy to help in any situation.

Thanks to all the friends at Caius for the time spent on the river and leaning and observing at the gate come rain or shine.

Thanks to my parents and sisters, who have made me come this far. Thank you, Angela and Hendrik Kneusels, for being the amazing parents that you are with your constant support, encouragement and immeasurable love.

Lena Kneusels, we came to Cambridge to start a new life together. Your love, determination and humour have shaped my life since the day we met. You challenge me and bring out the best in me every day. Thank you for your trust, support and never-ending love. I can't wait to see what God has in store for us and our beloved son Aaron Maximilian.

Contributions to Publications

During the work for this thesis, contributions have been made to the following publications:

“Identifying the Structural Basis for the Increased Stability of the Solid Electrolyte Interphase Formed on Silicon with the Additive Fluoroethylene Carbonate” Y. Jin, N.-J. H. Kneusels, P. C. M. M. Magusin, G. Kim, E. Castillo-Martínez, L. E. Marbella, R. N. Kerber, D. J. Howe, S. Paul, T. Liu, C. P. Grey, *J. Am. Chem. Soc.* **2017**, *139*, 14992.

“Understanding Fluoroethylene Carbonate and Vinylene Carbonate Based Electrolytes for Si Anodes in Lithium Ion Batteries with NMR Spectroscopy” Y. Jin, N.-J. H. Kneusels, L. E. Marbella, E. Castillo-Martínez, P. C. M. M. Magusin, R. S. Weatherup, E. Jónsson, T. Liu, S. Paul, C. P. Grey, *J. Am. Chem. Soc.* **2018**, *140*, 9854.

„NMR Study of the Degradation Products of Ethylene Carbonate in Silicon-Lithium Ion Batteries” Y. Jin, N.-J. H. Kneusels, C. P. Grey, *J Phys Chem Lett.* **2019**, *10* (20), 6345–6350.

Table of Contents

Chapter 1	Introduction	1
1.1	Global Energy Demand and Climate Effects	1
1.2	Lithium Ion Batteries (LIBs).....	3
1.2.1	Anode Materials	5
1.2.2	Cathode Materials	7
1.2.3	Electrolytes.....	7
1.2.4	Other LIB Components	8
1.3	Solid Electrolyte Interphase (SEI).....	9
1.4	Silicon as an Anode Material for LIBs.....	11
1.4.1	Nanosized Silicon Anodes	12
1.4.2	Electrochemical Properties and Lithiation Mechanisms of Silicon	14
1.5	Artificial SEIs for Silicon Anodes.....	16
1.6	Synthesis and Applications of Poly(phosphazenes) in LIBs.....	20
1.6.1	Molecular Structures	21
1.6.2	Polymerisation and Functionalisation	22
1.6.3	Polyphosphazenes as Electrolytes for LIBs	24
1.7	Project Aims	25
Chapter 2	Methods	27
2.1	Metal Sputter Coating	27
2.1.1	Direct Current (DC) Sputter Coating	28
2.1.2	Radio-frequency (RF) Sputter Coating	28
2.1.3	Profilometer.....	28
2.2	Electrochemical Measurements.....	28
2.2.1	Galvanostatic Cycling	29
2.3	Electron Microscopy & Energy-Dispersive X-ray Spectroscopy	31

2.3.1 Scanning Electron Microscopy (SEM)	34
2.3.2 Sample Transfer under Inert Atmosphere	34
2.3.3 Energy-dispersive X-ray Spectroscopy (EDS).....	34
2.3.4 Focussed Ion Beam (FIB) SEM	34
2.4 Contact Angle Measurements	35
2.5 Synthetic Procedures and Substance Characterisation.....	35
2.5.1 Schlenk techniques	35
2.5.2 Purification Methods	35
2.5.3 Nuclear Magnetic Resonance Spectroscopy (NMR).....	36
2.5.4 Gel-permeation Chromatography (GPC)	36
2.5.5 Mass Spectrometry (MS)	36
Chapter 3 Degradation of the Silicon Thin-film Anode	37
3.1 Characteristics and the Current State of Silicon Thin-films for LIBs.....	39
3.1.1 Fabrication Methods.....	39
3.1.2 Crack Formation and Delamination	39
3.1.3 Electrode Thickness and Crack Sizes.....	41
3.1.4 Performance Factors of the Silicon Thin-film Anode.....	42
3.2 Results and Discussion.....	45
3.2.1 Electrode Preparation	45
3.2.2 Electrochemical Processes and Structural Changes during Cycling.....	46
3.2.3 Investigating the Process at ~0.45 V	55
3.2.4 Interim Analysis and Discussion of the Electrochemistry and Electron Micrographs	58
3.2.5 Substrate-dependent Parameters	59
3.2.6 Cycling Conditions.....	65
3.2.7 Degradation Mechanism of the Si Anode and Material Factors	74
3.2.8 Performance Comparison	75

3.3 Conclusion.....	79
3.4 Experimental Section	81
3.4.1 Materials.....	81
3.4.2 Methods.....	81
Chapter 4 Structural Impact of Fluoroethylene Carbonate and Vinylene Carbonate on the Si Anode	83
4.1 Identifying Decomposition Products of FEC and VC.....	84
4.1.1 Silicon Thin-film Anodes Cycled with FEC and VC.....	85
4.2 Results and Discussion.....	88
4.2.1 Synthesis of ¹³ C-labelled Fluoroethylene Carbonate for NMR Studies.....	88
4.2.2 Impact of FEC and VC as Electrolyte Additives on the Stability of the Silicon Thin-film Electrode.....	91
4.3 Conclusion.....	110
4.4 Experimental Section	111
4.4.1 Materials.....	111
4.4.2 Synthesis of ¹³ C ₃ -Fluoroethylene Carbonate 2	111
4.4.3 Methods.....	111
Chapter 5 Poly(phosphazene) Coatings to Stabilise the Si Thin-film Anode.....	113
5.1 Poly(phosphazene) Gel Electrolytes	114
5.2 Results and Discussion.....	116
5.2.1 Synthesis of the Poly(phosphazenes)	116
5.2.2 Coating Process onto the Thin-Film Electrode	120
5.2.3 Electrochemical Performance	123
5.2.4 Electron Microscopy and Energy-Dispersive X-ray Spectroscopy.....	130
5.2.5 Synergies of the PN(MEE) Coating with Electrolyte Additives.....	135
5.3 Silicon Anode Stabilisation with Phosphazene Coatings.....	138
5.4 Conclusions	140

5.5 Experimental	142
5.5.1 Materials.....	142
5.5.2 Experimental Details	142
5.5.3 Methods.....	143
Chapter 6 Preliminary Work Towards Poly(phosphazene) Silicon Surface Grafts.....	145
6.1.1 Synthesis.....	145
6.1.2 Attempted Functionalisation of Si-H Wafer and Nanoparticle Surfaces	147
6.1.3 Functionalisation of Oxide-covered Silicon Wafers	149
6.1.4 Direct Polymer Growth from Si Nanoparticles.....	150
6.2 Experimental	153
6.2.1 Materials.....	153
6.2.2 Phosphoranimine and Polymer Syntheses.....	153
6.2.3 Methods.....	156
Chapter 7 Summary and Conclusion	157
References	161

List of Figures

Figure 1.1: Working principle of a lithium ion battery	3
Figure 1.2: Specific energy and power of common rechargeable battery technologies and prospective lithium air technology	4
Figure 1.3: Three major anode technologies for LIBs: intercalation, conversion and alloying materials	5
Figure 1.4: Overview of intercalation materials in terms of capacity density and specific capacity.....	6
Figure 1.5: a) Chemical structures of the LP30 electrolyte: LiPF ₆ , EC and DMC. b) Tetrahedral coordination modes of the carbonates to the lithium ion	8
Figure 1.6: a) Advanced mosaic model of the SEI with inorganic and organic components in grains with conduction <i>via</i> grain boundaries. b) Proposed two-layer/two-mechanism model on an SEI composed of inorganic Li ₂ CO ₃ covered by a porous organic layer.	9
Figure 1.7: Relative energy diagram of the electrode potentials of a functioning LIB.....	10
Figure 1.8: SEI growth and continuous formation on silicon nanoparticles during electrochemical cycling.....	11
Figure 1.9: Presentation of the three most common nano-silicon anodes.....	12
Figure 1.10: Summary of the electrochemistry and structural changes during lithiation of silicon anode materials.....	14
Figure 1.11: a) Proposed lithiation mechanism of silicon nanoparticles b) Proposed lithiation mechanism of silicon thin-films	16
Figure 1.12: a) Ionic and electronic conductivities observed in thin LiPON layers depending on its thickness. b) Electrochemical performance of a 200 nm silicon thin-film electrode coated with LiPON c) Micro-channels forming in the material leading to electrolyte decomposition and delamination	17
Figure 1.13: a) Yolk-shell structures of Si nanoparticles. b) Performance of the yolk-shell material c) Pomegranate-inspired agglomerates	18
Figure 1.14: a)-b) TEM micrographs of pristine and LiF coated silicon nanoparticles. c) Electrochemical performance of the pristine and coated nanoparticles.....	19

Figure 1.15: Surface-grafted artificial SEIs reported by Gao <i>et al.</i> and Shen <i>et al.</i> for silicon anode materials.....	20
Figure 1.16: Monomeric, trimeric and polymeric phosphazenes.....	20
Figure 1.17: Molecular structure of A	21
Figure 1.18: Bond lengths and angles in $[\text{PCl}_2\text{N}]_n$ B	22
Figure 1.19: Overview of the concepts discussed in this thesis.....	25
Figure 2.1: Schematic of the principle functionality of a magnetron sputter coater.....	27
Figure 2.2: Coin cell components and active materials used for the lithium half-cells.	29
Figure 2.3: Exemplary a) voltage profile and b) differential plot thereof, of a typical first galvanostatic cycle of an amorphous silicon electrode	30
Figure 2.4: Interactions of the electron beam with the sample.	32
Figure 2.5 a) Incident of a high-energy electron with an atom. b) Stylised EDS	33
Figure 3.1: a) Micrograph of a Si thin-film after cycling (top), and a photograph of cracked mud of a dried-out lake (bottom). b) Delamination process of silicon islands	40
Figure 3.2: SEM micrographs of a) pristine 500 nm silicon thin-film anodes and cycled anodes: b) 1 μm , 5 cycles, c) 500 nm, 5 cycles, and d) 200 nm, 10 cycles. e) Comparison of the critical Si island size depending on the thin-film thickness.	42
Figure 3.3: Electrochemical cycling performance of a Si thin-film anode (275 nm) on different current collectors.	43
Figure 3.4: Illustration of the parameters investigated on the sputtered silicon thin-film electrodes.....	37
Figure 3.5: Photographs of the different stages during the preparation of the silicon thin-film anodes.....	45
Figure 3.6: SEM micrographs showing the area of EDS acquisition and the corresponding spectra (15 kV) of the 100 nm <i>a</i> -Si thin-film anodes on a) CR Cu and b) 250 nm Ni-coated CR Cu.....	46
Figure 3.7: Voltage profiles of several cycles of the 100 nm <i>a</i> -Si thin-film anode on Ni-coated CR Cu.....	47

Figure 3.8: Electrochemical performance of the 100 nm <i>a</i> -Si thin-film anode on Ni-coated CR Cu.....	49
Figure 3.9: Analysis of the voltage and height of the dQ/dV peaks of the 100 nm <i>a</i> -Si thin-film anodes on Ni-coated CR Cu.	50
Figure 3.10: a) Voltage profile and b) differential plot of the first cycle of a 100 nm <i>a</i> -Si thin-film anode on Ni-coated CR Cu. Electron micrographs (5 kV) of a c) fully lithiated anode and d) delithiated anode.	51
Figure 3.11: Electron micrographs (5 kV) of the 100 nm <i>a</i> -Si thin-film anodes on Ni-coated CR Cu after 30 cycles.....	52
Figure 3.12: SEM micrographs (5 kV) of the 100 nm <i>a</i> -Si thin-film anodes on Ni-coated CR Cu after 200 cycles.....	52
Figure 3.13: a-c) SEM micrographs (5 kV) of the FIB cross section of a 100 nm <i>a</i> -Si thin-film anode on Ni-coated CR Cu after 200 cycles.	53
Figure 3.14: SEM micrographs and EDS spectra (15 kV) of the surface (a) and the cross section (b) of a 100 nm <i>a</i> -Si thin-film anode on Ni-coated CR Cu after 200 cycles.....	54
Figure 3.15: a-c) SEM micrographs of a 100 nm <i>a</i> -Si thin-film anode on Ni-coated CR Cu after 200 cycles under increasing beam acceleration voltage. d) EDS element maps.....	55
Figure 3.16: a) Electrochemical performance of two cells with 100 nm <i>a</i> -Si thin-film anodes on Ni-coated GG Cu showing differences in CE and a highlighted process at ~0.45 V..	56
Figure 3.17: SEM micrographs and EDS element maps (15 kV) of the cycled 100 nm <i>a</i> -Si thin-film anodes on Ni-coated GG Cu from Cell A and Cell B after 75 cycles.	57
Figure 3.18: Electron micrographs (5 kV) of the 100 nm <i>a</i> -Si thin-film anodes on Ni-coated a) CR Cu and b) GG Cu.	60
Figure 3.19: Electrochemical performance over 200 cycles of a 100 nm <i>a</i> -Si thin-film anode on Ni-coated GG Cu.....	60
Figure 3.20: SEM micrographs (5 kV) of the 100 nm <i>a</i> -Si thin-film anodes on Ni-coated CR Cu and GG Cu after 0, 30, and 200 or 500 cycles, respectively.....	61
Figure 3.21: Electrochemical performance over 100 of the 100 nm, 200 nm and 600 nm <i>a</i> -Si thin-film anodes on Ni-coated GG Cu.	62

Figure 3.22: Voltage profiles for the first cycle (a, b) and the 15 th cycle (c, d) of the 100 nm and 600 nm <i>a</i> -Si thin-film anodes on Ni-coated CR Cu.....	63
Figure 3.23: a) Electrochemical performance of the 100 nm <i>a</i> -Si thin-film anode on GG Cu and on Ni-coated GG Cu.....	64
Figure 3.24: Electrochemical performance over 200 cycles of the 100 nm <i>a</i> -Si thin-film anodes on Ni-coated CR Cu and GG Cu at a rate of 1C..	66
Figure 3.25: a) Electrochemical performance over 30 cycles of the 100 nm <i>a</i> -Si thin-film anodes on Ni-coated CR Cu cycled at C/30, C/10, C/5 or 1C..	67
Figure 3.26: SEM micrographs (5 kV) of the 100 nm <i>a</i> -Si thin-film anodes on Ni-coated CR Cu.	68
Figure 3.27: SEM micrographs of the 100 nm <i>a</i> -Si thin-film anodes on Ni-coated CR Cu after 30 cycles.....	69
Figure 3.28: Impact of stress induced cracking of electrodes cycled at low rates and high rates indicating deeper lithiation at lower rates and finer crack formation in surface near region due to local high stress areas in the material at high rates.	70
Figure 3.29: Voltage plots (a, c) and the corresponding dQ/dV plots (b, d) of the 2 nd and 30 th cycle of the 100 nm <i>a</i> -Si thin-film anodes on Ni-coated CR Cu cycled to 5 mV, 45 mV and 100 mV, respectively.....	71
Figure 3.30: SEM micrographs (5 kV) of the 100 nm <i>a</i> -Si thin-film anodes on Ni-coated CR Cu after 10 cycles to a-b) 5 mV, c-d) 45 mV and e-f) 100 mV.	72
Figure 3.31: Impact of differences in cut-off voltage on the thin-film electrode expansion during electrochemical cycling.....	72
Figure 3.32: Li ₂ Si formation peak position in the differential plots for the first 30 cycles of the 100 nm silicon thin-film anode at different cut-off voltages.....	73
Figure 3.33: Outlined degradation mechanism of the 100 nm <i>a</i> -Si thin-film electrode following the CE (red trace) over the lifetime of the lithium half-cell.....	74
Figure 3.34: Proposed mechanism of accelerated delamination of cracked silicon pieces by levering forces of silicon flakes in contact during lithiation.....	74
Figure 3.35: Theoretical specific capacity for a full cell as the function of the specific capacity of the anode (silicon), employing a LiCoO ₂ cathode.....	73

Figure 4.1: Proposed decomposition products of FEC and VC and the proposed, cross-linked structure of poly(VC)..	85
Figure 4.2: a) Discharge capacity and b) CE of the first 80 cycles of a lithium half-cell with 200 nm silicon thin-film electrodes cycled in 1.3 M LiPF ₆ EC/DEC (3/7, v/v) with and without 3 wt.% FEC; c) SEM micrograph of the anode surface after 80 cycles from the cell without FEC and d) with FEC.	86
Figure 4.3: a) Capacity retention and CE over 500 cycles for lithium half-cells with 500 nm silicon thin-film electrodes in 1.0 M LiPF ₆ EC/propylene carbonate (PC)/DMC (1/1/3, v/v/v) with and without 2 wt.% VC. b-c) Micrographs of the electrode surface after the 30 th charge without and with 2% VC electrolyte additive; and FIB cross sections of the electrodes after 500 cycles without (d) and with 2% VC (e).	87
Figure 4.4: Possible polymer fragments formed from FEC or VC decomposition.	91
Figure 4.5: Electrochemical performance over 300 cycles of the 100 nm <i>a</i> -Si thin-film anodes on Ni-coated GG Cu cycled in pure LP30, LP30 + 10% FEC, and LP30 + 5% VC.	92
Figure 4.6: Voltage profiles (a, c, e) and differential plots (b, d, f) of the 100 nm <i>a</i> -Si thin-film anodes on Ni-coated GG Cu cycled with pure LP30, LP30 + 10% FEC and LP30 + 5% VC for the 1 st , 75 th , and 300 th cycle, respectively.	94
Figure 4.7: Maps of the intensity of the electrochemical processes observed in the dQ/dV plots below 650 mV for 100 nm <i>a</i> -Si thin-film anodes on Ni-coated GG Cu in a) pure LP30, b) LP30 + 10% FEC and c) LP30 + 5% VC over 200 cycles.	95
Figure 4.8: Capacity (a) and voltage (b) and height (c) of the Li ₂ Si dQ/dV peaks of the cells cycled with pure LP30, LP30 + 10% FEC and LP30 + 5% VC.	96
Figure 4.9: a) Capacity loss per cycle for cells with 100 nm <i>a</i> -Si thin-film anodes on Ni-coated GG Cu cycled with pure LP30, LP30 + 10% FEC and LP30 + 5% VC. b) Accumulated capacity loss over 350 cycles.	97
Figure 4.10: Photograph of the cycled 100 nm <i>a</i> -Si electrodes on Ni-coated GG Cu cycled in pure LP30 (a), LP30 +10% FEC (b) and LP30 +5% VC (c)	98
Figure 4.11: SEM micrographs of 100 nm <i>a</i> -Si thin-film anodes on Ni-coated GG Cu cycled in pure LP30 (a-c, 500 cycles), LP30 + 10% FEC (d-f, 400 cycles) and LP30 + 5% VC (g-i, 375 cycles).	99

Figure 4.12: SEM micrographs of 100 nm <i>a</i> -Si thin-film anodes on Ni-coated CR Cu after 200 cycles in pure LP30 (a-c), LP30 + 10% FEC (d-f) and LP30 + 10% VC (g-i).....	100
Figure 4.13: FIB SEM micrographs of 100 nm <i>a</i> -Si thin-film anodes on Ni-coated Cu current collectors cycled in pure LP30 (a-c, 200 cycles, CR Cu), LP30 + 10% FEC (d-f, 200 cycles, CR Cu) and LP30 + 5% VC (g-i, 375 cycles, GG Cu).	101
Figure 4.14: SEM micrographs and EDS point scan spectra (15 kV) of the FIB cross sections of 100 nm <i>a</i> -Si thin-film anodes on Ni-coated current collectors cycled in pure LP30 (a, 200 cycles, CR Cu), LP30 + 10% FEC (b, 200 cycles, CR Cu) and LP30 + 5% VC (c, 375 cycles, GG Cu)..	103
Figure 4.15: SEM micrographs and EDS element maps of the FIB cross sections of the 100 nm <i>a</i> -Si thin-film anodes on Ni-coated Cu current collectors cycled in LP30 (a, 200 cycles, CR Cu), LP30 + 10% FEC (b, 200 cycles, CR Cu) and LP30 + 5% VC (c, 375 cycles, GG Cu)..	105
Figure 4.16: Structural evolution of a cracked silicon thin-film anode during continuous cycling and SEI formation.	107
Figure 5.1: a) Photograph of a cross-linked poly(phosphazene) gel electrolyte. b) Possible coordination mode of a lithium cation by a fragment of the ethylene oxide substituted poly(phosphazene).	114
Figure 5.2: I) Structures of the poly(phosphazene) MEEP and LiBOB used in the studies. II) Experimental microscopy setup to monitor the formation of lithium dendrites, looking at the gel electrolyte in between two pieces of lithium metal. III) Continuous plating and stripping for 30 h each at 60°C and a current density of 0.1 mAcm ⁻³	115
Figure 5.3: Illustration of the lithium ion transport in the gel electrolyte	115
Figure 5.4: ³¹ P { ¹ H} NMR spectra (THF- <i>d</i> ₈ , 400 MHz) of PN(MEE) (top) and PN(CF) (bottom).	117
Figure 5.5: ¹ H NMR spectra (THF- <i>d</i> ₈ , 400 MHz) of PN(MEE) (top) and PN(CF) (bottom)..	118
Figure 5.6: MALDI TOF mass spectra of a) PN(MEE) and b) PN(CF).....	120
Figure 5.7: Photograph and SEM images of 100 nm <i>a</i> -Si thin-film anodes on Ni-coated CR Cu coated with PN(MEE) and PN(CF).....	121
Figure 5.8: Water contact angles measured for the a) bare, b) PN(MEE)-coated and c) PN(CF)-coated silicon thin-film anodes.	122

Figure 5.9: Electrochemical performance over 500 cycles of 100 nm <i>a</i> -Si thin-film anodes on Ni-coated CR Cu bare, and coated with PN(MEE) or PN(CF).....	123
Figure 5.10: Voltage profiles (a, c, e) and differential plots (b, d, f) of 100 nm <i>a</i> -Si thin-film anodes on Ni-coated CR Cu without a coating, and PN(MEE) and PN(CF) coatings. a-b) 1 st cycle, c-d) 10 th cycle and e-f) 100 th cycle.	125
Figure 5.11: Electrochemical performance of the PN(CF)-coated 100 nm <i>a</i> -Si thin-film electrode on Ni-coated CR Cu after lowering the cut-off voltage from 100 mV to 40 mV on the 500 th cycle and restarting after resting on the 550 th cycle for 3 days.	126
Figure 5.12: Maps of the intensities of the electrochemical processes observed in the dQ/dV discharge plots below 650 mV for the 100 nm <i>a</i> -Si thin-film anodes on Ni-coated CR Cu coated with a) PN(MEE) (400 cycles) and b) PN(CF) (650 cycles).	127
Figure 5.13: Capacity (a) and voltage and height of the Li ₂ Si (b-c) and electrochemical process at ~0.45 V (d-e) dQ/dV peaks of the cells cycled with and without PN(MEE) or PN(CF)...	128
Figure 5.14: a) Capacity loss per cycle for cells with 100 nm <i>a</i> -Si thin-film anodes on Ni-coated CR Cu without a coating and PN(MEE) and PN(CF) coatings. b) Inset showing the capacity loss between the 200 th and 500 th cycle. c) Accumulated capacity loss over 700 cycles.	129
Figure 5.15: SEM micrographs of the cycled 100 nm <i>a</i> -Si thin-film anodes on Ni-coated CR Cu with and without poly(phosphazene) coatings.	130
Figure 5.16: SEM micrographs of the blade-cut cross section of the 100 nm <i>a</i> -Si thin-film anodes on Ni-coated CR Cu coated with a) PN(MEE) after 500 cycles and b) PN(CF) after 525 cycles.	131
Figure 5.17: SEM micrographs (10 kV) of the FIB cross section of the 100 nm <i>a</i> -Si thin-film anodes on Ni-coated CR Cu with and without poly(phosphazene) coatings.	132
Figure 5.18: SEM micrographs and EDS element maps (15 kV) of the FIB cross section of the 100 nm <i>a</i> -Si thin-film anodes on Ni-coated CR Cu without and with poly(phosphazene) coatings.....	134
Figure 5.19: Electrochemical performance over 350 cycles of the 100 nm <i>a</i> -Si thin-film anodes on Ni-coated CR Cu coated with PN(MEE) with different electrolytes: pure LP30, LP30 + 10% FEC, LP 30 + 5% VC.....	135

Figure 5.20: a) Accumulated capacity loss in cells with PN(MEE)-coated with 100 nm <i>a</i> -Si thin-film anodes on Ni-coated CR Cu cycled in pure LP30, LP30 +10% FEC and LP30 + 5% VC electrolytes. b) Inset showing the accumulated capacity loss over the first 100 cycles. .	136
Figure 5.21: SEM micrographs of cycled 100 nm <i>a</i> -Si thin-film anodes on Ni-coated CR Cu in LP30 and a) 10% FEC (200 cycles), b) 5% VC (200 cycles), c) 10% FEC underneath the PN(MEE) coating (400 cycles), d) 5% VC underneath a PN(MEE) coating (375 cycles). e) Peeled-off PN(MEE) (10% FEC sample), f) partially peeled-off PN(MEE) (5% VC sample).	136
Figure 5.22: SEM micrograph and EDS element maps of the peeled-off PN(MEE) coating for the cell cycled with LP30 + 10% FEC.	137
Figure 5.23: FIB SEM images showing the different components and proposed stabilisation mechanisms thereof.	138
Figure 5.24: Summary of the impact found of the different polymer coatings on the long-term cyclability of the silicon thin-film electrode.	141
Figure 6.1: ¹ H NMR spectra of G before (top) and after 72 h (bottom) in non-dried CDCl ₃ .	147
Figure 6.2: ³¹ P{ ¹ H} NMR spectra of the stages of polymerisation from the allylamino phosphoranimine G .	148
Figure 6.3: Contact angles measured for the Piranha treated silicon wafers after 1 h at 70°C in a) toluene, b) 1 vol% APTES on toluene, c) 1 vol% 9 in toluene and d) 1 vol% 10 in toluene.	149
Figure 6.4: C 1s, N 1s and F 1s XPS scans of the silicon wafers treated with toluene and 1 vol% solutions of APTES, 9 , and 10 in toluene.	150
Figure 6.5: Vials containing 10 mg of pristine silicon nanoparticles and silicon nanoparticles from the polymer growth experiment in THF directly after sonicating (a), after 90 min (b) and after 24 h (c).	151
Figure 6.6: TEM micrograph (a) and EDS spectrum (b) and element maps (c) of the silicon nanoparticles after the attempted growth of a poly(phosphazene) from the surface.	152

List of Schemes

Scheme 1.1: Reaction pathways to yield poly(chlorophosphazene) B . Thermal polymerisation from the hexachlorotrimer A , thermal “living” condensation from the monomer C and catalysed cationic “living” polymerisation from the monomer D	23
Scheme 1.2: Functionalisation of B with alcohols (IV), amines (V) and organometallic compounds (VI).	24
Scheme 4.1: Synthesis of ¹³ C ₃ -FEC 2	88
Scheme 4.2: Top: Structural motifs identified by solution and solid-state NMR from silicon nanowires cycled in LP30 + 10 vol.% ¹³ C ₃ -FEC. The fragments are proposed to form following the degradation pathways shown and are shaded in the respective colours where appearing: (3.1) Initial reduction of fluoroethylene carbonate through fluoride abstraction to form radical A and subsequent formation of a vinoxyl radicals (B & C) or vinylene carbonate. (3.2 & 3.3) possible reaction of VC with fragments B or C to form species capable of forming poly(VC). (3.4 & 3.5) Reactions of vinoxyl radicals with alkene functionalities. (3.6) Possible reaction of the vinoxyl radical with an aldehyde. (3.7) Formation of branched polymeric species through the attack of the species formed in 3.5 onto an aldehyde. (3.8) Reaction of a PEO-type chain, proposed to be formed from ethylene carbonate with an alkene. Reprinted with permission from reference ^[171] . Copyright 2017, American Chemical Society.	89
Scheme 5.1: Synthetic pathway for PN(MEE) 6 and PN(CF) 7 ; synthesis of the Cl ₃ PN(SiMe ₃) monomer D ; living cationic polymerisation to yield poly(chlorophosphazene) 5 ; chloride substitution with alkoxide side-chain to form the substituted polymers 6 and 7 i) 2.1 eq. NaOEtOEtOMe, THF, 5 d; ii) 1.5 eq. NaOEtOEtOMe, THF, 2 d + 1.5 eq. NaOCH ₂ CF ₃ , THF, 2 d). The ratio of side chains in 7 was determined by ¹ H NMR.	116
Scheme 5.2: a) Depiction of the assumed structure of the cross-linked polymers; b) mechanism of the UV induced radical formation of the ethylene glycol side-chains with benzophenone. ^[209]	122
Scheme 6.1: Amino phosphoranimines with different linkers, that match the reactivity of common silicon surface functionalities.	146
Scheme 6.2: Synthetic pathway to amino phosphoranimines VII	147
Scheme 6.3: Synthesis of a poly(phosphazene) from the allylamino phosphoranimine G <i>via</i> the “living” cationic polymerisation.	148

List of Tables

Table 3.1: Performance comparison of cells cycled in this work and literature reports.	76
Table 4.1: Figures from the cycling data of the 100 nm <i>a</i> -Si thin-film electrodes on Ni-coated GG Cu cycled in pure LP30, LP30 + 10% FEC, and LP30 + 5% VC.	93
Table 5.1: Number average molecular weight (M_n), mass average molecular weight (M_w) and polydispersity index (\mathcal{D}) of the polymers PN(MEE) and PN(CF) determined by GPC in DMF.	119
Table 5.2: Figures from the cycling data of the 100 nm <i>a</i> -Si thin-film electrode on Ni-coated CR Cu without a coating and coated with PN(MEE) and PN(CF).	124

List of Abbreviations

δ	Chemical shift
μm	Micrometre
Å	Ångström
D	Polydispersity index
A	Ampere
a.u.	Arbitrary units
abs.	Absoluted
AFM	Atomic force microscopy
APTES	(3-Aminopropyl)triethoxysilane
C/n	Charge rate
ca.	Circa
calc.	Calculated
CE	Coulombic efficiency
CEI	Cathode electrolyte interphase
CR Cu	Cold-rolled copper foil
CVD	Chemical vapour deposition
d	Doublet (NMR)
Da	Dalton
DC	Direct current
DCM	Dichloromethane
DMC	Dimethyl carbonate
dQ/dV	First differentiation plot of a galvanostatic voltage profile
EC	Ethylene carbonate
EDS	Energy-dispersive X-ray spectroscopy
EELS	Electron energy loss spectroscopy
e.g.	<i>Exempli gratia</i>

eV	Electronvolt
FEC	Fluoroethylene carbonate
FIB	Focussed ion beam
g	Gram
GG Cu	Copper foil for graphene growth
h	Hour
HOMO	Highest occupied molecular orbital
Hz	Hertz
<i>i.e.</i>	<i>Id est</i>
ICL	Initial capacity loss
LCO	Lithium cobalt oxide
LIB	Lithium ion battery
LiBOB	Lithium bis(oxolato)borate
LiPON	lithium phosphorus oxynitride
LP30	Electrolyte: 1 M LiPF ₆ in EC and DMC, 50/50, v/v
LUMO	Lowest unoccupied molecular orbital
m	Multiplet (NMR)
\bar{M}_n	Number average molar mass
\bar{M}_w	Mass average molar mass
MALDI	Matrix-assisted laser desorption/ionisation
MeCN	Acetonitrile
mmHg	Millimetre of mercury
m/z	Mass per charge
nm	Nanometre
NMR	Nuclear magnetic resonance
Pa	Pascal
PN	Phosphazene

ppm	Parts per million
PVD	Physical vapour deposition
q	Quartet (NMR)
R	Organic side-group
RF	Radio frequency
s	Singlet (NMR)
sccm	Flow unit, $\text{cm}^3 \text{min}^{-1}$
SEI	Solid electrolyte interphase
t	Triplet (NMR)
TEM	Transmission electron microscopy
THF	Tetrahydrofuran
TM	Transition metal
ToF-SIMS	Time-of-flight secondary ion mass spectrometry
UV	Ultraviolet
VC	Vinylene carbonate
Vs.	Versus
W	Watt
WCA	Water contact angle
XPS	X-ray photoelectron spectroscopy
XRD	X-ray diffraction

Chapter 1 Introduction

1.1 Global Energy Demand and Climate Effects

Today's society relies on a constant supply of energy more than ever before. The global energy consumption has increased by 2.3% in 2018, this is higher than any year since 2010, and can be linked to the flourishing global economy and increased heating and cooling demands around the globe. The need for electrical energy has increased twice as fast (by 4%) as the overall energy demand.^[1] Most energy is generated from burning natural gas, oil and coal. While the consumption of fossil fuels rose once again in the last year, its share of the entire energy generated has decreased, with renewable energy sources on the rise. Renewables accounted for more than 25% of the global power output last year and in combination with nuclear power are the main sources of electricity. However, the increase in energy demand is still reflected in an increase in CO₂ emissions.^[1] Due to the large increase in greenhouse gas emissions, the United Nations body for assessing climate change-related science, the Intergovernmental Panel on Climate Change (IPCC), released a special report estimating that global warming may reach 1.5°C between 2030 and 2052.^[2] In its current state, global warming to ~1°C above pre-industrial levels has already led to catastrophic effects in many regions.^[2] A further increase may lead to extreme temperatures, heavy precipitation and higher risk of drought in some regions and, combined with an increase in sea-level, will require adaption of human and ecological systems.^[2] An overall increase in renewable energy sources is needed urgently so that the estimated 1.5°C increase in global mean-temperature is not exceeded.^[3]

A major problem is that renewable energy sources suffer from their intermittent nature. Solar power is available during the day and may only generate significant amounts of energy in certain months, depending on the geographical location. Wind turbines are affected by great uncertainty in weather conditions and may only be reliable in specific locations, on or near coastal areas for example.^[4] However, both technologies are capable of sustaining the grid at peak times and may generate surplus electrical energy.^[4] To succeed in generating greener energy, solutions must be found to store the surplus electrical energy and retrieve it during periods in which solar and wind power generation are not directly available. Most of the energy surplus generated during the day by any source is stored as pumped-storage hydropower by pumping water into an elevated reservoir to be released on demand, generating power by passing through turbines. However, this depends on the availability of hydroelectric facilities. There are many other solutions to grid storage that utilise mechanical, electrical, chemical, or

electrochemical ways of storing energy which have specific advantages and drawbacks.^[5-7] Electrochemical energy storage in the form of batteries is in many ways a highly favourable solution. Batteries provide high charge-discharge efficiencies and long cycle life, are flexible regarding their power and energy characteristics, and are pollution-free during operation while being low in maintenance. Due to their compact size, batteries can be used at specific locations to control energy fluctuations for parts of the grid or as off-grid solutions.^[6] Recent developments have significantly lowered the price for lithium ion battery packs, 75% since 2012 (volume-weighted average), currently costing an average of \$176 per kWh. The price is projected to drop further to almost half of this by 2024 and to a third by 2030.^[8] Even considering the initial expense of solar power generation, this can lead to cheaper energy than that obtained from burning fossil fuels. Large scale installations are already being considered for solar generation combined with battery storage. Recently, Los Angeles, California, has unveiled plans to construct a large solar farm backed by large lithium ion-batteries (LIBs) capable of providing 7% of the energy demand of the city by 2023 and reducing the need to burn natural gas when there is no sunlight.^[9] LIBs have also found application as energy-storage options in individual households. While these technologies are well-developed and improving every year, policy makers need to catch up with the current technology involved in battery storage to ensure year-on-year reduction of carbon emissions.^[10]

An enormous market has emerged for electric vehicles and LIBs are playing a key role. It is expected that battery-powered electric vehicles will make up more than half of the market by 2040, surpassing the sales of new vehicles fitted with internal combustion engines by 2035.^[11] The production and use of electric vehicles may not lower the carbon footprint per vehicle at this point in time, given the current grid-power mix, but will undoubtedly lower local pollutant levels in highly populated areas.^[12,13] Currently, the life cycle analysis of LIBs shows that especially the active cathode material, the aluminium used for current collectors and casing and the energy used for cell production have a high environmental impact.^[14] Finding cleaner ways to source the necessary materials or swapping them for greener options and choosing efficient fabrication methods may lead to a significant decrease in emissions.

To maintain the course towards reducing greenhouse gas emissions and to limit pollution, the development of better and cheaper energy storage solutions is key. LIBs, as the most sophisticated battery technology to date, need to be pushed further to increase capacity and functionality through the development of new materials, making them a viable option for small and middle-scale energy storage solutions.

This thesis aims to investigate ways of using silicon as an anode material better and make it a viable option to use in LIBs. This chapter provides information on the necessary battery components and outlines the difficulties for Si as an active electrode material as well as its importance to create LIBs of increased energy density.

1.2 Lithium Ion Batteries (LIBs)

The lithium ion battery was introduced commercially by the company Sony in the 1990s and followed decades of research on the electrochemical properties of lithium and materials that are capable of hosting lithium ions.^[15] Only recently, their impact has been acknowledged in form of the Nobel prize for Goodenough, Whittingham and Yoshino, who developed the concept, the necessary materials and laid the foundation for the LIB as we know it today.^[16] Figure 1.1 shows a schematic of the cell introduced by Sony which consists of a graphite anode, an organic electrolyte mixture and a lithium cobalt oxide (LCO) cathode.

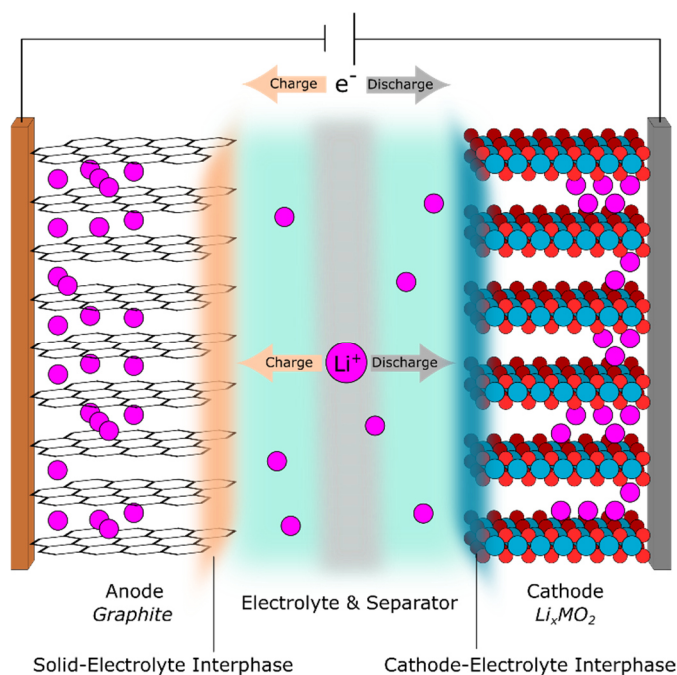


Figure 1.1: Working principle of a lithium ion battery bearing a graphitic anode, an organic electrolyte and separator and a lithium metal oxide cathode. Solid electrolyte interphases are formed on the electrodes during operation.

Upon charging, lithium ions move from the lithium metal oxide cathode to the graphitic anode where they recombine with electrons and intercalate in the layered carbon structure. Upon discharge the lithium ions migrate to the cathode, following an electrochemical potential gradient. This is not a perfect system since, during operation, the cell will lose capacity

irreversibly due to structural faults in the electrode materials and the degradation of the liquid electrolyte, forming solid-electrolyte interphases (SEIs) on the electrode surfaces. The SEI has proven to be beneficial for the cells comprising of stable electrodes that show little volume expansion. On graphitic materials, a sufficiently stable SEI is formed from the organic electrolyte that allows lithium ions to pass through and limits further reduction of the electrolyte on the surface. The term SEI is nowadays associated with the interphase formed on the anode, whereas the layer formed on the cathode is commonly referred to as the cathode-electrolyte interphase (CEI).

Today, LIBs stand out from other established battery technologies, like nickel-cadmium (NiCd), nickel metal hydride (NiMH) and lead-acid batteries, and may even be more applicable for energy storage on a larger scale than vanadium redox-flow technology in its current state (Figure 1.2).^[17]

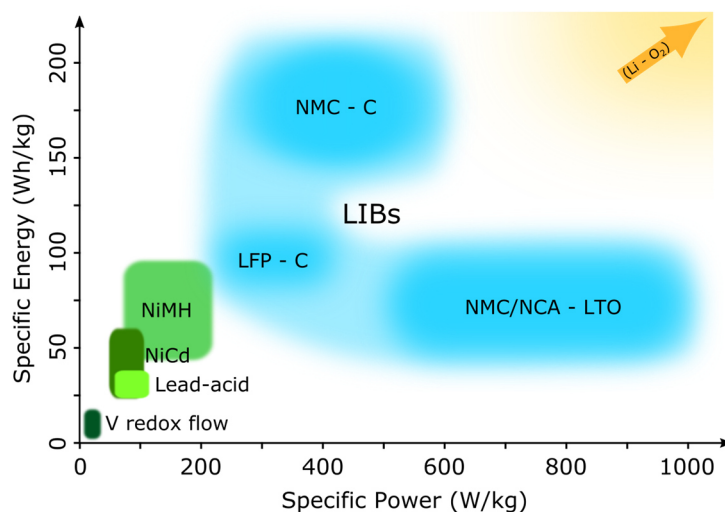


Figure 1.2: Specific energy and power of common rechargeable battery technologies and prospective lithium air technology with capacities beyond the scale. Adapted from references ^[6,18].

LIBs are currently available in different compositions and offer a choice of anode and cathode materials. LIBs with LCO cathodes are being replaced by cells comprising of lithium iron phosphate (LFP), lithium nickel manganese cobalt oxide (NMC) of different stoichiometries or lithium nickel cobalt aluminium oxide (NCA) cathodes combined with graphitic but also lithium titanate (LTO) anodes.^[19] The materials offer different advantages beyond their specific capacities, such as increased safety during cycling, charging speeds and levels of toxicity.

Offering enormous capacities, lithium metal anodes are currently used in disposable batteries. Enabling rechargeable lithium metal batteries is a major goal of ongoing research,

trying to mitigate the safety issues arising from lithium dendrite formation and short-circuiting that are characteristic of lithium metal electrodes. This technology could solve many capacity related issues, even if only a fraction of the 11680 Whkg^{-1} theoretical energy obtained by the oxidation of lithium can be used reversibly. The highest specific power could be achieved by creating a secondary lithium-air (Li-O_2) battery,^[20] but other technologies such as lithium-sulphur batteries also offer increased capacities and are moving towards specific applications.^[21]

1.2.1 Anode Materials

Anode materials can be divided into three major categories: intercalation, conversion and alloying materials (Figure 1.3).^[22] The characteristics of the anode materials affect the capacity, working potential and lifetime of the cell.

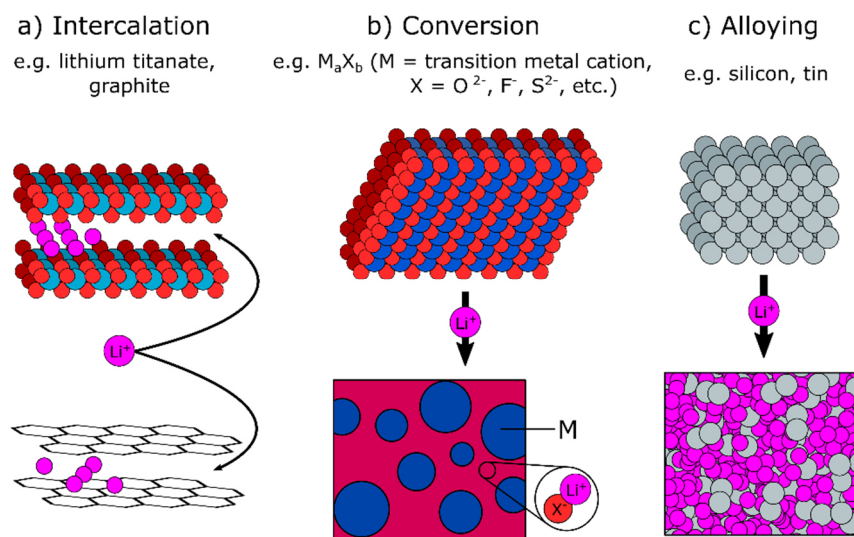


Figure 1.3: Three major anode technologies for LIBs: intercalation, conversion and alloying materials. a) Intercalation of lithium between 2D sheets of titanates or graphite. b) Conversion of a metal salt with lithium ions forming metal nanoparticles in the respective lithium salt. c) Lithium alloy formation from the elements such as tin or silicon.

Intercalation electrodes (Figure 1.3a), such as graphite or LTO, store lithium ions in between 2D sheets of material, occupying the respective coordination environments. Intercalation occurs to form compounds up to specific stoichiometries, LiC_6 and $\text{Li}_4\text{Ti}_5\text{O}_{12}$, respectively. The electrochemical potential is a crucial parameter for each anode's application. With its low operating potential ($< 200 \text{ mV vs Li/Li}^+$), graphite offers high voltages in a full cell. LTOs operate at a much higher potential ($1.2 \text{ V against Li/Li}^+$), narrowing the voltage window when used in a full cell with a TM-oxide cathode. The benefit of the lower voltage is, however, that

an SEI may not form, as electrolyte decomposition occurs outside the voltage range. This allows much faster charge and discharge rates.^[23,24]

In conversion electrodes (Figure 1.3b), such as binary transition metal compounds (M_aX_b , M = transition metal, X = O, S, F, P, etc.) the transition metal (TM) is fully reduced, and forms metal nanoparticles in a Li_yX matrix. These materials promise very high capacities, but suffer from their complicated transformation, resulting in pulverisation and loss of electrical contact and show a high voltage hysteresis (which is still poorly understood).^[25,26]

Alloying materials, just like conversion electrodes, have the advantage of exceeding the low lithium to active material stoichiometries in intercalation materials. There are phases of different lithium content that can form and affect the capacity of the anode (e.g. $Li_{4.4}Sn$ or $Li_{3.75}Si$).^[22]

Figure 1.4 shows the capacity density and specific capacity of prospective alloying materials against carbon, with increasing specific capacity from left to right.

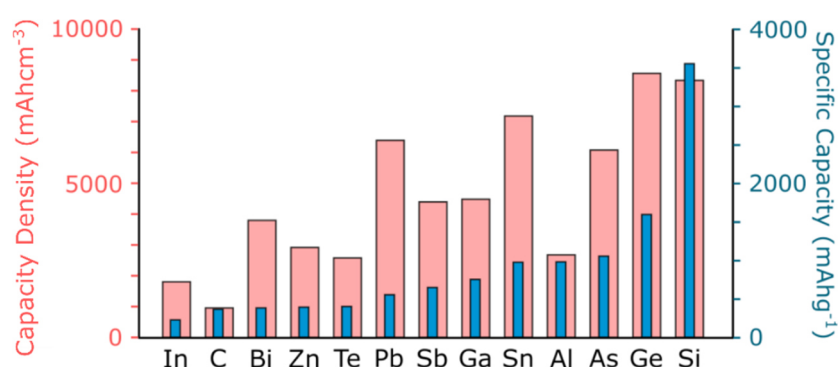


Figure 1.4: Overview of intercalation materials in terms of capacity density and specific capacity. Adapted from reference ^[22].

While elements in groups 13–15 can form lithium alloys, the lighter elements are the most promising regarding potential specific capacities. Some of the heavier elements promise high capacity densities (group 14 in particular: Si, Sn, Ge, Pb). Counterbalancing their prospective high capacities, alloying materials suffer severely from large volume expansion during lithiation, leading to fracturing and pulverisation, combined with an increased amount of SEI formed which leads to loss of electrical contact.^[22]

It should be added, that there are other materials that may influence the field of novel anode materials for LIBs, such as organic polymers (e.g. anthraquinone-based).^[27] Each of the novel anode systems has properties that impede their commercialisation which need to be addressed to make them real competitors to current intercalation anodes.

1.2.2 Cathode Materials

Currently, layered lithium metal oxides are used as cathode materials in commercial LIBs. Layered mixed-metal oxides achieve higher capacities than LCO while being more cost-efficient by using less cobalt. The maximum capacity for reversible cycling is found in NMC-811 ($\text{LiNi}_{0.8}\text{Mn}_{0.1}\text{Co}_{0.1}\text{O}_2$) at just above 200 mAhg^{-1} .^[28] Similar to NMCs, NCA has been identified as an improved cathode material offering high capacities and has been employed in commercial LIBs.^[29] Another prominent cathode material is LFP. This material may hold less lithium in its olivine structure but is a cheaper and safer option than the cobalt containing materials and is found in many commercially available LIBs.^[30] The current capacities of the cathode materials, compared to the high values expected in prospective anode materials, will make the cathode the limiting factor in designing new high energy-density batteries and therefore needs to be improved also.

1.2.3 Electrolytes

The electrolyte enables the transfer of lithium ions between the electrodes. Most LIBs use liquid mixtures of organic carbonates and inorganic lithium salts. Apart from liquid electrolytes, polymer electrolytes are currently used in LIBs and there is a strong interest in solid electrolytes for all solid-state LIBs.^[31]

Liquid organic electrolytes need to dissolve a reasonable concentration of lithium ions and allow a high transfer rate for a well-functioning LIB. As such, crucial properties are viscosity, dielectric constant and electrochemical and thermal stability for the electrolyte to operate at a given voltage and temperature. Organic carbonates are usually linear or cyclic species with aliphatic functionalities. The most common species are dimethyl carbonate (DMC), diethyl carbonate (DEC), ethylene carbonate (EC) and propylene carbonate (PC).^[32] The inorganic electrolyte salts usually feature non-coordinating anions to counter the lithium cation and increase cation mobility. Lithium salts such as lithium hexafluorophosphate (LiPF_6), lithium bis(trifluorosulfonyl)imide (LiTFSI) and lithium bis(oxolato)borate (LiBOB) are commonly found for systems reported in the literature.^[32,33] Some standard electrolyte mixtures are commercially available and consist of two or three different carbonates and a lithium salt. One of the common mixtures, LP30, is a 1 M LiPF_6 in a 50/50,v/v mixture of EC and DMC. The chemical structures of the components of LP30 and tetrahedral lithium coordination of the carbonates are shown in Figure 1.5.

Lithium can coordinate to the carbonate oxygen atoms and steric demands of the ligands play a large role in restricting the number of molecules coordinating to Li^+ ions. Therefore, while the coordination to four EC molecules is feasible, the formation of a first lithium coordination sphere with four DMC molecules may not be as favourable and may mainly be limited to three molecules depending on the lithium salt concentration. The lithium salt concentration largely affects the properties of the electrolyte.^[34,35]

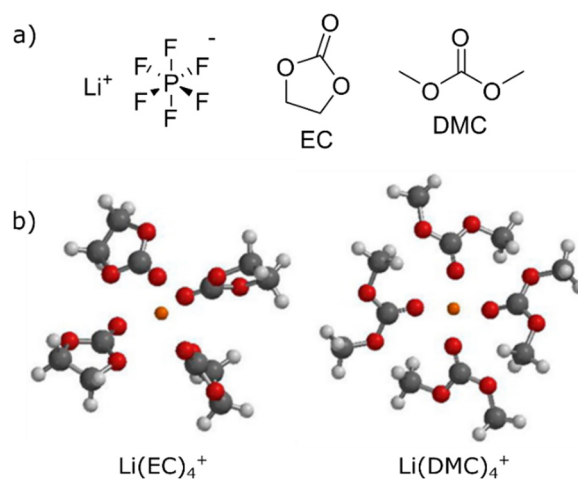


Figure 1.5: a) Chemical structures of the LP30 electrolyte: LiPF_6 , EC and DMC. b) Tetrahedral coordination modes of the carbonates to the lithium ion (grey: carbon, red: oxygen, orange: lithium, white: hydrogen). Other carbonate coordination environments and mixtures are possible. Adapted with permission from reference ^[34].

Copyright 2015 American Chemical Society.

There are many other organic carbonates and organic and inorganic salts that can be used as additives to boost the cells performance and the best performing electrolyte mixtures are rarely limited to mixtures of two aliphatic carbonates. Two of the most commonly used additives are fluoroethylene- and vinylene carbonate. The additives mainly affect the electrochemical performance by altering the composition of the SEI through different electrolyte decomposition products.^[32,36,37]

1.2.4 Other LIB Components

LIBs also contain several non-active components such as the current-collector, the separator and the casing. Particle-based active materials need conductive materials, usually high surface area carbons, and binders to form a functioning electrode and these have a significant impact on the performance. Prominent binders are different polymers such as polyvinylidene fluoride (PVDF) and carboxymethyl cellulose (CMC), but a range of conventional and unconventional novel binders have been explored.^[38,39]

Current collectors are chosen for their stability against reduction or oxidation such as copper and aluminium for the anode and cathode side, respectively. The casing is usually made of stainless steel for coin cells and polymer-coated foils for pouch cells. Separators provide a physical barrier between the electrodes to avoid short circuiting during operation. These are usually porous polymer membranes but can also be made of simple materials such as glass-fibre. Different polymer membranes have been introduced for the use in LIBs.^[40]

Recently, the design of mechanically flexible batteries has come into focus to support novel technologies such as wearable devices and flexible electronics. These require specific designs to not only provide reliable electrochemistry but also withstand mechanical stress.^[37]

1.3 Solid Electrolyte Interphase (SEI)

The SEI may be the most crucial factor for a functioning LIB and yet is still one of the least understood parts of the system.^[41] Decades of research have been dedicated to exploring its structure and composition.^[42] In a common LIB, the SEI forms on the highly reductive surface of the anode from the electrolyte and passivates it. A stable SEI will limit further degradation of the electrolyte and allow stable cycling. Two models of the SEI that have developed over time are shown in Figure 1.6

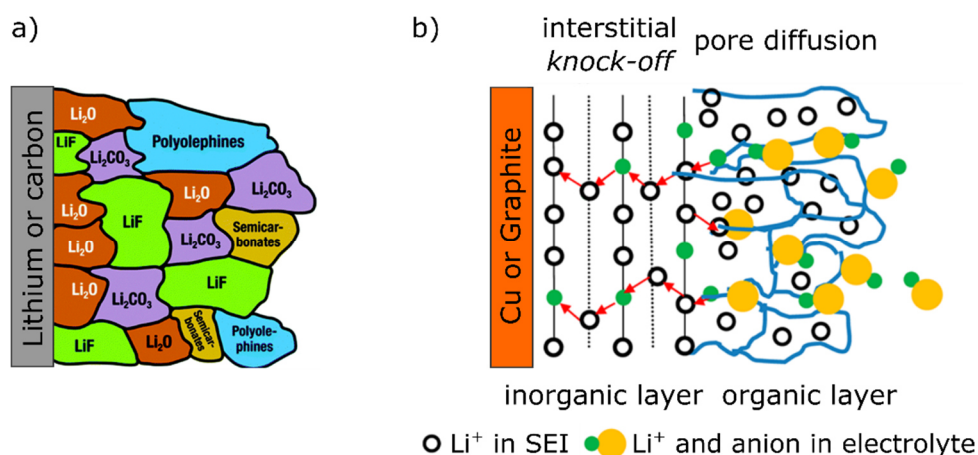


Figure 1.6: a) Advanced mosaic model of the SEI with inorganic and organic components in grains with conduction *via* grain boundaries. Adapted with permission from reference ^[43]. Copyright 1997, The Electrochemical Society. b) Proposed two-layer/two-mechanism model on an SEI composed of inorganic Li_2CO_3 covered by a porous organic layer. Lithium ions diffuse through the organic layer and go through the carbonate via a “knock-off” mechanism. Adapted with permission from reference ^[44]. Copyright 2012, American Chemical Society.

The concept of the SEI was introduced by Peled in the late 1970's as an interface between the electrode and the liquid electrolyte and has similar properties to a solid electrolyte.^[45] Later, Peled suggested that the SEI forms a mosaic like structure on the electrode, containing degradation products in the form of inorganic salts such as lithium fluoride, oxide and carbonate as well as alkoxides and polymeric structures. In this model, electrons will experience a specific resistance for each of the domains, and electron and lithium ion conductivity is mostly enabled over the grain boundaries.^[43] In later work by Shi *et al.*, the mosaic structure was proposed to be separated into an inorganic near-surface layer covered by a porous organic top layer.^[44] Their work suggests a two-step diffusion mechanism, where lithium ions diffuse through the organic layer and then initiate a “knock-off” mechanism inside the inorganic layer, allowing lithium ions to be moved stepwise towards the anode.

The SEI will form if the electrolyte readily decomposes in the cell. The principle is outlined in Figure 1.7.

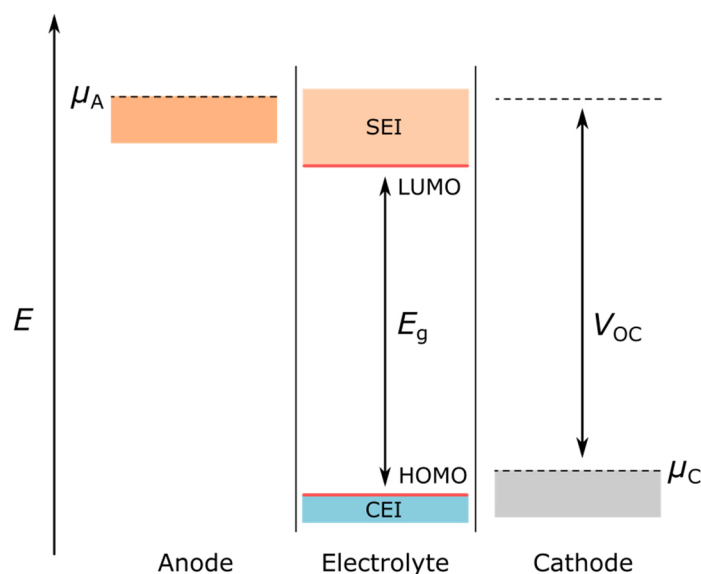


Figure 1.7: Relative energy diagram of the electrode potentials of a functioning LIB. μ_A and μ_C are the anodes and cathodes electrochemical potentials, V_{OC} is the open circuit voltage defined as $V_{OC} = \mu_A - \mu_C$. E_g is the energy gap between the HOMO and LUMO of the electrolyte. If μ_A lies outside E_g (above electrolyte LUMO) the electrolyte decomposes and forms the SEI which can stabilise the system and avoid continuous reduction of the electrolyte as V_{OC} must be $\leq E_g$. The same applies if μ_C lies outside E_g forming a CEI.

A cell will cycle stably, if the lowest unoccupied molecular orbital (LUMO) of the electrolyte components (e.g. organic carbonates, lithium salts) is higher in energy than the electrochemical potential (μ_A) of the anode and the highest molecular orbital (HOMO) is lower than that of the cathode (μ_C). If the redox potential is larger than the electrochemical stability window of the electrolyte, it will decompose. The redox potential of TM oxide cathode

materials is usually within the energy gap E_g of the organic molecules so that only very thin CEIs are observed. Anodes, however, form a large amount of SEI, as μ_A usually lies outside the stability window of the organic electrolytes (e.g. graphite, lithium metal and silicon anodes).

The formation of an SEI will reduce the energy difference between the LUMO of the electrolyte and μ_A to allow stable cycling without further electrolyte reduction. The SEI will be formed of the decomposition products of most electrolyte components, as each has a different energy gap that usually falls outside the stability window. Calculations on the stability of most common electrolyte components have been presented in the literature.^[46–48]

1.4 Silicon as an Anode Material for LIBs

As introduced on page 6 in section 1.2.1, Figure 1.4, silicon as an anode material excels at both capacity density and specific capacity. This has sparked immense scientific and commercial interest in incorporating this alloying material into LIBs. Apart from promising extremely high capacities compared to currently used anode materials (3579 mAhg⁻¹ for Li_{3.75}Si; 372 mAhg⁻¹ for LiC₆)^[49] benefits lie in the relatively low working potential (< 0.4 V vs Li/Li⁺), resulting in high voltages when applied in a full cell, and the low cost and high abundance of silicon. However, the large volume expansion during lithiation (> 300%) and the highly reductive surface, typically result in continuous SEI formation during repeated cycling adversely impacting the cycle-life.^[50]

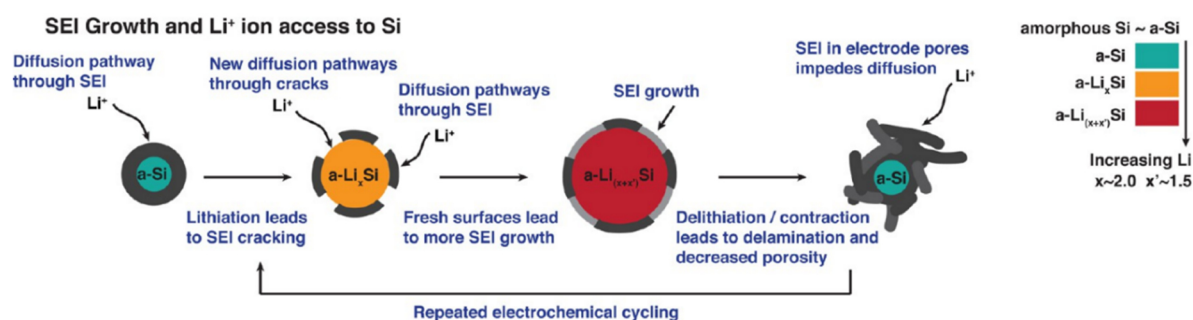


Figure 1.8: SEI growth and continuous formation on silicon nanoparticles during electrochemical cycling. Lithium ions diffuse through the SEI leading to silicide formation and volume expansion. The cracks in the SEI give rise to further SEI formation that will remain upon delithiation, continuously building up in mass over multiple cycles. Reprinted with permission from reference ^[51]. Copyright 2016, American Chemical Society.

Figure 1.8 outlines the major problems associated with silicon anodes.^[51] As the SEI is a crucial component of LIBs (see Chapter 1.3), its formation is necessary to allow stable cycling. After forming the SEI, repeated volume expansion and contraction will lead to cracking,

exposing fresh silicon surface. The bare, reductive surface will allow further SEI to be formed, building up to a large total amount of SEI over time, leading to capacity loss.

Strategies to create functional Si anodes are the design of structures that mitigate the large volume expansion and the effective preservation of the materials shape and electrical contact to the current collector. This can be achieved by employing nanomaterials and shape-preserving artificial SEIs. Additionally, the depth of lithiation can be limited to limit the volume expansion or electrolyte additives can be used to adjust the SEI formation such that it is more stable.

1.4.1 Nanosized Silicon Anodes

To overcome the stress-induced degradation of the silicon anode during volume expansion, the most efficient solution to date is the application of nanosized materials. The three most common nanomaterials; nanoparticles,^[52] thin-films^[53,54] and nanowires^[52,55–57], and their intrinsic properties are shown in Figure 1.9. Each nanoelectrode utilises a different mechanism to mitigate the volume expansion and mechanical stress during cycling and has different requirements for their effective application as an anode material.^[54,56,58–62]

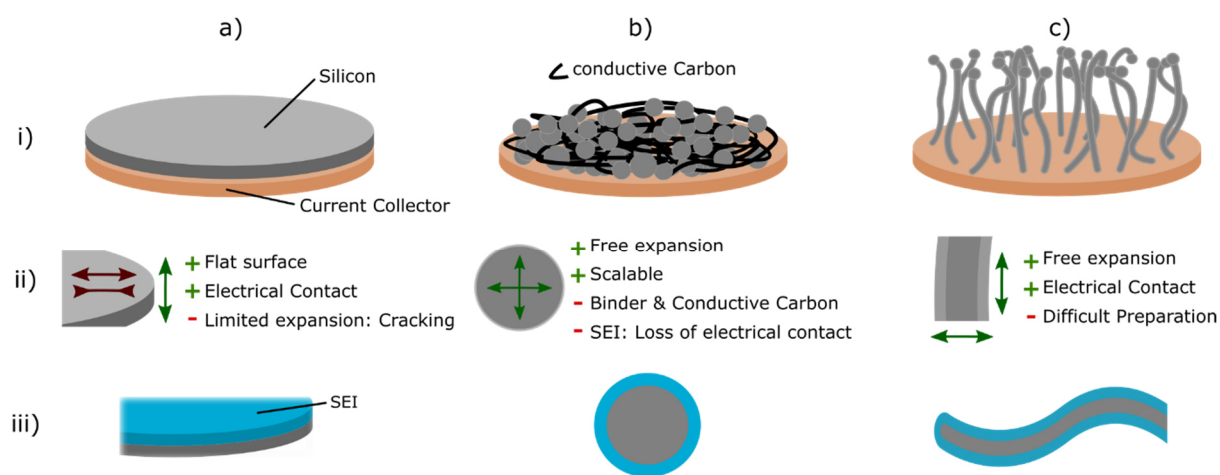


Figure 1.9: Presentation of the three most common nano-silicon anodes. a) Thin-films, b) nanoparticles c) nanowires. i) Typical appearances as anode: direct deposition by physical or chemical vapour deposition (thin-films), slurry (nanoparticles; including conductive carbon and binder), or growth from catalytic seeds by chemical vapour deposition (nanowires; globular structure at the end of the wires represents the catalytic seed) on the current collector. ii) Characteristic properties of each system, indicating the direction of growth during volume expansion (green: free expansion; red: restricted expansion). iii) Modes of SEI deposition or formation: simple deposition applying a thin surface coating (thin-film) and coating of individual nanoparticles and nanowires.

The main differences between these nanomaterials are their fabrication methods, mass loadings and stress relief mechanisms. Silicon thin-films are relatively straightforward to

produce by physical or chemical vapour deposition (PVD, CVD) onto a current collector. The anode thickness can be increased simply by a longer deposition. The direct deposition onto a metal substrate will provide the necessary electronic conduction pathway for electrochemical cycling of the material. The major flaw of thin-film electrodes is their inability to accommodate large volume expansion across the surface, leading to cracking during operation. Magnetron sputtered silicon thin-films have been chosen as model systems for the studies presented in Chapters 3 to 5. Further, more specific discussion on the evolution and degradation of the silicon thin-film anode during cycling in LIBs is found in the introduction to Chapter 3.

Silicon nanoparticles are cast onto the current collector from a slurry, mixed with conductive carbon and binders. The partially electrochemically active (conductive carbon) and inactive components (binder) add complexity and weight to the system. Nonetheless, this type of material is the most promising for commercialisation, as slurries are scalable and adjustable.

Silicon nanowires are an elegant solution to mitigate the stress during volume expansion. Even after many cycles, the material may only show small structural changes and limited fracturing. Nanowires are, however, the most difficult and expensive to manufacture. The CVD process requires the deposition of catalytic seeds, high temperatures and a gaseous precursor, usually silane (which is explosive in air).

The reported limitations in thickness/size for stable cycling are 2.5 μm for thin-films,^[63] 150 nm for nanoparticles^[61] and 300 nm for nanowires^[62] (all avoiding the formation of the crystalline silicide phase of $\text{Li}_{3.75}\text{Si}$ during cycling). Below the critical size, fracturing and the chance of pulverisation of the material are minimised. Nanoparticles and nanowires can accommodate mechanical stress best, while the high internal stresses arising in thin-films can only be relieved through cracking, forming silicon islands of a specific size. Nonetheless, these stay connected to the current collector allowing stable electrochemical cycling properties.^[64]

Artificial SEIs have been reported to extend the lifetime of nanoanodes effectively.^[53,65–67] Applying thin carbon-based surface coatings on silicon nanoparticles and nanowires showed an increase in mechanical stability, containing the volume expansion during lithiation and limiting SEI formation.^[56] However, these coatings are challenging to manufacture. Silicon thin-films are particularly good substrates for the deposition of artificial SEIs allowing the use of numerous techniques such as PVD, CVD, drop casting and spin coating. The PVD of lithium phosphorus oxynitride (LiPON) onto thin-film electrodes is just one example that has been shown to greatly improve the anode cycle life.^[67,68] Maintaining an electron conduction pathway directly to the current collector is a fundamental consideration in the design of artificial

SEIs, as these SEIs should be electronically insulating to limit further electrolyte degradation on their surface.^[68]

1.4.2 Electrochemical Properties and Lithiation Mechanisms of Silicon

Amorphous silicon (*a*-Si) materials undergo several structural transitions during lithiation that depend on the silicon to lithium ratio. Figure 1.10 shows the typical charge-discharge curves of an exemplary 275 nm thin-film anode as reported by Obrovac *et al.* over several cycles as well as the lithiation stages of the lithium silicides that are formed. This work focusses on *a*-Si anodes and does not present data of crystalline silicon (*c*-Si) materials.

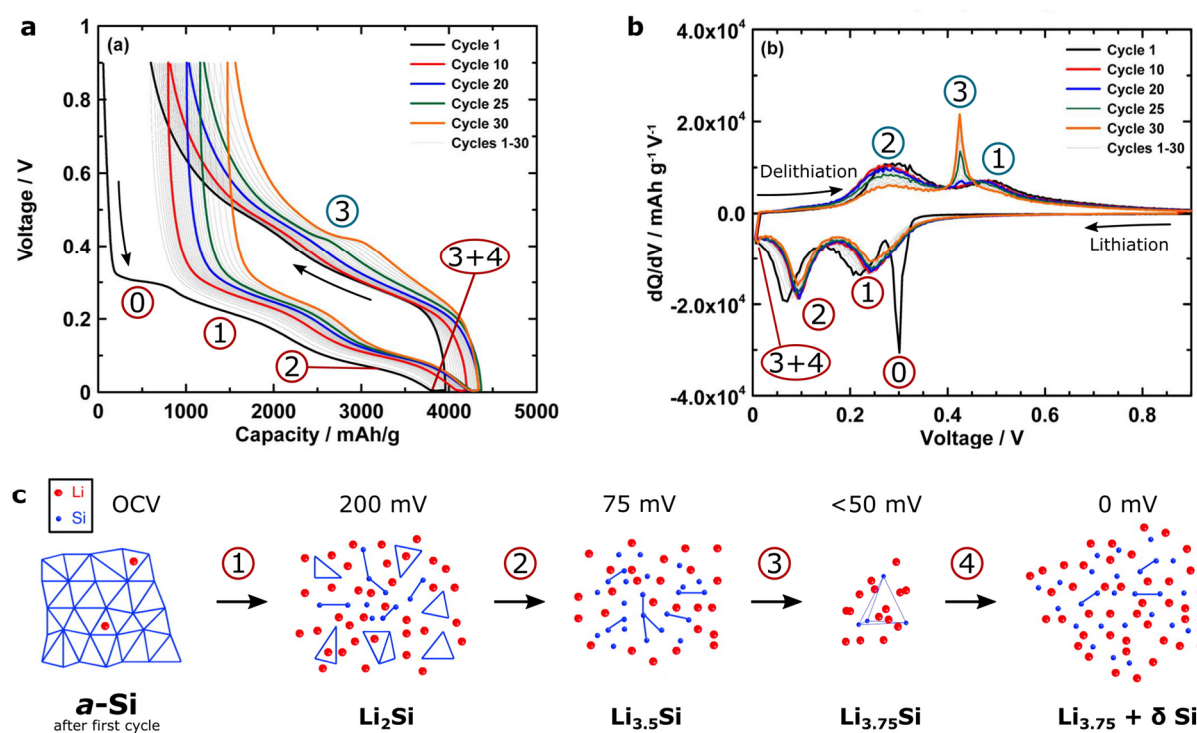


Figure 1.10: Voltage profiles (a) and differential capacity plots (b) of a 275 nm *a*-Si thin-film anode at a rate of $C/2$ (1st cycle: $C/20$).^[69] The lithiation steps and phase formations have been highlighted in red, the corresponding steps during delithiation in blue. Process (0) only occurs in the first cycle. c) Structural representations of the voltage dependent stages of lithiation (1–4) as determined from NMR studies.^[70–72] Adapted and reprinted with permission from references ^[69,72–74]. Copyright 2016 The Electrochemical Society, 2009 American Chemical Society.

c-Si would show different electrochemical behaviour in the first cycle with a pseudo plateau at ~ 125 mV due to the long-range ordering in the material causing a sharp two-phase lithiation process that is slowly dropping in voltage. An *a*-Si anode may allow silicon-silicon bonds to be broken more easily. The as-sputtered material moreover features some weaker silicon bonds and more facile lithiation pathways. The lithiation of such is seen as a short plateau in the

electrochemistry is labelled as ‘0’ in Figure 1.10a. Wang *et al.* were able to follow the lithiation of both *a*-Si and *c*-Si as sharp interfaces in transmission electron micrographs and have proposed a two-phase mechanism in either case. To drive the phase boundary further they say that a high, local lithium concentration is necessary to break Si atoms away from the bulk.^[73] After the first lithiation, a structurally similar amorphous silicide forms from both *c*-Si and *a*-Si in which Si-Si bonds are now equally weak and will show similar electrochemistry for the second and following lithiation cycles which can be better described as single-phase lithiation.^[49,63] In addition to the lithiation of silicon, the SEI formation is seen in Figure 1.10a as a slight slope in the higher voltage region above 0.4 V. Large amounts of SEI are formed in the early cycles.

Following the reorganisation step (‘0’ in Figure 1.10), the profile and differential plots of the amorphous silicon thin-film anode (Figure 1.10h and i) show two pseudo-plateaus for the formation of amorphous lithium silicides *a*-Li_xSi. The first reaction ‘1’ forms a silicide of a ratio (x) up to $x \leq 2$ between 0.3 V to 0.2 V, and the second ‘2’ will form a ratio $2 \leq x \leq 3.5$ at around 0.1 V. These regions will be described as the ‘Li₂Si’ and ‘Li_{3.5}Si’ stages, phases or peaks, respectively, throughout this thesis.

Depending on the conditions, a metastable, crystalline Li_{3.75}Si phase, ‘3’, may form at lower voltages, observed as a small plateau towards the end of the cycle. The phase delithiates at a higher voltage and is detected as a sharp peak at 0.42 V in Figure 1.10i. It has been associated with the accelerated delamination and failure of silicon thin-film anodes.^[69] Holding the material at a lower voltage can further lead to the formation of a lithium-rich phase, Li_{3.75+δ}Si in ‘4’, which has been shown to self-discharge and be detrimental to the cell performance.^[71]

During lithiation the silicon structure breaks into smaller fragments (Figure 1.10j). Starting from the diamond matrix in *c*-Si or the freshly sputtered *a*-Si, the material will form smaller silicon clusters with increasing lithiation. Reaching the Li₂Si stage, silicon has predominately formed clusters and some dimers. At the Li_{3.5}Si stage, most of the material will have formed dimers. At the lower voltages, the silicon dimers can break apart and rearrange into the metastable Li_{3.75}Si phase ‘3’, where Si₄-clusters form. While there are four crystalline lithium silicide phases reported in the binary phase diagram (Li₁₂Si₇, Li₇Si₃, Li₁₃Si₄ and Li₂₁Si₅),^[75] none of these are formed during electrochemical cycling at room temperature.^[76] Only at high temperatures does the formation of the crystalline phases occur.^[77] Under standard conditions the only crystalline phase that forms is metastable Li_{3.75}Si.

The physical pathways of lithiation can vary depending on the dimensions of the material and the electron and ion conducting pathways. The mechanisms by which silicon nanomaterials and thin-films are believed to lithiate are shown in Figure 1.11.

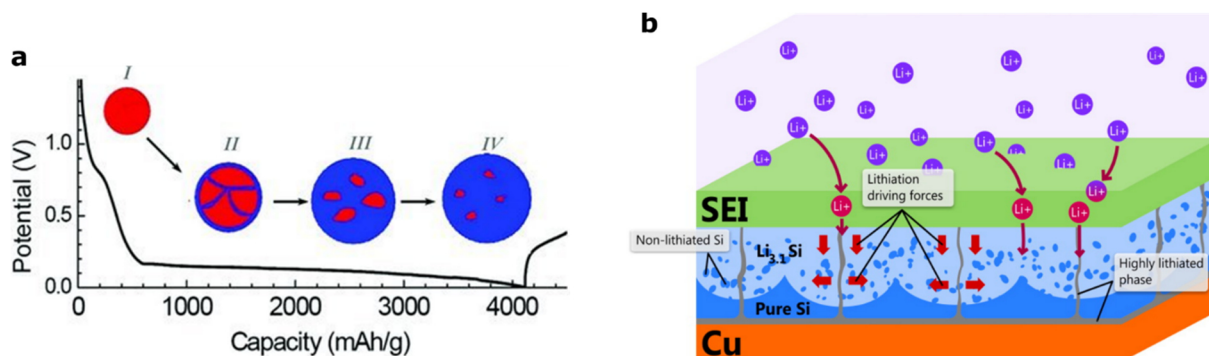


Figure 1.11: a) Proposed lithiation mechanism of silicon nanoparticles based on *in situ* XRD and TEM-EELS data. Reprinted with permission from reference [50] Copyright 2013 WILEY-VCH Verlag GmbH & Co KGaA, Weinheim. b) Proposed lithiation mechanism of silicon thin-films based on XPS and ToF-SIMS data. Reprinted with permission from references [78]. Copyright 2015 American Chemical Society.

Lithium will not only react with silicon nanomaterials from the surface, but through grain boundaries and planar defects which are abundant in nanoscale silicon. During lithiation this will lead to amorphization of the material rather than the linear two-phase lithiation observed for the first discharge of *c*-Si and bulk material. There are likely to be concentration gradients in the material, as seen in Figure 1.11a. Silicon thin-films have similar lithiation characteristics. Lithiation will occur primarily from the surface and fast diffusion pathways found in surface defects. This leads to high lithium concentrations near the interphase to the current collector and the defects found in the thin-films (Figure 1.11b).

1.5 Artificial SEIs for Silicon Anodes

The motivation for applying an artificial SEI to the silicon anode surface is to accommodate the large volume expansion effectively and to limit electrolyte degradation. Ideally, an artificial SEI should be ionically conductive and electrically insulating, efficiently passivating the anode surface while allowing the lithiation of the silicon anode. Creating an artificial SEI fulfilling these criteria is challenging and largely depends on the dimensions and properties of the electrode material.

Silicon is a difficult system to coat for its operation in LIBs given its large volume expansion during lithiation. However, there is a selection of artificial SEIs that have been reported to increase the cycle-life of the nano-silicon anode greatly. Three prototypical strategies are

presented in Figure 1.12 – Figure 1.14. These are the deposition of lithium phosphorus oxynitride (LiPON) onto silicon thin-films, the encapsulation of silicon nanoparticles in a carbon sphere bearing void space, and the deposition of a lithium fluoride coating.^[67,68,79–83]

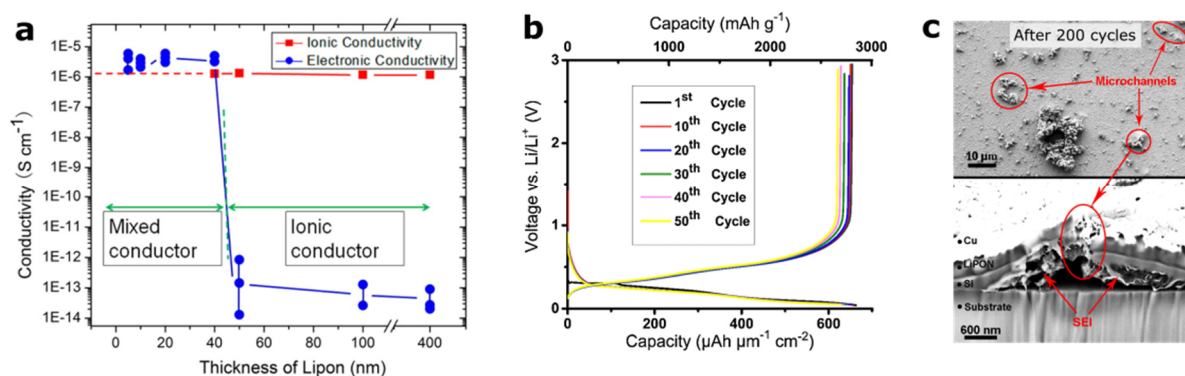


Figure 1.12: a) Ionic and electronic conductivities observed in thin LiPON layers depending on its thickness. An ideal SEIs should only exhibit ionic conductivity. b) Electrochemical performance of a 200 nm silicon thin-film electrode coated with LiPON showing no significant degradation over 50 cycles. c) Micro-channels forming in the material leading to electrolyte decomposition and delamination. Adapted with permission from references ^[67,68]. Copyright 2014 American Chemical Society, 2016 Elsevier Ltd.

LiPON is an ionic conductor, which was previously shown to stabilise the LCO cathode, and has recently been applied on silicon thin-film and graphitic anodes.^[67,68,84,85] Li *et al.* were able to identify the critical thickness of LiPON thin-films at which they become electronically insulating (~50 nm, Figure 1.12a). They argue, that an artificial SEI will be effective once electronic conductivity has been eliminated.^[67] Jouybari and Berkemeier have later studied the electrochemical performance of a 200 nm silicon thin-film anode and its decay mechanism when coated with a 400 nm thick LiPON layer.^[68] The coated anode loses barely any capacity and does not crack (Figure 1.12b,c). Eventually, the anode will fade due to micro-pores emerging in the LiPON coating, allowing electrolyte to reach the silicon material, forming an SEI and causing delamination (Figure 1.12c).

Multiple studies have shown that carbon coatings can stabilise silicon anodes.^[86–91] Two outstanding studies have been presented by Liu *et al.* on yolk-shell silicon-carbon anodes and their pomegranate-like agglomerate structures.^[91,92]

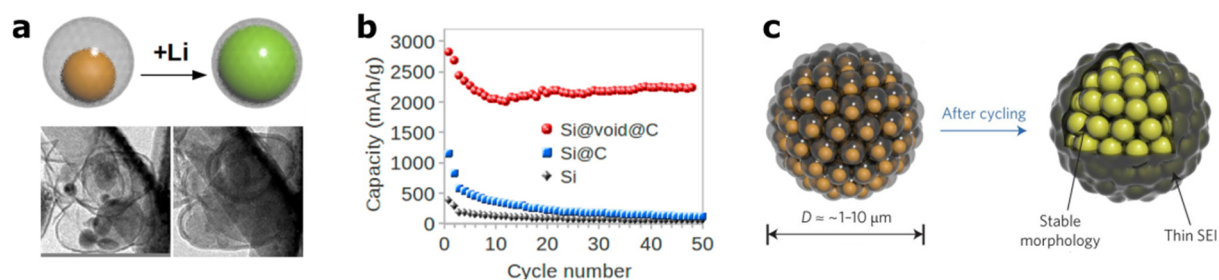


Figure 1.13: a) Yolk-shell structures of Si nanoparticles in carbon and TEM images before and after lithiation. b) Performance of the yolk-shell material compared to the uncoated and the carbon coated particles without void space. c) Pomegranate-inspired agglomerates before and after cycling. Adapted with permission from references ^[91,92]. Copyright 2012 American Chemical Society, 2014 Springer Nature.

The yolk-shell particles allow the silicon nanoparticles inside the carbon shell to expand during lithiation, filling the void (Figure 1.13a). The performance depends largely on the void space, as a too constrictive carbon shell will crack and show poor electrochemical performance of the coated silicon nanoparticles similar to pristine ones (Figure 1.13b). Successfully synthesised yolk-shell structures can cycle efficiently for 1000 cycles and beyond. The void is created by coating silicon in a thick silica layer followed by carbon. The silica is etched away leaving only the silicon nanoparticles inside the carbon shells. Through processing the material in an emulsion, Liu *et al.* were able to form micron-sized particles, further increasing the performance of the anode. These micron-sized particles will only form an SEI on the surface (Figure 1.13c) which is less than that found for the combined yolk shell particles.

Lithium fluoride has been found to play a role in stabilising silicon anodes in LIBs and is usually formed as a degradation product from LiPF_6 or additives such as fluoroethylene carbonate (FEC).^[41] Some work on the silicon anode indicates, that it may act as an artificial SEI when deposited in small amounts by PVD.^[93] Yang *et al.* recently reported the benefits of coating silicon nanoparticles with LiF .^[82]

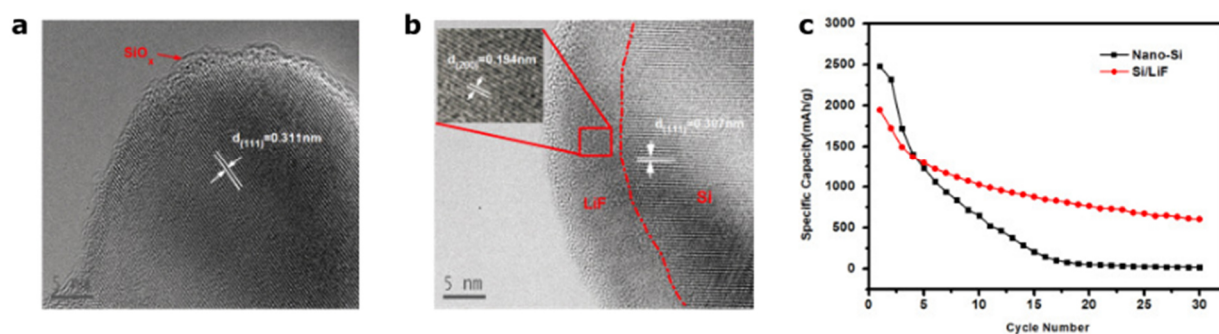


Figure 1.14: a)-b) TEM micrographs of pristine and LiF coated silicon nanoparticles. c) Electrochemical performance of the pristine and coated nanoparticles. Adapted with permission from reference [82]. Copyright 2016 Elsevier B.V.

Thin layers of the material (Figure 1.14b) show increased cyclability over the bare particles (Figure 1.14a). One must consider the weight an artificial SEI adds to the system. The anodes specific capacity will decrease with a coating in place (Figure 1.14c). However, over longer periods of cycling the higher capacity retention will outweigh the initial deficit in specific capacity.

More recently, a novel approach has been presented in creating artificial SEIs by tethering organic chains to silicon nanoparticles and thin-films (Figure 1.15):

Gao *et al.* have grafted organic oligomers and small molecules on silicon nanoparticles *via* a click reaction between an organic azide and the alkyne-functionalised silicon surface (Figure 1.15a). The coated particles show superior performance to nanoparticles, possessing a silicon oxide layer (Figure 1.15c). The coated particles show much less of an SEI being formed on their surface, as shown in the micrographs in Figure 1.15b, leading to the conclusion that a suitable organic layer on the particle may induce the formation of a beneficial SEI.

In a study by Shen *et al.*, silicon thin-films were coated with polymer brushes by first grafting a triethoxysilane onto the surface followed by the addition of methyl methacrylate, growing polymer chains from the surface (Figure 1.15d). Again, the system appears to limit the amount of SEI that forms on the surface, leading to an increase in lifetime depending on the thickness of the polymer layer (Figure 1.15e-f).

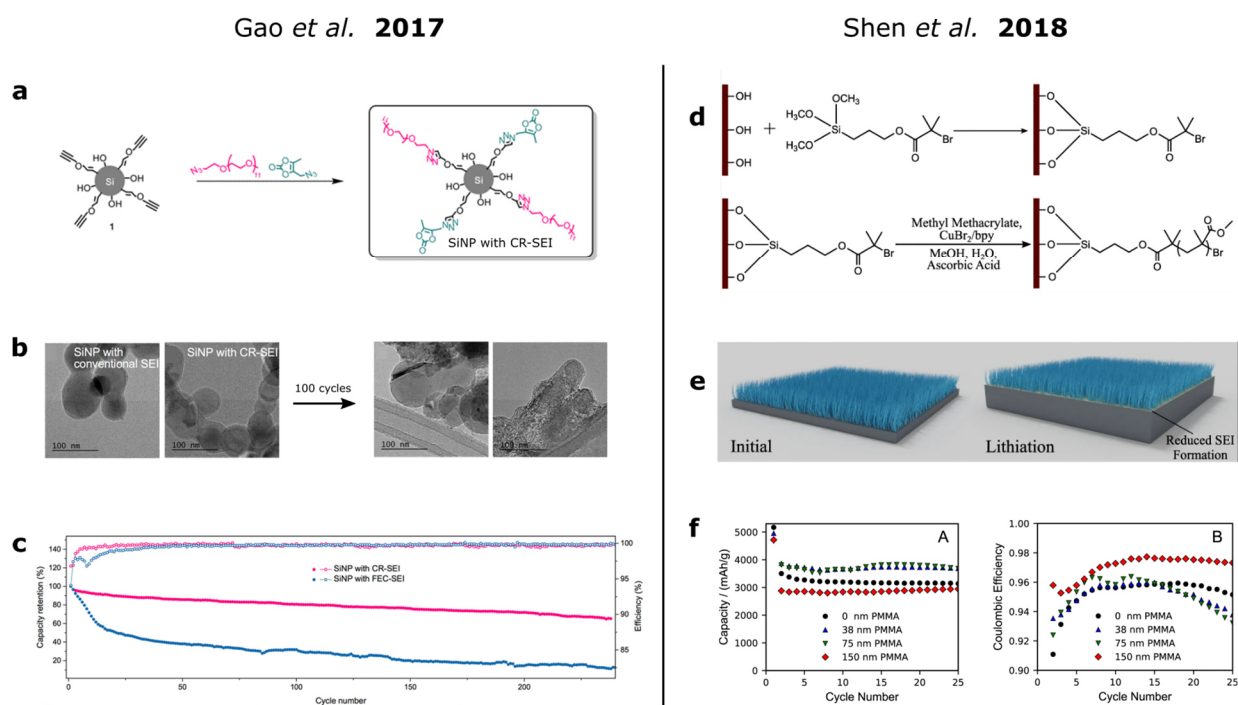


Figure 1.15: Surface-grafted artificial SEIs reported by Gao *et al.* and Shen *et al.* for silicon anode materials.

a) Reaction pathway for tethering organic azides to the alkyne-functionalised silicon surface. b) TEM micrographs of the anode materials before and after 100 cycles. c) Electrochemical performance of the coated and uncoated silicon nanoparticles. d) Grafting and methyl methacrylate-polymerisation to form polymer brushes on a silicon surface. e) Visualisation of the reduced SEI formation on the coated electrode. f) Electrochemical performance of the thin-film anode with increasing thicknesses of polymer coatings. Adapted with permission from references [94,95]. Copyright 2017 American Chemical Society, 2018 Springer Nature.

1.6 Synthesis and Applications of Poly(phosphazenes) in LIBs

Poly(phosphazenes) are inorganic-organic hybrid polymers based on a phosphorous(V)-nitrogen backbone, substituted with a large variety of substituents on the phosphorus atom. Phosphazenes are generally found as monomers **I**, cyclic oligomers **II** and polymeric species **III**, as pictured in Figure 1.16.

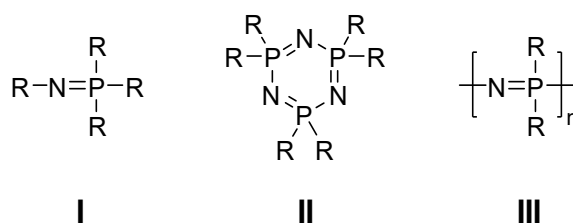


Figure 1.16: Monomeric, trimeric and polymeric phosphazenes.

Cyclic chloro-phosphazenes [PCl₂N]_n (n = 3 or 4) were first synthesised in Liebig's laboratory in 1832, however, it was Gladstone and Holmes who, more than thirty years later,

determined their composition.^[96] It was not until 1895, that a trimeric phosphorus-nitrogen structure of $[\text{PCl}_2\text{N}]_3$ was proposed by Stokes.^[97] Since then, the field of phosphazene chemistry has flourished, leading to many publications on oligomers and polymers based on $[\text{PCl}_2\text{N}]_n$, an area which was largely shaped by the work of Allcock *et al.*^[98–101]

Poly(phosphazenes) have a large spectrum of possible applications such as biomaterials for drug delivery, elastomers, fire retardants, and electrolytes, although their industrial applications have not been fully realised.^[102–105]

In addition to being stable under standard conditions, these polymers show great elasticity and the possibility of pre- and post-functionalisation of the polymer chains. Their versatile and controllable polymer synthesis make them ideal materials for many areas of research.

1.6.1 Molecular Structures

The structure of Hexachlorocyclotriphosphazene $[\text{PCl}_2\text{N}]_3$ (**A**) was determined by single crystal X-ray diffraction (XRD) in 1960 and further refined more than a decade after.^[106,107] All P-N bonds in cyclotriphosphazenes are of the same length when homogeneously substituted (1.575(4) Å for all Cl-substituents in compound **A**, the structure is shown in Figure 1.17).

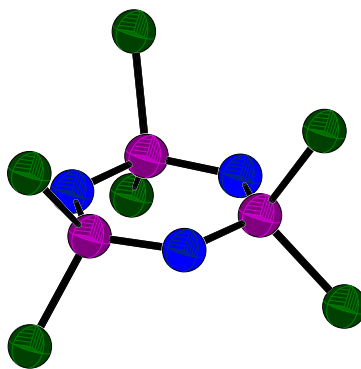


Figure 1.17: Molecular structure of **A** (blue: nitrogen; violet: phosphorous; green: chlorine).

Each phosphorus atom has an almost tetrahedral environment with a Cl-P-Cl angle of $101.20(11)^\circ$ and N-P-N angle of $118.2(2)^\circ$.^[107] To date many oligomeric structures of this type, based on $[\text{PX}_2\text{N}]_n$, with different substituents (X) have been reported. The shortest bonds are found for small, electronegative substituents, such as fluorine.^[108]

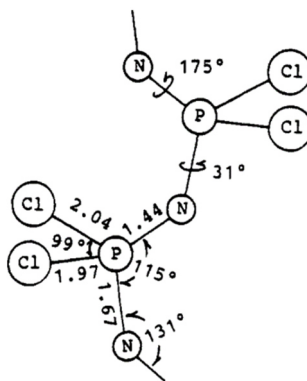


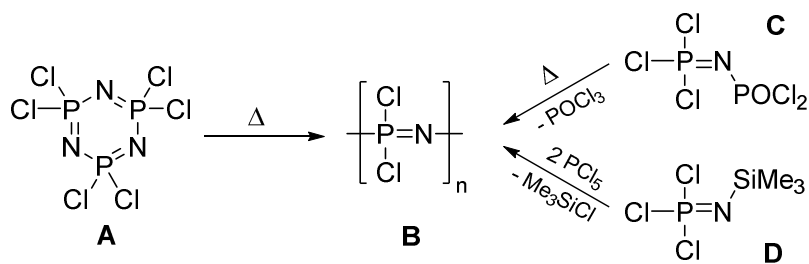
Figure 1.18: Bond lengths and angles in $[\text{PCl}_2\text{N}]_n \mathbf{B}$. The PN-units may rotate around the longer PN-bond.

Reprinted with permission from reference ^[109]. Copyright 1987 American Chemical Society.

In contrast to the equal bond lengths found in small oligomers, polymers show alternating bond lengths, such as in poly(chloro)phosphazenes \mathbf{B} ,^[109] in which alternating bonds of 1.67(8) Å and 1.44(5) Å in length are observed (Figure 1.18).^[109] The bonding situation has long been discussed and many different approaches have been presented throughout the decades, even suggesting the contribution of the phosphorus d-orbitals,^[110] a model, which has since been replaced by findings based on density functional theory (DFT) calculations. Most recent studies attribute the strong P-N bonds to a zwitterionic interaction and negative hyperconjugation. The negative hyperconjugation of the nitrogen lone pairs into the P-Cl σ^* -orbitals stabilises the bonds. The large degree of charge separation (N^-/P^+) accounts for much of the high P-N bond strength and shortness of the P-N bonds. In addition, delocalised MOs can stabilise the ring-systems.^[111,112]

1.6.2 Polymerisation and Functionalisation

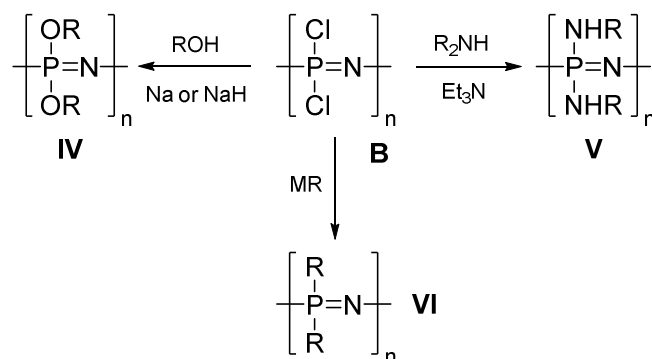
Polyphosphazenes are prepared *via* two major routes, thermally induced ring-opening polymerisation from the chloro-trimer $[\text{PCl}_2\text{N}]_3 (\mathbf{A})$ or condensation reactions from monomeric precursors such as \mathbf{C} or \mathbf{D} . The synthetic pathways are outlined in Scheme 1.1.



Scheme 1.1: Reaction pathways to yield poly(chlorophosphazene) **B**. Thermal polymerisation from the hexachlorotrimer **A**, thermal “living” condensation from the monomer **C** and catalysed cationic “living” polymerisation from the monomer **D**.

The synthetic procedures in Scheme 1.1 yield different qualities of poly(chlorophosphazenes). The thermal ring-opening polymerisation of **A** allows only limited control over the polymer product **B** in terms of average polymer weight and structure (Scheme 1.1, left). The product has a broad distribution of chain-length and is highly cross-linked. However, polycondensation reactions of monomers are generally more controllable (Scheme 1.1, right). The use of the dichlorophosphoryl monomer **C** was recently introduced.^[113] Its synthesis is cheap and polymerisation does not require any solvent. The product is obtained as a mixture of soluble, more or less cross-linked polymers with a narrower molecular weight distribution. Using the trimethylsilyl-substituted monomer **D** yields almost exclusively linear poly(chlorophosphazene) following a cationic “living” polymerisation, initiated by the addition of PCl_5 .^[114] The choice of starting material and polymerisation method allows the synthesis of materials suitable for specific applications.

Polymeric dichlorophosphazenes $[\text{PCl}_2\text{N}]_n$ (**B**) obtained by the above routes provide excellent substrates for functionalisation. A large variety of organic and organometallic side groups have been introduced into these polymers,^[105,115] as well as mixtures of side groups. The most common functional groups are alkoxides, amines or organometallic fragments. Alkoxy groups can be introduced simply by reacting **B** with RO^- anions (with the elimination of Cl^-), while the introduction of amino groups (R_2N) is normally carried out by the reactions of **B** with R_2NH in the presence of triethylamine as a base. Organometallic reagents including organolithium and Grignard reagents react directly with **B**.^[116] More than 250 different side-groups have been introduced into poly(organophosphazenes) both alone or in combination with other groups.^[117] The general reaction pathways are shown in Scheme 1.2.

Scheme 1.2: Functionalisation of **B** with alcohols (**IV**), amines (**V**) and organometallic compounds (**VI**).

Substitution reactions can take place *via* either a geminal or non-geminal route. By increasing the electrophilicity of a P-atom, the substitution of the second P-Cl atom is activated. Hence, non-geminal substitution is preferred for groups with π -donor properties such as secondary amines and most alkoxides as these tend to deactivate the phosphorous atom. Primary amines bound to the P-atom may favour geminal substitution when being deprotonated, forming a trigonal planar intermediate between the P-N bond and another nitrogen atom from an amine.^[99] Geminal substitution may occur for softer bases such as thiolates.^[99] The choice of side-groups allows the chemist to adjust the physical properties of the polymer such as elasticity, hydrophobicity and -philicity, glass transition temperature, water solubility, crystallinity, biostability as well as ionic and electronic conductivity.^[117]

1.6.3 Polyphosphazenes as Electrolytes for LIBs

Phosphazenes have been tested as electrolytes in lithium ion batteries as solid, gel and liquid electrolytes. Solid electrolytes were formed from linear poly(phosphazenes) by cross-linking or straight from oligomers, generally bearing polyether side-groups for lithium ion conduction. Lithium ion conductivity was found to be within reasonable levels of $\sim 10^{-5} \text{ Scm}^{-1}$ at room temperature and $\sim 10^{-4} \text{ Scm}^{-1}$ at elevated temperatures.^[118–120] Phosphazenes provide high thermal stability, can act as flame retardants and show low volatility – properties that make them ideal as gel and liquid electrolytes to mitigate most of the safety issues that lithium ion batteries face.^[104] High lithium ion conductivities were achieved with soft gel electrolytes in the extensive work presented by the group of Wiemhöfer *et al.*, additionally limiting lithium dendrite formation in systems with a lithium metal anode.^[121–125] Further discussion on the use of poly(phosphazene)-gel electrolytes is found in Chapter 5.

1.7 Project Aims

Silicon anodes are prospective next-generation electrodes promising a significant increase in capacity for LIBs, if problems arising from the large volume expansion and continuous SEI formation during operation can be solved. The aims of the project are therefore to better understand the degradation mechanism of the silicon anode and to improve the cycling performance by altering the SEI through additives and the application of polymer surface coatings. An illustration of the concepts of each research chapter is presented in Figure 1.19.

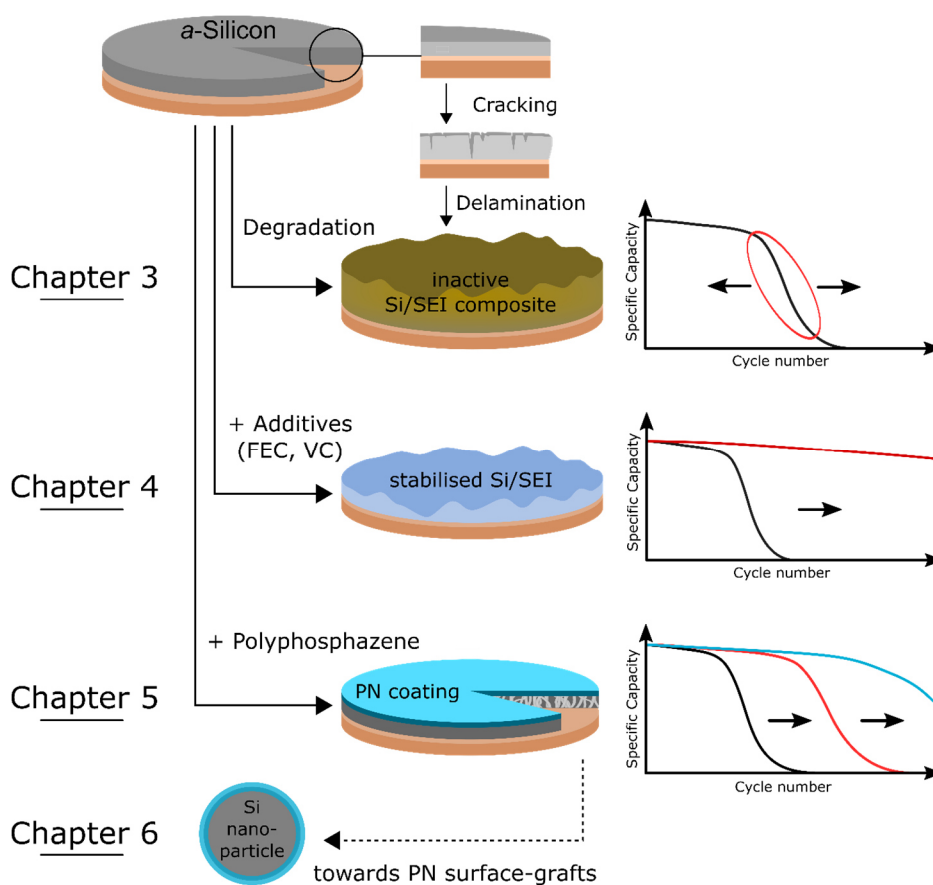


Figure 1.19: Overview of the concepts discussed in this thesis. The majority of the experiments were carried out on amorphous silicon thin-film electrodes and affect the electrochemical performance as indicated on the right.

Chapter 3: Investigation of the degradation of the thin-film anode through cracking, delamination and SEI formation in a standard electrolyte. The adjustment of materials and cycling parameters affects the lifetime.

Chapter 4: Studies on FEC and VC as electrolyte additives to stabilise the thin-film electrode. Chapter 5: Synthesis and deposition of poly(phosphazenes) as artificial SEIs, to improve the electrochemical performance depending on the phosphazenes chemical composition. Chapter 6: proof-of-principle studies on phosphazene surface-grafts to allow the growth of ultra-thin PN-coatings on silicon nanoparticles and other nanomaterials as artificial SEIs.

Chapter 3 presents the fabrication and properties of the silicon thin-film anodes used in the studies. Silicon thin-film electrodes have been presented widely in the literature, yet every system shows some unique properties. To understand the electrochemical properties and structural changes that occur during cycling, a thorough analysis of the system is necessary. We have created silicon thin-film anodes from magnetron sputtering on a selection of substrates in different thicknesses. Galvanostatic cycling is performed to determine the electrochemical performance and identify specific processes. The structural changes and chemical compositions of the anodes after cycling are investigated by electron microscopy and energy-dispersive X-ray spectroscopy (EDS), based upon which a detailed degradation mechanism is proposed.

Chapter 4 discusses the effects of FEC and VC on nano-silicon electrodes. The additives are known to create a beneficial SEI, that stabilises the electrode and have been widely applied to increase the performance of the silicon electrode, yet their composition and stabilisation mechanisms are not fully understood. In the first half, the synthesis of $^{13}\text{C}_3$ -fluoroethylene carbonate is described and a brief summary on the NMR studies that it was used for is provided, identifying SEI components formed with the electrolyte additive. Inspired by the findings, the stabilisation of the thin-film anode from Chapter 3 using FEC and VC is investigated by the methods described in the previous chapter.

Chapter 5 introduces poly(phosphazene) coatings to stabilise the silicon thin-film electrode. Artificial SEIs promise increased lifetime for the silicon thin-film anode and have been reported in various forms in the literature. Poly(phosphazenes) have previously been studied as electrolytes for LIBs. Using two different linear phosphazenes, suitable solutions for the spin coating of thin-film electrodes are created. The polymer coatings are tested again for their structural and chemical impact on the silicon surface with standard electrolyte solutions and additives.

Chapter 6 presents strategies of coating silicon surfaces with thin phosphazene layers. Phosphoranimines, molecular poly(phosphazene) precursors, based on surface grafting molecules, were synthesised. Four molecules are presented and characterised that may potentially react with different functionalised silicon surfaces. The molecules have the potential to be used as “anchors” for growing polymers from the surface which was tested and followed by NMR experiments and transmission electron microscopy (TEM). Wafers bearing a native oxide layer have been treated with silane precursors and were analysed by water contact angle measurements and X-ray photoelectron spectroscopy (XPS).

Chapter 2 Methods

2.1 Metal Sputter Coating

Silicon anodes in this thesis were prepared with a magnetron sputter coater. The technique allows the straightforward and controllable deposition of silicon onto any substrate. The basic principle of sputter coating is shown in Figure 2.1.

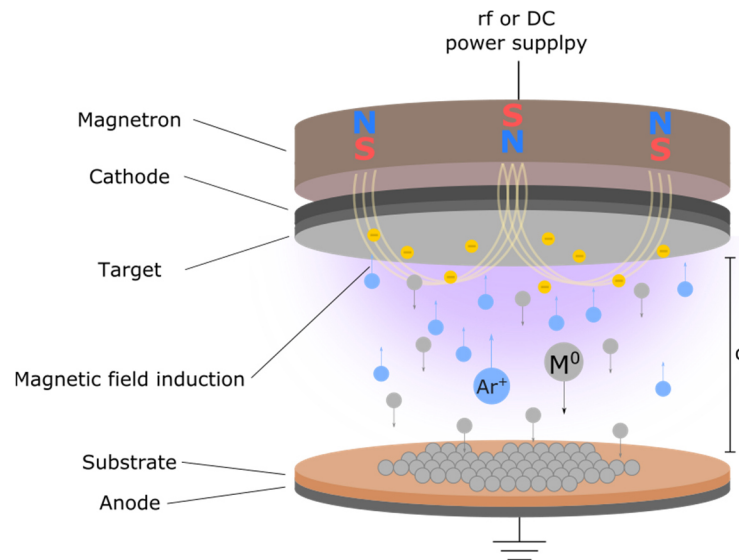


Figure 2.1: Schematic of the principle functionality of a magnetron sputter coater.

During the sputtering process, positively charged ions hit a target which sits at a high negative potential, ejecting material that is then deposited on the substrate. There are different sputtering techniques available. In this work, silicon thin-films were created by sputter coating a current collector in a radio frequency (RF) magnetron sputter coater and an underlying nickel base was deposited using a direct current (DC) magnetron sputter coater.

When a high current is applied, a magnetron can induce a plasma through a magnetic field and positively charged ions (formed from the inert gas) bombard the target placed on the cathode. Atoms from the target are ejected and will condense on the substrate surface, placed in close proximity. Both the applied power and the distance between the target and substrate determine the rate of the deposition and the materials' physical properties (e.g. density).

The choice of the sputter coater depends on the properties of the target and the substances sputtered regularly with the machine (to avoid cross-contamination). DC sputter coaters are easy to control, but require a conductive target for the sputtering process, which is ideal for the deposition of nickel. A non-conductive target, however, will build up charge, leading to issues during deposition. For silicon as a semi-conductor, a RF magnetron sputterer is used which

does not necessarily require a conductive target. The electric field, controlled by the RF power source, alternates the charges and mitigates the build-up of charge on the target.

Sample preparation and deposition were carried out in a class 10.000 cleanroom to minimise impurities and defects of the thin-films.

2.1.1 Direct Current (DC) Sputter Coating

Nickel coatings were deposited in a DC metal sputter coater using a nickel metal target (>99.999%). The copper substrates were placed in the chamber which was pumped down to a base pressure of $\leq 2.0 \cdot 10^{-5}$ mbar. An argon flow of 20 sccm was set yielding a pressure of $3.5 \cdot 10^{-3}$ mbar. The nickel target was pre-sputtered for 10 minutes at 100 W. Under these conditions 1830 s of sputtering were necessary to form ~ 250 nm Ni thin-films.

2.1.2 Radio-frequency (RF) Sputter Coating

Silicon thin-film electrodes were prepared by PVD in a modified CCR RF sputter coater using a pure silicon wafer target (>99.999%). Substrates were placed in the chamber which was purged with argon and evacuated to a base pressure of $\leq 1.0 \cdot 10^{-5}$ mbar. A flow of 50 sccm of argon was set yielding a pressure of $1.8 \cdot 10^{-2}$ mbar. The plasma was struck at a high voltage and the reflected power from the RF power source was minimised *via* a matching unit. The silicon target was pre-sputtered for 10 minutes at 150 W. Under these conditions 550 s of sputtering were necessary to form ~ 100 nm Si thin-films.

2.1.3 Profilometer

Film thicknesses were determined using a Dektak II Profilometer. Clean pieces of silicon wafer, masked partially with permanent marker, were placed alongside the copper substrates for the sputtering process. The mask was washed off in acetone in an ultrasonic cleaner and the thickness of the silicon thin-film was measured on the edges to the freshly-exposed surface.

2.2 Electrochemical Measurements

Silicon anodes were deployed in lithium half-cells and galvanostatically cycled. The lithium metal electrode acts as a counter and reference electrode and does not impact the electrochemical features observed for changes of the anode significantly. Furthermore, it provides an abundance of lithium throughout the experiment.

Technically, given the lower potential, silicon would be regarded as the cathode in this scenario. For clarity we will continue to refer to the silicon electrode as the silicon anode throughout the thesis.

In a glovebox of the type MBRAUN UNIlab, operating with an argon atmosphere, anodes were placed in a CR3032 coin cell base followed by a glass-fibre separator soaked in LP30 electrolyte (1 M LiPF₆ in EC and DMC, 50/50, v/v), a lithium chip, separator, spring and lid. Casing components are made of stainless steel. The cells were sealed and rested before galvanostatic cycling.

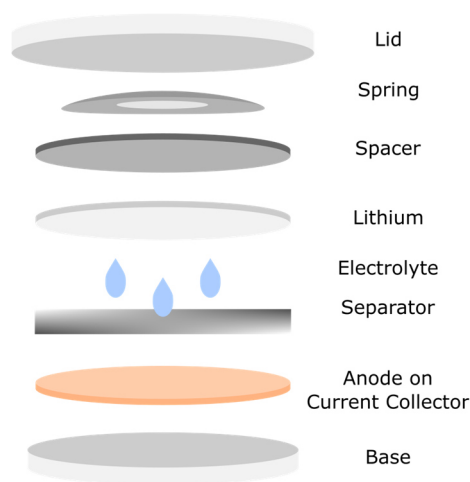


Figure 2.2: Coin cell components and active materials used for the lithium half-cells.

Coin cells were cycled on a LANDT potentiostat. The cells were charged to 2 V at the end of the experiment.

2.2.1 Galvanostatic Cycling

Galvanostatic cycling is the standard in testing electrode materials. A constant current is applied, and the changes in voltage are recorded. Any electrochemical processes will show as a feature in the voltage profile. The current applied is set depending on the materials' specific capacity to fully charge or discharge the electrode over a certain amount of time, noted as C/n . If a charge process should take 5 h, a rate of $C/5$ is set. The theoretical specific capacity, C_{th} is

$$C_{th} = \frac{\Delta x \cdot F}{M} \cdot \frac{1000}{3600}$$

where Δx is the number of moles of lithium that can react with the active material of a molecular weight M , F is the Faraday constant which is multiplied by a conversion factor to yield the specific capacity in mAhg^{-1} .

Exemplary plots for a galvanostatic cycle of a silicon anode in a lithium half-cell are shown in Figure 2.3. A voltage profile (Figure 2.3a) will show electrochemical processes that happen at a certain voltage. Taking the first differentiation thereof creates a differential plot, or dQ/dV plot (Figure 2.3b), that may further emphasize electrochemical processes that are otherwise difficult to observe in the voltage profile.

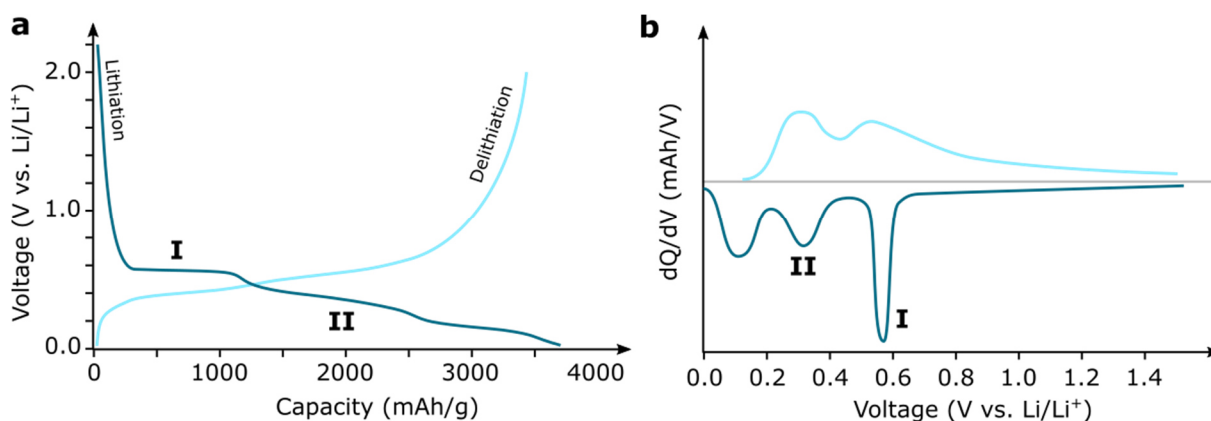


Figure 2.3: Exemplary a) voltage profile and b) differential plot thereof, of a typical first galvanostatic cycle of an amorphous silicon electrode, showing both two-phase (I) and solid-solution (II) lithiation mechanisms.

The reaction of an active material can occur either *via* a solid solution or a two-phase mechanism, depending on the material. A true two-phase reaction occurs when the chemical potential of the product remains the same which would appear as a plateau similar to that observed in Figure 2.3. For silicon, however, process ‘I’ (Figure 2.3) occurs on sputtered thin-films and may not be a true two-phase reaction.^[73] We rather speak of pseudo-plateaus in the voltage profile that appear as a peak in the dQ/dV plot. The lithiation during standard operation is a solid-solution or single-phase reaction, which occurs if the material that is being lithiated does not undergo large structural changes, such as the later stages in lithiation and following cycles (see section 1.4.2 on page 14 for more information). The lithium concentration appears as a gradient throughout the material until it is fully lithiated. This is seen as sloping pseudo-plateaus in the voltage profiles and broad peaks in the dQ/dV plot.

During cycling, parasitic side reactions occur that will be reflected in the lack of capacity being observed during delithiation. This is reflected in the Coulombic efficiency (CE), that is described as the ratio of energy stored during charge (Q_{cha}) and discharge (Q_{dis}):

$$CE = \frac{Q_{cha}}{Q_{dis}} \cdot 100$$

The capacity that is lost during each cycle as lithium is consumed is called slippage.^[126,127] We use this tool to estimate how much lithium is consumed to form the SEI. This is of particular interest when comparing electrolytes with varying components.

Using electrochemical measurements to gain information on electrochemical processes on only one battery component, the silicon electrode in our case, is difficult. While the electrochemistry observed will correspond largely to processes involving silicon, reactions on the lithium metal and other battery components will affect the observed values. It is important to search for further information on changes occurring on the electrode during cycling in other analytical techniques.

2.3 Electron Microscopy & Energy-Dispersive X-ray Spectroscopy

Microscopy is the technique of choice to identify changes in the surface morphology that are caused by electrochemical cycling of the thin-film anodes. To observe changes on the nanoscale, electron beams are necessary to overcome the limitations of visible light as the resolution is limited by the wavelength of the illumination source as it stands

$$\Delta x = \frac{\lambda_0}{2(n \sin\theta)}$$

where Δx is the point resolution, λ_0 is the wavelength of the light and $n \sin\theta$ is the numerical aperture (achieving up to 1.4 in state-of-the-art microscopes), which in turn leads to a maximum resolution of 160 nm for visible light. Using electrons, higher resolutions are achieved. The wavelength at which electrons propagate depends on the acceleration voltage. Considering relativistic effects, wavelengths of >2 pm are achieved for electron beams at voltages as high as 300 kV in transmission electron microscopes.

Scanning electron microscopes usually operate at lower voltages. Here, ~ 1 nm resolution can be at voltages of 30 kV. This technique scans the surface of a sample with a focused electron beam. The interaction of the electron beam with the sample leads to the emission of different sorts of radiation that can be detected.

Figure 2.4a shows the various signals detectable from incidents with the electron beam: Auger electrons, secondary electrons, backscattered electrons, Bremsstrahlung and secondary fluorescence from continuum or characteristic X-rays. For the analysis in this report, secondary and backscattered electrons, as well as the Bremsstrahlung are of importance. A detailed description of the processes can be found in the literature.^[128]

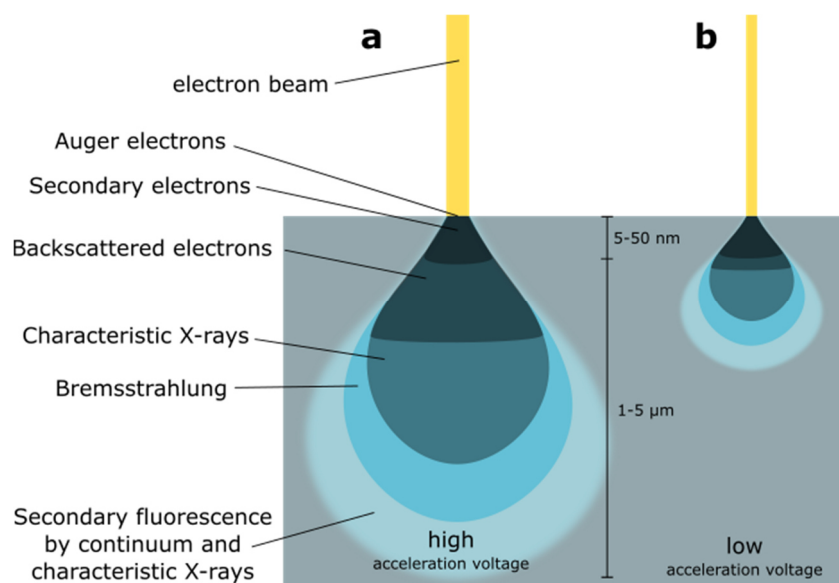


Figure 2.4: Interactions of the electron beam with the sample. a) Interaction volume of an electron beam at high acceleration voltage (e.g. 15 kV, used for energy-dispersive X-ray spectroscopy (EDS)) showing the origin of the emitted Auger electrons (depth: first few Å), secondary electrons (SE, depth: 5-50 nm), backscattered electrons, Bremsstrahlung, and secondary fluorescence in penetration depths of $\sim 1-5 \mu\text{m}$. b) Stylised interaction volume at lower voltages showing a smaller interaction volume. Adapted from reference ^[128].

Secondary electrons are produced from inelastic scattering of the incident electrons with the weakly-bound valence band electrons of the material. These are characteristically low in energy and originate from a depth of 5-50 nm. Secondary electrons that originate from deeper in the material cannot escape the material. As we investigate thin-films of thicknesses as low as 100 nm we exclusively examine the surfaces with a secondary electron detector.

Backscattered electrons are, however, to be considered to cause incidents that affect the secondary electron count. The electrons may originate from deeper within the sample and are higher in energy than secondary electrons. On their path to the surface, they may change their trajectories through elastic scattering that lowers their energy to a level similar to secondary electrons.

To limit the interaction volume, a lower acceleration voltage can be applied to make the technique more surface sensitive (Figure 2.4b). At lower acceleration voltages, the backscattered electrons will not contribute as much to the signal observed. The depth at which secondary electrons are detected is not affected as much.

We couple SEM with EDS to gain information of the chemical composition. Characteristic X-rays that are detected in EDS analysis may be emitted from a larger part of the interaction volume. It is important to understand, that the information gained from EDS may arise from

underneath the features observed by the secondary electron detector. A schematic showing the origin of the characteristic X-rays and stylised EDS spectrum are shown in Figure 2.5.

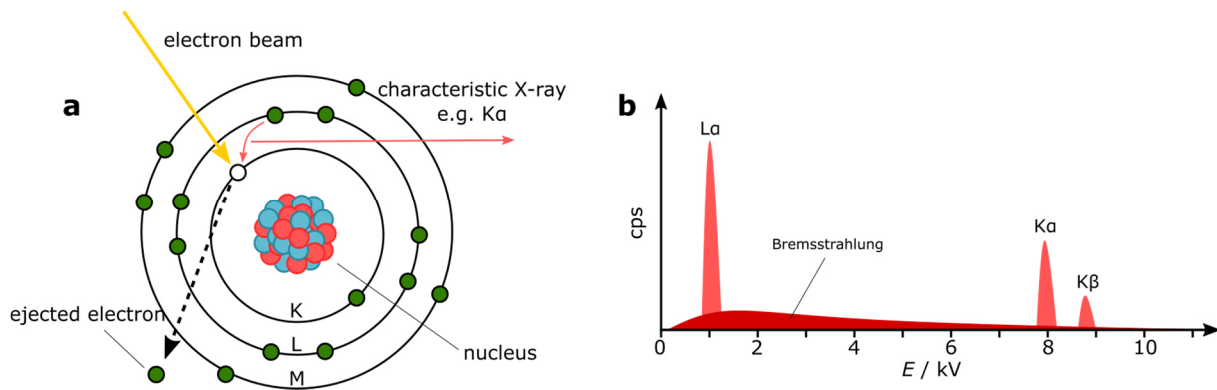


Figure 2.5 a) Incident of a high-energy electron with an atom, removing an electron near the nucleus leaving an electron hole. A higher energy electron will fill the hole position in the lower shell, emitting characteristic X-rays in the process. b) Stylised EDS spectrum of copper showing characteristic peaks, superimposing the Bremsstrahlung.

Upon the incident with the electron beam, electrons near the nucleus are ejected, after which higher energy electrons of an outer shell can fill the electron hole releasing energy in form of characteristic X-rays (Figure 2.5a). Their energy depends on the position of the electron that was removed and the electron filling the hole. A spectrum will show a peak for each of these processes observed within the energy range, e.g. $K\beta$ being the radiation from an electron in the M shell relaxing to fill the K shell and $L\alpha$ for the same process from the M- to the L-shell. We have recorded all EDS spectra at 15 kV. This guarantees the observation of the heavier elements such as nickel and leads to high electron counts for X-rays emitted from lighter elements. However, the high acceleration voltage means that the information of a large interaction volume is recorded, hence being less surface sensitive.

Bremsstrahlung arises from electrons being deflected off the nuclei in the atoms found in the sample. Losing kinetic energy, Bremsstrahlung is emitted, showing as a continuous spectrum in the EDS. This will be superimposed on the actual signal arising from characteristic X-rays. It limits the possibilities of quantifying small amounts of lighter elements in the lower voltage regions. Furthermore, heavier elements will show a different shape in interaction volume, typically wider and shallower. This is known as the Z-effect (from z, for atomic number). The broader interaction volume will yield a more diffuse element map.

Both SEM and EDS are techniques that provide information on a local environment. Cells were inspected visually and at lower magnification under the SEM to identify different areas.

Cycled electrodes that were not coated with poly(phosphazenes) generally showed to be homogeneously covered. Where areas on the electrodes are found that appear significantly different, both areas are shown in the SEM micrographs.

2.3.1 Scanning Electron Microscopy (SEM)

Electron micrographs (other than those obtained from FIB SEM) were recorded on a TESCAN MIRA3 FE bearing a Schottky field emission (FE) electron gun using a secondary electron detector. Samples were studied at a working distance of 6 mm from the objective lens at acceleration voltages of 2, 5 or 15 kV.

2.3.2 Sample Transfer under Inert Atmosphere

Samples investigated under the TESCAN MIRA3 were transferred from the glovebox to the microscopes vacuum chamber using a Kammrath & Weiss Transfer Module, where possible. The module has a motorised, air-tight lid that can be closed in the glovebox and opened in the microscopes vacuum chamber.

2.3.3 Energy-dispersive X-ray Spectroscopy (EDS)

EDS spectra were recorded using an Oxford Instruments X-Max^N with an 80 mm² sensor, fitted to the Tescan MIRA3 SEM. Samples were analysed at an acceleration voltage of 15 kV a beam intensity of 14 (electron beam spot size: 20 nm), and a working distance of 15 mm. Data was processed using the program Aztec 3.3 SP1.

2.3.4 Focussed Ion Beam (FIB) SEM

FIB SEM was performed on a ZEISS CrossBeam 540 SEM/FIB or a FEI Helios Nanolab SEM/FIB at the Wolfson Electron Microscopy Suite in Cambridge.

Samples for FIB SEM analysis were sputter-coated with a few nanometres of gold prior to the transfer into the microscope chamber. In the process, all sample for FIB SEM were exposed to air. A gallium ion beam was used to deposit a platinum bar on the site of interest to limit the damage to the surface during the milling process. After the deposition of 1–2 μm Pt, the surface was milled under the ion beam stepwise with lower intensities to minimise damage to the cross section studied with the SEM. SEM micrographs were recorded at 10 kV.

2.4 Contact Angle Measurements

Contact angle measurements were carried out to determine the wettability of the polymer coatings in section 5.2.2 and to identify the deposition of thin surface coatings with silane-based grafts in section 6.1.3. Measurements were carried out on a First Ten Angstroms FTA1000.

2.5 Synthetic Procedures and Substance Characterisation

Any syntheses described in this thesis were carried out in a fume hood or under inert atmosphere when necessary. Glassware was cleaned in a potassium hydroxide/*iso*-propanol bath followed by protonation in a hydrochloric acid bath and was rinsed with deionised water and distilled acetone, then dried before use. Characterisation of the compounds was carried out by nuclear magnetic resonance spectroscopy (NMR) and mass spectrometry (MS).

2.5.1 Schlenk techniques

Synthetic steps involving air- and moisture sensitive substances were carried out on a Schlenk line, connected to a rotary vacuum pump and nitrogen. Nitrogen was passed through a column of dried silica and potassium hydroxide to remove possible traces of water in the gas. Glassware used for the reactions was heated under vacuum with a heat gun and flushed with nitrogen after cooling. The process was repeated a total of three times. Reactants and solvents were either added under nitrogen flow, through a septum, or in a glovebox from the company Saffron under a nitrogen atmosphere. A positive nitrogen pressure was maintained throughout the reaction.

2.5.2 Purification Methods

Solvents and chemicals were dried and purified according to best-practice procedures.^[129]

Distillation: Liquid reactants (PCl_3 , SO_2Cl_2 , CDCl_3 , $\text{THF-}d_8$) were distilled under a nitrogen atmosphere and ambient pressure from an oil bath 15°C above their boiling point. The first fraction was discarded (PCl_3 and SO_2Cl_2 , only) and the distillation was terminated leaving a residue in the distillation flask. The reactants were stored in Young's tap Schlenk tubes.

Dialysis: Poly(phosphazenes) were purified *via* dialysis in deionised water. The crude product was dissolved or suspended in deionised water and transferred into cellulose tubing with a 12 to 14 kDa molecular weight cut-off, sealed, and suspended in 2 L of deionised water. The water was replaced every two hours on the first day and daily for four more days before recovering the sample from the tubing.

2.5.3 Nuclear Magnetic Resonance Spectroscopy (NMR)

NMR spectra were recorded on a 400 MHz Avance III HD Smart Probe Spectrometer at 298.0 K (^1H : 400 MHz, ^{13}C : 101 MHz, ^{19}F : 376 MHz, ^{31}P : 162 MHz). Deuterated solvents were used as received or dried prior to use if the sample was air and moisture sensitive. The chemical shifts δ for ^1H and ^{13}C NMR spectra are given relative to the used solvent or acetone- d_6 that in a glass capillary. Chemical shifts in the ^{31}P NMR and ^{19}F NMR spectra are recorded relative to an external 85% H_3PO_4 and CCl_3F external standard, respectively. ^{13}C , ^{19}F and ^{31}P NMR spectra were proton-decoupled. The chemical shifts of the residual solvents were assigned to literature known values.^[130]

2.5.4 Gel-permeation Chromatography (GPC)

Molecular weights (\bar{M}_n , \bar{M}_w) and dispersity values (\mathcal{D}) of the synthesised polymers were determined by size exclusion chromatography (SEC) with dimethylformamide (DMF, HPLC grade, VWR) as eluent containing 1 g L⁻¹ lithium bromide (98%, Sigma-Aldrich) using a Shimadzu LC system equipped with a diode-array detector (SPD-M20A DAD) and a refractive index detector (RI, Viscotek VE3580). One precolumn (50 x 8 mm), followed by three PSS GRAM gel columns (300 x 8 mm), were applied with a flow rate of 1.0 mL min⁻¹ at 25 °C. The diameter of the gel particles measured 10 μm , the nominal pore widths were 100 Å once and 3000 Å twice, respectively. Samples were dissolved in DMF and filtered prior to analysis.

2.5.5 Mass Spectrometry (MS)

Time-of-flight positive atmospheric solids analysis probe (TOF ASAP+) spectra were recorded on a Waters' Xevo G2-S bench top QTOF. Small amounts of samples were measured in an acetonitrile solution. Measurements were carried out at a probe temperature of 100°C.

Matrix-assisted laser desorption/ionisation time-of-flight (MALDI TOF) mass spectrometry was used to characterise the polymers presented in section 5.2.1 on page 116. The technique uses a laser-absorbing matrix that allows the ionisation of larger fragments with little fragmentation.^[131] Spectra were recorded on a Bruker ultrafleXtreme MALDI with a TOF detector.

Chapter 3 Degradation of the Silicon Thin-film Anode

Silicon thin-films as anodes for LIBs are relatively easy to manufacture and provide a good model system for studies on the electrochemical performance of silicon and the analysis of its SEI. Numerous publications have applied thin-films to investigate the degradation mechanism of silicon and the impact of material and cycling parameters.^[53,54,68,69,132,133] While there are identifiable trends of the thin-film electrodes' electrochemistry and post-cycling morphology, each system shows unique properties making a direct comparison of individual results challenging. It is crucial to thoroughly investigate the implications of the anode and cycling conditions for an individual system to understand the correlation between structural changes of the anode and its electrochemical performance. A recent review on silicon thin-film anodes has addressed the issue of the disparity by gathering data on parameters such as fabrication, the choice of materials and cycling conditions and consequently provides an outline for the analysis of the silicon thin-film anode.^[54]

This chapter aims to identify and characterise a model, binder-free silicon thin-film anode in great detail. The anodes are the basis for experiments in the following chapters applying electrolyte additives and polymer coatings. The anode provides an excellent system to follow changes in the electrochemistry and morphology of silicon as an anode material. A list of parameters and their implications on the cycling performance of the sputtered silicon thin-film system used throughout the thesis is discussed, which are outlined in Figure 3.1.

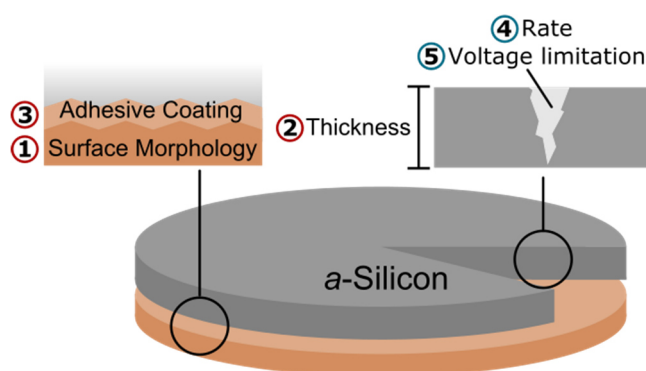


Figure 3.1: Illustration of the parameters investigated on the sputtered silicon thin-film electrodes. Substrate specific parameters (red): (1) The current collector surface morphology, (2) the anode thickness, (3) a nickel interlayer. Electrochemical cycling parameters (blue): Impact of (4) the current density (cycling rate) and (5) cut-off voltage on the lithiation capacity, crack formation and propagation and surface morphology.

The silicon anode cracks during lithiation and undergoes various changes in morphology during long-term cycling. We were able to follow the degradation and determine a degradation

mechanism based on the results from galvanostatic cycling and electron microscopy. Interesting correlations were observed between the anodes electrochemical performance and surface structure, which itself depends on the film thickness, the deposition of a nickel interlayer, and the surface morphology of the current collector as well as cycling conditions such as rate and voltage window.

In Figure 3.1, the fabrication specific parameters that are discussed in this chapter are ‘1’ the morphology of the copper current collector, ‘2’ the electrodes thickness and ‘3’ the sputtered nickel interlayer. During cycling, the variation of the cycling rate, ‘4’, and cut-off voltage, ‘5’, are investigated for their impact on the electrodes structure over the initial 30 cycles. Electrochemical cycling data and SEM micrographs of the anodes post cycling are analysed to identify changes in the silicon surface structure. In combination with chemical information from EDS analysis, electrochemical processes and the degradation mechanisms taking place are discussed. Data obtained on the thin-film thicknesses in section 3.2.5.2 was provided by Robert Weatherup. Figures of the dQ/dV peak positions and intensities in this and the following chapters were created by Ben Smith.

Over the following pages, the relevant literature is presented to show the state of research on the silicon thin-film anode and elaborate the various challenges and influences of materials and cycling parameters. To date, a multitude of systems have been presented that each investigate specific parameters of the thin-film electrode. Most publications limit the analysis to a specific variable and may miss the analysis of other factors. As an example, the detailed work by Obrovac *et al.* shows the impact of the $Li_{3.75}Si$ formation on film delamination, which is convincing and well described, while the impact of the different copper and nickel substrates and the roughness on the thin-film anodes performance were not further discussed in the study.^[69] A general problem is that electrochemical processes occurring during cycling of the thin-film anodes that show in the voltage profiles are often poorly described. Processes may be assigned to “SEI formation” or other unknown reactions without absolute certainty. It is crucial to carefully investigate each silicon thin-film anode system and identify the nature and implications of the electrochemical and physical changes during operation.

3.1 Characteristics and the Current State of Silicon Thin-films for LIBs

3.1.1 Fabrication Methods

Pure silicon thin-films are usually created by physical vapour deposition (PVD) or chemical vapour deposition (CVD), but other techniques, such as electroplating have also been employed and are summarised in recent reviews.^[53,54] Due to the range of deposition techniques available, the absolute structure of the deposited material differs in each case which leads to the wide range of electrochemical performance seen in the literature.^[54]

PVD offers a convenient way to deposit pure silicon thin-films by using a silicon wafer as a target. Adjusting the deposition conditions allows for control of the morphology and thickness. Without annealing, PVD usually yields amorphous silicon thin-films. The most common techniques are DC and RF sputtering, although other examples include electron beam (EB) or pulsed laser deposition (PLD) and thermal evaporation. PLD in particular allows for the formation of nano-crystalline silicon thin-films. Each type of PVD allows for the deposition onto substrates that have different requirements with their own advantages and disadvantages.

Whilst PVD is a physical process, CVD uses the decomposition of a gaseous precursor, such as silane, on or near the substrate to create a film of elemental silicon. By exposing a heated substrate to a flow of the precursor, high quality films can be obtained. The form of the film, either amorphous or crystalline, depends on temperature and rate of precursor flow.

3.1.2 Crack Formation and Delamination

During lithiation of the silicon thin-film electrode, the silicide phases can expand by more than 300% and experience large stresses both internally and at the interface with the current collector.^[134–136] These compressive and tensile stresses, during lithiation and delithiation, respectively, will lead to cracking of the material. During lithiation, silicon thin-films (< 100 nm) experience a compressive stress of about 1.5 GPa when bound to a current collector. This has been quantified by experimental and theoretical studies by Sethuraman *et al.* who identified a coupling of internal stress and the potential observed of the electrochemical reactions, causing a shift in lithiation voltage of 100–125 mV GPa⁻¹,^[136,137] so that silicides form at lower voltages under high stresses. During delithiation, however, stress levels decrease to ~0.5 GPa as the surface cracks. After continuous cracking into sufficiently small fragments the stress levels during cycling reach a minimum. The correlation between internal stresses and the

voltage at which the silicides form is due to changes in the thermodynamics of the process. The voltage observed depends on multiple factors that alter both the kinetics and thermodynamics of the lithiation, including the internal stresses created by a large change in volume impeded by an SEI, for example. Electron micrographs of a cracked silicon thin-film electrode and a sketch of the stepwise delamination process of the thin-films are shown in Figure 3.2.

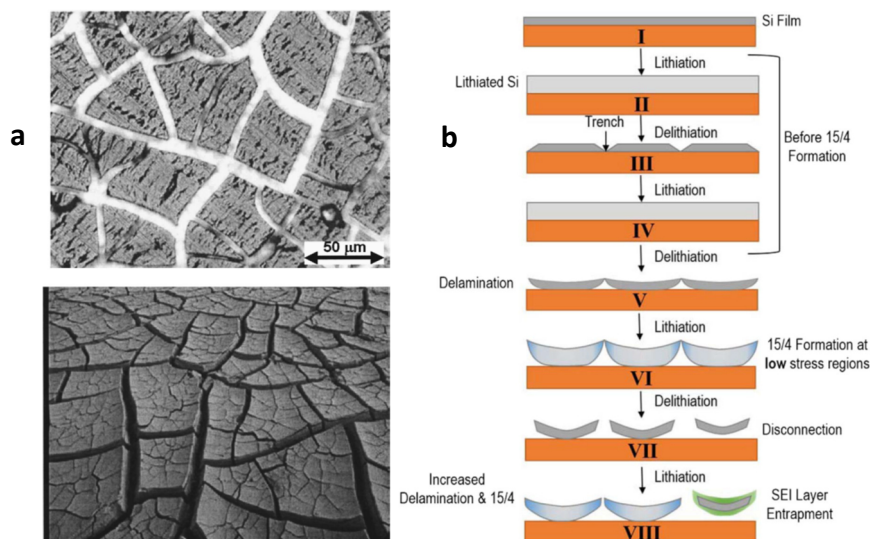


Figure 3.2: a) Micrograph of a Si thin-film after cycling (top), and a photograph of cracked mud of a dried-out lake (bottom). b) Delamination process of silicon islands linked to $\text{Li}_{3.75}\text{Si}$ formation (noted as 15/4 in the figure). Adapted with permissions from [64,69]. Copyright 2001, 2016 The Electrochemical Society.

The large tensile stresses placed on the electrode during expansion causes cracks to form. This will expose fresh silicon surfaces and edges, separating the thin-film into silicon islands that allow for stable cycling with enough space in between to accommodate the volume expansion. A comparison can be drawn to the “drying of mud on a lake bed”, where sharp cracks will separate large tiles of ground, and when more water is removed these patches may continue to shrink in size without further cracking (Figure 3.2a). Similarly, silicon islands will stay connected to the substrate through a patch at the centre of each island. The delamination of the silicon anode from the current collector, as reported by Dahn *et al.*, follows a gradual decrease in connectivity of the patches to the current collector as the anode is repeatedly cycled.^[64]

Furthermore, a major factor accelerating the anode’s degradation is the formation of the metastable, crystalline $\text{Li}_{3.75}\text{Si}$ phase. Its formation has been linked to the accelerated delamination mechanism through increased mechanical stress.^[69] Figure 3.2b shows the mechanism, where $\text{Li}_{3.75}\text{Si}$ forms in low stress regions leading to more disconnected silicon islands becoming entrapped in SEI. Iaboni and Obrovac have shown that $\text{Li}_{3.75}\text{Si}$ forms more

readily when there is no substrate-induced stress by comparing the electrochemistry of loose silicon flakes to flakes that are bound to the copper current collector. This suggests that the thin-films that experience increased stress, due to being attached to the current collector by virtue of not showing the $\text{Li}_{3.75}\text{Si}$ phase, have an extended lifetime. The phase is mostly observed when cells are cycled at a slow rate and to very low potentials. To avoid any chance of forming the detrimental, metastable phase, researchers therefore typically limit the operating voltage in lithium half-cells.^[54] In light of the presented results in this thesis it has to be made clear, that the absence of the crystalline lithium silicide observed as $\text{Li}_{3.75}\text{Si}$ (see Chapter 1, Figure 1.10) is desired. This can be attributed to strong interactions of the active material with the current collector and the use of a high enough current for moderate cycling rates.

3.1.3 Electrode Thickness and Crack Sizes

In the literature, silicon thin-films of varying thickness have been prepared and tested, ranging from only a few nanometres to several micrometres.^[54,138] The electrode thickness determines its absolute capacity, area capacity and affects its longevity as thicker electrodes lead to a faster loss of electric contact, faster degradation and therefore a shorter lifetime.^[133] The Griffith-Irwin relation describes the correlation between fracture stress levels and the thickness of the film:

$$\sigma_{fr} = \frac{K}{\sqrt{\pi d}} \quad (3.1)$$

where σ_{fr} is the critical fracture stress, K is the fracture toughness of the material and d is the film thickness. The critical fracture stress (σ_{fr}) will hence be lower the thicker the silicon thin-films are, allowing cracks to form more easily. This is in-line with reports that electrochemical performance decreases when the anode exceeds a certain thickness.^[54] For long-term cycling, this limit has been found to be between 100–200 nm, which is similar to that of free standing nanoparticles.^[61]

The thickness-dependent cracking patterns of silicon thin-film anodes and the calculated internal and interfacial stress of the anode on the current collector are shown in Figure 3.3.

As expected, the morphology of the cracking pattern appears to be sensitive to the thickness with thicker films showing the proposed island formation and thinner films forming a network of cracks resulting in interconnected islands (Figure 3.3d).^[139] Thicker films will expand and contract more, leading to isolation and larger crack sizes. The critical sizes of the islands that

separate during cracking follow a linear trend and are around 2 μm for thinner films ($<200\text{ nm}$) and 9–10 μm for 1 μm thick electrodes (Figure 3.3e).

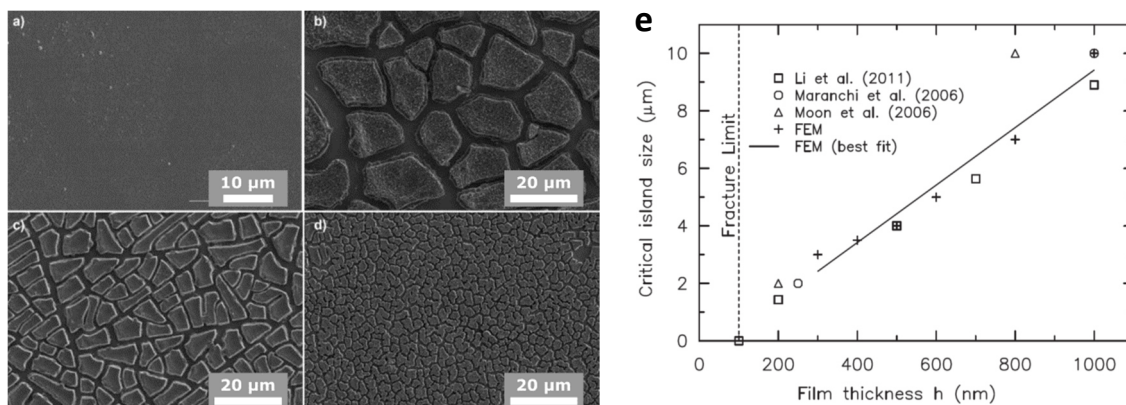


Figure 3.3: SEM micrographs of a) pristine 500 nm silicon thin-film anodes and cycled anodes: b) 1 μm , 5 cycles, c) 500 nm, 5 cycles, and d) 200 nm, 10 cycles. e) Comparison of the critical Si island size depending on the thin-film thickness h from experiments and simulations. Adapted and reprinted with permissions from references ^[139,140]. Copyright 2011 The Electrochemical Society, 2014 Elsevier Ltd.

3.1.4 Performance Factors of the Silicon Thin-film Anode

3.1.4.1 Surface Roughness and Transition Metal Interlayers

Roughening the surface of the current collector creates a larger surface area for improved adhesion, offering more pathways to relieve stress and “anchor-points” for the active material. Better adhesion generally improves the electrochemical cycling properties of the thin-film electrodes.^[52,141,142] However, roughening the surface can also be detrimental, as shown in Figure 3.4 where silicon thin-film electrodes (275 nm) deposited on roughened and as-received copper substrates show different performance.

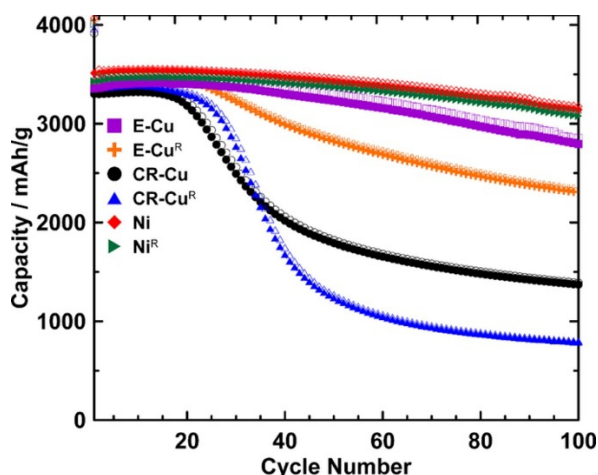


Figure 3.4: Electrochemical cycling performance of a Si thin-film anode (275 nm) on different current collectors (E-Cu: flat surface copper, CR-Cu: cold-rolled, rougher copper). Open symbols: lithiation capacity, closed symbols: delithiation capacity. Reprinted with permission from [69]. Copyright 2016 The Electrochemical Society.

In the same study, the best performance was found for the anode sputtered onto a nickel substrate (Figure 3.4).^[69] Without a detailed explanation, the increased performance was said to arise from better adhesion of silicon to the nickel layer.^[69] In general, the performance of thin-films has been shown to greatly increase by the *in situ* deposition of a metal layer, such as chromium or copper, onto the current collector before the silicon deposition.^[135,143] Without exposure to oxygen in between deposition steps, the silicon will be deposited on metal, rather than metal oxide, improving adhesion. An oxide interlayer may otherwise be reduced, leading to structural instability of the interphase that can accelerate delamination. In this work, nickel was chosen due to its availability in the magnetron sputterers used in this work to create a metallic interlayer between the copper substrate and active silicon material. Nickel is also said to bear very thin surface oxide layers making it a particularly useful material.^[144]

3.1.4.2 Cycling Rate and Voltage Limitation

Results throughout the literature show that fast cycling rates (high current densities applied) can lead to accelerated capacity loss and an observed limited capacity by affecting the lithiation kinetics of the silicon thin-film anode.^[54] Lithiation-induced stress is affected by the migration speed of the interface between the different silicide phases, which depends on the cycling rate and the size of the silicon material.^[145] A faster cycling rate lowers the amount of electrochemically accessible silicon, as observed by Georgoulas *et al.*^[146] This is due to limitations that arise from the lithium diffusion coefficient in *a*-Si which is in the order of $10^{-16} \text{ m}^2\text{s}^{-1}$, as the phase boundary may only advance as much.^[147] For example, one study showed silicon thin-films cycled at an extremely high rate (8C) which caused electrochemical

inactivity after a few cycles, however, in this case capacity was be recoverable by lowering the rate.^[148]

The cut-off voltage also affects the capacity and cyclability of silicon thin-film anodes. A narrower voltage window will limit the volume expansion but also limit the amount of lithium silicide formed. A limit of 100 mV has been shown to increase cycle life greatly and voltage cut-offs around 50 mV may be set to avoid the formation of the detrimental $\text{Li}_{3.75}\text{Si}$ phase.^[49,69,149,150] However, most literature studies appear to have been performed with a cut-off voltage of 10 mV or less to access the anode's full capacity. Moreover, it must be noted that the upper voltage cut-off does not appear to have a significant impact on the cycle life, although there is a lack of conclusive studies on this matter.^[54]

3.2 Results and Discussion

3.2.1 Electrode Preparation

Images of the silicon thin-film electrodes prepared *via* magnetron sputtering are shown in Figure 3.5. Commonly, copper foil is used as the current collector for anodes in LIBs due to its electrochemical stability under the electrochemical conditions. As multiple anode discs were sputtered at once, the thickness of the silicon film varies within a few nanometres depending on the position of the individual electrode disc relative to the target. Thicknesses were confirmed using a profilometer on a masked silicon wafer that was placed near the substrates for the sputtering process. On copper foil discs with a diameter of 12 mm, a ~250 nm nickel layer was deposited. Nickel is added to provide a fresh metal surface and minimise the impact of a potential metal oxide layer to the silicon thin-film adhesion, as will be discussed in Chapter 3.2.5.3. The discs were transferred to another magnetron sputterer for the deposition of ~100 nm of silicon (Figure 3.5a-c). Given that sputtering is carried out at 10^{-2} mbar in argon which corresponds to a relatively short mean free path (a few millimetres) compared to the target-sample distance (12 cm), the coatings conformally coat the copper surface, as seen in Figure 3.5d.

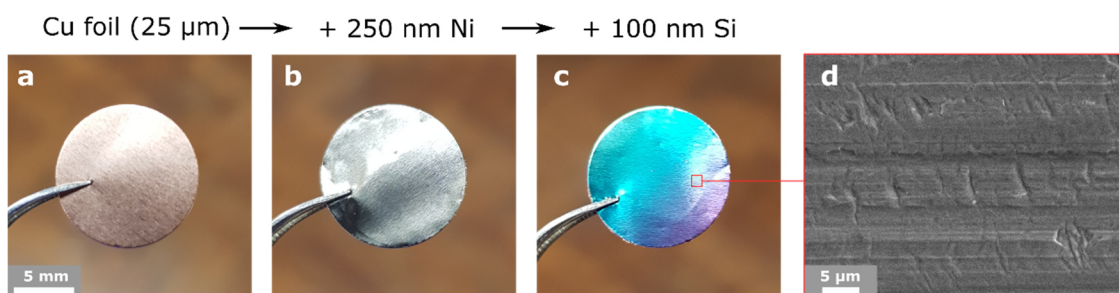


Figure 3.5: Photographs of the different stages during the preparation of the silicon thin-film anodes: a) CR Cu current collector, b) CR Cu coated with 250 nm nickel, c) CR Cu substrate coated with 250 nm nickel and 100 nm silicon. d) SEM micrograph of the silicon and nickel-coated CR Cu anode.

The EDS spectra (Figure 3.6) of the anodes shows small amounts of oxygen and argon. The oxygen stems from the native oxide layer that is formed on the metal surfaces when exposed to air. The presence of argon is attributed to the sputtering process. Negligible amounts of nitrogen and carbon signals arise from surface contamination of the sample and in the microscopy chamber.

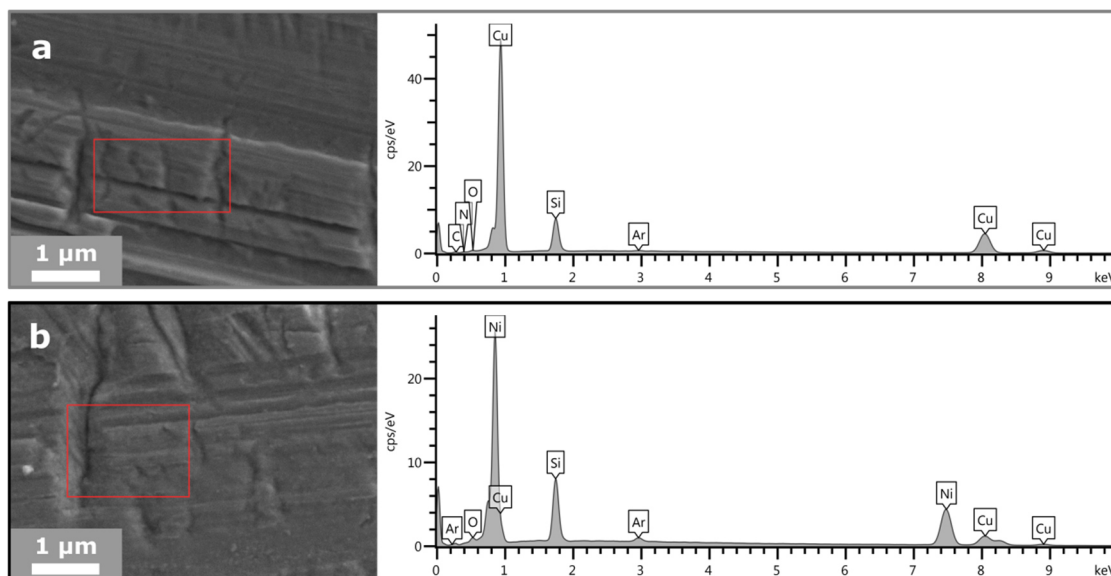


Figure 3.6: SEM micrographs showing the area of EDS acquisition and the corresponding spectra (15 kV) of the 100 nm *a*-Si thin-film anodes on a) CR Cu and b) 250 nm Ni-coated CR Cu.

The weight of the active material is estimated based on geometrical parameters, assuming a density of 2.33 g cm^{-3} for the amorphous silicon being $\sim 28 \mu\text{g}$.^[151] However, having weighed various anodes, the found masses vary between 24-27 μg , with some electrodes weighing less than the expected 28 μg . Given that the weight of the copper substrate holds a significant fraction of the weight ($\sim 21 \text{ mg}$), and the multistep preparation process, these measurements are therefore fairly unreliable. Therefore, weights of 28 μg are assumed for the following capacity calculations which can lead to slight discrepancies in the absolute capacities between samples.

It must be noted, that the silicon density resulting from sputtering at different rates, temperatures and target distances has been reported to affect the electrochemical performance, with lower density films showing superior cycling performance.^[143] Sputtered thin-films usually show very high porosity. Hence, argon, detected by EDS in the thin-film, should not be detrimental to the anode's performance as it lowers the density of the silicon material and is likely to escape during cycling.

3.2.2 Electrochemical Processes and Structural Changes during Cycling

A description of the electrochemical processes that are observed during cycling and the analysis for one particular cell in this section aim to introduce the system to better understand the changes made to the material in the following subchapters when discussing specific parameters.

3.2.2.1 Electrochemical Features

The electrochemistry observed for the RF magnetron sputtered silicon electrodes is similar to that described in the introduction (see Figure 1.10, page 14). The anode presented here is of the composition shown in Figure 3.5c: A 100 nm *a*-Si thin-film electrode on a nickel-coated cold-rolled copper (CR Cu) current collector.

The voltage profile and respective differential plots (dQ/dV) from galvanostatic cycling with the individual lithiation stages indicated are presented in Figure 3.7. The cell was first discharged and charged at a lower rate of $C/30$ followed by $C/5$, in subsequent cycles. Cycling to full discharge (5 mV) was chosen to show all of the relevant electrochemical processes clearly.

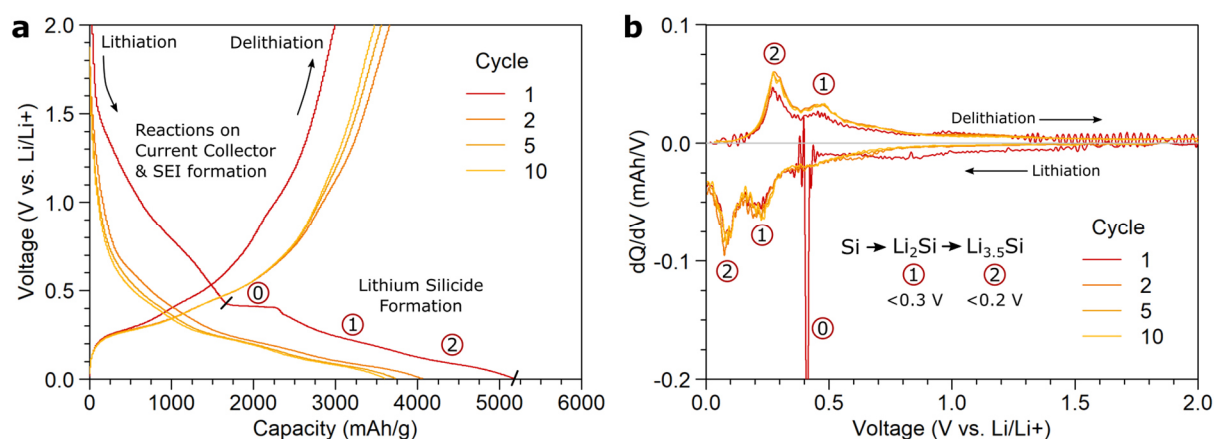


Figure 3.7: a) Voltage profiles of several cycles of the 100 nm *a*-Si thin-film anode on Ni-coated CR Cu with indicated regions of the reactions of the electrolyte on the current collector and the SEI formation, and the lithium silicide formations pseudo-plateaus '0', '1' and '2'. The process '0' occurs only in the first cycle. b) Differential capacity plot (dQ/dV) showing the peak positions for the two major lithium silicides Li_2Si '1' and $Li_{3.5}Si$ '2', and process '0'. Rate: 1st $C/30$, 2nd+ $C/5$; cut-off voltage: 5 mV.

Voltage profiles in Figure 3.7a, from galvanostatic cycling, show capacities close to, and above, the active material's theoretical value of 3579 mAhg^{-1} (full lithiation to $Li_{3.75}Si$). Generally, the capacity observed is affected by variations in thickness, density and electrochemical processes of both the active material and other processes in the cell such as the formation of the SEI. The first lithiation of the thin-film anode (Figure 3.7, red trace) shows a large amount of capacity in the higher voltage region between 2.0 and 0.4 V, which decreases in the following cycles. During the first delithiation less lithium moves from the anode to the cathode, showing a large discrepancy in capacities. This initial capacity loss (ICL) is present in all freshly prepared batteries.^[152] The difference in capacity is also known as coulombic

efficiency (CE). Following the conditioning cycle, the efficiency increases, as less side-reactions occur, and more lithium reacts reversibly with the active material.

Following the side-reactions, a pseudo-plateau '0' in Figure 3.8a at 0.4 V is observed. The feature is observed for amorphous silicon thin-film anodes prepared by PVD, as discussed in the introduction (Figure 1.10, page 15), where the sputtered silicon thin-film consists of disordered silicon atoms with weak Si-Si bonds that require less energy to break. The plateau voltage can be affected by the sputtering parameters and electrode thickness. The native oxide layer which is reduced to lithium silicates at similar voltages does not show as a separate process and may only provide a small contribution to the overall capacity during the first discharge.^[153,154]

The next processes are the α - Li_xSi formation '1' and '2', that are also present in subsequent cycles. '1' corresponds to the lithiation towards " Li_2Si " with $x \leq 2$ at a voltage between 0.3 and 0.15 V, followed by '2' when " $\text{Li}_{3.5}\text{Si}$ " ($2 \leq x \leq 3.5$) is formed at lower voltages. During delithiation the process is reversed. The processes appear as peaks in Figure 3.7b. Under the chosen conditions the data does not show any evidence of the metastable, crystalline $\text{Li}_{3.75}\text{Si}$ phases' presence (a reference spectrum is found on page 14 in section 1.4.2, Figure 1.10), although it cannot be ruled out. A cut-off voltage of 100 mV was chosen for long-term cycling experiments to not risk forming any of the detrimental $\text{Li}_{3.75}\text{Si}$.

3.2.2.2 Long-term Cycling Performance

The anode presented in this section was a 100 nm silicon thin-film that was used as the reference for the studies performed on poly(phosphazene) coatings as artificial SEI in Chapter 5. Figure 3.8 shows the electrochemical performance, voltage profiles and dQ/dV plots of selected cycles of the anode cycled 200 times between 2.0 V and 100 mV.

Limiting the voltage window limits the lithiation, making the Li_2Si phase the dominant feature in the differential plots (Figure 3.8c) with small amounts of $\text{Li}_{3.5}\text{Si}$ observed as a partial peak at 0.1 V during discharge and a shoulder during charge at 0.4 V (for comparison at full discharge: Figure 3.7b). This is reflected in the limited capacity observed. During stable cycling, the cell holds a specific capacity of between 1600 and 1800 mAhg^{-1} . There is a large initial capacity loss (ICL) on the first cycle of 21%, which is common for silicon anodes in lithium half-cells.^[152] Over subsequent cycles the cell gains capacity, reaching a maximum on the 47th cycle.

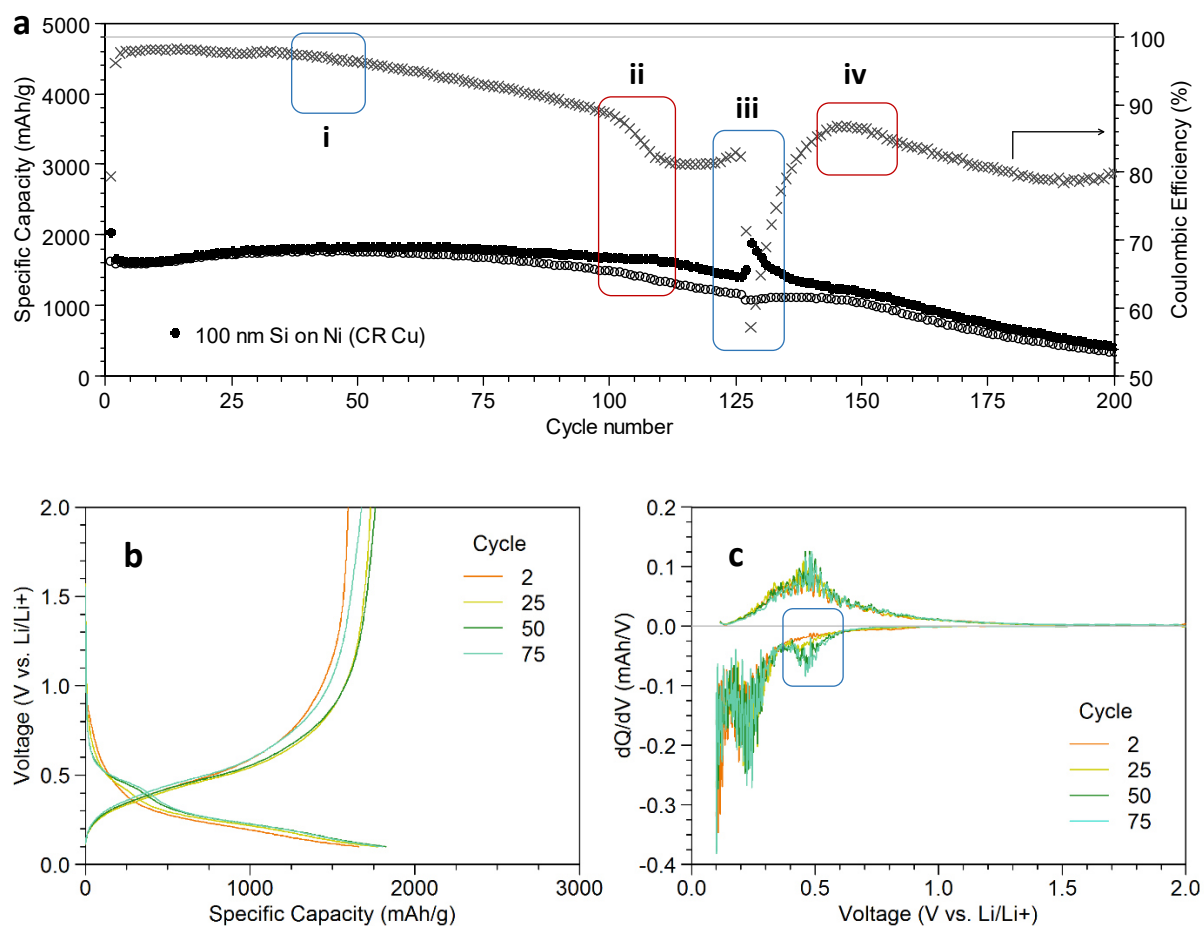


Figure 3.8: a) Electrochemical performance of the 100 nm α -Si thin-film anode on Ni-coated CR Cu. The four significant decreases in CE are highlighted. b-c) Combined voltage profiles and dQ/dV plots for cycles number 2, 25, 50 and 75. The electrochemical process associated with 'i' is highlighted. Filled symbols: lithiation; empty symbols: delithiation; **x**: Coulombic efficiency; rate: 1st C/30, 2nd+ C/5; cut-off voltage: 1st 5 mV, 2nd+ 100 mV.

After the first cycle, the cell reaches efficiencies of > 98% that are maintained until the 30th cycle. Efficiency slowly drops to < 90% by the 100th cycle, caused by event 'i'. Hereafter, the efficiency drops noticeably due to the second event 'ii' as an increase in irreversible capacity is observed (more lithium being moved during discharge than during charge). This process is referred to as the "dip" in efficiency in this and the following chapters, as it is characteristic for all cells that are cycled under similar conditions. We find that the "dips" occur after a similar number of cycles and are associated with imminent cell failure when using standard electrolytes. In this cell, around the 129th cycle, another sudden, severe decrease in efficiency, 'iii', occurs. The cell then recovers over the next 10 cycles but shows an accelerated capacity loss from the 150th cycle onwards, 'iv'. From the 25th cycle onwards an electrochemical process at ~0.45 V, that may be connected to the decrease in efficiency 'i', grows in intensity (highlighted in Figure 3.8c).

Extracting the Li_2Si peak voltage and height, resembling the current used for the process (in mAhV^{-1}), (Figure 3.9) from the differential plots shows that the processes associated with forming the Li_2Si phase evolves over time and change around the position of the “dip” (event ‘ii’) and event ‘iii’ (see Figure 3.8). The trends in Figure 3.9 provide information on the changes in lithiation dynamics.

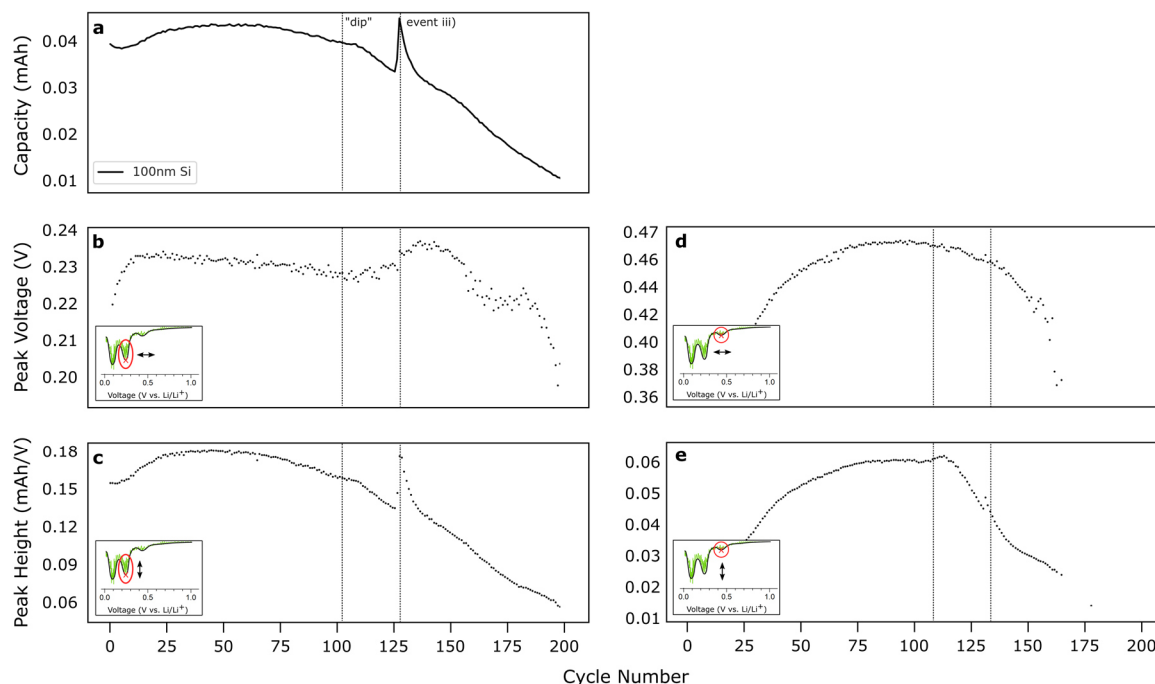


Figure 3.9: Analysis of the voltage and height of the dQ/dV peaks of the 100 nm *a*-Si thin-film anodes on Ni-coated CR Cu corresponding to b-c) Li_2Si and d-e) the electrochemical process at ~ 0.45 V. The insets show the studied peak positions in a typical dQ/dV plot for clarification.

The Li_2Si peak height (Figure 3.9c) mirrors the trend in capacity (Figure 3.9a) as it is the major process occurring during discharge. During the sudden decreases in efficiency, the Li_2Si peak height increases, showing more lithiation occurring for this process, particularly during the event ‘iii’. After the “dip” it only slightly increases and shows a steady decline until reaching ‘iii’, after which it continues to fade at a similar rate. The peak shifts noticeably during the first 20 cycles towards higher voltages, followed by a slowly decreasing voltage until reaching the “dip”, likely caused by stress relieve due to cracking. The voltage at which Li_2Si is formed then gradually increases towards ‘iii’ and falls quickly after, plateauing during the capacity decrease between the 160th and 180th cycle before the peak fades.

The process at ~ 0.45 V, observed to arise after 25 cycles in this cell, shows a more gradual increase in intensity (Figure 3.9e) and reaches its maximum voltage after 75 cycles (Figure 3.9d), when the CE decreases in ‘i’. The first “dip” affects the process with an increase in peak

height which then quickly drops, and a slow, gradual shift of the peak towards lower voltages. Event ‘iii’ does not appear to affect the ~ 0.45 V process in the same way as the silicide formation, however it shows an increase in peak height the two cycles before it.

3.2.2.3 SEM and EDS Analysis of the Cycled Electrodes

Electron micrographs of the Si thin-film anodes were taken after an increasing number of cycles. Figure 3.10 shows the electrochemistry of the first cycle and electron micrographs of the silicon thin-film anode surfaces at 5 mV and 2 V. At full lithiation (cell held at 5 mV, Figure 3.10c), the anode’s surface appears smooth due to the increase in volume of the lithium silicide. At full delithiation (cell held at 2 V, Figure 3.10d), small cracks evolve in areas with distinct topological features. The cracks propagate with increasing cycle number: Figure 3.11 shows the electron micrographs of the electrode after 30 cycles at full discharge and charge.

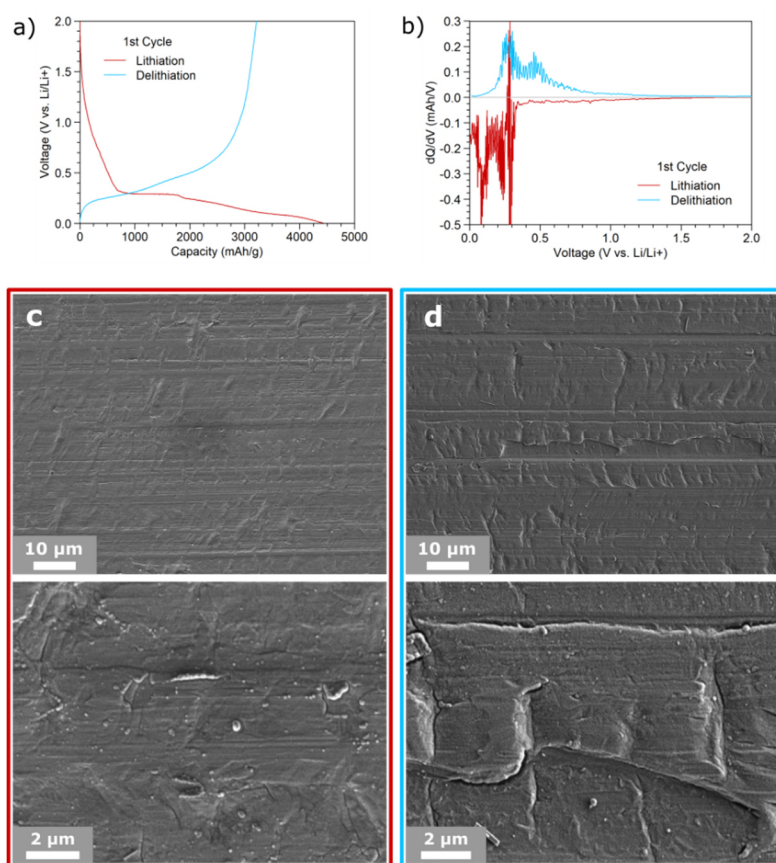


Figure 3.10: a) Voltage profile and b) differential plot of the first cycle showing the lithiation (red) and delithiation (blue) traces (discharge and charge, respectively) of a 100 nm *a*-Si thin-film anode on Ni-coated CR Cu. Electron micrographs (5 kV) of a c) fully lithiated anode, held at 5 mV and d) delithiated anode, held at 2 V.

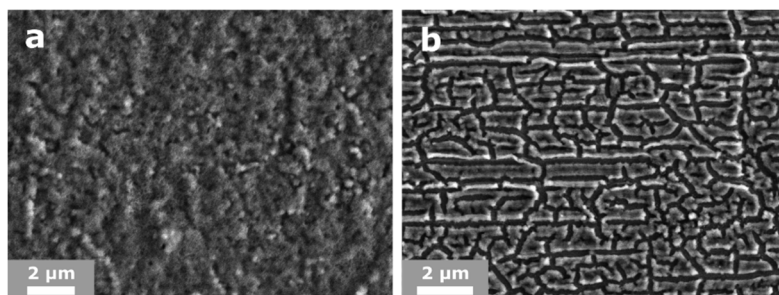


Figure 3.11: Electron micrographs (5 kV) of the 100 nm *a*-Si thin-film anodes on Ni-coated CR Cu after 30 cycles: a) fully lithiated anode, held at 5 mV and b) delithiated anode, held at 2 V

After the 30th discharge, the electrode shows a diffuse, grainy surface (Figure 3.11a). The material contracts into connected silicon islands of less than 1 μm in one dimension (Figure 3.11b) separated by ~200 nm gaps.

Figure 3.12 shows the electrode, whose electrochemistry was presented in Figure 3.8, after 200 cycles, having formed an amorphous Si/SEI material before and after drying. We observe the lacy structure in Figure 3.12b, when the electrochemical process at 0.45 V is present and the CE decreases, as discussed in the next subitem.

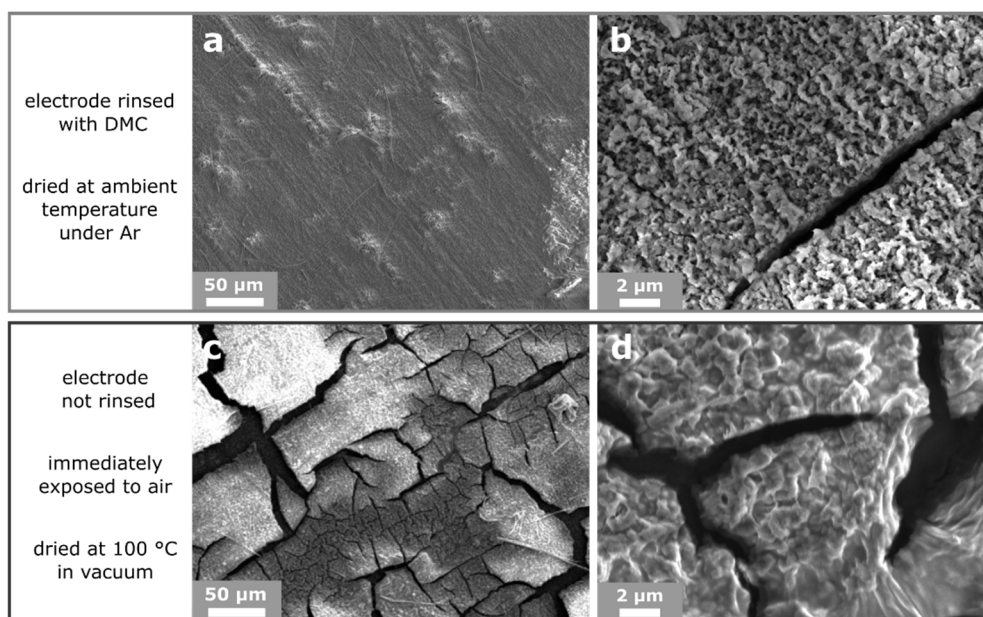


Figure 3.12: SEM micrographs (5 kV) of the 100 nm *a*-Si thin-film anodes on Ni-coated CR Cu after 200 cycles. a) & b) Micrographs of a cycled electrode that was rinsed with dimethyl carbonate (DMC) and left to dry in an argon filled glovebox. c) & d) Electron micrographs of a cycled electrode not rinsed, exposed to air and dried in a vacuum oven at 100°C. Both electrodes were transferred to the SEM vacuum chamber under air.

Apart from the large crack at higher magnification there are very few cracks found on the surface in Figure 3.12a. The sample in Figure 3.12a-b was rinsed with DMC and left to dry in an argon filled glovebox.

A similar electrode shown in Figure 3.12c-d was transferred to a vacuum oven to dry at 100°C. The cracks differ in shape to those expected to arise from the silicon island formation and must arise from the material drying out during which parts of the silicon/SEI material chip off of the current collector (Figure 3.12c). The surface layer also appears to have fused in the oven (Figure 3.12d).

The deep crack observed in the micrograph in Figure 3.12b indicates a massive increase in anode thickness which is confirmed in the electron micrographs of the focused ion-beam (FIB) milled cross section in Figure 3.13.

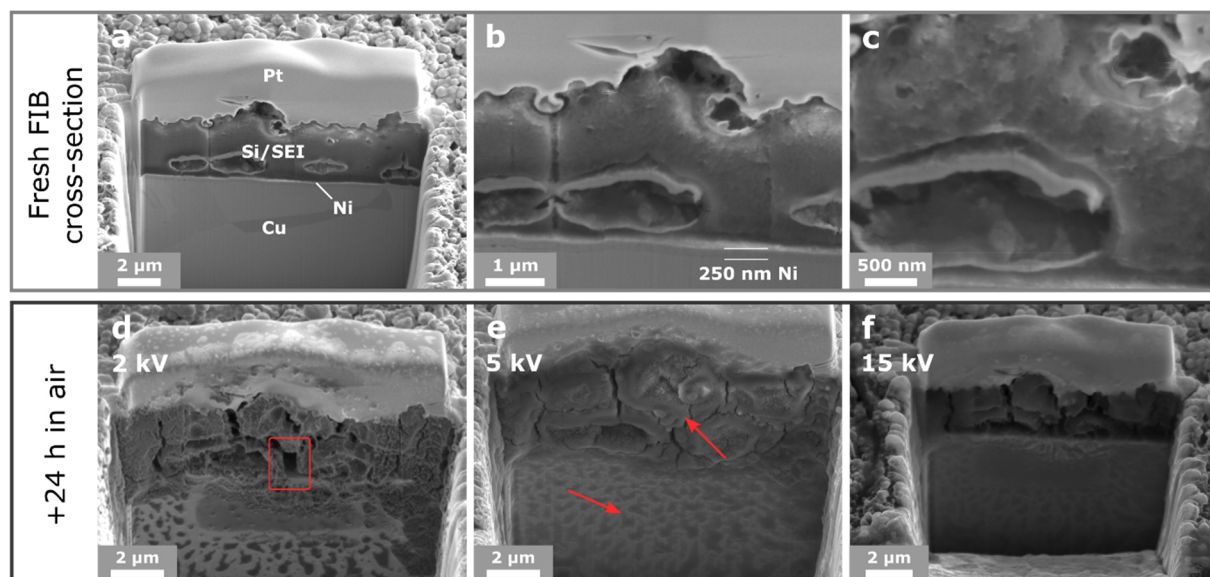


Figure 3.13: a-c) SEM micrographs (5 kV) of the FIB cross section of a 100 nm *a*-Si thin-film anode on Ni-coated CR Cu after 200 cycles. The 250 nm nickel layer is marked in b) as a vertical reference. d-f) Micrographs of the cross section under different acceleration voltages after exposure to air (2 kV, 5 kV, 15 kV; beam damage in d) and f) was inflicted by the 15 kV electron beam; order of acquisition: e - f - d; the highlighted area in d) clearly shows the beam damage from the long exposure during EDS. The arrows in e) show the bulging material and the dried electrolyte stains. The surface was coated with several nanometres of gold followed by a platinum bar (~2 μm) on the FIB milling site. Micrographs were recorded at an angle of 53°.

The micrographs show that the Si/SEI material has a thickness of 2–3 μm after 200 cycles (Figure 3.13a) and the 250 nm nickel layer appears intact with the Si/SEI material peeling off from it (Figure 3.13b). Moreover, there are hollow areas in the SEI morphology, that appear to have contained trapped electrolyte. This electrolyte seeped through the material, over the course

of 24 h between the FIB milling and the EDS analysis, to the exposed cross section where it dried (highlighted in Figure 3.13e).

Exposing the Si/SEI material to the electron beam at 15 kV acceleration voltage for a longer period of time damages the material. This is seen in a micrograph at 2 kV after prolonged exposure to the electron beam at 15 kV (Figure 3.13d and f, respectively).

The EDS spectra in Figure 3.14 of the surface and cross section show significant amounts of oxygen, carbon, fluorine and phosphorous from the degradation of the electrolyte.

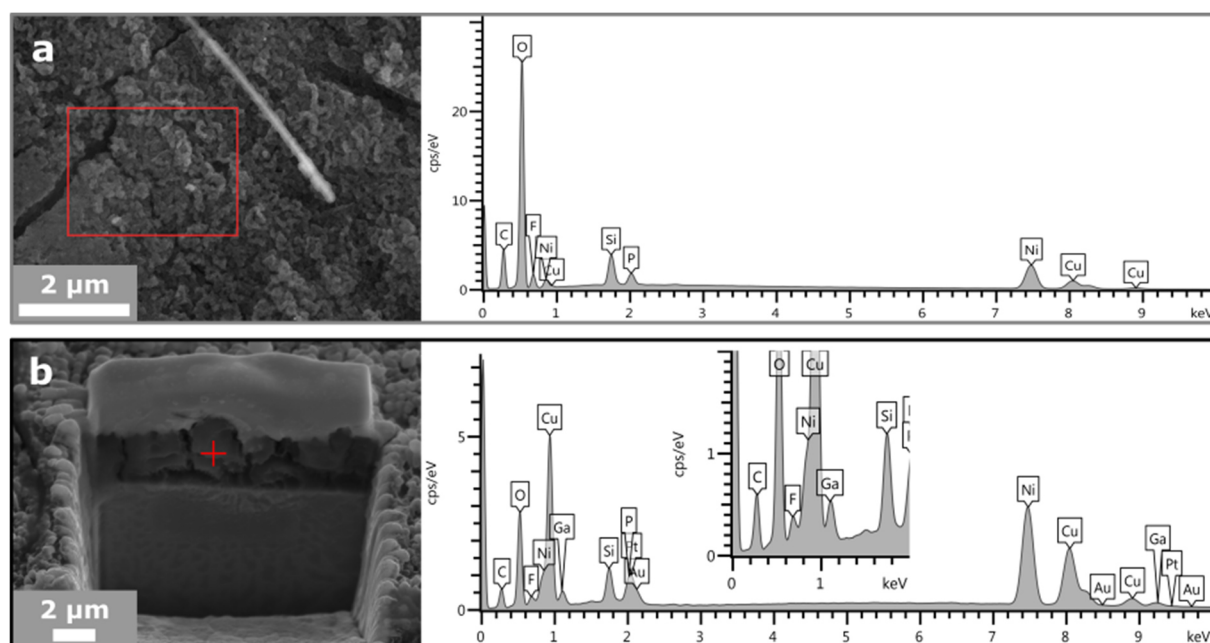


Figure 3.14: SEM micrographs and EDS spectra (15 kV) of the surface (a) and the cross section (b) of a 100 nm *a*-Si thin-film anode on Ni-coated CR Cu after 200 cycles. The inset shows an enlarged region of the voltage range between 0 and 2 keV. Gold, platinum and gallium signals in b) arise from substances used for the sample preparation and FIB milling process.

The ratio of SEI and electrolyte specific elements (oxygen, carbon, fluorine) to silicon on the surface (Figure 3.14a) is higher than for the cross section (Figure 3.14b). The surface is likely composed of large amounts of SEI and dried electrolyte. Similarly, the mixture on the cross section must in large parts show the presence of dried electrolyte from the nanoporous Si/SEI material.

The effect of the beam acceleration voltage on the appearance of the micrographs, already observed in Figure 3.13a-c, is further demonstrated in Figure 3.15 on the vacuum dried electrode. EDS element maps, recorded at 15 kV are shown in Figure 3.13d.

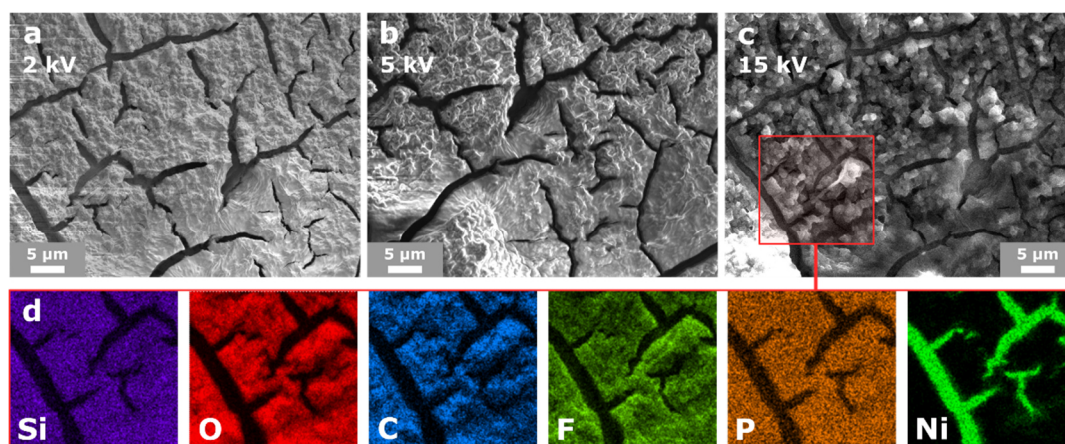


Figure 3.15: a-c) SEM micrographs of a 100 nm *a*-Si thin-film anode on Ni-coated CR Cu after 200 cycles under increasing beam acceleration voltage. The electrode was dried overnight in a vacuum oven at 100°C, without being rinsed with DMC. d) EDS element maps for the highlighted area in c).

Increasing the beam acceleration voltage gives less surface sensitive information due to the larger interaction volume of the beam with the material. All images were recorded with a secondary electron detector. Secondary electrons are emitted from the first 5–50 nm below the surface. However, at higher acceleration voltages the interaction volume increases, and backscattered electrons will contribute to the secondary electron count increasing bulk sensitivity. At 2 kV the micrographs show the electrodes surface morphology best (Figure 3.15a). At 5 kV more of the underlying structure becomes visible and at 15 kV the larger amount of SEI and dried electrolyte are virtually omitted, showing a dense, granular Si material beneath it.

X-rays detected during EDS analysis are emitted from an interaction volume down to several microns deep in the material, making the technique less surface sensitive. The element maps in Figure 3.15d show the fine distribution of oxygen, carbon, fluoride and phosphorous, that all stem from the decomposition and drying of the electrolyte. Silicon is found in the same areas evenly distributed in the same locations as these SEI specific elements. Nickel appears only in the cracked areas and is seemingly undamaged from cycling and drying.

3.2.3 Investigating the Process at ~ 0.45 V

The electrochemical process at ~ 0.45 V, which has shown to gain in intensity over time (Figure 3.9e), does not appear for every electrode but has implications on the structures observed. It was most noticeable on electrodes coated with nickel and on anodes sputtered onto CR Cu. However, the process may occur on any substrate as was demonstrated when two electrodes were processed the same way, but only one showed significant contributions of the

process. The cycling performance over 75 cycles and the voltage profile and dQ/dV plots of the 50th cycles are presented in Figure 3.16.

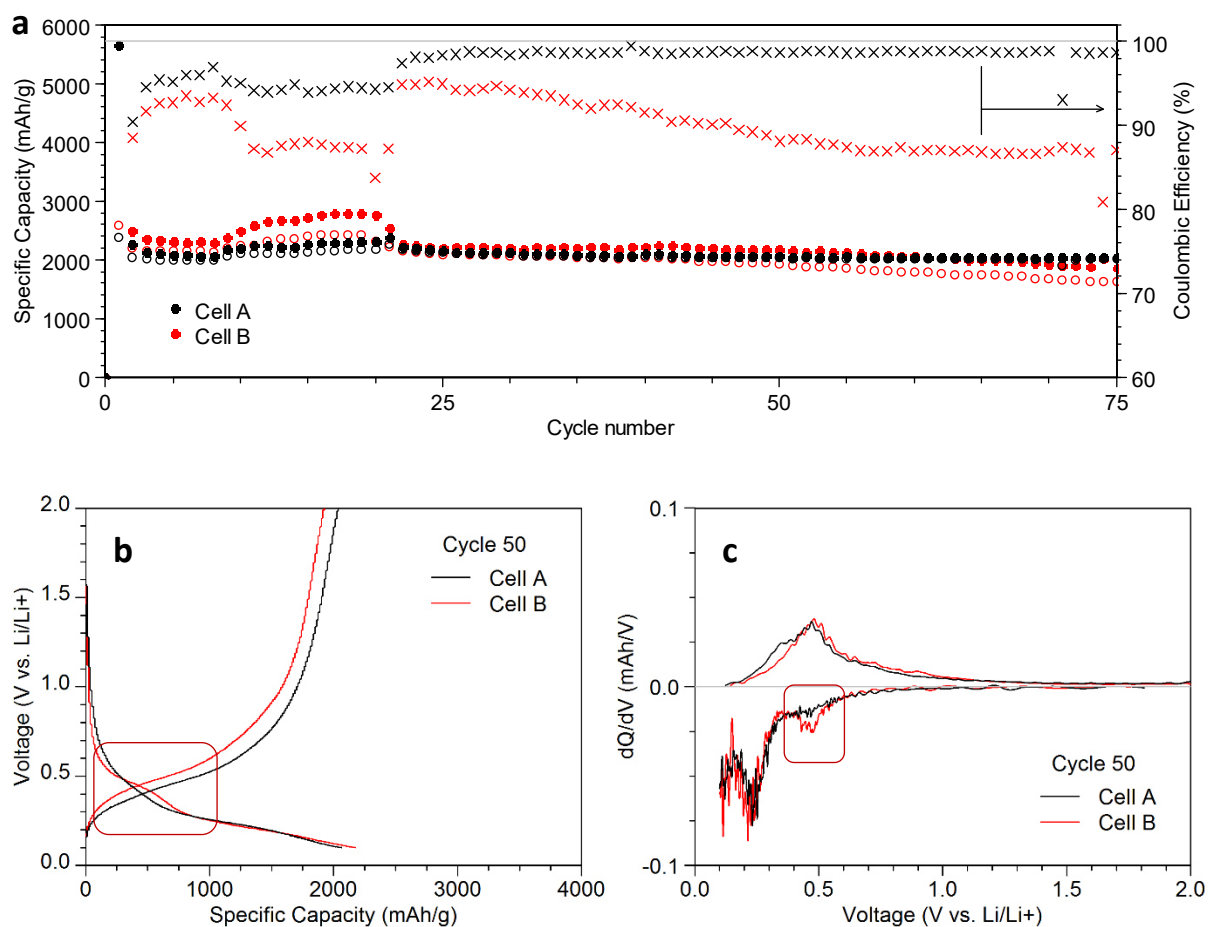


Figure 3.16: a) Electrochemical performance of two cells with 100 nm *a*-Si thin-film anodes on Ni-coated GG Cu showing differences in CE and a highlighted process at ~ 0.45 V. b-c) Voltage profile and dQ/dV plot of the 50th cycle. Filled symbols: lithiation; empty symbols: delithiation; **x**: Coulombic efficiency; rate: 1st C/30, 2nd+ C/10; cut-off voltage: 1st 5 mV, 2nd+ 100 mV.

The two cells, on a copper substrate that is originally intended for graphene growth, GG Cu (presented in more detail in section 3.2.5.1, page 59), show similar capacities but different CEs (Figure 3.16a). The fluctuations apparent during the first 10 cycles are due to changes in ambient temperature during a local heatwave. The voltage profiles and dQ/dV plots of the 50th cycle show that the process at ~ 0.45 V has a large contribution to the overall capacity of Cell B.

SEM micrographs and EDS element maps of the electrodes after 75 cycles in Figure 3.17 show the differences in morphology and chemical composition. Cell A exhibits the previously observed silicon islands (Figure 3.17a) and elemental maps show that oxygen covers the islands and has higher concentrations on the edges, filling the surface cracks partially. Cell B shows a thicker, space-filling Si/SEI material with curly surface features (Figure 3.17d,f). EDS element

maps show much higher oxygen concentrations in these ripples and an even distribution of silicon underneath (Figure 3.17e).

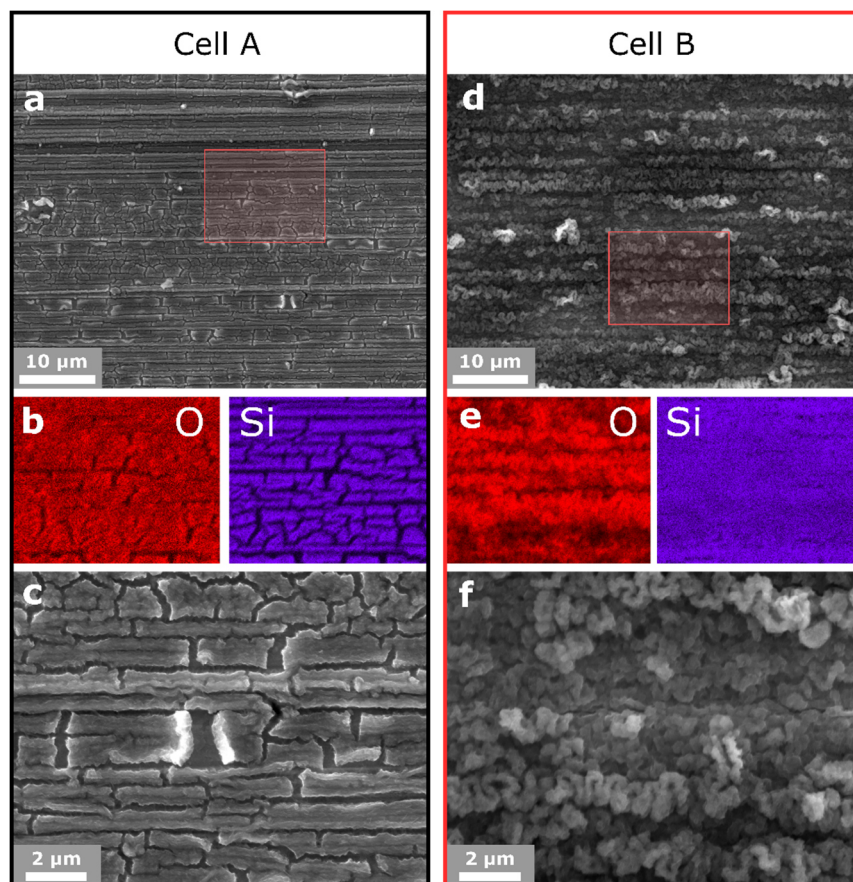


Figure 3.17: SEM micrographs and EDS element maps (15 kV) of the cyclized 100 nm *a*-Si thin-film anodes on Ni-coated GG Cu from Cell A and Cell B after 75 cycles. The areas of the EDS analysis are highlighted. a) Surface structure formed in the absence of the electrochemical process. b) Oxygen and silicon maps tracing the cracking pattern. c) Magnified area showing delamination and flat surfaces of the silicon islands. d) Surface structure formed in the presence of the electrochemical process. e) EDS element maps showing the even coverage of the current collector with Si with a few cracks and extensive amounts of oxygen in the wrinkled surface features. f) Magnified area showing the rippled surface features.

Clearly, the structure formed in Cell B has a much larger surface area and significant SEI formation. We may therefore consider a surface reaction regarding the process at 0.45 V, although the exact chemical reaction that occurs remains unknown. It must arise from decomposition of the electrolyte on the anode surface and may involve silicon, for example in the formation of lithium silicates. Further studies are necessary to identify potential causes for this electrolyte degradation but in light of our studies we can assume that an increase in the process at ~ 0.45 V indicates enhanced surface reactions that affect and relate to the anode structure.

3.2.4 Interim Analysis and Discussion of the Electrochemistry and Electron Micrographs

Generally, the anodes show good cycling properties over more than 100 cycles. By this point we are able to identify the major electrochemical processes taking place during the individual cycles.

The voltage at which the reaction of lithium forming Li_2Si occurs changes over the cycle-life of the electrode as shown in Figure 3.9. Over the first 25 cycles it moves towards higher voltages showing that less energy is necessary to form the silicide. Given that we see cracks forming progressively until the 30th cycle in Figure 3.11, that remain similar to those found after 75 cycles (Figure 3.17) we can assume that the films are sufficiently cracked once a maximum voltage of the Li_2Si formation is reached. In the process, stress is gradually released as cracks propagate, forming smaller silicon islands. One can refer to the work by Sethuraman *et al.* who showed the effects of stress-potential coupling and base their findings on a thermodynamic argument.^[137]

Judging by the appearance of the Si electrodes after 75 cycles in Figure 3.17, the process at 0.45 V is due to the formation of an unidentified species associated with the formation of an increased amount of SEI. The process requires a large silicon surface area that is in contact with the electrolyte. It appears largely irreversible, as it lowers the CE significantly. The formation of a surface layer goes together with a shift in voltage of the Li_2Si formation in Figure 3.9. The lower observed voltage may arise from increased stress-levels or kinetic effects of the SEI.

The long-term cycling has shown four significant features ‘i’ - ‘iv’. We can now assign ‘i’ to the surface reactions of the anode with the electrolyte at ~0.45 V. Feature ‘ii’ is characteristic for most thin-films and will be referred to as the “dip” throughout the rest of chapter. It signals the degradation of the anode, likely due to delamination. As observed in Figure 3.8 it occurs in combination with an increase in lithiation voltage and intensity. New lithiation pathways formed through either cracking or delamination, should make lithiation inherently easier which is reflected in the data.

Event ‘iii’ is different, as the process at ~0.45 V does not significantly increase around the process, but large amounts of Li_2Si are formed, as seen in the CE and the peak intensity in Figure 3.8a and Figure 3.9c, respectively. Given the continuous film-like Si/SEI material observed to arise from the presence of the process at ~0.45 V in Figure 3.17, the cause of event ‘iii’ is likely delamination of the material as one big flake from the current collector. This allows

electrolyte to flow beneath the film and access an increased amount of pristine silicon. While the material may not fully detach, lithium may become trapped precluding extraction as existing conductive pathways are broken. Some pathways remain or are re-established, which is indicated by the similar cycling behaviour before and after 'iii'. However, eventually delamination and SEI formation will separate the material electronically from the current collector.

The fourth feature 'iv' causes a further decrease in efficiency. The drop in efficiency is likely to be caused by significant amounts of SEI between the active silicon and the current collector. Detached silicon islands may form further SEI and fracture due to the missing stress from being attached to the current collector.

The electron micrographs and EDS spectra recorded for this electrode show different features depending on the sample preparation. The drying process significantly alters the electrode structure and composition and therefore we believe that the most representative description of the *in situ* surface can be obtained from micrographs on electrodes that were dried by evaporation in argon without the immediate exposure to heat, vacuum or air. Furthermore, the surface morphology observed is affected by the acceleration voltage of the electron beam which needs to be considered when discussing specific topographic features (Figure 3.15).

Ultimately, the instance at which electrode degradation occurs depends on a multitude of factors. In light of information demonstrated on this electrode, a range of parameters (thickness, current collector surface morphology, nickel interlayer, cycling rate and voltage cut-off) are discussed in the following section followed by a summary of the degradation mechanisms implied by the changes observed for each.

3.2.5 Substrate-dependent Parameters

3.2.5.1 Morphology of the Current Collector

In the previous sections we already presented electrochemical data and electrode surface from anodes on the two different copper foils that were used as current collectors for our studies: cold-rolled copper foil (CR Cu) and copper foil for graphene growth (GG Cu). The choice between these two substrates was initially made based on availability but has subsequently proven to be of interest for the study. Figure 3.18 shows the electron micrographs of the sputtered silicon thin-film electrodes on the respective current collector.

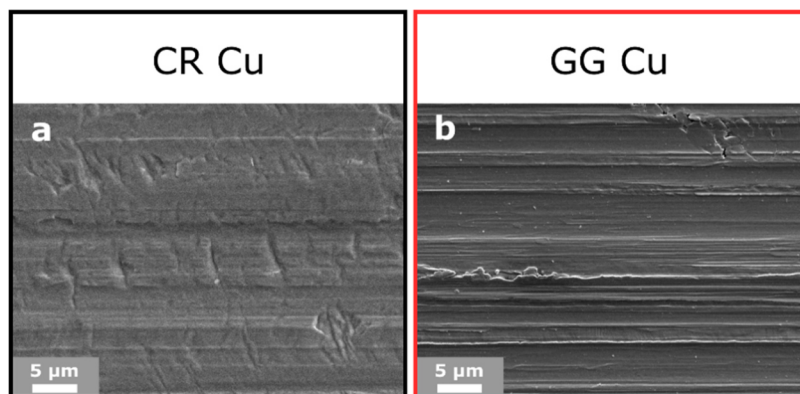


Figure 3.18: Electron micrographs (5 kV) of the 100 nm *a*-Si thin-film anodes on Ni-coated a) CR Cu and b) GG Cu.

The surface of the CR Cu shows more distinct, local features like cracks and dents on a microscopic level compared to the surface of GG Cu (Figure 3.18a-b). GG Cu shows long, flat channels that are aligned horizontally. The long-term cycling performance of the anode on GG Cu is shown in Figure 3.19. This is the reference electrode used in Chapter 3 for studies on the impact of additives. Features associated with the degradation of the electrodes, as discussed in section 3.2.2.1 for the anode on CR Cu, are highlighted.

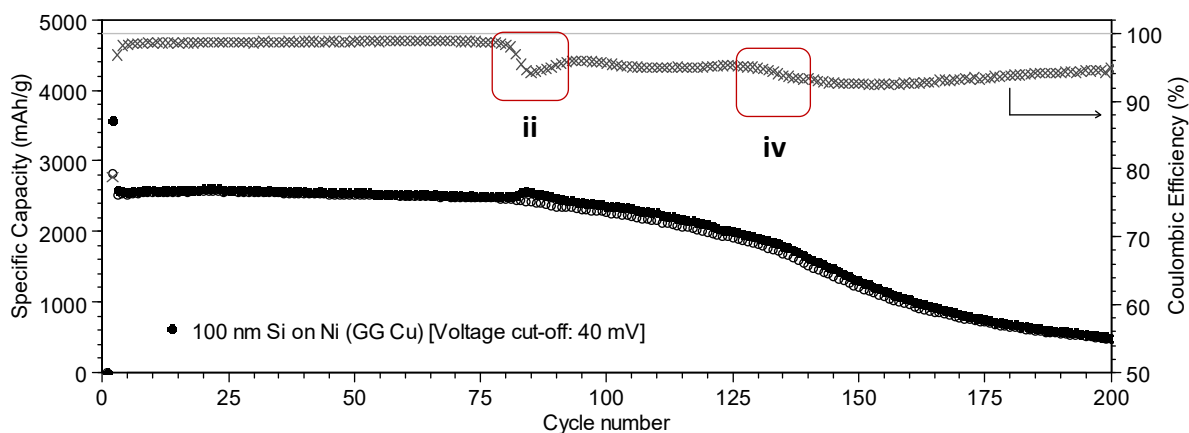


Figure 3.19: Electrochemical performance over 200 cycles of a 100 nm *a*-Si thin-film anode on Ni-coated GG Cu. The two steps that show the initiation and acceleration of the anode degradation are marked. Filled symbols: lithiation; empty symbols: delithiation; **x**: Coulombic efficiency; rate: 1st C/30, 2nd+ C/10; cut-off voltage: 1st 5 mV, 2nd+ 40 mV.

This cell was cycled to a lower voltage cut-off showing comparably higher capacities and an earlier degradation than the anode on CR Cu, previously shown in Figure 3.8a. The implications of the voltage cut-off are discussed in section 3.2.6.2. We observe events ‘ii’ (the “dip”) and ‘iv’ similar to the cell presented in Figure 3.8. The data shows less of the process at 0.45 V to which we attributed the absences of similar events to ‘i’ and ‘iii’.

The structural changes of the silicon anodes on different copper substrates during cycling are compared in Figure 3.20.

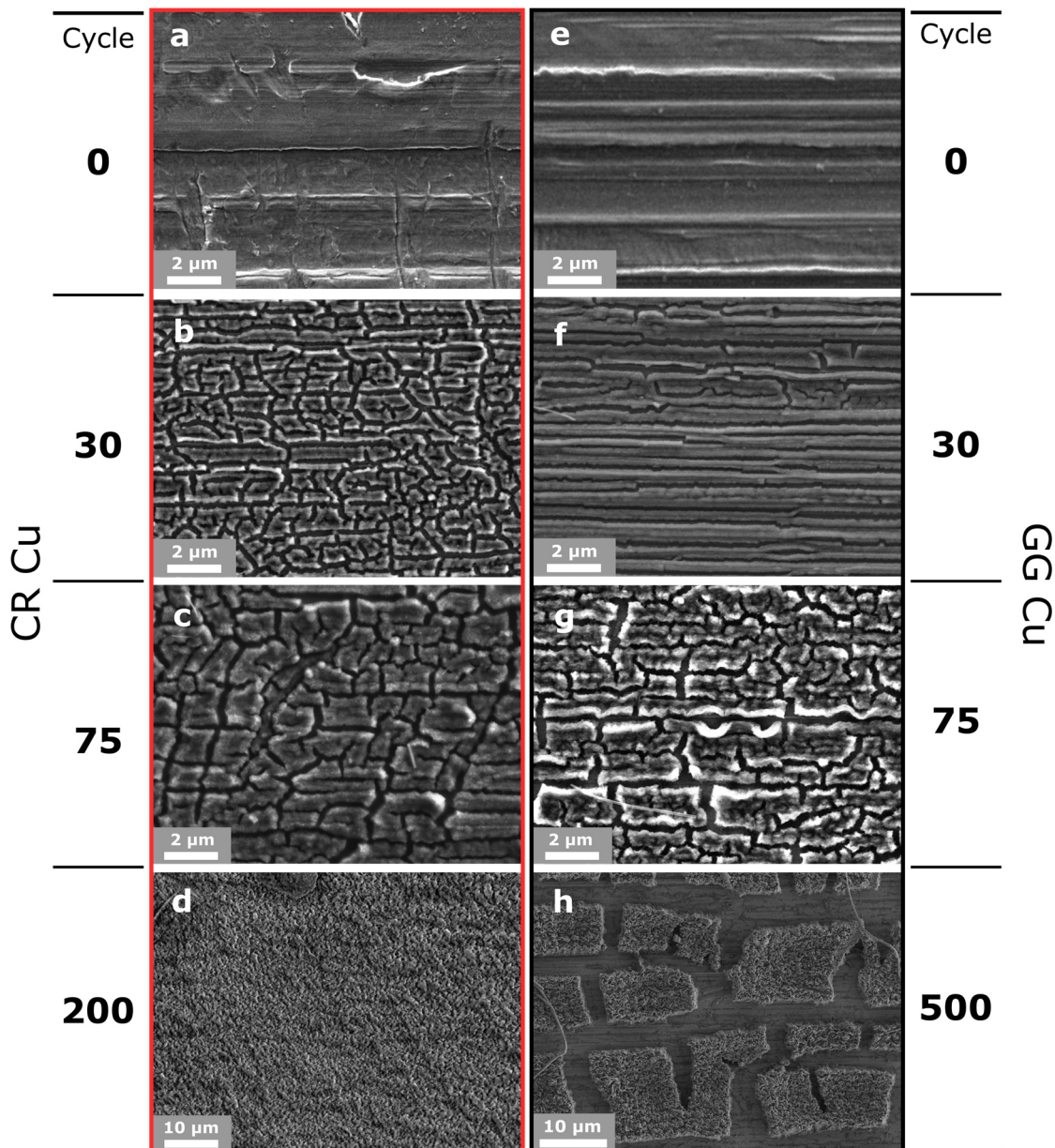


Figure 3.20: SEM micrographs (5 kV) of the 100 nm *a*-Si thin-film anodes on Ni-coated CR Cu and GG Cu after 0, 30, and 200 or 500 cycles, respectively. Cells were cycled to a cut-off voltage of 100 mV apart from h) which was cycled to 40 mV.

After 30 cycles, the flatter structure of the CR Cu current collector leads to the formation of more randomly orientated cracks, forming interconnected silicon islands (Figure 3.20b). GG Cu, with its channel like structure, shows more directed cracking with fewer cracks evolving in directions perpendicular to the direction of the substrates surface features (Figure 3.20f). By the 75th cycle, more lateral cracks and signs of delamination are observed for anodes on both substrates and towards the end of the cells lifetimes these structures appear to form

either a continuous surface layer (Figure 3.20d) or larger islands of the Si/SEI material (Figure 3.20g, please note the scale bars change). The nanostructures show a granular, interconnected Si/SEI material (Figure 3.20d and h) that is similar for both materials. The differences after prolonged cycling may not solely arise from the differences in the copper substrates surface structures but also from the intensity of the process at ~ 0.45 V and the different voltage cut-offs used.

3.2.5.2 Anode Thickness

Figure 3.21 shows the electrochemical cycling performance of 100 nm, 200 nm and 600 nm silicon thin-film electrodes on nickel-coated GG Cu.

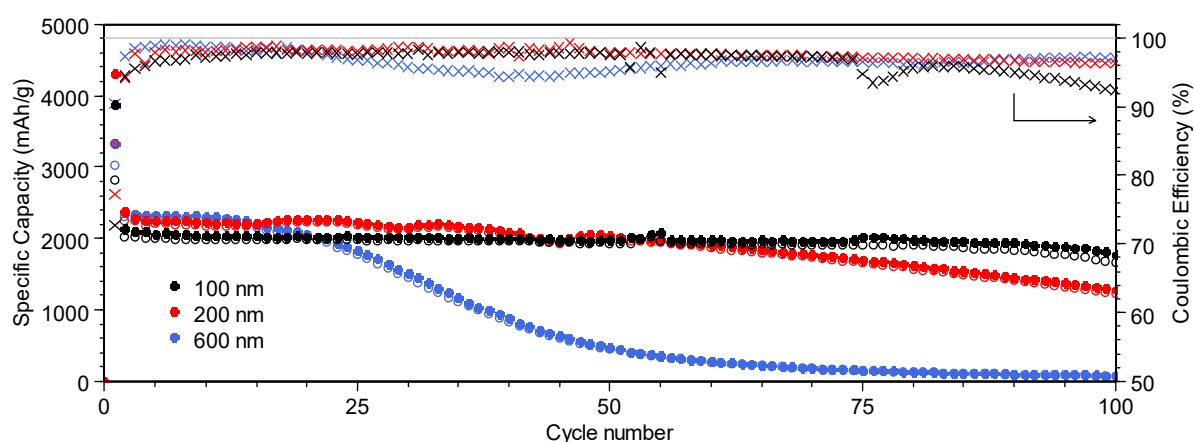


Figure 3.21: Electrochemical performance over 100 of the 100 nm, 200 nm and 600 nm *a*-Si thin-film anodes on Ni-coated GG Cu. Filled symbols: lithiation; empty symbols: delithiation; **x**: Coulombic efficiency; rate: 1st C/30, 2nd+ C/10; cut-off voltage: 1st 5 mV, 2nd+ 100 mV.

In terms of lifetime *vs.* specific capacity, a thinner electrode provides better performance. The thicker 600 nm silicon electrode degrades after only 15 cycles, while a 200 nm thin-film cell's degradation begins after 50 cycles and the 100 nm thin-film electrode retains its capacity for more than 75 cycles. However, thicker electrodes have greater CEs as less irreversible SEI formation occurs on the thicker electrodes due to the lower surface-to-bulk ratio. During stable cycling, the 600 nm electrode shows an average CE of 98.9% (cycles 5–10) compared to the 200 nm electrode which exhibits CEs of 98.3% (cycles 30–50), whilst the 100 nm electrode demonstrates CEs of 97.9% (cycles 30–40). The fast degradation of the 600 nm thin-film anode can be assigned to an accelerated delamination mechanism during cracking. As shown in Figure 3.3, thicker films may form fully separated islands due to experiencing larger changes in volume and needing to employ different mechanisms to mitigate stress during cycling.

The differing amounts of SEI formation owing to the different surface-to-bulk ratios can be seen in the voltage profiles comparing the 100 nm and 600 nm electrodes regarding their specific and absolute capacities (Figure 3.22).

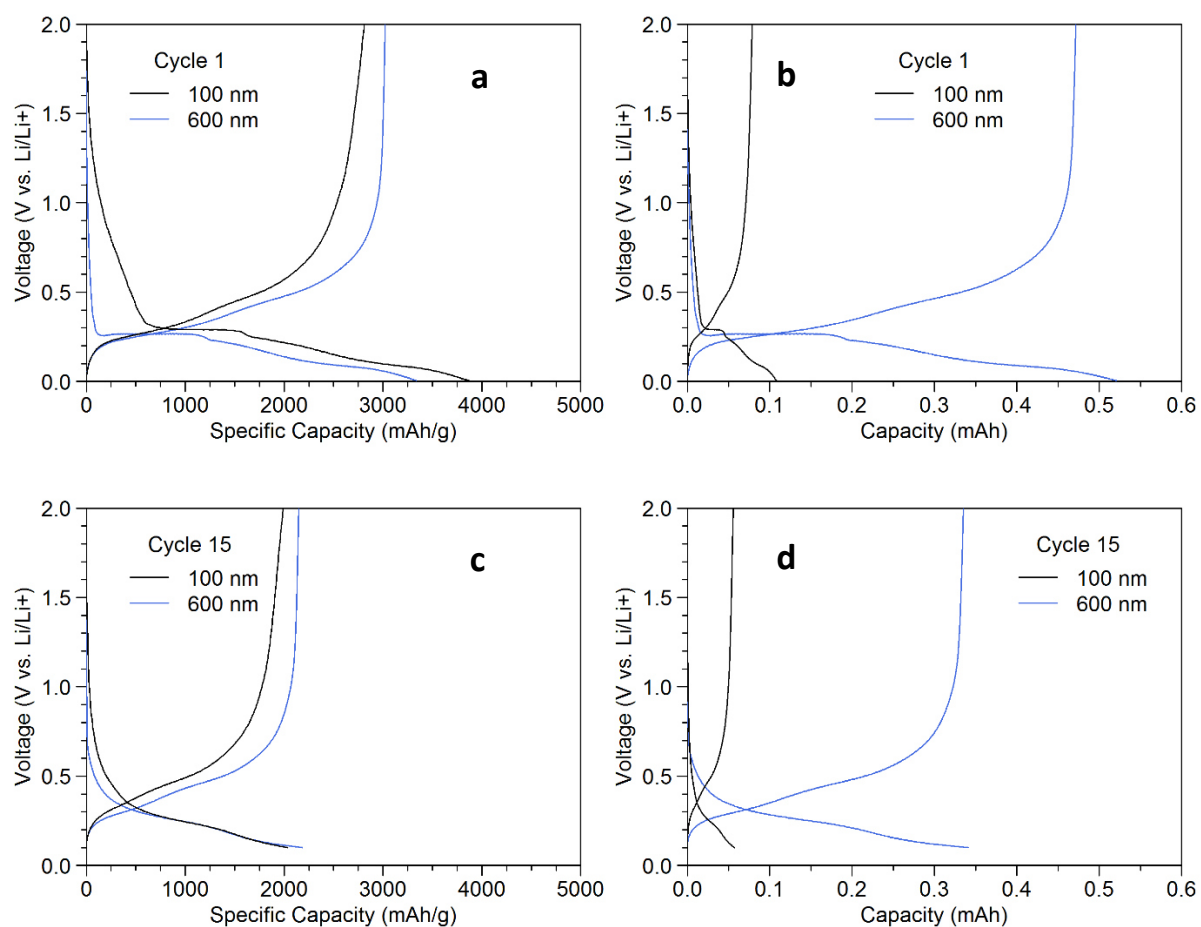


Figure 3.22: Voltage profiles for the first cycle (a, b) and the 15th cycle (c, d) of the 100 nm and 600 nm *a*-Si thin-film anodes on Ni-coated CR Cu. Left: specific capacity vs. voltage, right: capacity vs. voltage. The arrow in a) marks the delayed lithiation due to the native oxide layer. Rate: 1st C/30, 2^{nd+} C/10; cut-off voltage: 1st 5 mV, 2^{nd+} 100 mV.

While the specific capacity plot of the 100 nm film shows a larger capacity loss in the high voltage region (>0.3 V, Figure 3.22a), the absolute capacity plots show similar cycling behaviour for both thin-films (Figure 3.22b) in both the first and 15th cycle (Figure 3.22 d). A similar amount of energy input is required by the high voltage processes suggesting that these are mostly due to the surface area of the electrode and/or other cell components. Another feature that becomes apparent in Figure 3.22a-b is that the first lithiation phase during the initial cycle at below 0.3 V is a bulk phenomenon with the actual voltage at which it occurs varying from sample to sample, as discussed in section 3.2.2.1. We speculate, that this could be due to the silicon layers intrinsic resistivity being larger in thicker films resulting in a larger overpotential.

3.2.5.3 Nickel Interlayer

Nickel was previously associated with a longer lifetime of the thin-film anode.^[69] Our experiments show similar results. The cycling performance over 100 cycles and the voltage profile and dQ/dV plots of the 50th cycle of the 100 nm silicon thin-film electrode on nickel-coated and bare GG Cu current collectors are shown in Figure 3.23.

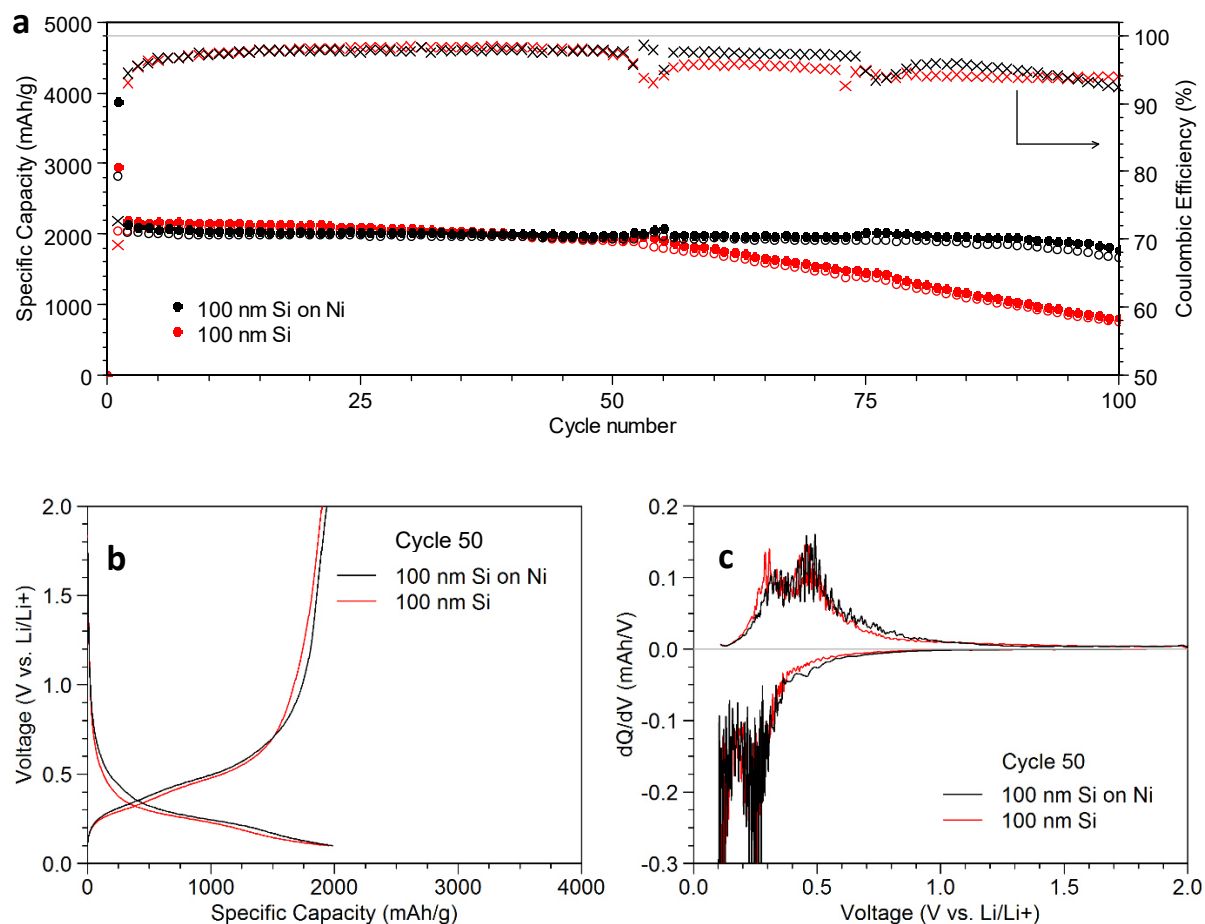


Figure 3.23: a) Electrochemical performance of the 100 nm *a*-Si thin-film anode on GG Cu and on Ni-coated GG Cu. b) Voltage profiles and c) differential plots for the 50th cycle comparing electrodes with and without a nickel interlayer. Filled symbols: lithiation; empty symbols: delithiation; **x**: Coulombic efficiency; rate: 1st C/30, 2nd+ C/5; cut-off voltage: 1st 5 mV, 2nd+ 100 mV.

Silicon anodes on nickel show a 50% longer lifetime than those on bare copper before the onset of significant degradation. The voltage profiles with and without Ni appear mostly similar. A slight increase in intensity of the process at ~0.45 V is, however, observed for anodes on nickel, see Figure 3.23c. Although ultimately the CEs are similar throughout stable cycling for both cells.

The literature offers some insights as to the cause of the increased performance:

First and foremost, the native oxide layer has been shown to be very thin for nickel surfaces.^[155] A shallow oxide layer will yield better adhesion, as more contact between the two metals can be established. The benefits of the Si-metal interactions have been shown by the *in situ* deposition of chromium or copper interlayers.^[143,156] Conversely, a thicker oxide layer would be reduced during cycling, leading to the loss of contact on the silicon-metal interphase and subsequent delamination.

Second, given the ~1 nm oxide layer expected for nickel, nickel silicides may form on the interface during the sputtering process. Nickel silicide in various stoichiometries has been subject to investigations for its use as an anode material in bulk or as nano-NiSi₂.^[157,158] In general, the lithiation of nickel silicide will form lithium silicide and elemental nickel (Eq. 2.2).^[159,160]



Therefore, loss of silicon to nickel silicide formation during the sputtering process should be recovered *via* electrochemical cycling, and also, potentially leaving a roughened nickel surface structure to benefit adhesion. This may account in part for a general increase in lifetime.

Third, the formation of specific components on and near the silicon/nickel interphase. Kawai *et al.* have proposed, that given a conduction pathway through nickel, silicon oxides form lithium silicates and lithium oxide on the nickel surface reversibly.^[161,162] Nickel may further act as a catalyst for the decomposition of lithium oxide.^[163] Lithium oxide and silicates have been associated with increased cycle life of nickel-silicide nanowires, forming a protective layer reversibly.^[164] The observed process at 0.45 V could be associated with lithium oxide and/or lithium silicates, as it is predominately observed for thin-film electrodes prepared on nickel.

3.2.6 Cycling Conditions

The analysis of silicon thin-film electrodes sputtered onto CR Cu over the first 30 cycles shows structural changes resulting from changes in the applied current density and the voltage cut-off. The anodes used in this section were a quarter of the size used for long-term cycling experiments, thus increasing the ICL of the lithium half-cells due to a lower ratio of the anode surface to that of the other battery components.

3.2.6.1 Rate

The cycling rate is defined as the time it takes for the electrode to be fully charged or discharged and is noted as “C/n”. A rate of C/5 indicates that a cell will take 5 hours to charge or discharge at the applied current. For galvanostatic cycling of 100 nm thick silicon thin-film anodes with a specific capacity of 3579 mAhg^{-1} (for $\text{Li}_{3.75}\text{Si}$) on copper discs of 12 mm diameter, 1C is equivalent to a current density of $\sim 100 \mu\text{Acm}^{-2}$.

The electrochemical cycling performance at a high rate of 1C is shown in Figure 3.24 for silicon thin-film electrodes on nickel-coated GG Cu and CR Cu.

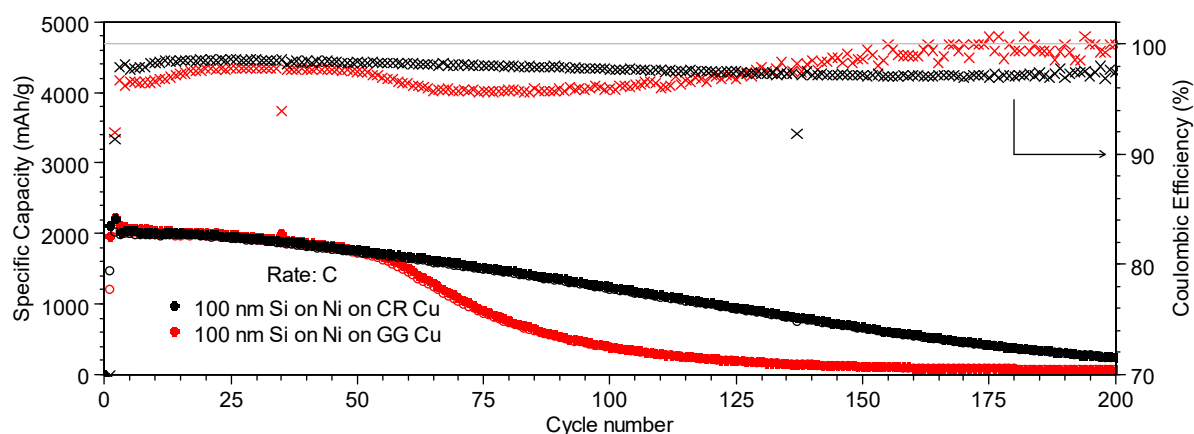


Figure 3.24: Electrochemical performance over 200 cycles of the 100 nm *a*-Si thin-film anodes on Ni-coated CR Cu and GG Cu at a rate of 1C. Filled symbols: lithiation; empty symbols: delithiation; x: Coulombic efficiency; rate: 1st C/30, 2nd+ 1C; cut-off voltage: 1st 5 mV, 2nd+ 100 mV.

Both electrodes in Figure 3.24 degrade more quickly and show capacity fade from the first cycle onwards. The anode sputtered onto CR Cu appears to cope better with the higher rate, not showing a “dip” as electrodes cycles at lower rates (Figure 3.8a, event ‘ii’). However, the anode on GG Cu shows similar behaviour in early cycles but shows the characteristic “dip”, similar to the cell cycled at C/10 in Figure 3.19.

To investigate the implications of a faster cycling rate on the electrode structure, silicon thin-films on CR Cu were cycled for one conditioning cycle at C/30 followed by a faster rate to 5 mV. The electrochemistry is shown in Figure 3.25. Capacity and CE appear similar at rates of C/10, C/5 and 1C, whilst the cell cycled at C/30 shows decreased efficiencies.

However, a significant shift of $\sim 100 \text{ mV}$ of the Li_2Si voltage peaks is observed at the highest rate compared to the other plots (Figure 28c).

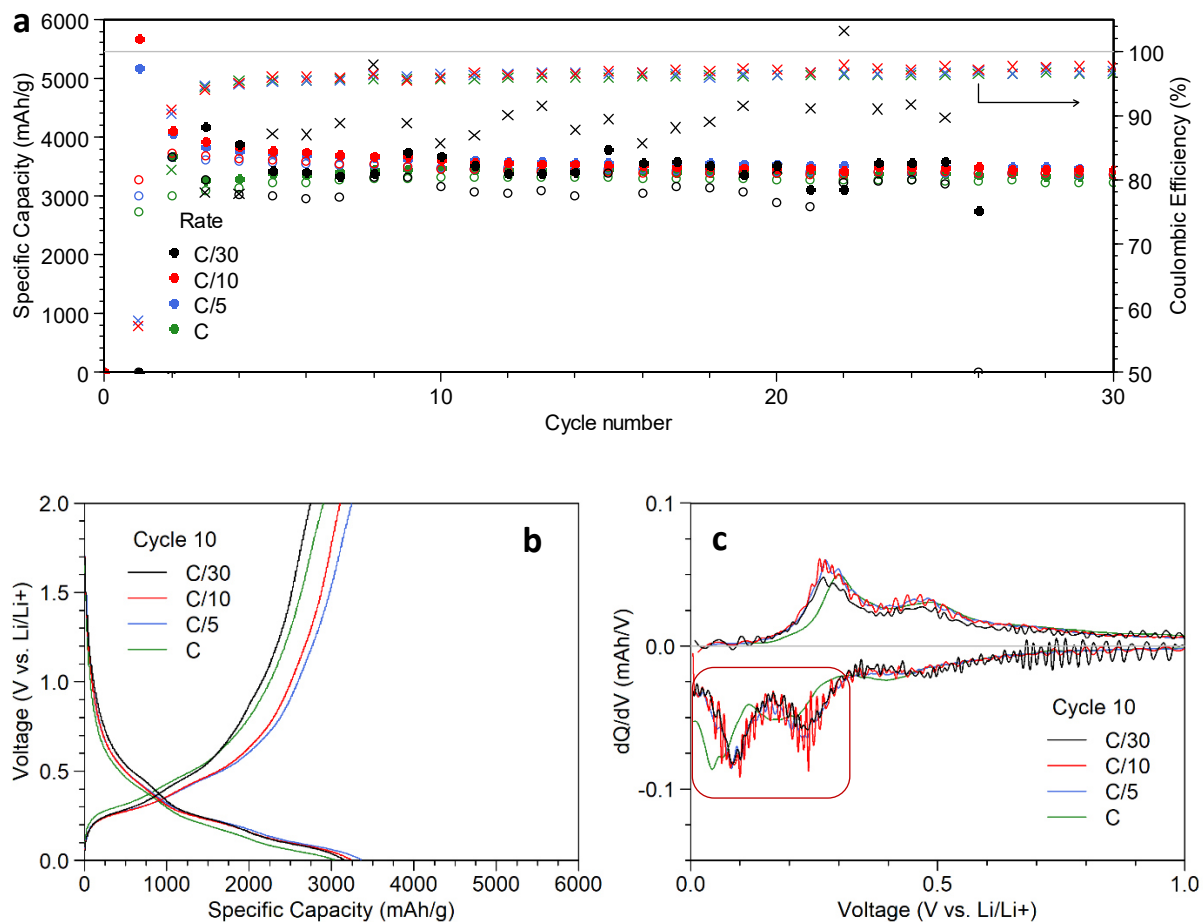


Figure 3.25: a) Electrochemical performance over 30 cycles of the 100 nm *a*-Si thin-film anodes on Ni-coated CR Cu cycled at C/30, C/10, C/5 or 1C. b) Voltage profile and c) differential plots for the 10th cycle. The peaks in lithiation voltage are highlighted showing a shift for the cell cycled at 1C. Filled symbols: lithiation; empty symbols: delithiation; x: Coulombic efficiency; rate: 1st C/30, 2nd+ C/30, C/10, C/5 or 1C; cut-off voltage: 5 mV.

Figure 3.26 shows the anode surfaces after the conditioning cycle followed by one and nine cycles at 1C and C/10, respectively.

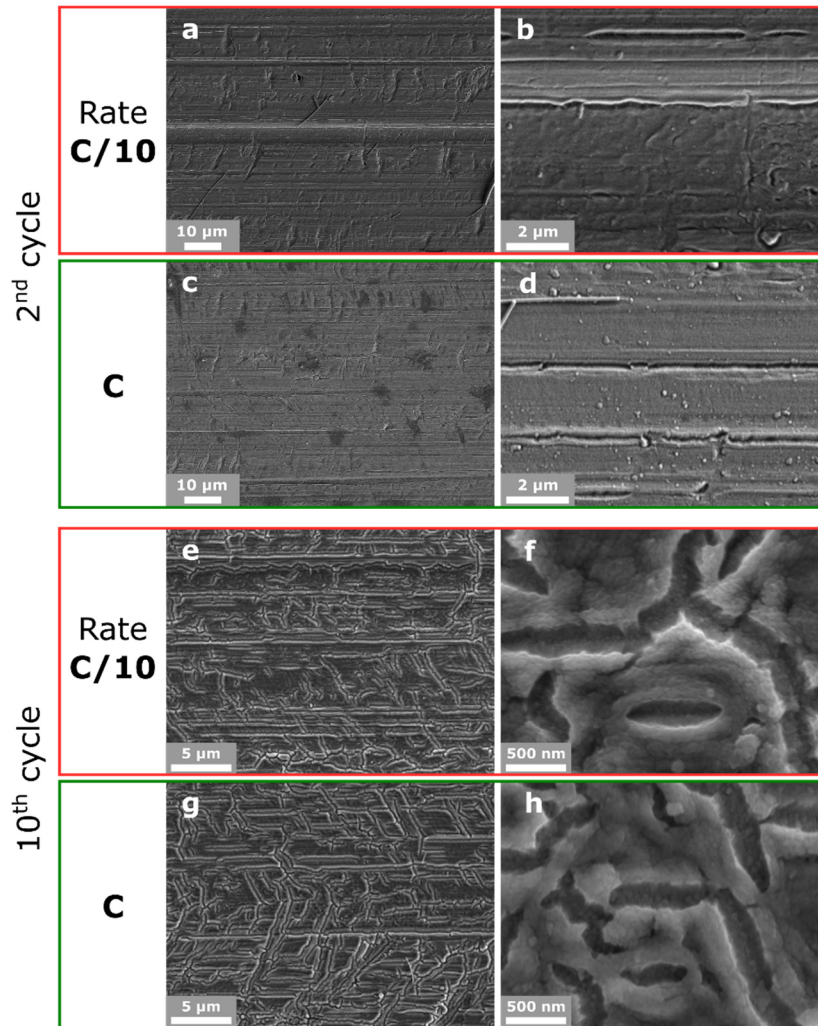


Figure 3.26: SEM micrographs (5 kV) of the 100 nm *a*-Si thin-film anodes on Ni-coated CR Cu. The initial cycle at C/30 is followed by one cycle at a-b) C/10 and c-d) 1C, or 9 cycles at e-f) C/10 and g-h) 1C, respectively.

After the initial couple of cycles (C/30, followed by C/10 and 1C, respectively) the surface shows only a few cracks. Cracks form in-line with the substrate and on distinct surface features. Edges around the local features seem to be smooth, whereas cracks parallel to the surface structure are more distinct. At 1C especially, the cracks appear to form more jagged edges (Figure 3.26d) and after 10 cycles the differences appear more visible with rounder edges forming at a lower cycling rates (Figure 3.26f). Figure 3.27 shows electrodes cycled at C/30, C/10, C/5 and 1C after 30 cycles.

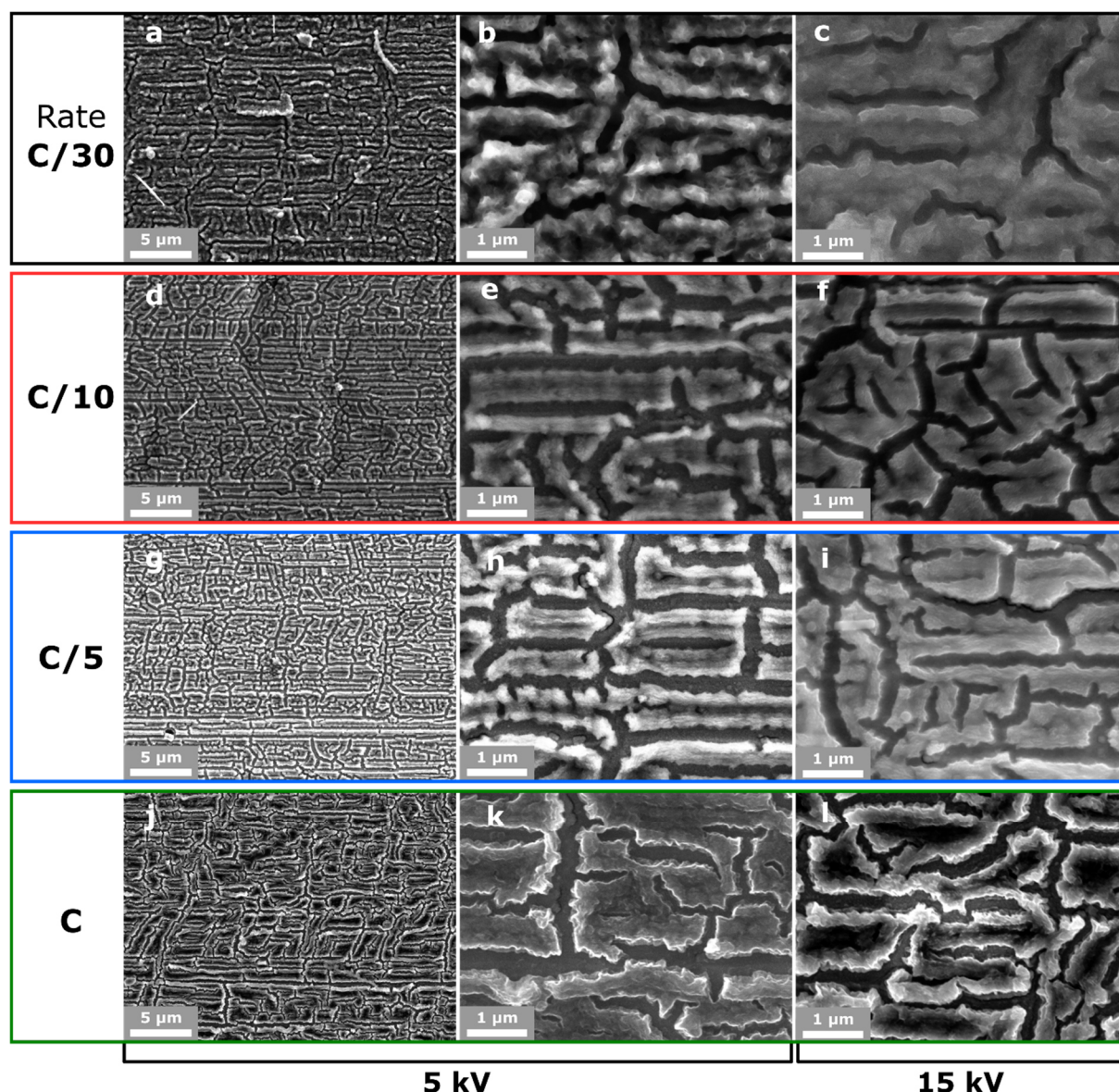


Figure 3.27: SEM micrographs of the 100 nm *a*-Si thin-film anodes on Ni-coated CR Cu after 30 cycles at different beam acceleration voltages (2, 5, 15 kV). The initial cycle at C/30 is followed by a-c) C/30, d-f) C/10, g-i) C/5 and j-l) 1C, respectively, to 5 mV.

In the above micrographs, at lower magnification extensive cracking both parallel and orthogonal to the copper substrates structure can be observed. Cracks separate $\sim 1 \mu\text{m}$ wide silicon islands that reveal significant structural differences at higher magnification depending on the rate they were cycled at. Cracks and edges appear smoother after 30 cycles at C/30 in Figure 3.27b compared to the other surfaces. For example, edges become less round in Figure 3.27e and h when cycled at C/10 and C/5, respectively. Finally, at 1C, frayed edges are observed instead, separating the silicon islands by wider cracks (Figure 3.27k-l). The anode cycled at C/30 also shows overall smaller cracks compared to anodes cycled at higher rates. The average crack-sizes and variance observed at 15 kV increases with rate at $230 \pm 60 \text{ nm}$ for C/30, similar

values with 250 ± 60 nm for C/10 and 240 ± 80 nm for C/5, followed by a large variation with 300 ± 160 nm for 1C.

This large spread in variance could, hypothetically, be caused by uneven lithiation of the silicon material, which may occur if the rate is too high as outlined in Figure 3.28. Thin-films cycled at a higher rate may not allow sufficient lithium ion diffusion through the material and promote the expansion of the near-surface areas over the bulk reflected in the higher stress-levels, shown as the shift in voltage in Figure 3.25e.

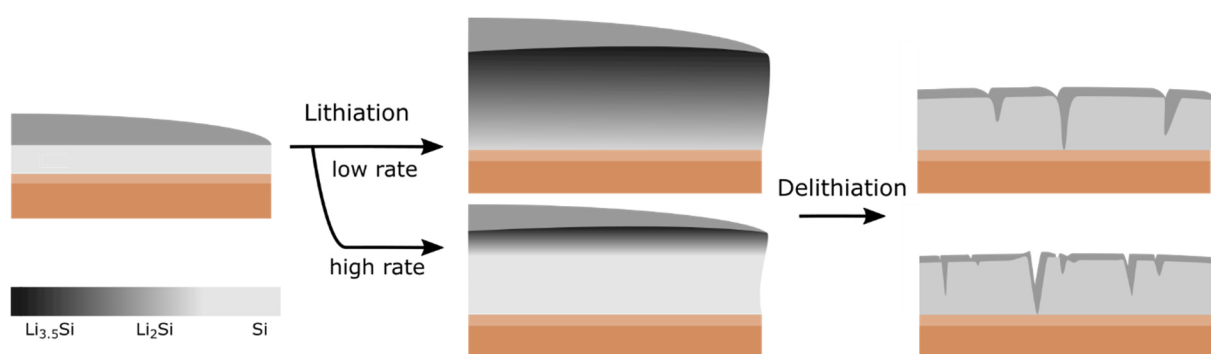


Figure 3.28: Impact of stress induced cracking of electrodes cycled at low rates and high rates indicating deeper lithiation at lower rates and finer crack formation in surface near region due to local high stress areas in the material at high rates.

Conversely, silicon thin-films cycled at lower rates will not exceed kinetic limitations and be lithiated more evenly and expand and contract in a more uniform way.

3.2.6.2 Cut-off Voltage

Figure 3.29 shows voltage profiles and dQ/dV plots of the 2nd and 30th cycles of 100 nm Si thin-film anodes cycled to voltage cut-offs of 5 mV, 45 mV and 100 mV.

A higher cut-off voltage results in longer cycle life of the silicon thin-film anode but limits its capacity. The reversible capacities on the 30th cycle yields almost theoretical capacity at 3500 mAhg^{-1} for a cut-off voltage of 5 mV, only 2500 mAhg^{-1} at 45 mV and less than 2000 mAhg^{-1} at 100 mV.

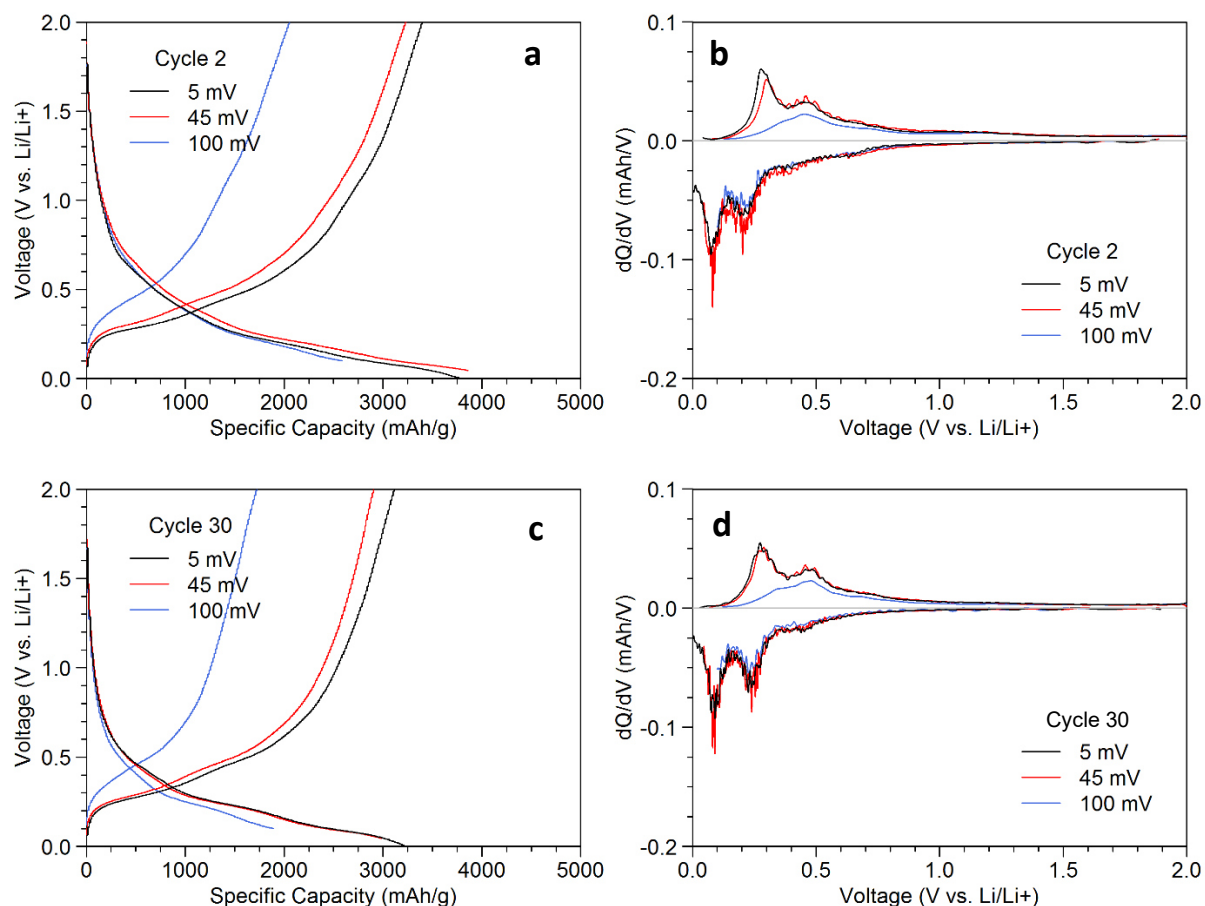


Figure 3.29: Voltage plots (a, c) and the corresponding dQ/dV plots (b, d) of the 2nd and 30th cycle of the 100 nm *a*-Si thin-film anodes on Ni-coated CR Cu cycled to 5 mV, 45 mV and 100 mV, respectively. Filled symbols: lithiation; empty symbols: delithiation; **x**: Coulombic efficiency; rate: 1st C/30, 2nd+ C/5.

The difference in lithiation depth is apparent in the peak heights of the two major delithiation steps in the differential plots Figure 3.29b and d. The peak corresponding to the Li₂Si phase is well developed for all three conditions but due to the higher voltage cut-offs the peak corresponding to the Li_{3.5}Si phase in the sample cycled to 45 mV is truncated, and for 100 mV the peak only just begins to appear.

Figure 3.30 shows micrographs of the electrode surfaces after 10 cycles. Cracking of the silicon surface is most severe for the sample cycled to 5 mV (Figure 3.30b) with fewer cracks showing for the sample cycled to only 45 mV (Figure 3.30d). At a cut-off voltage of 100 mV almost no lateral cracking in the direction of the copper substrate's structure can be seen (Figure 3.30f).

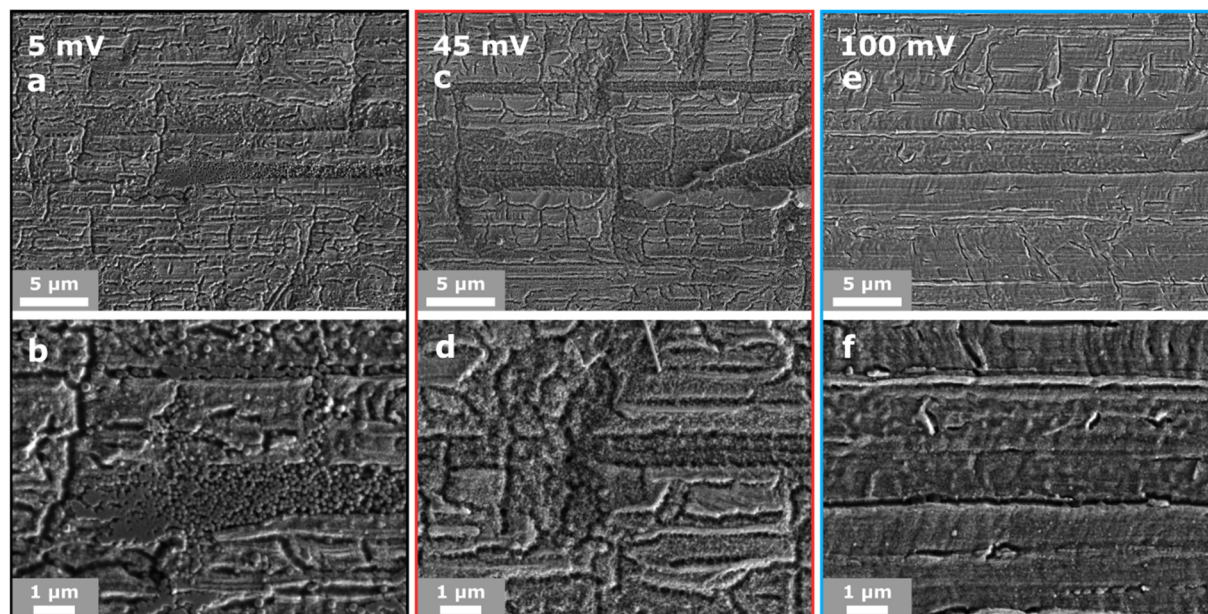


Figure 3.30: SEM micrographs (5 kV) of the 100 nm *a*-Si thin-film anodes on Ni-coated CR Cu after 10 cycles to a-b) 5 mV, c-d) 45 mV and e-f) 100 mV. Spherical particles on the surface are dried electrolyte and SEI, found on most cycled electrodes even after rinsing with DMC.

Limiting the lithiation through a higher cut-off voltage has two effects: a limited capacity and limited volume expansion, outlined in Figure 3.31.

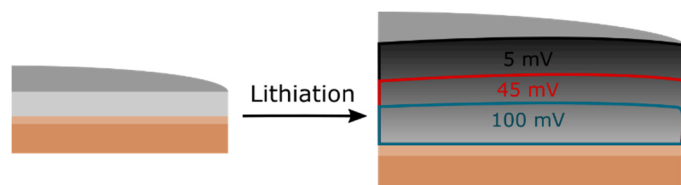


Figure 3.31: Impact of differences in cut-off voltage on the thin-film electrode expansion during electrochemical cycling.

The anode may expand by more than 300% when fully lithiated but if lithiation is limited, then the anode will experience less stress and therefore crack less. Following the Li_2Si peak voltage in Figure 3.32 shows that cells cycled to voltage cut-offs of 5 mV and 45 mV show a similar trend, while a cell with an even higher voltage cut-off will take more cycles relieve stress and crack.

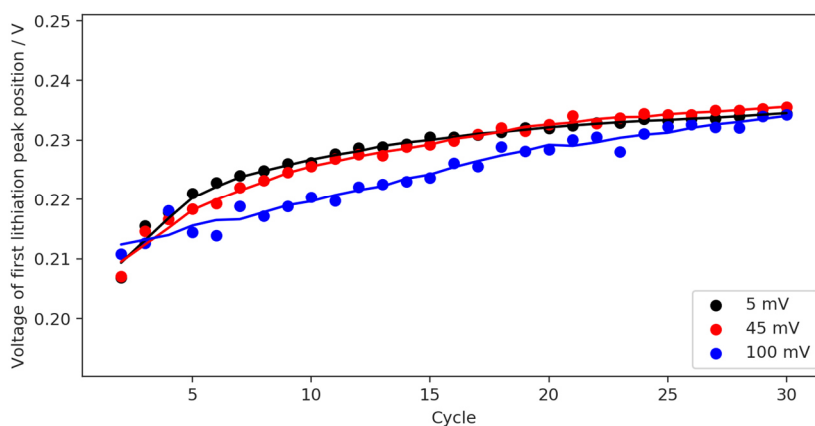


Figure 3.32: Li_2Si formation peak position in the differential plots for the first 30 cycles of the 100 nm silicon thin-film anode at different cut-off voltages.

Limiting the capacity of a silicon anode through a limited voltage window to gain lifetime at the current state of lithium ion battery development is a welcome trade. Currently, the cathodic capacity is the bottleneck that limits the cells specific capacity. Figure 3.33 shows the correlation of the specific capacity of the anode and the cell specific capacity with lithium cobalt oxide as cathode material (theoretical capacity of LiCoO_2 : 147 mAhg^{-1}).^[52]

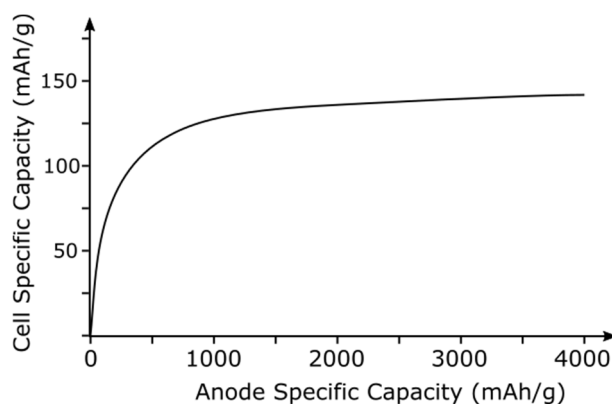


Figure 3.33: Theoretical specific capacity for a full cell as the function of the specific capacity of the anode (silicon), employing a LiCoO_2 cathode. Adapted from reference ^[52].

At 2000 mAhg^{-1} anode specific capacity, the weight gain by the cathode material will be the limiting factor to increase the specific capacity overall. Even with the best performing cathode materials to date, such as NMC811 (practical capacity of $\text{Ni}_{0.8}\text{Mn}_{0.1}\text{Co}_{0.1}\text{O}_2$: $\sim 200 \text{ mAhg}^{-1}$), using the full capacity of a pure silicon anode will not achieve a significant reduction in overall cell weight.^[165] Therefore, a voltage cut-off as high as 100 mV should yield sufficient capacity to achieve practical levels whilst also lowering the cell weight.

3.2.7 Degradation Mechanism of the Si Anode and Material Factors

Generally, the degradation mechanism of the thin-film electrodes can be described as illustrated in Figure 3.34.

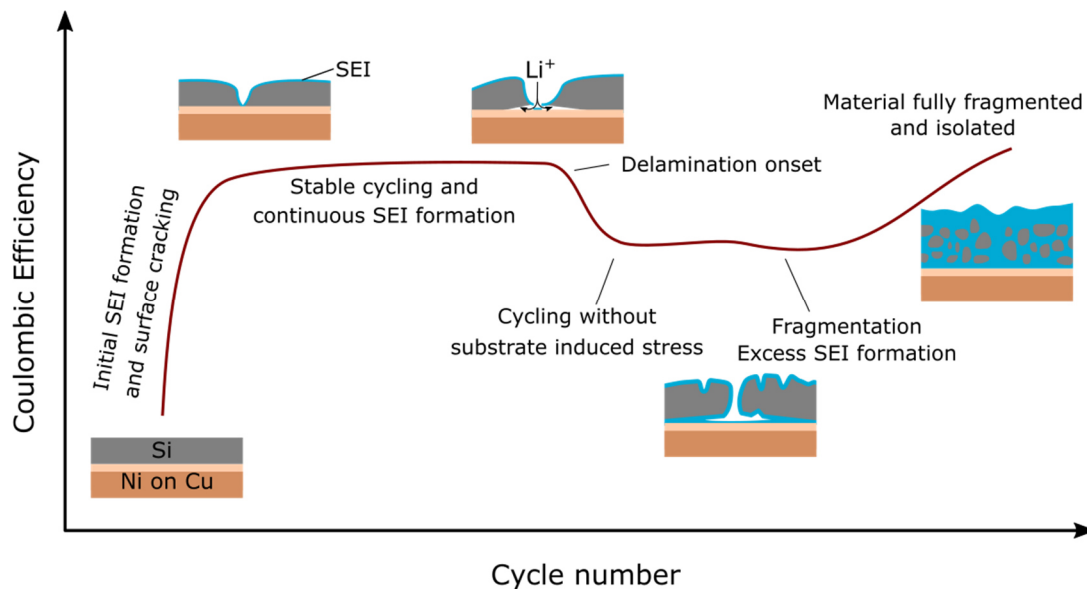


Figure 3.34: Outlined degradation mechanism of the 100 nm *a*-Si thin-film electrode following the CE (red trace) over the lifetime of the lithium half-cell.

All cells with silicon thin-film electrodes will form cracks in the electrode during the initial cycles, observed in the electron micrographs throughout this chapter, minimising stress which can be followed by the Li_2Si peaks voltage in the differential plots (see Figure 3.9, page 50). Cracking opens up pathways for the electrolyte to reach larger areas of silicon allowing for easier lithiation and the material forms stable silicon islands that can then cycle reversibly. We have observed by EDS analysis, that the cracks gradually fill with SEI, demonstrated by the high oxygen concentrations in Figure 3.17. The “dip” (event ‘ii’) is likely to arise from the gaps being filled so that expanding silicon islands delaminate when in contact with adjacent islands, as illustrated in Figure 3.35.

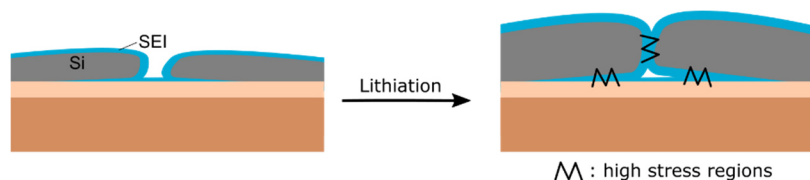


Figure 3.35: Proposed mechanism of accelerated delamination of cracked silicon pieces by levering forces of silicon flakes in contact during lithiation.

Following the delamination, the material will cycle free from substrate induced stress, seen in the increase in voltage for the Li_2Si lithiation, allowing it to fragment and form large amounts of SEI that electrically isolate the material from the current collector. Here, we usually observe another process 'iv' that indicates lithation and subsequent disconnection of the material causing irreversible capacity loss. Finally, the material takes the form of a large layer or large islands of inactive Si/SEI.

It is worth noting that after 500 cycles, the island sizes of the Si/SEI material on nickel-coated GG Cu are within the proposed dimensions for stable cycling of pure silicon thin-film electrodes with an estimated thicknesses of 1–2 μm of the Si/SEI material.^[140] Although, even though that may be the case and the islands that form during degradation continue to cycle for a number of cycles after their formation, eventually failure occurs due to loss of electronic connectivity as the SEI layer continues to build beneath.

A continuous large layer of Si/SEI may rather form following a process at ~ 0.45 V. After the process appears another feature 'iii' was observed, that we may associate with an event where a large amount of the Si/SEI material delaminates partially. At this moment, we are uncertain what the chemical composition of the species formed during lithiation at 0.45 V is. It may be related to lithium silicates or lithium oxide, as the peak intensity is reflected in an increase in surface area (Figure 3.17). Some literature reports suggest, that these species can be formed reversibly on nickel, but this would only account for the area of the nickel-silicon interface. On-the-other-hand it would also reflect the similar efficiencies of anodes on either nickel or copper (Figure 3.23). Nevertheless, without absolute certainty, this process may only provide a tool to estimate the internal surface area of the anode at this juncture.

3.2.8 Performance Comparison

As discussed in the beginning: The performance of silicon thin-film electrodes in the literature varies due to the multitude of factors that affect the physical appearance of the anode and the many options in cycling parameters, such as rate and voltage cut-off. There are no two results from different research groups that are identical in their thin-film properties and chosen cycling parameters. However, clear trends are identified in this thesis that can be found in the literature. To roughly evaluate the performance of the thin-film anodes in this thesis, a summary of some of the most similar silicon thin-film electrodes found in the literature is presented in Table 3.1. The comparison is largely based on the methods presented by Salah *et al.* who compared the most impactful literature in the field between 1999 and 2018 and who chose to

determine capacity retention relative to the first cycle.^[54] Given the change in cycling parameters between the initial conditioning cycle and the following cycles, values relative to the first or second cycle discharge capacities are chosen to determine the point of 70% capacity retention.

Table 3.1: Performance comparison of cells cycled in this work and literature reports.

	Preparation, Thickness, Ref.	Substrate	Voltage window, Rate	Notes	Discharge Capacity under steady Conditions (1 st or 2 nd Cycle)	Cycle No at 70% SoH	Cycle No at 10% SoH
A	RF sputtering, 100 nm, this work	Ni on GG Cu	2.0 – 0.1 V C/10		2797	>100 (83.3%)	-
B	RF sputtering, 100 nm, this work	Ni on CR Cu	2.0 – 0.1 V C/10	Highest capacity on 50 th cycle	1833 (Cycle 50)	145	>200 (22.7%)
C	RF sputtering, 100 nm, this work	Ni on GG Cu	2.0 – 0.045 V C/5		2600	134	240
D	RF sputtering, 200 nm, this work	Ni on GG Cu	2.0 – 0.1 V C/10		2733	81	>100 (55.8%)
E	RF sputtering, 100 nm, this work	Ni on GG Cu	2.0 – 0.005 V C/10		2535	67	>100 (20.1%)
F	RF sputtering, 100 nm, this work	GG Cu	2.0 – 0.1 V C/10		2254	42	>100 (12.8%)
G	RF sputtering, 600 nm, this work	Ni on GG Cu	2.0 – 0.1 V C/10		2294	27	58
H	RF sputtering, 100 nm, this work	Ni on GG Cu	2.0 – 0.1 V C		2239	59	121
I	RF sputtering, 100 nm, this work	Ni on CR Cu	2.0 – 0.1 V C		2217	73	205
J	RF sputtering, 100 nm, [166]	Cu foil	1.0 – 0 V C/3		~2800	~90	>200 (~2%)
K	RF sputtering, 500 nm, [166]	Cu foil	1.0 – 0 V C/3	Highest capacity on 30 th cycle	~2400	~50	>200 (~15%)
L	Plasma-enhanced CVD, 40 nm, [148]	Untreated Cu	assumed cut-off at 5 mV C/3	SiN coated	~3500	~75	>200 (~25%)

Table 3.1 continued

M	RF sputtering, 90 nm, [167]	Cr on Cu	1.5 – 0.1 V 50 μ A (\sim C/2)	Highest density Si from series	\sim 2300	\sim 40	>200 (\sim 45%)
N	Vacuum deposition, 100 nm, [168]	Planar Ni	assumed cut- off at 5 mV C/4		\sim 2650	\sim 20	>50 (\sim 65%)
O	CVD, 50 nm, [150]	Mo on glass	3.0 – 0.2 V, \sim 5C		\sim 500	\sim 400	
P	CVD, 50 nm, [150]	Mo on glass	3.0 – 0.1 V, \sim 5C		\sim 3600	\sim 90	-
Q	CVD, 50 nm, [150]	Mo on glass	3.0 – 0.0 V, \sim 5C		\sim 3700	\sim 35	\sim 45
R-X: Cells cycled with electrolyte additives. R and S are discussed in detail in Chapter 4.							
R	RF sputtering, 100 nm, this work	Ni on GG Cu	2.0 – 0.045 V C/5	10% FEC	2846	>350 (78.7%)	-
S	RF sputtering, 100 nm, this work	Ni on GG Cu	2.0 – 0.045 V C/5	5% VC	2603	>350 (78.7%)	-
T	RF sputtering, 275 nm, [69]	Ni	0.9 – 0.005 V C/2	10% FEC	\sim 3500	>100 (\sim 90%)	-
U	RF sputtering, 275 nm, [69]	Flat Cu	0.9 – 0.005 V C/2	10% FEC	\sim 3400	>100 (\sim 80%)	-
V	E-beam evaporation, 200 nm, [169]	Cu foil	2.0 – 0.005 V C/5	3% FEC	\sim 3800	>80 (\sim 85%)	-
W	RF sputtering, 100 nm, [166]	Cu foil	1.0 – 0 V C/3	2% VC	\sim 2800	>200 (\sim 75%)	-
X	RF sputtering, 500 nm, [166]	Cu foil	1.0 – 0 V C/3	2% VC	\sim 1900	>200 (\sim 90%)	-

Again, it has to be emphasised, that there are no two identical thin-films reported in the literature as they have been prepared under varying conditions using different techniques and were cycled with different electrolytes and setups. Our studies show that the cycling conditions and the materials selected affect the performance, reflecting some of the results found in the literature. The overall capacities of the thin-film anodes are not comparable and depend on the voltage cut-off and the information on the thin-film itself, often being based on theoretical values. These are however affected by the anodes weight and density which is difficult to measure.

In general, the system used for this study shows an overall good performance compared to literature results with purely alkyl carbonate based electrolytes (rows A-O). The films performance is affected by their thickness (see row A, D and G). Similar results were presented by Ulldemolins *et al.* with thinner films (100 nm vs. 500 nm) performing better (row J and K).^[166] The 600 nm thin-films used in this study (row G) do not reach similar performance levels, which could be an effect of the increased thickness or different sputtering parameters. The 100 nm thin-films perform similar.

Factors such as voltage-window and rate. Capacity appears to fade quicker with an increased voltage-window by cycling to lower voltages, similar to results in the literature. A good example is found in the work by Jung *et al.* (row O to Q) where an increase in cycle-life is traded for loss in capacity, showing that a voltage cut-off set above 100 mV limits the capacity significantly.^[150] Their thin-film anodes could potentially perform better through applying a lower current, hence reducing the rate. Faster rates have shown to accelerate the degradation of the anode in this work (row H and I). Generally, slower rates have been chosen throughout the literature, rarely exceeding C/3.

Further difficulties for comparing thin-film anodes arise when electrolyte additives are used, as thinner films appear to perform exceptionally well through the formation of a beneficial SEI. The 100 nm thin-films in this study are no exception to this and a detailed discussion of the additives used and the SEI formation is provided in Chapter 4. The work by Iaboni and Obrovac, that was discussed earlier in this chapter shows results of cells cycled with fluoroethylene carbonate.^[69] The thin-films used for this thesis (row R and S) appear to perform better, but thicknesses and voltage windows need to be considered. An apparent finding in these studies is, however, that the silicon electrodes sputtered onto nickel perform better. This is also seen in the trend observed in rows A-O with nickel coated current collectors showing better performance. Other systems in the literature using electrolyte additives show similar performance.

Overall, the thin-films used in this report perform well compared to others regarding their cycle-life. Cells cycled under the identified ideal conditions (row A – C: nickel base layer, medium rate, not too low voltage cut-off, and thicknesses of 100 nm) perform particularly well.

3.3 Conclusion

The preparation and properties of a-Si thin-film anodes have been presented, outlining the impact of certain parameters on the anode's lifetime, capacity, and degradation. Thin-films were prepared by PVD. The method of preparing the thin-films is reproducible and may allow future use of the anodes for further studies of the silicon. The 100 nm thin-film anodes were cycled and used for SEM and EDS studies after a different number of cycles showing different degrees and features of degradation. We have observed the cracking and degradation of the material during continuous cycling depending on the cycling conditions, structure of the current collector and electrochemical processes occurring in the cell.

The following factors have shown to affect the electrodes performance:

Copper current-collector: The substrates surface structure affects the long-term cycling of the thin-film electrodes. The cracks formed during cycling may adopt the substrates morphology but will ultimately form a similar Si/SEI material, regardless of the substrate, after extensive cycling. The electrochemistry observed is largely independent of the current collector and the degradation observed is more sensitive to other factors.

Nickel interlayer: A 250 nm layer of nickel extends the lifetime of the anode significantly. The reasons for this that have been proposed are increased adhesion due to the electrochemistry of a potential nickel silicide forming an atomically roughened surface or the reversible formation of chemical species such as lithium oxide or lithium silicates on the interface.

Anode Thickness: An increase in thickness yields a faster degradation but higher areal capacities. CEs are higher for thicker films due a larger surface-to-bulk ratio.

Rate: Electrochemical cycling with higher rates can lead to earlier degradation. Cracks form less uniformly and may be larger. The electrodes capacity may not be fully accessed if the lithium transfer is kinetically hindered.

Cut-off voltage: A higher cut-off voltage increases the cycle life but limits accesible capacity simply as less lithium forming the silicide means a smaller increase in volume. Smaller changes in volume lead to slower crack propagation and delamination. Voltage limitations may be difficult to implement in a real battery as voltage slippage due to changes of the potential of the electrodes will make it inherently difficult to control.

This work shows the most extensive summary of physical changes of the silicon thin-film anode, depending on a change in parameters observed by SEM. As seen by comparing this system to other, similar systems, clear trends in the life-time expectancy of the electrodes were

shown which are linked to changes in surface morphology. This detailed description of a step-wise evolution of the anode surface will help the understanding the Si thin-film anode and may proof to be a guide to choose the ideal conditions for designing stable silicon anodes.

Many literature reports avoid the discussion about the films failing by limiting the number of cycles to the cell being fully functional and show only a small part of the cell's lifetime and degradation. As seen in this work, the decay may happen abruptly and can be linked to many different factors. The degradation should in general be addressed in more detail, as otherwise the illusion of an almost linear capacity fade is created. Discussing the actual degradation of the material will ultimately enable finding solutions making silicon a considerable choice as an anode material in LIBs.

In regards to their further use, the 100 nm thin-films used in this thesis may not be applicable in common battery applications as several microns are needed to match the capacity of state-of-the-art cathode films.^[138] However, in addition of providing an excellent model for further studies on the Si anode, these thinner anodes can be of interest for the manufacturing of batteries in small electronic devices and chips.

3.4 Experimental Section

3.4.1 Materials

Copper foil for graphene growth (Alfa Aesar, 0.025 mm, 99.8%, “GG Cu”) and cold-rolled copper foil (0.018 mm, “CR Cu”). Electrolyte solution (LP 30: 1M LiPF₆ in 1:1 ethylene carbonate and dimethyl carbonate), fluoroethylene carbonate, and vinylene carbonate (all battery grade) were obtained from Sigma Aldrich and used as received. Coin cell components were obtained from Cambridge Energy Solutions.

3.4.2 Methods

Detailed descriptions of the techniques and instruments used can be found in Chapter 2 Methods. Measurements were performed under standard operating conditions.

3.4.2.1 Electrode Preparation

All Si thin-film anodes (100 nm, 200 nm, 600 nm) used were prepared in the CCR sputter coater on bare and nickel-coated (250 nm) current collectors. Both cold-rolled copper (CR Cu) and copper for graphene growth (GG Cu) discs were used.

3.4.2.2 Coin Cells

Full electrode discs and discs cut into four equal pieces (for experiments in sections 3.2.6.1 and 3.2.6.2) were used with 0.1 mL of LP30 electrolyte.

3.4.2.3 Galvanostatic Cycling

Cells were cycled on a LANDT potentiostat at C/30 to 5 mV for the first cycle, followed by C/n for consecutive cycles (n = 1, 2, 5, 10, 30) to different voltage cut-offs (100 mV, 45 mV, 40 mV or 5 mV), depending on the experiment.

3.4.2.4 Electron Microscopy

Coin cells were disassembled at full charge (2 V) and the anodes were rinsed with DMC. The electrodes were analysed in the TESCAN MIRA3 FEG-SEM. Most samples were transferred using the inert atmosphere transfer module. Samples were coated with gold, using a sputter coater for FIB-SEM analysis on a Zeiss Cross-beam 540 and the FEI Helios Nanolab SEM/FIB. EDS spectra and maps were recorded using the Oxford Instruments Aztec Energy X-maxN 80 EDS system on the TESCAN MIRA3 FEG-SEM.

Chapter 4 Structural Impact of Fluoroethylene Carbonate and Vinylene Carbonate on the Si Anode

Electrolyte additives have been a central part of research in the area of silicon anodes, with the aim of improving their performance by altering the composition of the SEI that is formed on the anode.^[170] A wide range of additives has been tested including non-fluorinated (e.g. vinylene carbonate (VC)) and fluorinated (e. g. fluoroethylene carbonate (FEC)) carbonates, nitrogen-containing additives, silanes, various inorganic electrolyte salts and other compounds such as succinic anhydride and carbon dioxide.^[170] To date, the most common and prevalent additives are FEC and VC. Their degradation mechanisms and products are subject of ongoing research, as the composition of the SEIs formed and their effects on the anode are still not fully understood.

In Chapter 4.2, the synthesis of ¹³C-labeled FEC which has enabled solution and solid-state NMR studies for better understanding of the SEI formed on silicon nanowire anodes is presented.^[171,172] Using the ¹³C₃-FEC additive, Y. Jin was able to identify crucial SEI fragments formed from FEC, presented in two recent publications with the author.^[171,172] Polymers, oligomers and small molecules that are formed from the additive and, at least in part, are located in the SEI on Si are identified, and are linked to the superior performance of using the additives over standard electrolyte mixtures. The authors contribution to this part of the chapter are the synthesis of ¹³C₃-fluoroethylene carbonate and the work presented on the silicon thin-film anode to gain further understanding in the structural changes induced by the chemically different SEIs that form from the electrolyte additives.

The work presented in Chapter 4.3 applies the knowledge of the chemical composition of the SEI to the interpretation of the structural changes occurring of the 100 nm silicon thin-film anodes using FEC and VC. This part of the work was done solely by the author. It shows the deformation of the electrode during cycling and how the SEI that forms from either additive stabilises the thin-film anode. Results clearly suggest the practical dimensions of silicon features that form from the thin-film during degradation and SEI formation that may cycle continuously without significant capacity loss. Furthermore, a quantitative analysis of its composition and a closer look at the trends in electrochemistry show the origin of the varying efficiency, that is dependent on the electrolyte mixture. It becomes clear, why systems with FEC in particular struggle with depletion of the additive over multiple cycles.

In the following, an overview on the state of research on the silicon anodes SEI formed with the additives FEC and VC in general and thin-films in particular are presented. Numerous techniques have been applied to identify and quantify the components that make up the SEI formed during cycling with varying, yet directing, results.

4.1 Identifying Decomposition Products of FEC and VC

In recent years, our group has contributed to understanding the decomposition mechanism and identifying decomposition products *via* solution and solid-state NMR.^[51,171–174] Work by Michan *et al.* has identified important fragments formed from chemical reduction of the organic electrolytes FEC and VC on silicon nanoparticle material electrodes at specific voltages which helped to explain the stability of the SEIs.

Previously, other techniques such as infrared spectroscopy (IR)^[175], X-ray photoelectron spectroscopy (XPS),^[175,176] time-of-flight secondary ion mass spectrometry (TOF SIMS),^[176] EDS,^[177] mass spectrometry (MS)^[178] and electron paramagnetic resonance spectroscopy (EPR)^[179] have identified decomposition products of FEC. FEC decomposes at a higher voltage (>1.2 V) than EC (~0.8 V) and has a strong influence on the SEI's composition. Some of the fragments and species that have been identified to form from decomposition and become part of the SEI are lithium fluoride, carbon dioxide, lithium oxide (from reaction with the silicon oxide surface)^[132] and polymers. FEC can form a number of radical anions,^[180] such as the postulated vinoxyl radicals (HC(O)CH₂·),^[179,180] that allows the formation of organic and inorganic carbonates.^[179]

VC has been shown to produce a unique structural motif that adds stability to the anode surface, poly(VC) (Figure 4.1). Using NMR and gas-chromatography (GC), Ota *et al.* were able to identify the formation of poly(VC)^[181] which was later confirmed by comparing the SEI formed to a synthetic poly(VC) reference.^[182] The high polymer content of the SEI formed with VC improves the stability of silicon anode materials, but a higher concentration of VC leads to poorer power performance than baseline electrolytes.^[183]

Some of the degradation products of FEC and VC, as identified by Michan *et al.*, including cross-linked poly(VC), are shown in Figure 4.1.^[174]

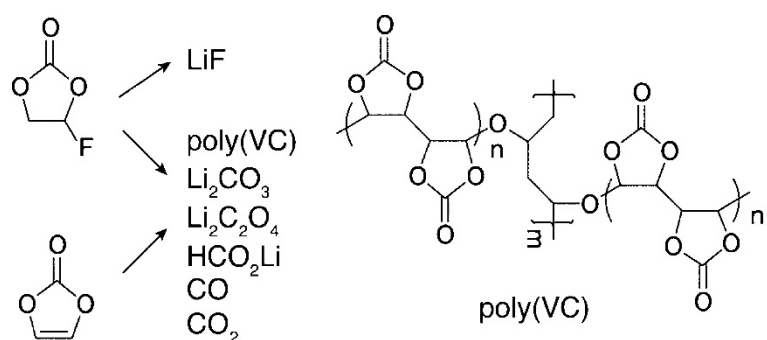


Figure 4.1: Proposed decomposition products of FEC and VC and the proposed, cross-linked structure of poly(VC). Reprinted with permission from reference [174]. Copyright 2016 American Chemical Society.

Ethylene carbonate (EC) based electrolytes on the other hand form more alkyl carbonates,^[184] large amounts of poly(ethylene oxide) (PEO) fragments,^[51,173,185] and lithium ethylene dicarbonate (LEDC).^[186,187] These different chemical components lead to different physical properties of the SEI. The more inorganic and cross-linked SEI formed from FEC and the polymeric SEI from VC impart superior properties to the SEI formed from ethylene carbonate, composed of more linear alkyls and PEO-fragments. These decomposition products cannot sufficiently stabilise the electrode and therefore form continuously upon cycling, leading to accelerated capacity loss.^[51,171,173]

4.1.1 Silicon Thin-film Anodes Cycled with FEC and VC

A range of electrolyte additives have been tested on silicon thin-film anodes in LIBs including fluoroethylene carbonate, vinylene carbonate but also electrolyte salts such as LiBOB and other compounds such as silanes.^[166,169,188–191] For fluoroethylene carbonate and vinylene carbonate literature reports are largely in agreement for a range of silicon anode materials, that the additives increase the capacity retention immensely.^[132,179,192,193] Both FEC and VC have been shown to stabilise the electrode by altering the SEI composition and the electrode morphology, yet there are only a few reports that show the structural changes in detail.^[166,169,183,194] Findings by Choi *et al.* discussed the structural impact of 2 wt.% FEC in EC/DEC on a 200 nm silicon thin-film electrode (Figure 4.2).^[169]

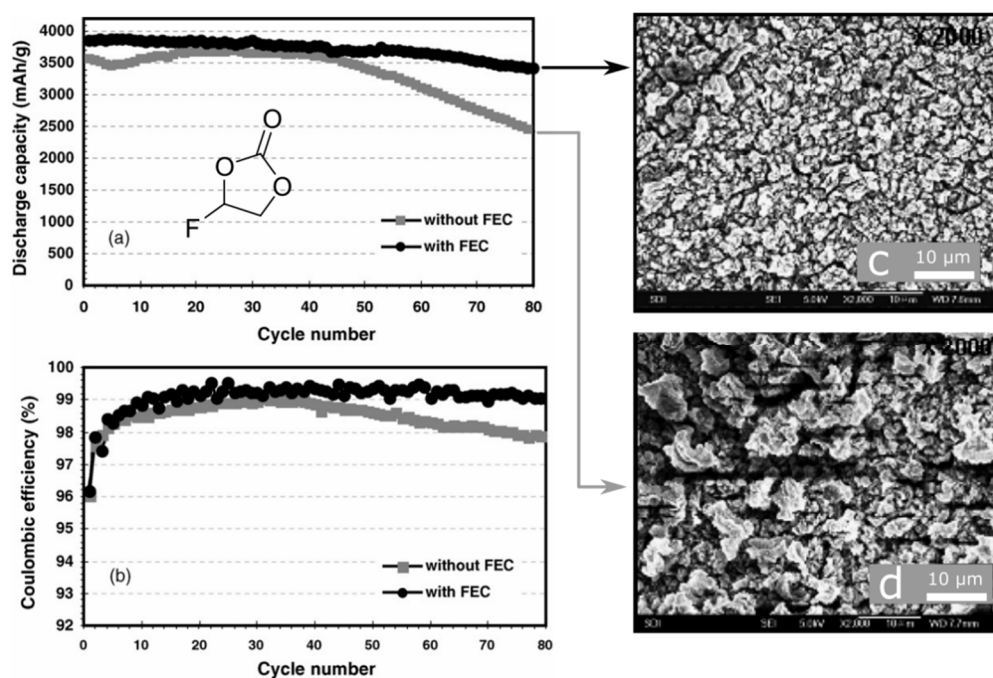


Figure 4.2: a) Discharge capacity and b) CE of the first 80 cycles of a lithium half-cell with 200 nm silicon thin-film electrodes cycled in 1.3 M LiPF₆ EC/DEC (3/7, v/v) with and without 3 wt.% FEC; c) SEM micrograph of the anode surface after 80 cycles from the cell without FEC and d) with FEC. Adapted with permission from reference [169]. Copyright 2006 Elsevier B.V.

As shown in Figure 4.2a, the addition of FEC leads to better capacity retention for the 200 nm silicon thin-film anode compared to an anode cycled without additive over 80 cycles. This is accompanied by increased CE (Figure 4.2b). After 80 cycles, the surface of the electrode cycled with FEC appears less rough (Figure 4.2c) than that of the electrode cycled in pure EC/DEC (Figure 4.2d) which also appears more porous. The authors propose that the SEI is more stable due to increased amounts of LiF and species with Si-F bonds, as identified by XPS studies.^[169]

Results from a study on the impact of VC on the silicon thin-film electrode morphology by Le Cras *et al.* is shown in Figure 4.3.^[166] Like FEC, VC increases capacity retention significantly (Figure 4.3a) and allows the 500 nm thin-film anode to cycle stable for more than 500 cycles. Electron micrographs of the surfaces after 30 cycles show that the electrode surface less coated when VC is present (Figure 4.3c), compared to the surface when cycling in the EC/PC/DMC electrolyte (Figure 4.3b). FIB cross sections further show that the electrode cycled with VC (Figure 4.3d) maintains a denser morphology compared to that cycled without additive (Figure 4.3c).

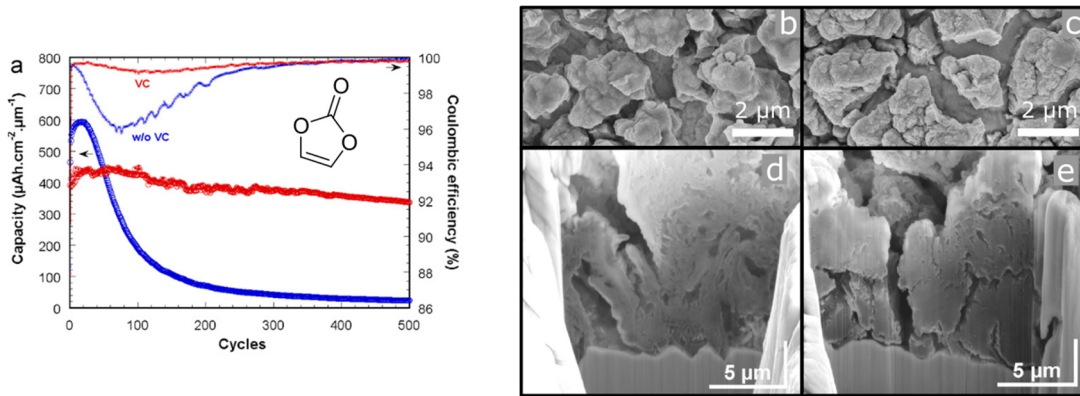
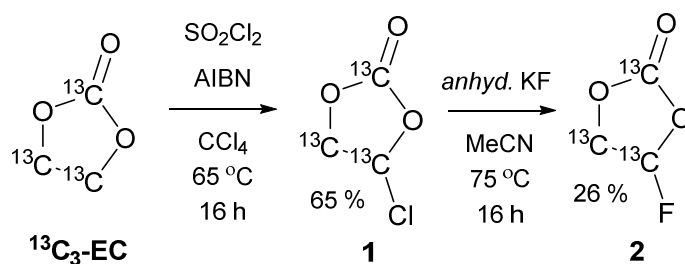


Figure 4.3: a) Capacity retention and CE over 500 cycles for lithium half-cells with 500 nm silicon thin-film electrodes in 1.0 M LiPF₆ EC/propylene carbonate (PC)/DMC (1/1/3, v/v/v) with and without 2 wt.% VC. Micrographs of the electrode surfaces after the 30th charge without (b) and with 2% VC electrolyte additive (c) and the FIB cross sections of the electrodes after 500 cycles without (d) and with 2% VC (e). Adapted with permission from reference ^[166]. Copyright 2012 Elsevier B.V.

4.2 Results and Discussion

4.2.1 Synthesis of ^{13}C -labelled Fluoroethylene Carbonate for NMR Studies

To allow the ^{13}C -NMR analysis of the SEI, particularly in its solid state, ^{13}C -enriched electrolytes are necessary to overcome the low natural abundance (1.1%) of the isotope and increase the signal intensity. Previously, using commercially available $^{13}\text{C}_3$ -labeled carbonate, studies on the SEI were carried out in our group which clearly identified some of the degradation products on the silicon anode by solid- and solution-state ^{13}C -NMR.^[51] The chemical structures formed when using fluoroethylene carbonate remained unconfirmed until recently. $^{13}\text{C}_3$ -FEC was therefore synthesised in order to enable detailed NMR studies, to identify the differences between the SEI formed from pure LP30 and that formed with FEC.^[171,172] The two-step synthesis of $^{13}\text{C}_3$ -FEC, following the description of Yao and Duan, is shown in Scheme 4.1.^[195]



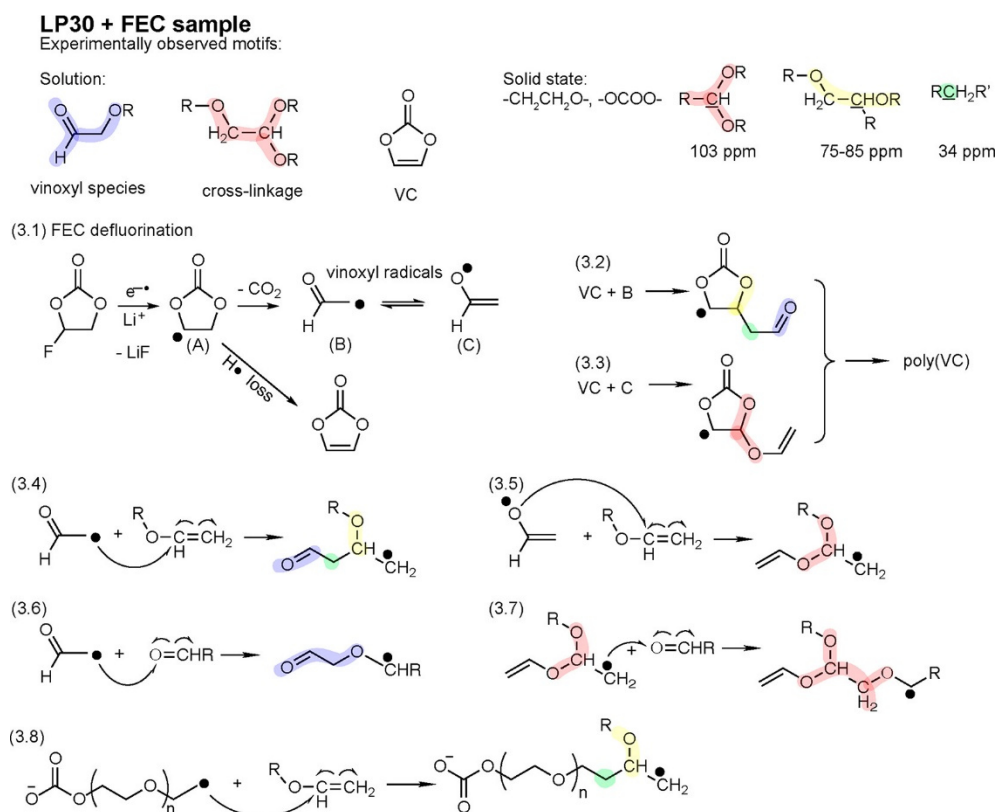
Scheme 4.1: Synthesis of $^{13}\text{C}_3$ -FEC **2**.

For the small-scale synthesis of FEC, commercially available $^{13}\text{C}_3$ -EC is used as starting material. A direct fluorination using fluorine would lack regioselectivity and yield a number of different substituted fluoroethylene carbonates that are difficult to separate. A pathway *via* the controlled single chlorination of the ethylene carbonate, followed by a halogen exchange will form the mono-fluorinated compound.

The first step from $^{13}\text{C}_3$ -EC to $^{13}\text{C}_3$ -ClEC **1** was performed using a radical chlorination reaction. Through a radical initiator (azobisisobutyronitrile, AIBN), a C-H bond is homolytically cleaved. Sulfuryl chloride (SO_2Cl_2) provides chloride radicals to form a C-Cl bond and the reaction stops after the monosubstitution. The reaction requires elevated temperatures and carbon tetrachloride as a proton-free solvent. Monitoring the 50:1 stoichiometric reaction of **1** with AIBN using thin-layer chromatography showed that it stalls after 2 h at 65°C . A larger excess of AIBN was therefore required to bring it to completion. The product was obtained in 65% yield.

The halogen exchange was performed by adding anhydrous potassium fluoride in large excess to **1** in acetonitrile. Stirring the suspension over night at 75°C converted most of the reactant to $^{13}\text{C}_3$ -FEC **2** as seen by thin-layer chromatography. The retention factors of **2** and **1** are very similar so that the yield of the extracted, pure **2** after column chromatography was moderately low (26%).

The pure $^{13}\text{C}_3$ -FEC facilitated the in-depth 1D- and 2D-NMR analysis of the SEI on silicon nanowires.^[171,172] The major findings are the presence of highly cross-linked polymers to which we attribute the increased stability of the SEI. Degradation products identified by NMR are vinoxyl species, vinylene carbonate and cross-linked ether functionalities in solution and acetals, the cross-linked polymeric species and alkane functionalities in the solid state.^[171]



Scheme 4.2: Top: Structural motifs identified by solution and solid-state NMR from silicon nanowires cycled in LP30 + 10 vol.% $^{13}\text{C}_3$ -FEC. The fragments are proposed to form following the degradation pathways shown and are shaded in the respective colours where appearing: (3.1) Initial reduction of fluoroethylene carbonate through fluoride abstraction to form radical **A** and subsequent formation of a vinoxyl radicals (**B** & **C**) or vinylene carbonate. (3.2 & 3.3) possible reaction of VC with fragments **B** or **C** to form species capable of forming poly(VC). (3.4 & 3.5) Reactions of vinoxyl radicals with alkene functionalities. (3.6) Possible reaction of the vinoxyl radical with an aldehyde. (3.7) Formation of branched polymeric species through the attack of the species formed in 3.5 onto an aldehyde. (3.8) Reaction of a PEO-type chain, proposed to be formed from ethylene carbonate with an alkene. Reprinted with permission from reference^[171]. Copyright 2017, American Chemical Society.

Most species could potentially be formed *via* degradation pathways shown in Scheme 4.2. The fluoride abstraction forming lithium fluoride during the reduction of FEC is shown in 3.1, resulting in an EC radical (**A**). Hereafter, **A** may either lose a hydrogen radical to form VC or release carbon dioxide to form vinoxyl radicals **B** and **C**.

Another finding from the work is the transient formation of LEDC, suggesting that this species may not be as significant to the composition of the SEI as previously thought. In addition, the cross-linking motifs (both poly(VC) and PEO like structures, identified in the NMR experiments) are suspected to form the basis of increased stability for the SEI formed on the silicon nanowire anode.

Further studies using the $^{13}\text{C}_3$ -FEC identified larger organic fragments that are formed from the electrochemical reduction of pure FEC and VC electrolytes.^[172] Figure 4.4 displays some of the fragments and the corresponding 2D NMR spectrum that confirms the earlier findings and adds further information on the larger structural motifs. Through dynamic nuclear polarization the signals in the double-quantum single-quantum (DQ–SQ) ^{13}C dipolar correlation experiment have been sufficiently enhanced to identify connected fragments. PEO fragments are connected through alkyl chains and *vice versa*. Acetal-type fragments are directly bound to PEO-type units, acting as cross-linkers in the larger, organic structures in the SEI.

Additionally, using DNP-enhanced ^1H - ^{29}Si - cross-polarisation NMR, siloxanes that are chemically bound on the Si surface were identified. These form when organic molecules are reduced on the silicon surface. No evidence was found for fluorinated polymers and only a small amount of SiO_xF_y -type species was detected, which is thought to arise from the glass-fibre separator.

In summary of the conducted NMR experiments, FEC forms a more cross-linked polymeric SEI that better stabilises the Si electrode, potentially reducing solvent penetration and limiting the continuous degradation on the reductive silicon surface. It may yield mechanical stability that can better accommodate the volume expansion and furthermore improve lithium ion-conductivity compared to the SEI formed from an ethylene carbonate electrolyte.

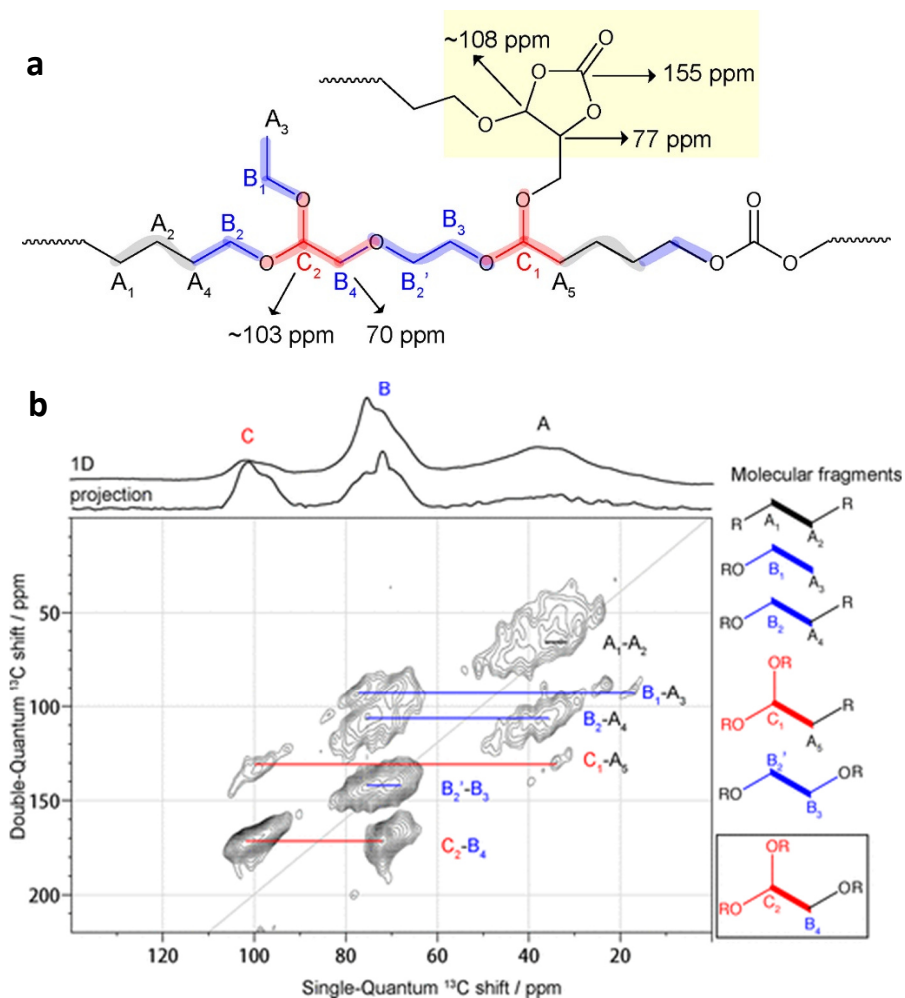


Figure 4.4: a) Possible polymer fragments formed from FEC or VC decomposition. Fragments are colour coded: branching in red, ethylene oxides in blue and alkyl functionalities in black. The yellow shaded area shows the cyclic poly(VC) like unit. b) dynamic nuclear polarization (DNP)-enhanced 2D NMR spectra of the single and double quantum dipolar correlation spectra of silicon nanowires cycled in FEC +5% $^{13}\text{C}_3$ -FEC over 100 cycles. The 1D spectra of the ^1H - ^{13}C cross-polarisation NMR and total projection in the single quantum dimension are shown at the top. Adapted with permission from reference ^[172]. Copyright 2018, American Chemical Society.

4.2.2 Impact of FEC and VC as Electrolyte Additives on the Stability of the Silicon Thin-film Electrode

To understand the stabilisation mechanism of the SEI formed from FEC and VC further, studies of their impact on the morphology of the silicon thin-film anode were carried out by the author. It appears that the electrolyte additives not only increase the capacity retention of the cell but also induce structural changes of the electrode material that prevent the loss of electronic contact.

4.2.2.1 Electrochemical Performance

Adding fluoroethylene carbonate (FEC) or vinylene carbonate (VC) to the LP30 electrolyte allows stable cycling of the 100 nm silicon thin-film anode for more than 300 cycles. The electrochemical performance of cells with the additives is shown in Figure 4.5a compared to a cell cycled with pure LP30 (black trace), and some of the key figures for the 1st, 2nd, 100th and 300th cycle are listed in Table 4.1.

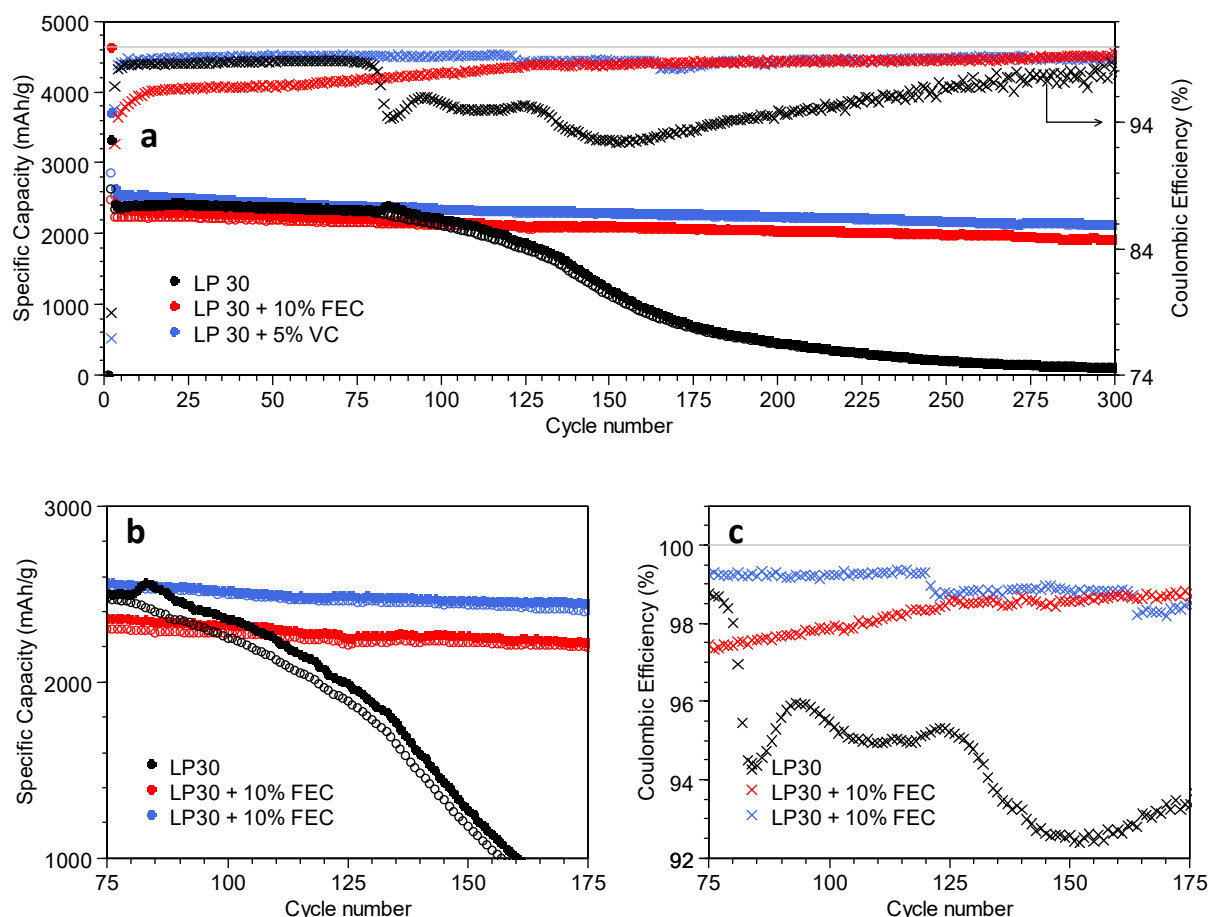


Figure 4.5: a) Electrochemical performance over 300 cycles of the 100 nm *a*-Si thin-film anodes on Ni-coated GG Cu cycled in pure LP30, LP30 + 10% FEC, and LP30 + 5% VC. b) Magnified areas for the 75th to 175th cycle and c) Coulombic efficiencies thereof. Filled symbols: lithiation; empty symbols: delithiation; **x**: Coulombic efficiency; rate: 1st C/30, 2nd+ C/5; cut-off voltage: 1st 5 mV, 2nd+ 45 mV.

While the cell cycled in pure LP30 begins to lose capacity after about 85 cycles following the usual decay pattern, the cells with electrolyte additives continue cycling and show very little capacity loss over 300 cycles. While both additives, FEC and VC, allow stable cycling, their CEs differs over the first 200 cycles.

Table 4.1: Figures from the cycling data of the 100 nm *a*-Si thin-film electrodes on Ni-coated GG Cu cycled in pure LP30, LP30 + 10% FEC, and LP30 + 5% VC.

Cycle	1 st			2 nd		100 th			300 th		
	Charge mAhg ⁻¹	Discharge mAhg ⁻¹	CE %	Charge mAhg ⁻¹	CE %	Charge mAhg ⁻¹	CE %	Ret*	Charge mAhg ⁻¹	CE %	Ret*
LP30	3292	4171	78.8	2942	96.9	2625	95.5	89.2	129	27.8	4.3
+ FEC	3108	5792	53.7	2800	92.2	2658	97.9	94.9	2413	99.3	86.2
+ VC	3575	4646	76.9	3158	95.1	2917	99.3	92.4	2642	99.1	83.6

*Capacity retention relative to the second cycle

The initial capacity loss is largest for the cell cycled with FEC with 46%, followed by the cell that was cycled with added VC at 23%, and the cell cycled in pure LP30 at 11%. FEC lowers the CE significantly only just slowly creeping up to above 98% after more than 100 cycles. However, it further increases over time and settles at around 99.2% from cycle 280 onwards with occasional maxima at 99.3%. At first, the cell containing 5% VC additive shows a higher CE of 99.0%+ by the 10th cycle, reaching 99.3% by the 120th cycle. This is followed by two drops in efficiency over the following 50 cycles to 98.7% and 98.3%, that are best followed in the plot shown in Figure 4.5c. The overall capacity is not affected (Figure 4.5b) during these dips. The cell only recovers to 99.0% after the 240th cycle, being lower than on the 100th cycle and lower than the cell with FEC on the 300th cycle.

The cycling profile and differential capacity plots for the 1st, 75th and 300th cycle of the cells cycled with additives are shown in Figure 4.6. The voltage plot for the three cells' first cycles in Figure 4.6a reveals the origin of the initial capacity loss with electrochemical processes in the high voltage region between 2.0 V and 0.4 V. The FEC containing cell shows a process starting at ~1.2 V that gives a significant contribution to the overall capacity. At lower voltages, the lithiation of the silicon material shows the familiar lithiation pattern. The sample with FEC shows an extra ~700 mAhg⁻¹ capacity compared to cells with the LP30 and LP30 + 5% VC cells from the onset of the initial lithiation plateau to reaching 5 mV. The plateau at ~0.4 V was discussed in section 1.4.2 on page 14, and again on this particular system in section 3.2.2.1 on page 47. During delithiation, the FEC cell shows the lowest capacity but a very similar curve to the pure LP30 cell. The VC sample recovers a small amount of capacity in the high voltage region, leading to a similar initial CE to the pure LP30 sample, despite the additional capacity in the high voltage region during discharge.

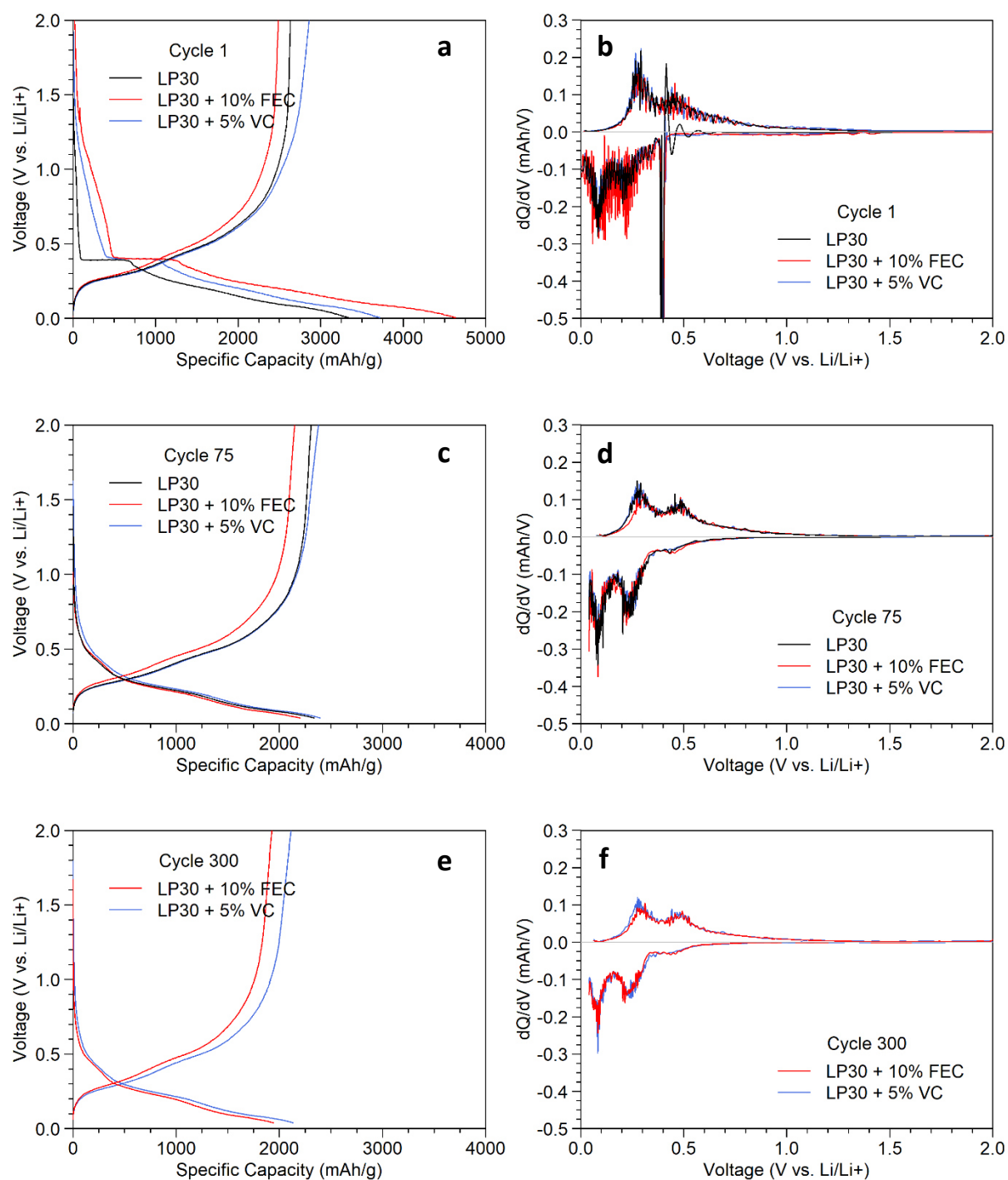


Figure 4.6: Voltage profiles (a, c, e) and differential plots (b, d, f) of the 100 nm α -Si thin-film anodes on Ni-coated GG Cu cycled with pure LP30, LP30 + 10% FEC and LP30 + 5% VC for the 1st, 75th, and 300th cycle, respectively. Filled symbols: lithiation; empty symbols: delithiation; \times : Coulombic efficiency; rate: 1st C/30, 2nd+ C/5; cut-off voltage: 1st 5 mV, 2nd+ 40 mV.

Later cycles show very similar cycling behaviour of the material, with only a process arising at 0.45 V for the cells cycled with pure LP30 and FEC (Figure 4.6c-d). By the 300th cycle, the pure LP30 sample has failed. The voltage profiles and dQ/dV plots of the cells with additives look very similar, again only with the VC cell showing less of the process at ~0.45 V (Figure 4.6e-f).

The changes in peak height and position of the electrochemical processes observed during discharge in the dQ/dV plots over the first 200 cycles are presented in Figure 4.7.

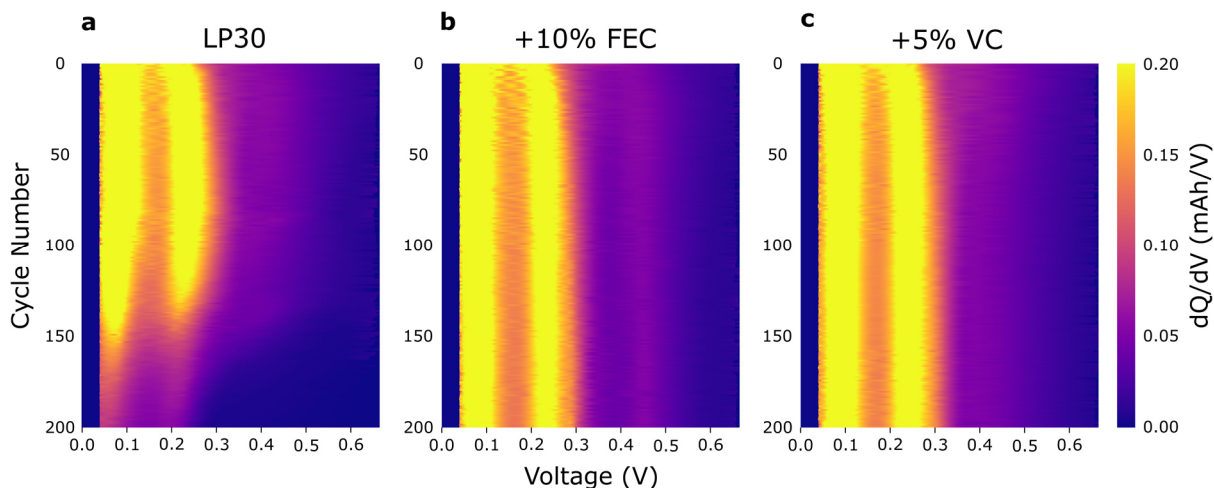


Figure 4.7: Maps of the intensity of the electrochemical processes observed in the dQ/dV plots below 650 mV for 100 nm *a*-Si thin-film anodes on Ni-coated GG Cu in a) pure LP30, b) LP30 + 10% FEC and c) LP30 + 5% VC over 200 cycles.

The capacity fade without additive is seen in the decreasing intensities around 0.25 V and 0.1 V for the formation of Li_2Si and $\text{Li}_{3.5}\text{Si}$, respectively (Figure 4.7a). The peak position shifts towards higher voltages during the first few cycles and decreases again at a later point when pure LP30 was used, seen in Figure 4.7a. Both FEC and VC establish stable cycling after a few cycles, with the sample cycled in FEC showing a more distinct process emerging around 0.45 V over time. To quantify the changes, the dQ/dV peak position and height are plotted against the cycle number in Figure 4.8.

The anode cycled in pure LP30 will form Li_2Si around a voltage maximum of 0.23 – 0.24 V until reaching the “dip” (Figure 4.8b, black trace), which then drops at the onset of degradation, plateauing at 0.21 V during the linear decrease in peak height (Figure 4.8c, black trace). Over the last 50 cycles, when most capacity is lost, the voltage decreases significantly until the peaks become undetectable.

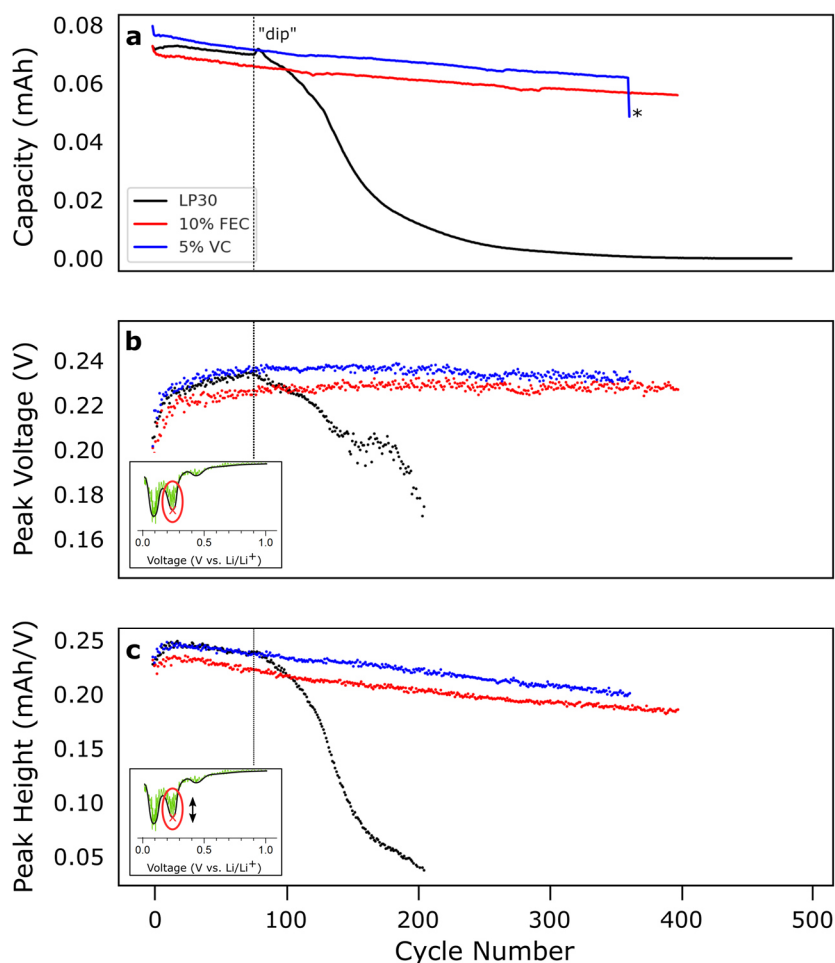


Figure 4.8: Capacity (a) and voltage (b) and height (c) of the Li_2Si dQ/dV peaks of the cells cycled with pure LP30, LP30 + 10% FEC and LP30 + 5% VC. The vertical line marks the characteristic “dip” in efficiency for the sample in pure LP30. The insets show the studied peak positions in a typical dQ/dV plot for clarity. *The cell with added VC was stopped during cycling and the cycle was finished on a different cyclers.

Electrodes cycled with added FEC and VC do not show signs of severe degradation up to 400 and 375 cycles, respectively. The Li_2Si peak of the anode cycled with VC shifts up to a voltage of 0.24 V (Figure 4.8b, blue trace), similar to the cell with pure LP30. This is followed by only a slight decrease over time. The voltage observed for the sample cycled with FEC shifts more slowly to higher voltages (Figure 4.8b, red trace), only reaching 0.23 V after more than 300 cycles, approaching the level of VC.

To estimate how much of the electrolyte is being consumed during cycling, the irreversible capacity loss over 350 cycles is calculated and shown in Figure 4.9.

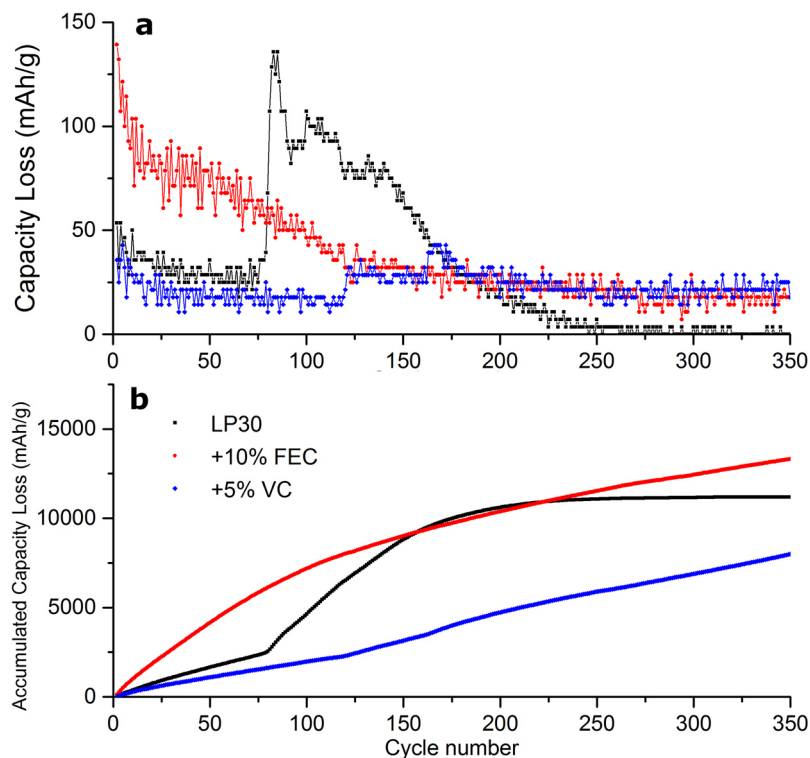


Figure 4.9: a) Capacity loss per cycle for cells with 100 nm *a*-Si thin-film anodes on Ni-coated GG Cu cycled with pure LP30, LP30 + 10% FEC and LP30 + 5% VC. b) Accumulated capacity loss over 350 cycles.

The cell with FEC consumes the most capacity per cycle, and the cell with VC the least (Figure 4.9a). The capacity loss in the FEC cell decreases significantly over the first 150 cycles which is followed by a more gradual fade to the 350th cycle. The cell in pure LP30 shows the largest loss in capacity from the “dip”, between the 75th cycle and cell failure. The decreasing efficiency for VC (Figure 4.5) yields two increases in capacity loss on the 120th and 160th cycle. After 350 cycles, the FEC sample has a combined capacity loss of 13325 mAhg⁻¹ exceeding the amount of lithium consumed by the failed cell in pure LP30. The VC additive shows only a combined 9360 mAhg⁻¹ capacity loss. However, at this point the loss per cycle is higher than that observed for the cell with FEC (Figure 4.9a).

4.2.2.2 Electron Microscopy and Energy-Dispersive X-ray Spectroscopy

After cycling, the electrode surfaces have changed significantly, as seen in the photograph of the electrodes taken after cell disassembly (Figure 4.10).

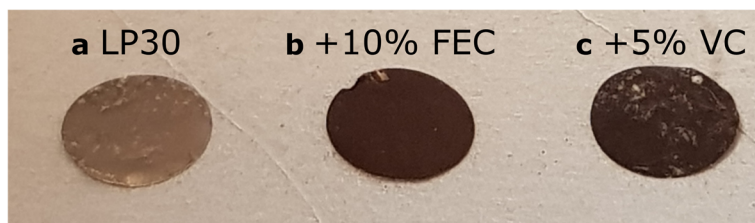


Figure 4.10: Photograph of the 100 nm *a*-Si electrodes on Ni-coated GG Cu cycled in pure LP30 (a, 500 cycles), LP30 +10% FEC (b, 400 cycles) and LP30 +5% VC (c, 375 cycles) after disassembling the half-cells and rinsing with DMC inside an argon filled glovebox.

The electrodes' surfaces appear homogeneous with only some glass fibres from the separator stuck to the electrode cycled with VC (Figure 4.10c). This shows that the features observed in the SEM micrographs can be representative of the surface.

Figure 4.11 shows the electrode surfaces on GG Cu after up to 500 cycles and Figure 4.12 shows anodes on CR Cu after 200 cycles. The differences of the copper current collectors were discussed in section 3.2.5.1 on page 59. Differences in the structures may also in part come from the different number of cycles and different cut-off voltages. However, micrographs show similar features of the electrodes as all electrodes were extracted from the half-cells that were stopped during stable cycling. Figure 4.13 shows the FIB cross sections of the anodes on CR Cu cycled in pure LP30 and 10% FEC, and on GG Cu cycled with 5% VC. Some glass-fibres (e.g. Figure 4.12) and imprints of such (e.g. Figure 4.11g) are observed on the surfaces.

In pure LP30, large Si/SEI islands have formed on the GG Cu foil that have lost any electrochemically activity (Figure 4.11a-c). These should not be mistaken for the islands observed during the initial cracking as their size and composition differs largely. The exposed nickel surface appears as a metallic lustre on the anode in Figure 4.10a. At lower acceleration voltage (Figure 4.11b), fine surface features are visible. The Si/SEI mass appears mainly homogeneous, revealing only a few topological features in the micrographs recorded at higher acceleration voltage. On CR Cu, the material covers the surface, showing a similar nanostructure (Figure 4.12a).

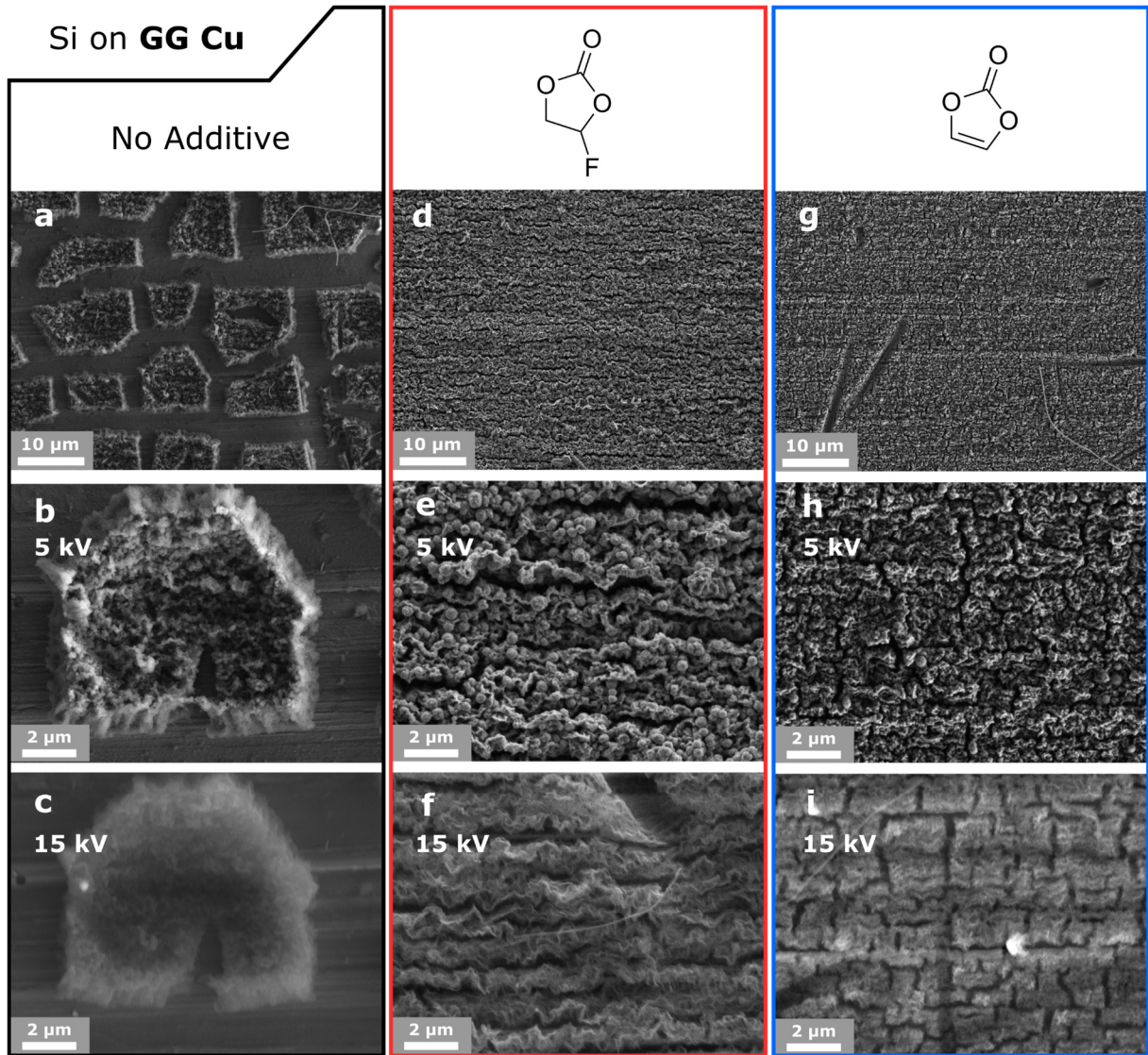


Figure 4.11: SEM micrographs of 100 nm *a*-Si thin-film anodes on Ni-coated GG Cu cycled in pure LP30 (a-c, 500 cycles), LP30 + 10% FEC (d-f, 400 cycles) and LP30 + 5% VC (g-i, 375 cycles).

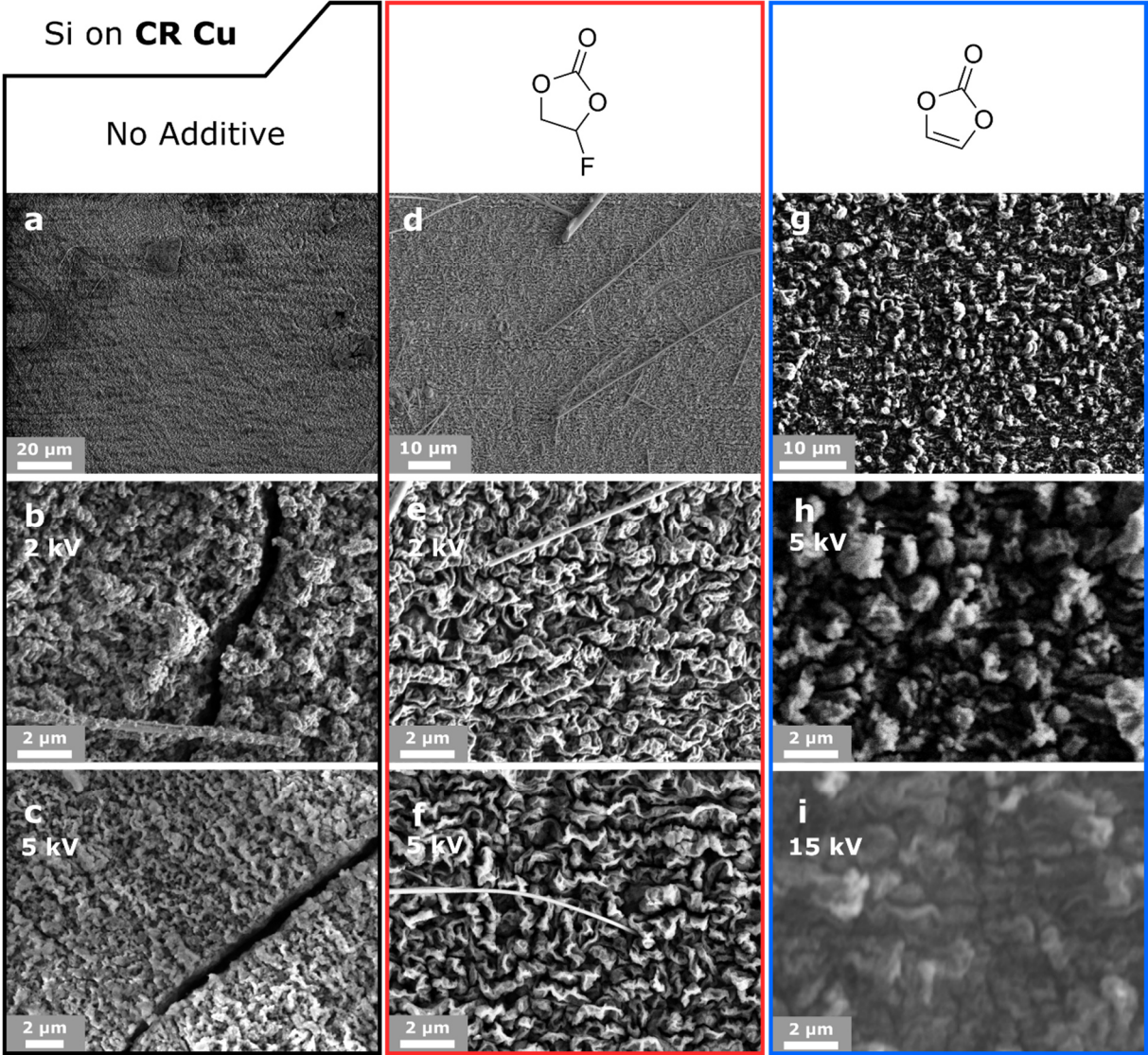


Figure 4.12: SEM micrographs of 100 nm *a*-Si thin-film anodes on Ni-coated CR Cu after 200 cycles in pure LP30 (a-c), LP30 + 10% FEC (d-f) and LP30 + 10% VC (g-i). Surfaces were exposed to air during sample transfer.

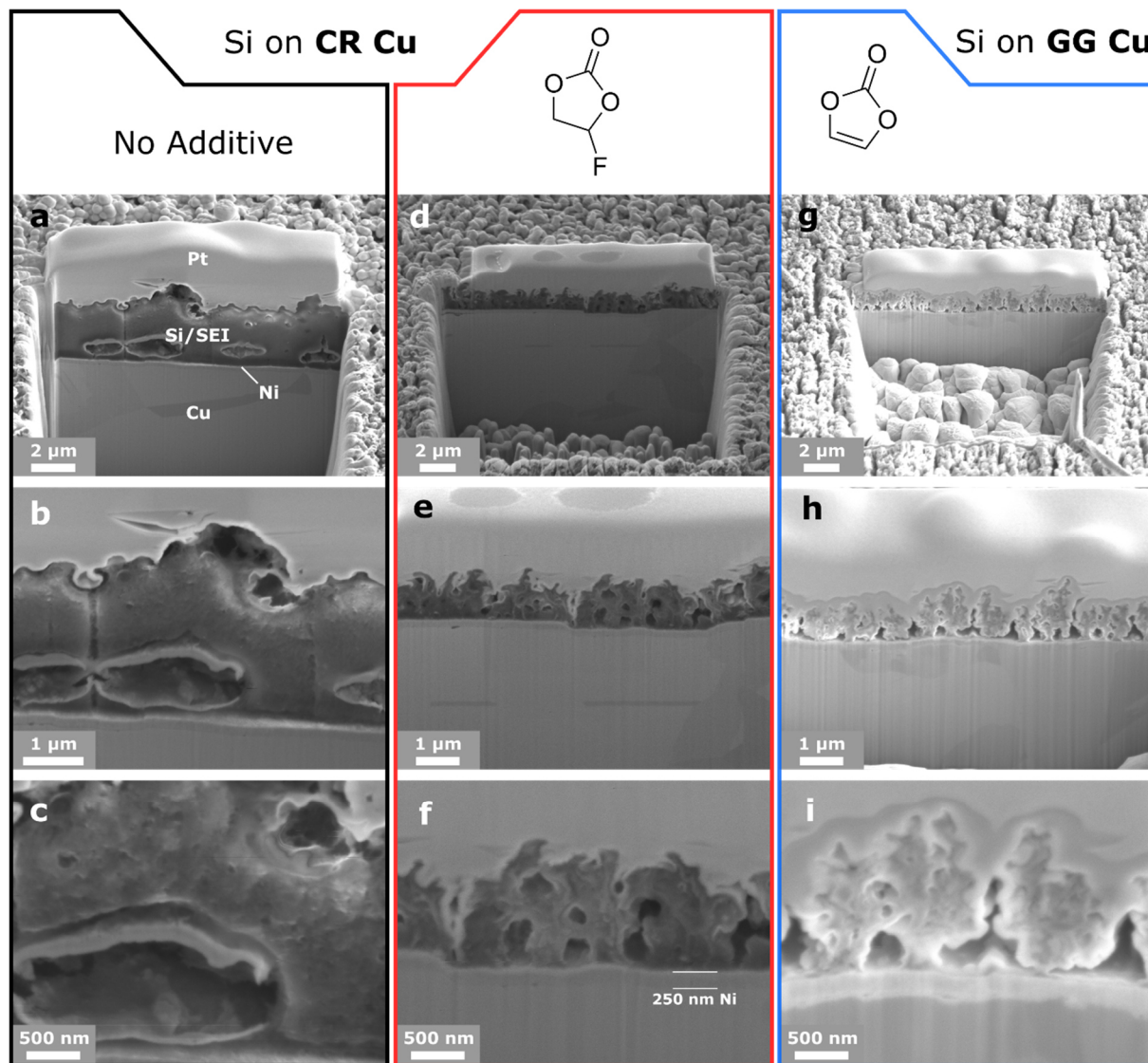


Figure 4.13: FIB SEM micrographs of 100 nm *a*-Si thin-film anodes on Ni-coated Cu current collectors cycled in pure LP30 (a-c, 200 cycles, CR Cu), LP30 + 10% FEC (d-f, 200 cycles, CR Cu) and LP30 + 5% VC (g-i, 375 cycles, GG Cu). The surface was coated with gold and a platinum bar was deposited on the FIB milling site. The different layers observed are described in a). The nickel interlayer is highlighted in f) as a vertical reference. Micrographs were recorded at an angle of 53°.

A lamellar surface structure of the Si/SEI material is observed in the FEC-containing sample, particularly in the micrograph recorded at the highest acceleration voltage showing the denser structure underneath a layer of softer SEI on both copper substrates (Figure 4.11f and Figure 4.12f). The sheets on GG Cu are 100–180 nm wide and gathered in mostly 0.7–2 μm wide ribbons, separated by small void spaces (Figure 4.11f). Sheets have a similar width on CR Cu, however, the material covers the surface more evenly (Figure 4.12f).

The silicon thin-film anode on GG Cu, cycled with VC (Figure 4.11e), shows a different cracking pattern, more like that observed after 30 cycles in Chapter 3, section 3.2.2.3, from page 51 onwards. The structure is composed of large, interconnected silicon material islands that have a size of 1 μm maximum in at least one direction and are divided by cracks. A finer surface structure is observed with similar widths to that formed from FEC (~100–200 nm) (Figure 4.11h-i). The electrode on CR Cu shows a more space-filling but similar cracking pattern of 1–2 μm wide islands (Figure 4.12i) and globular features sticking out that are up to 1 μm wide (Figure 4.12h).

Micrographs of the FIB cross sections (LP30, FEC: 200 cycles; VC: 375 cycles) show the morphology of the anode material and the area of contact to the current collector. The silicon/SEI material formed from pure LP30 is bulky and shows signs of beam damage in Figure 4.13b. Continuous cracking has led to pulverisation of the anode and accumulation of SEI, creating the large amount of material. The nanoporous structure formed from pure LP30 must have a largely increased internal surface area, which is in accordance with findings by Jensen *et al.* who identified a sharp increase in surface area for silicon graphite material anodes in cells cycled with LP30 over a sample with LP30 and 10% FEC.^[196]

The addition of FEC has created a structure of interwoven sheets and pillars that have shown good electrochemical performance before disassembly (Figure 4.5). Some cracks from top to bottom of the material that are visible in the cross section, filled with deposited gold and platinum from the FIB SEM preparation (Figure 4.13e). The material is attached to the current collector by ~300–900 nm wide patches. Similarly, to the LP30 sample, electrolyte slowly leaks from the porous surface after removing the sample from the FIB SEM chamber and is seen as stains on the copper in Figure 4.14b, on the next page.

The anode cycled with VC shows a different microscopic structure of anode material. The outermost layers charge under the electron beam, appearing bright in contrast to the rest of the material (Figure 4.13h). The overall material appears curled with diameters of the nanostructures being 100–200 nm. The material is mostly disconnected from the current

collector but remains attached by small, 160–300 nm wide patches holding the larger silicon islands in place. Where nickel is not in contact with the Si/SEI material, it appears to be covered with a thin layer of material (Figure 4.13i).

EDS spectra of the surfaces and elemental maps of the cross sections are presented in Figure 4.14 and Figure 4.15, respectively. Figure 4.14 shows representative spectra of the cross-section. Over at least 3 scans in different regions of the SEI/Si the spectra looked alike.

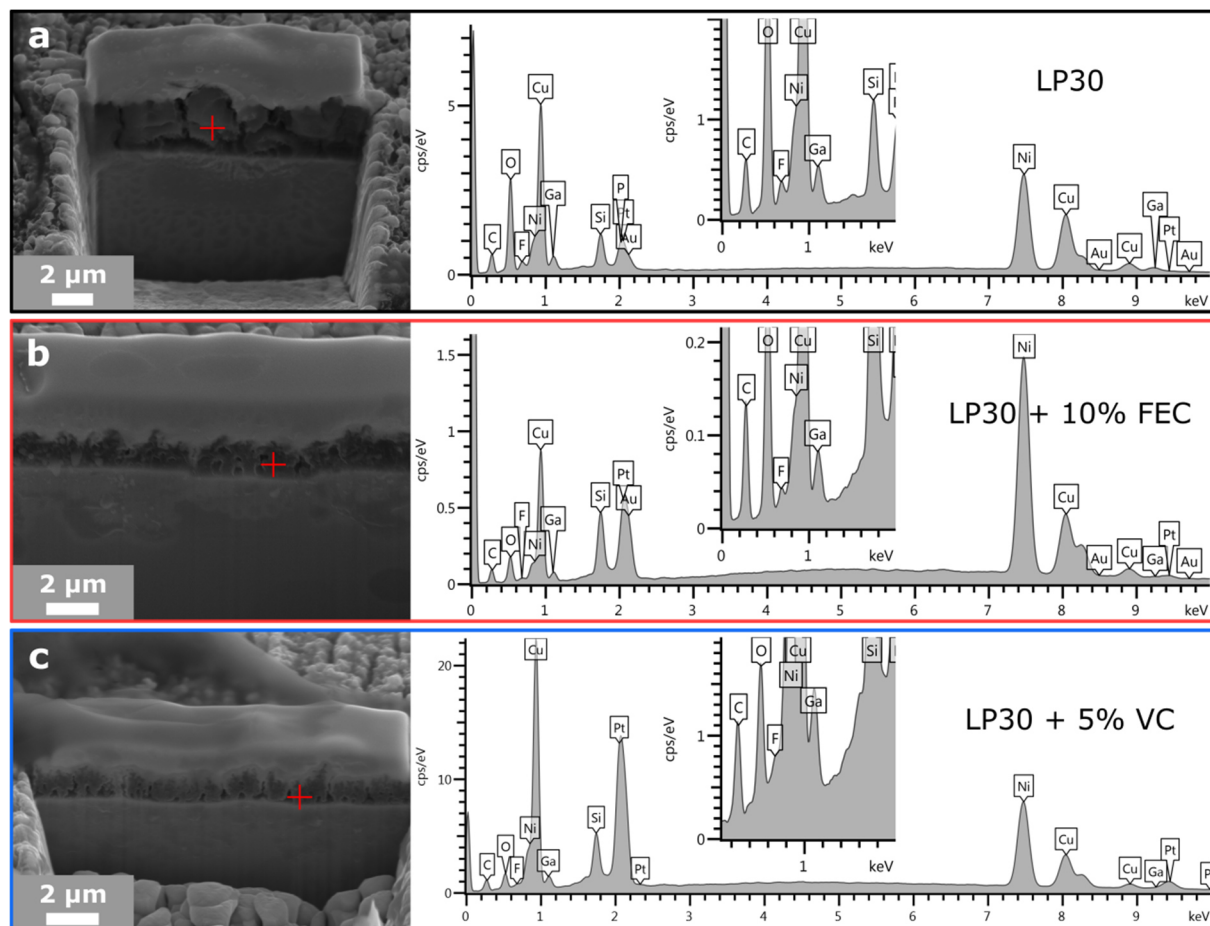


Figure 4.14: SEM micrographs and EDS point scan spectra (15 kV) of the FIB cross sections of 100 nm α -Si thin-film anodes on Ni-coated current collectors cycled in pure LP30 (a, 200 cycles, CR Cu), LP30 + 10% FEC (b, 200 cycles, CR Cu) and LP30 + 5% VC (c, 375 cycles, GG Cu). The insets show the voltage range between 0 and 2 keV showing decreasing amounts of fluorine from a) to c).

A strong indicator for the amount of SEI formed is the ratio of oxygen, carbon and fluoride to silicon. High fluoride and oxygen contents can be associated with inorganic salts (LiF , Li_2O , Li_2CO_3) and high carbon contents may indicate the presence of organic compounds.

As discussed in Chapter 2 Methods, the EDS analysis of lighter elements in close proximity to heavier elements proves to be difficult. The way the software constructs the maps disregards the correction for the Bremsstrahlung, hence shows intensity for light elements where only

heavy TMs are be present. The insets in Figure 4.14 show the region of 0–2 keV to identify the intensity of the fluorine signal as it is difficult to observe given the Ni $L\alpha$ line being close in energy.

The electrode cycled in pure LP30 shows a significantly higher silicon to oxygen ratio compared to the samples cycled with additives (Figure 4.14a). Detected fluorine may stem mostly from the decomposition of the PF_6^- counter ion. Overall, the high counts for C, O and F must stem from both the SEI and the electrolyte that was contained by the porous Si/SEI material and has dried on the cross section. Still, we can assume that a larger amount of SEI is present near the current collector, comparing the electrode thicknesses and EDS spectra of all three electrodes.

Both spectra of the anodes cycled with additives show less carbon and oxygen and the spectrum from the VC cross section shows almost no fluorine (Figure 4.14c). Even after almost double the cycles, the amounts of O and C appear similar for the samples. The differences in fluorine concentrations were obviously expected, as the degradation of FEC requires the breaking of the C-F bond forming inorganic species. The low fluorine content in VC further shows that the SEI formed does not contain a high amount of decomposed PF_6^- .

The EDS element maps in Figure 4.15 show the local concentrations of silicon and the lighter elements in between the TM layers. The geometry of the setup demands a careful analysis of the elemental maps. Its impact is seen by nickel appearing with increasing intensity from top to bottom due to the tilted alignment of the sample to the electron beam and the depth of beam penetration. To focus on the relevant information in the element maps, only the components inside the pink borders are discussed as these represent the Si/SEI composite.

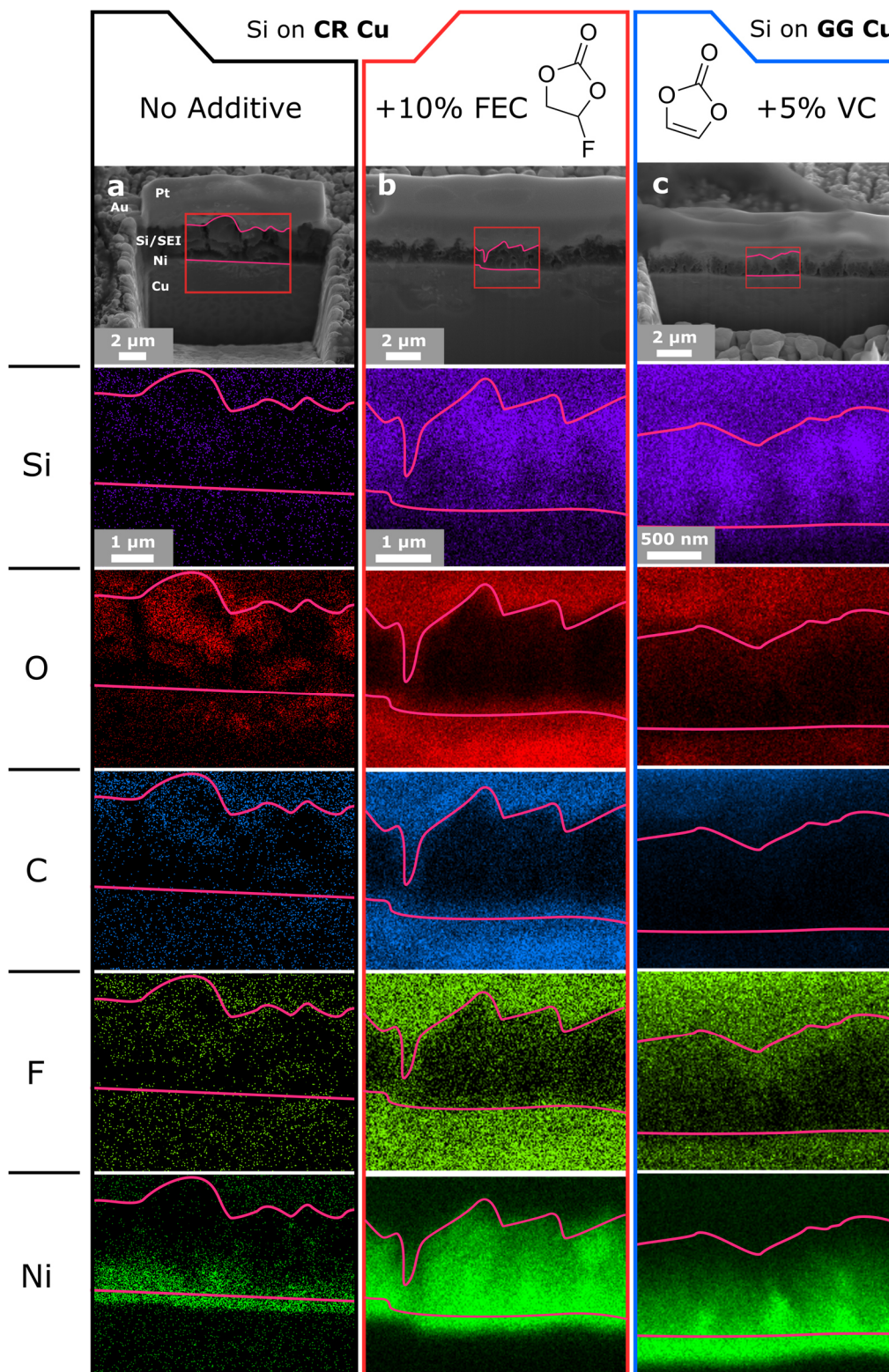


Figure 4.15: SEM micrographs and EDS element maps of the FIB cross sections of the 100 nm *a*-Si thin-film anodes on Ni-coated Cu current collectors cycled in LP30 (a, 200 cycles, CR Cu), LP30 + 10% FEC (b, 200 cycles, CR Cu) and LP30 + 5% VC (c, 375 cycles, GG Cu). The different layers observed are described in a). The highlighted areas in the micrographs correspond to the EDS element maps with marked borders enclosing the area between the platinum bar and the nickel interlayer. Micrographs were recorded at an angle of 53°.

The element maps in Figure 4.15a, of the electrode cycled in pure LP30, show the highest concentrations of oxygen, carbon and fluoride spread over the cross section separated by cracks, as visible in the oxygen map. The low amount of silicon detected is spread out evenly. The nickel signal is more prevalent in the samples cycled with additives. Due to the angle of the incident beam, the nickel signal is strongest at the bottom of the Si/SEI composite and fades in the upper regions. The holey structure of the composite formed from the additives allows the beam to penetrate further hence showing an increased intensity of the nickel signal also in the upper areas.

Similar to the point scans in Figure 4.14, the element maps of the cross section of the electrode cycled with FEC (Figure 4.15b), shows decreased concentrations of the elements associated with the SEI (O, C, F) and an increase in silicon, compared to the pure LP30 sample. The silicon rich areas match the porous structure seen in the electron micrograph.

The electrode cycled with VC shows silicon located in the centre of the material islands, and some SEI or dried electrolyte as seen in the increased concentration of O and F in the upper middle of the maps between areas of high Si-content.

4.2.2.3 Stabilisation Mechanism

The combined information from galvanostatic cycling, SEM micrographs, and EDS analyses allows a stabilisation mechanism to be proposed, outlined in Figure 4.16, for the different SEIs that are formed when using the electrolyte additives.

The thin-film electrodes cycled in pure LP30 fail due to the continuous cracking, pulverisation and SEI formation resulting in an amorphous Si/SEI material, losing electronic pathways to current collector (Figure 4.16a). This is supported in the anode's electrochemistry by its poor CE (Figure 4.5) and an early degradation. The micrographs of the FIB cross section in Figure 4.13a show the material being disconnected from the current collector and having morphed into a material containing large amounts of oxygen, carbon and fluorine both from the SEI and dried electrolyte in the nanoporous structure (Figure 4.14).

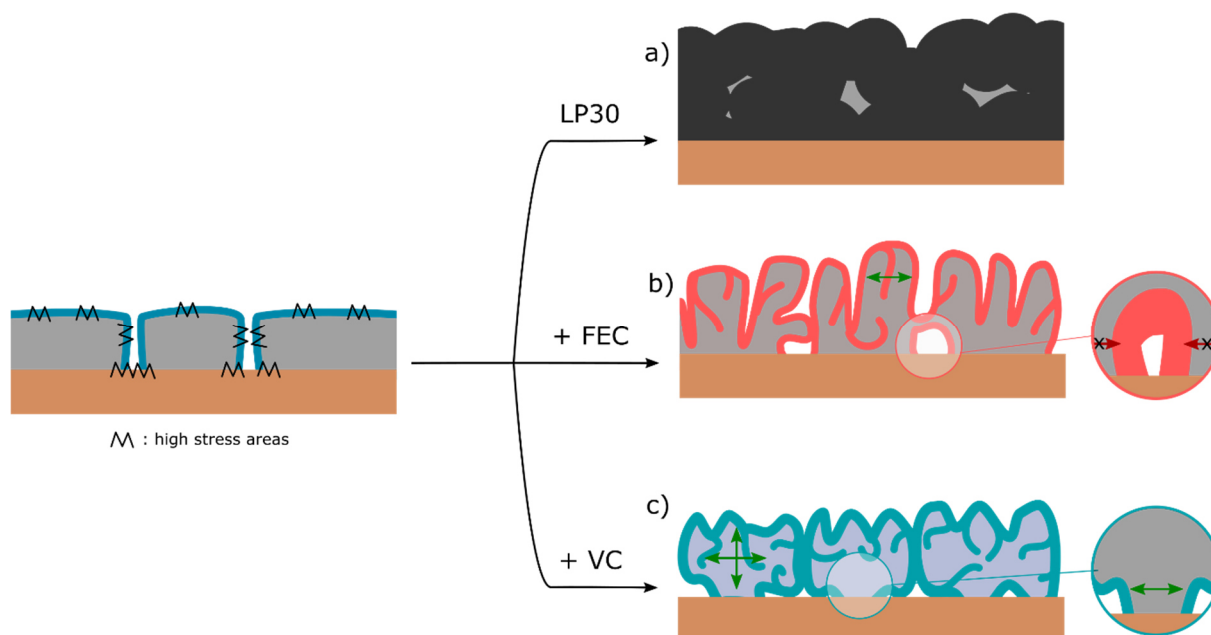


Figure 4.16: Structural evolution of a cracked silicon thin-film anode during continuous cycling and SEI formation. a) Entrapped silicon material due to the weak SEI formed from LP30 cracking and accumulating over time. b) Porous silicon structure that can freely expand near the surface, stabilised by the SEI formed with FEC, maintaining electrical contact by limiting the volume expansion on the current collector. c) Porous silicon islands that can expand and are stabilised by the SEI formed with VC, maintaining electrical contact through small, stabilised patches, highlighted as a magnified region.

The addition of FEC yields an SEI capable of supporting nanosized, interwoven, sheet-like features that form during cycling. The electrode can utilise the void spaces in between the silicon sheets to expand into during lithiation. The poor CE over the first 120 cycles, seen in Figure 4.5, suggests that the SEI forms at an early stage from extensive reduction of FEC. The material formed possesses the mechanical stability to allow the silicon sheets to expand and contract and suppress the delamination during volume expansion near the current collector, judging by the structure observed in the FIB SEM micrographs in Figure 4.13b. The strong presence of the electrochemical process at 0.45 V in Figure 4.7 suggests a larger surface area to participate in reactions with the electrolyte as confirmed by SEM (Figure 4.11 and Figure 4.12). The excellent CEs during later cycles indicate that this process may be reversible, likely due to the retained electron conduction pathway.

The SEI formed from the electrolyte containing 5% VC stabilises the anode as large silicon islands that maintain electrical contact to the current collector through small anchoring patches (Figure 4.16c). The islands roughly match the dimensions of those initially formed by cracking after 30 cycles in pure LP30 (Figure 3.15, page 55). The electrochemistry in Figure 4.5 indicates that the SEI stabilises the anode early as silicon islands with an elastic SEI, shown in the high

CE over the first 100 cycles. Drops in efficiency indicate that structural changes occur during cycling. Reaching a critical amount of SEI or deformation during cycling, the material may partially delaminate, exposing surface near the current collector. More SEI is formed underneath the silicon islands and on the current collector. The patches that connect the material with the current collector may shrink to a size where they are stabilised by the VC-SEI, seen in the FIB SEM micrographs in Figure 4.13g-i. The high contrast near the edges indicates the presence of a thick SEI surrounding the silicon islands. The anode shows similar electrochemical properties to the one cycled in pure LP30 at first, judging by the trends seen in Figure 4.8. However, for the reasons above the anode does not show the same degradation mechanism over the 375 cycles. The dQ/dV plots in Figure 4.6 and the corresponding map in Figure 4.7c show less of the process at ~ 0.45 V (Figure 4.7c), supporting the idea of a more passivating SEI formed with VC and less Si surface area being exposed.

EDS studies are by far not as surface sensitive as NMR. However, in the EDS spectra in Figure 4.14 and Figure 4.15 we find that the SEI formed from VC shows a higher carbon and lower fluorine content than the SEI formed from FEC, hinting towards a more organic SEI formed from VC. From the NMR studies on the SEI formed from FEC and VC we have observed increased mechanical stability which may be attributed to more cross-linked SEIs. The Si/SEI structures and amount of material formed that we observe seem to confirm this, as only an SEI that is sufficiently stable will allow the expansion and contraction without the material losing its structural integrity.

Electrochemical data obtained during the NMR project further suggested that VC will build up a larger amount of SEI while FEC would form less of an SEI and be more ion conductive. However, it is difficult to estimate the actual amount of SEI formed from our data on the thin-films. Over the first 200 cycles, FEC accumulates a large amount of capacity loss during cycling (Figure 4.9) suggesting that actually FEC decomposes more. The lower CE associated with this, compared to VC, has also been observed for Si nanowires for the NMR studies, however, only a limited number of cycles were part of the investigation and the difference was less striking (CE over the first 50 cycles: Si nanowires: $\sim 98.5\%$ (FEC), $\sim 99.2\%$ (VC); Si thin-films: $\sim 96.7\%$ (FEC), $\sim 99.1\%$ (VC)).

The examined silicon nanostructures are inherently different: Si nanowires provide a system that may not significantly change its structure during cycling, while thin-films crack and continuously expose fresh surfaces. A stable SEI is formed from FEC once the structural changes of the electrode during cycling are manageable with features of a maximum width of

approx. 200 nm in at least one dimension. Once the critical feature size is reached, the capacity loss per cycle decreases and is observed to be lowest for FEC (Figure 4.9a). Until that point, FEC will continue to decompose. The SEI formed from VC, which we believe is of a less cross-linked polymeric nature, appears to support larger Si/SEI features that will undergo distinct changes during cycling. The late drop in Coulombic efficiency suggests, that the SEI may be less protective and allow more of the electrolyte to permeate and decompose than with the SEI formed from FEC. Overall, the passivation appears to occur as a similar process with either additive, where VC, and VC that is formed *in situ*, play an important part.

Previously, thin-films were regarded to cycle stable in an unnamed standard electrolyte to a thickness of 2.5 μm by Dahn *et al.* This brings up the question of how the thickness that is achievable with thin-films is affected by the addition of FEC or VC. Both have shown to yield Si/SEI structures with enough void space to use during cycling for the 100 nm thin-film anodes. The observed silicon nanostructures, during stable cycling, after cracking, are roughly of the size that is reported for the stable cycling of nanoparticles and nanowires (150 nm and 300 nm, respectively).

4.3 Conclusion

$^{13}\text{C}_3$ -FEC has enabled studies by Jin *et al.* identifying fragments of the SEI formed from FEC on the silicon nanowire anode.^[171,172] The studies report that the species formed from FEC are highly cross-linked and may better support the silicon anode mechanically, allowing less solvent permeation and good lithium ion conductivity.

The authors work has shown the impact of the SEIs formed with FEC and VC on the electrochemical performance and changes in morphology of the 100 nm silicon thin-film anode. The additives increase the capacity retention and allow stable cycling for more than 300 cycles without significant capacity losses.

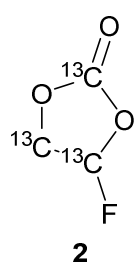
FEC predominately decomposes over the first 100 cycles. It induces the formation of a lamellar anode surface structure, stabilising ~200 nm wide silicon sheets that are capable to expand during lithiation and are attached to the current collector by wider patches (~400 nm), maintaining electrical contact. VC forms a thick SEI in early cycles, stabilising silicon islands of nanosized Si/SEI composite material. The islands partially delaminate and maintain electrical contact to the current collector through small patches which are stabilised by the formation of the VC-SEI near the current collector. We suggest that the polymeric nature of the SEI aids to stabilise such features and that the composition of the SEIs from FEC or VC influences the macroscopic appearance of the electrode. Qualitative EDS analyses on the FIB cross sections of the anodes support findings from previous studies, that the SEI formed from VC is more organic than that formed from FEC. Judging by the SEM micrographs, an SEI with high elasticity is necessary, such as suggested by the NMR studies in form of cross-linked polymers, to support the anode during cycling and maintain the anode nanostructures. From the observed structures we conclude that the films must break into sufficiently small fragments that are supported by the SEI formed from the electrolyte including either additive. The superior performance of the silicon anodes cycled with FEC in the NMR studies,^[171,172] was reported for silicon nanowires that fulfilled the size criteria being small enough to avoid fracturing. Other silicon anodes of micron size and larger could exhibit a degradation pathway similar to that of the thin-films with additives and are likely to remain active as long as the formed nanostructures maintain electronic conduction pathways.

4.4 Experimental Section

4.4.1 Materials

Electrolyte solution (LP 30: 1M LiPF₆ in 1:1 ethylene carbonate and dimethyl carbonate), ¹³C₃-ethylene carbonate (99 atom% ¹³C, 97%), fluoroethylene carbonate and vinylene carbonate (battery grade) were obtained from Sigma Aldrich and used as received.

4.4.2 Synthesis of ¹³C₃-Fluoroethylene Carbonate **2**



¹³C₃-ethylene carbonate (200 mg, 2.27 mmol, 1.00 eq.) was suspended in carbon tetrachloride (5 mL) and sulfuryl chloride (0.19 mL, 2.38 mmol, 1.05 eq.) and azobisisobutyronitrile (AIBN) (15 mg, 0.91 mmol, 0.04 eq.) were added. Two additional portions of AIBN were added in 30 min intervals. The mixture was stirred at 65°C for 16 h and the solvent was removed in vacuo. The liquid crude product was purified by column chromatography (silica 100:1, DCM, R_f = 0.50). ¹³C₃-Chloroethylene carbonate **1** (180 mg, 1.47 mmol, 65%) was received as a colourless liquid. Potassium fluoride (anhydrous, 2.50 g, 43.0 mmol, 29.3 eq.) was suspended in acetonitrile (abs., 7 mL) to which the ¹³C₃-chloroethylene carbonate, dissolved in acetonitrile (abs., 3 mL), was added. The mixture was stirred at 75°C for 16 h before filtering. The filter cake was washed with 10 mL of acetonitrile. The solvent of the combined filtrates was removed, and the dark liquid was purified by column chromatography (silica 100:1, DCM, R_f = 0.45). ¹³C₃-Fluoroethylene carbonate **2** (40 mg, 0.38 mmol, 26%) was received as a colourless liquid.

¹H NMR (399.6 MHz, chloroform-*d*): δ = 6.28 (m, ¹J_{H-C} = 193.9 Hz, ²J_{H-F} = 63.9 Hz, ³J_{H-H cis} = 7.8 Hz, ³J_{H-H trans} = 7.8 Hz, 1 H), 4.62 (bm, ¹J_{H-C} = 157.7 Hz, 1 H), 4.53 (bm, ¹J_{H-C} = 157.9 Hz, 1 H) ppm.

¹³C {¹H} NMR (100.5 MHz, chloroform-*d*): δ = 152.4 (t, ²J_{C-C} = 1.8 Hz, 1 C), 104.8 (ddd, ¹J_{C-F} = 237.3, ¹J_{C-C} = 37.1, ²J_{C-C} = 1.8 Hz, 1 C), 70.59 (dd, ¹J_{C-C} = 37.1, ²J_{C-F} = 28.4 Hz, 1 C).

4.4.3 Methods

Detailed descriptions of the techniques and instruments used can be found in Chapter 2 Methods. Measurements were performed under standard operating conditions.

4.4.3.1 Electrode Preparation

All 100 nm Si anodes used were prepared in the CCR sputter coater onto nickel-coated (250 nm) current collectors. Both cold-rolled copper (CR Cu) and copper for graphene growth (GG Cu) discs were used.

4.4.3.2 Coin Cells

0.1 mL of LP30 electrolyte with and without additives was used for the coin cells. Additives were mixed with the electrolyte prior to adding them to the cell (FEC: 10 vol%, VC: 5 vol%).

4.4.3.3 Galvanostatic Cycling

Cells were cycled on a LANDT potentiostat at C/30 to 5 mV for the first cycle, followed by C/n for consecutive cycles (n = 5, 10) to different voltage cut-offs (100 mV, 45 mV), depending on the experiment.

4.4.3.4 SEM and EDS

Coin cells were disassembled at full charge (2 V) and the anodes were rinsed with DMC. The electrodes were analysed in the TESCAN MIRA3 FEG-SEM samples were transferred into the microscope using the inert atmosphere transfer module from Kamrath & Weiss for the initial surface analysis but exposed to air after. Samples were coated with gold, using a sputter coater for FIB-SEM analysis on a Zeiss Cross-beam 540 and the FEI Helios Nanolab SEM/FIB. EDS spectra and maps were recorded using the Oxford Instruments Aztec Energy X-maxN 80 EDS system on the TESCAN MIRA3 FEG-SEM.

Chapter 5 Poly(phosphazene) Coatings to Stabilise the Si Thin-film Anode

In the previous chapter we identified changes in the SEIs' composition and how it affects the silicon thin-film electrodes structure during electrochemical cycling. Additives may provide extended cycle life, yet we do not actively control the surface of the electrode and rely on the degradation of the electrolyte to stabilise the system. Artificial SEIs are one promising, yet challenging, way to stabilise the silicon anode.^[79] Strategies include carbon-based coatings, ion conductive solid electrolytes and the combination of polymeric binders and carbon additives.^[52,65,67,85,197]

In this chapter, we introduce poly(phosphazene) coatings for the silicon thin-film electrode to gain control over the electrode-electrolyte interphase and provide stability by design. It is intended to act as the basis for an elastic SEI that provides reasonable lithium ion conductivity while withstanding the expansion of the silicon material. Phosphazenes such as ethyleneoxy phosphazenes have been reported as potential electrolytes, and electrolyte additives for lithium ion batteries for some decades.^[104,118,198,199] Apart from being tuneable lithium ion conductive materials, phosphazenes, similar to phosphates, act as flame retardants, making these materials appealing from a safety perspective.^[200-202]

We utilise the mechanical and chemical flexibility of the polymers to cast thin poly(phosphazene) coatings on silicon thin-film anodes and have observed longer lifetime and interesting structural changes of the electrode from electrochemical data, SEM micrographs and EDS spectra. Based upon the findings, we were able to propose stabilisation mechanisms. The findings provide a synthetic pathway to a range of tuneable polymer coatings that have large potential not only for silicon thin-films but other materials and applications.

The synthesis of two chemically different poly(phosphazenes) and their deposition on the silicon thin-film anode are described. The coated anodes are cycled and changes in the surface morphology and chemical composition are studied after cycling. The polymers compatibility with the electrolyte additives FEC and VC is investigated showing different results to the bare electrodes and clear limitations of the system. Finally, the mechanisms by which the two polymers stabilise the anode are discussed which depends on the interaction of the coating with the SEI formed during electrolyte degradation and may be linked to the polymers chemical structure.

5.1 Poly(phosphazene) Gel Electrolytes

In recent years, the group of Wiemhöfer have performed studies on poly(phosphazene) in-gel electrolytes towards their application on lithium metal anodes for lithium ion batteries.^[121–125,203,204] Their work has investigated the ion-conductive properties in great detail.

In the work published by Wiemhöfer, poly(phosphazenes) were synthesised in three steps: formation of the monomeric precursors, polymerisation to a chain-length of ~500–700 units and substitution of the side-groups with either sodium methoxy(ethoxy) ethoxide or sodium methoxy[ethoxy(ethoxy)] ethoxide. The polymers were then mixed with an electrolyte salt and benzophenone, pressed to a thickness of ~350 μm and exposed to UV radiation for cross-linking. The polymer in-gel electrolytes have been shown to be stable over a potential range of 0–4.5 V vs Li/Li⁺, have high ion conductivity $\sigma_{\text{total}} = 2.3 \text{ mScm}^{-1}$ at 30°C and have high lithium transfer numbers of 0.31 (at 90°C). A photograph of the polymer film and the possible coordination mode of the poly(phosphazene) to lithium cations are shown in Figure 5.1.

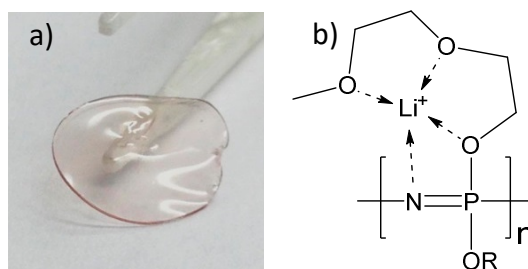


Figure 5.1: a) Photograph of a cross-linked poly(phosphazene) gel electrolyte. b) Possible coordination mode of a lithium cation by a fragment of the ethylene oxide substituted poly(phosphazene). Adapted with permission from reference ^[122]. Copyright 2015 Elsevier Ltd.

Polymers substituted with moieties containing ether functionalities provide multiple lone pairs to coordinate to lithium cations. Furthermore, the backbone's nitrogen functionality may also coordinate (Figure 5.1b). Different lengths of the polyether moieties have been studied.^[121,122,204] Applying the polymers as gel electrolytes in a symmetrical lithium cell that was cycled for a large number of plating/stripping cycles showed that lithium dendrite growth was slowed down significantly. This was observed using a specialised microscopy set-up (Figure 5.2 II) to follow the changes of the electrodes surface during operation. The electrolyte used was a gel electrolyte of poly[bis(2-(2-methoxyethoxy)ethoxy) phosphazene] (MEEP) with dimethyl carbonate, ethylene carbonate and LiBOB (Figure 5.2).

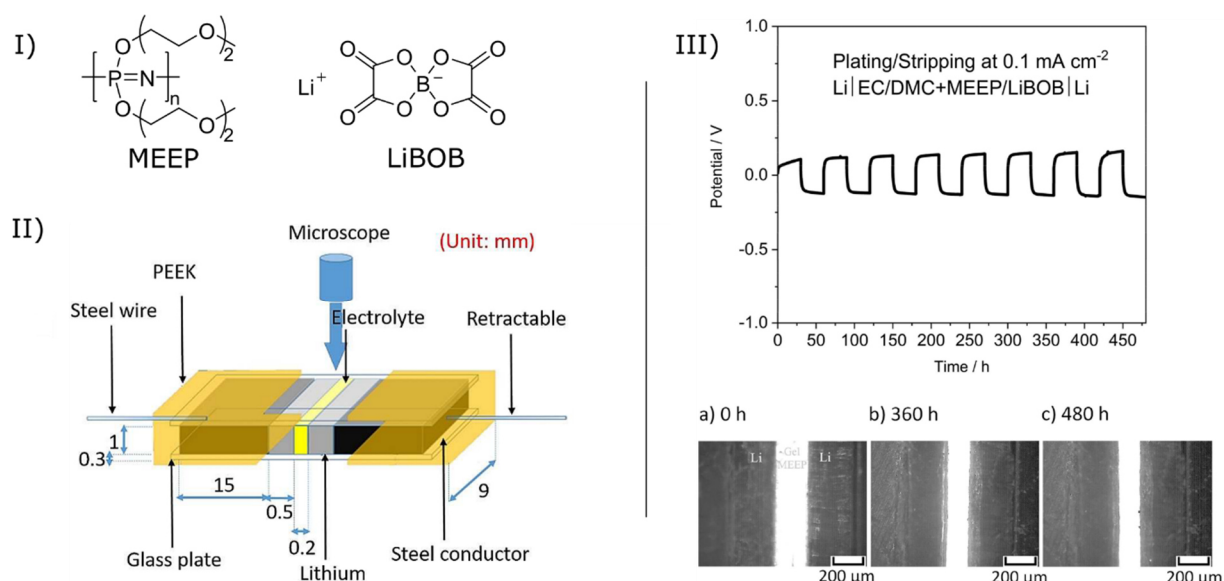


Figure 5.2: I) Structures of the poly(phosphazene) MEEP and LiBOB, used in the studies. II) Experimental microscopy setup to monitor the formation of lithium dendrites, looking at the gel electrolyte in between two pieces of lithium metal. III) Continuous plating and stripping for 30 h each at 60°C and a current density of 0.1 mAcm⁻², showing no noticeable dendrite growth. Adapted with permission from reference [125]. Copyright 2019 Wiley-VCH Verlag GmbH & Co. KGaA, Weinheim.

The cross-linked poly(phosphazenes) will swell with the organic electrolyte and the lithium ions are distributed between the liquid electrolyte and the stationary polyether side-groups, as outlined in Figure 5.3.

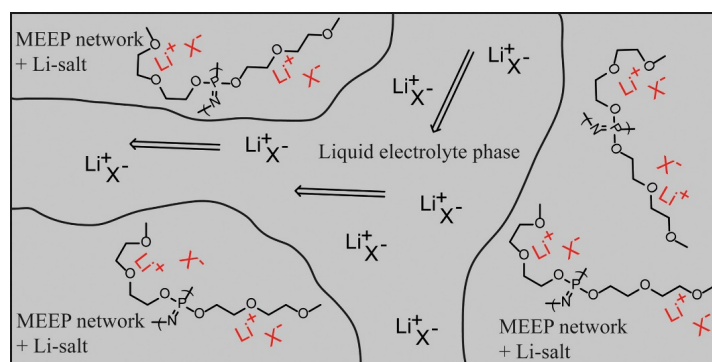


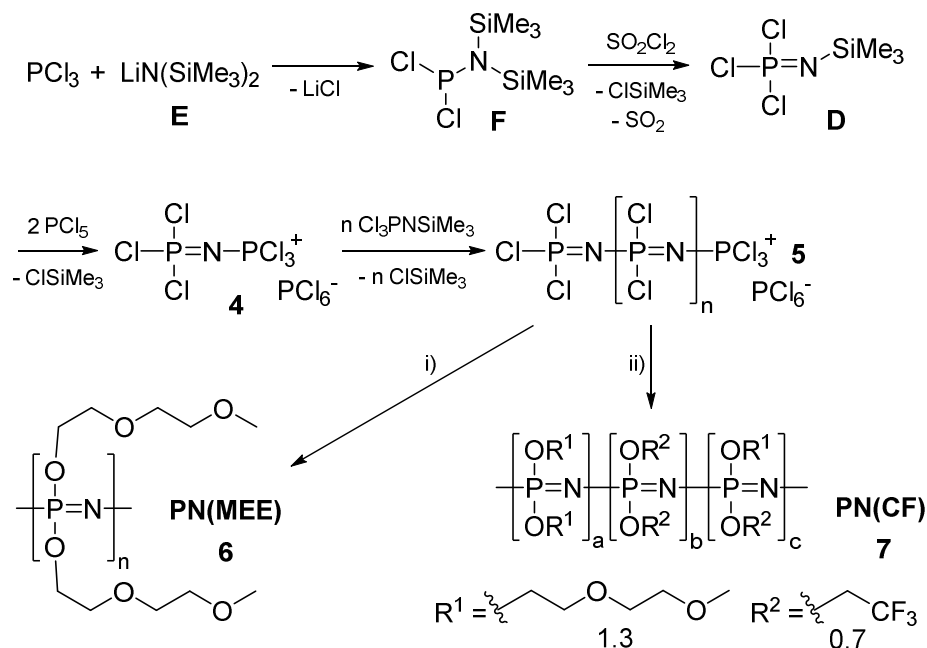
Figure 5.3: Illustration of the lithium ion transport in the gel electrolyte as the electrolyte salt is distributed between the solvent and polymer. Reprinted with permission from reference [203]. Copyright 2015 Elsevier Ltd.

The poly(phosphazene) gel electrolyte system has been well established and provides a detailed insight into the physical properties of the films for use in lithium ion batteries, such as the lithium ion conductivity and transfer number. These factors are assumed to be similar for the system reported in this chapter and allows for the use of the material on silicon thin-films for the first time, without quantifying these parameters at this stage. The reported mechanical stability of the films is encouraging for their use on silicon materials.

5.2 Results and Discussion

5.2.1 Synthesis of the Poly(phosphazenes)

The polymers were prepared following the synthesis previously described by Wang *et al.*^[205] Starting from phosphorous trichloride, a monomeric precursor **D** was synthesised and polymerised to form **5**, followed by a side-chain substitution reaction to yield the final polymers **6** and **7** (Scheme 5.1).



Scheme 5.1: Synthetic pathway for PN(MEE) **6** and PN(CF) **7**; synthesis of the $\text{Cl}_3\text{PN}(\text{SiMe}_3)$ monomer **D**; living cationic polymerisation to yield poly(chlorophosphazene) **5**; chloride substitution with alkoxide side-chain to form the substituted polymers **6** and **7** i) 2.1 eq. NaOEtOEtOMe , THF, 5 d; ii) 1.5 eq. NaOEtOEtOMe , THF, 2 d + 1.5 eq. $\text{NaOCH}_2\text{CF}_3$, THF, 2 d). The ratio of side chains in **7** was determined by $^1\text{H NMR}$.

The monomer synthesis was performed with high purity and yields, following the optimised procedure by Manners.^[206] Reacting phosphorus trichloride with lithium hexamethyldisilazide ($\text{LiN}(\text{SiMe}_3)_2$) forms the phosphorus(III) species **F** that can be oxidised with sulfuryl chloride to yield precursor **D**. It was found that the use of freshly prepared $\text{LiN}(\text{SiMe}_3)_2$ from the reaction of hexamethyldisilazane and *n*-butyl lithium increases the yield, as commercially available LiHMDS can contain impurities that initialise polymerisation.

The polymerisation is performed with two equivalents of PCl_5 , added to freshly-distilled **D**. The cationic species **4** is formed, that reacts with more of **D** in a “living” cationic polymerisation, forming chlorotrimethylsilane in the process. By controlling the amount of the monomer, polymer chains grow to a certain number of PN-units and show narrow chain-length

distributions. The monomer to initiator (PCl_5) ratio in this study was 100:1 to receive short-chained polymers of low viscosity. The reaction in DCM was followed by $^{31}\text{P}\{^1\text{H}\}$ NMR spectroscopy and full conversion to poly(chlorophosphazene) **5** was observed after 2 days as a peak at -18.2 ppm. This is in agreement with the literature known values.^[122]

Adding the fresh poly(chlorophosphazene) solution to a stirred solution of sodium methoxy(ethoxy) ethoxide in dry THF yields the fully alkoxy-substituted polymer PN(MEE) **6** after 5 days. To form PN(CF) **7**, only 1.5 equivalents of sodium methoxy(ethoxy) ethoxide were added and the solution was stirred for 2 days. Then 1.5 equivalents of sodium trifluoroethoxide were added and the mixture was stirred for another 2 days to react with any P-Cl bonds still present after the first substitution.

The polymers were purified by dialysis in deionised water over 5 days in cellulose tubing with a 12 to 14 kDa molecular weight cut-off. The isolated PN(MEE) polymer appears like clear honey as a viscous, pale yellow substance that is soluble in most solvents. The partially fluorinated polymer PN(CF) appears turbid, is less viscous but also has good solubility in common solvents. The $^{31}\text{P}\{^1\text{H}\}$ NMR spectra of the two polymers are displayed in Figure 5.4.

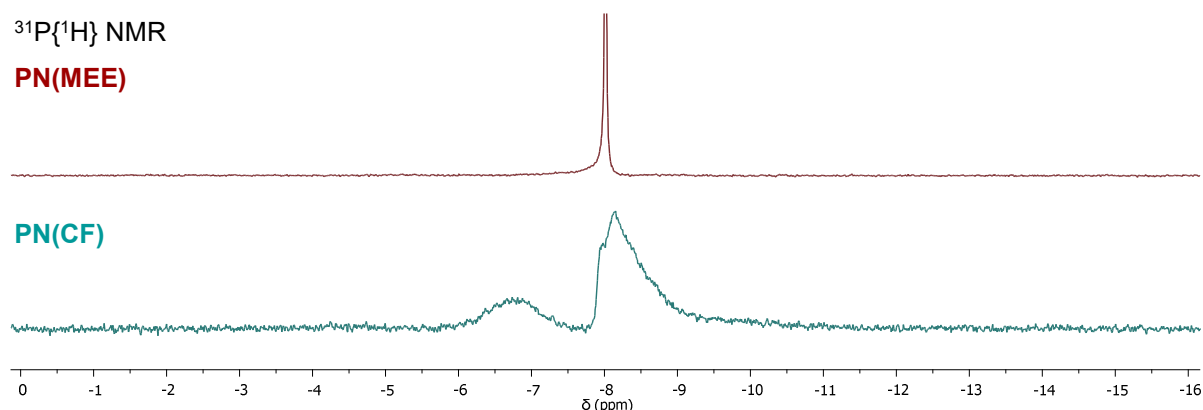


Figure 5.4: $^{31}\text{P}\{^1\text{H}\}$ NMR spectra (THF- d_8 , 400 MHz) of PN(MEE) (top) and PN(CF) (bottom).

The purely polyether-substituted polymer shows a sharp signal in the $^{31}\text{P}\{^1\text{H}\}$ NMR spectrum at -8.0 ppm in THF- d_8 (Lit.: -8.3 ppm in CDCl_3).^[203] PN(CF) shows two broad signals: one at -6.8 ppm, the other at -8.1 ppm with a shoulder at -8.0 ppm. The purely fluoroether-substituted polymer has been reported to show as a singlet at -6.9 ppm in THF- d_8 .^[207] The broad peaks and the shoulder indicate a mixture of substitution patterns. The ^1H NMR spectra show the protons on the side-groups for both polymers and the ratio of the polyether and trifluoroethoxy substituents in PN(CF) (Figure 5.5).

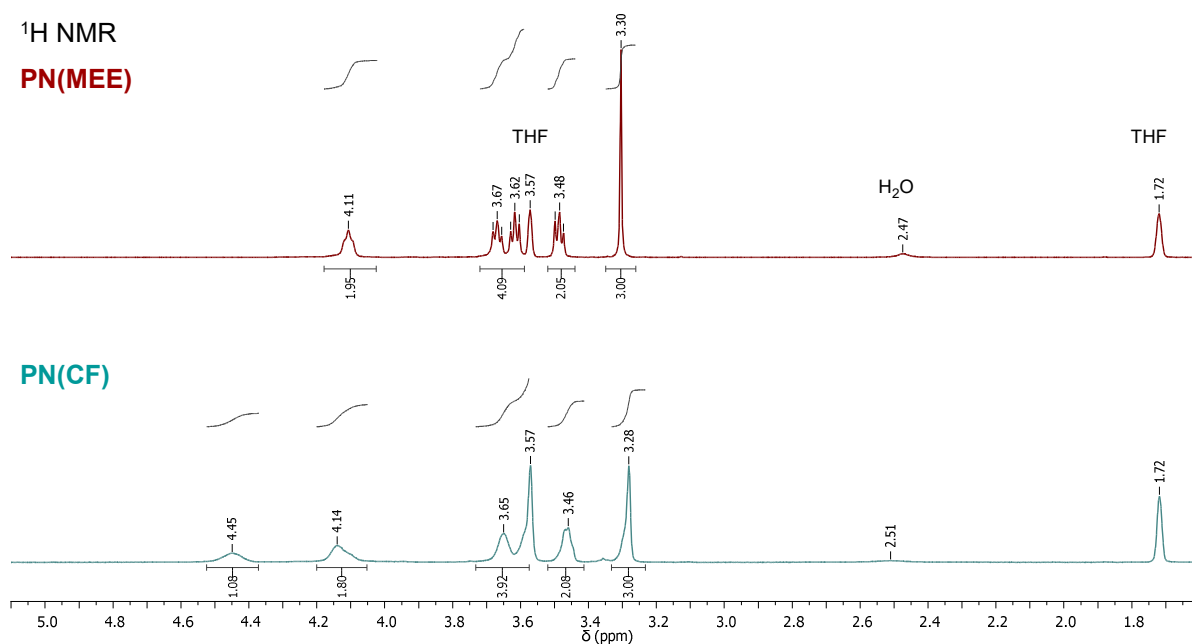


Figure 5.5: ¹H NMR spectra (THF-*d*₈, 400 MHz) of PN(MEE) (top) and PN(CF) (bottom). Residual proton signal from the THF solvent are found at 1.72 ppm and 3.57 ppm and traces of water are present at ~2.5 ppm.

The proton NMR spectra show the predicted stoichiometry for the methoxy(ethoxy) ethoxide side-groups for both polymers with the terminal methoxy group at ~3.3 ppm and four further signals of an integral of ~2 H at a higher chemical shift. The peaks in the PN(CF) spectrum are broadened and shifted, indicating irregular substitution patterns. The two protons corresponding to the trifluoroethoxide side-group at a shift of 4.45 ppm show an integral of just more than half of the CH₂-peaks of the polyether side-groups. This equals a ratio of approximately 1.3:0.7 of polyether and trifluoro ether side-groups per PN unit. Gel-permeation chromatography (GPC) results of the two polymers in dimethylformamide (DMF) are shown in Figure 5.7. The number and mass average molecular weights and polydispersity indexes are presented in Table 5.1.

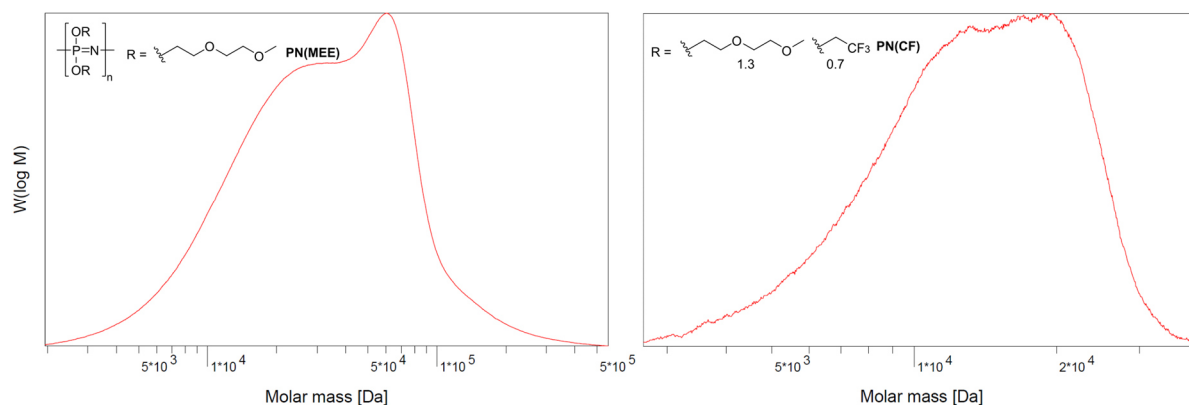


Figure 5.6: GPC results of PN(MEE) and PN(CF) in DMF.

Table 5.1: Number average molecular weight (\bar{M}_n), mass average molecular weight (\bar{M}_w) and polydispersity index (D) of the polymers PN(MEE) and PN(CF) determined by GPC in DMF.

	PN(MEE)	PN(CF)
\bar{M}_n (g mol ⁻¹)	$2.08 \cdot 10^4$	$1.13 \cdot 10^4$
\bar{M}_w (g mol ⁻¹)	$4.52 \cdot 10^4$	$1.46 \cdot 10^4$
D	2.17	1.29

The two polymers differ both in their average molecular weight and polydispersity. PN(MEE) shows a broader spectrum of chain-lengths that appear less homogeneously distributed. PN(CF) has a low polydispersity index that would be expected from an ionic polymerisation pathway. Given the subsequent cross-linking step it is arguable that the absolute weight may not matter as much as long as homogeneous coatings can be formed.

The substitution pattern was investigated through matrix-assisted laser desorption/ionization (MALDI) time of flight (TOF) mass spectrometry. Figure 5.7 shows the mass per charge distribution as a broad spectrum of fragments. The highest molecular weights are found to be above 18 kDa and 14 kDa for PN(MEE) and PN(CF), respectively and are similar to the GPC measurements within the limitations of both techniques.

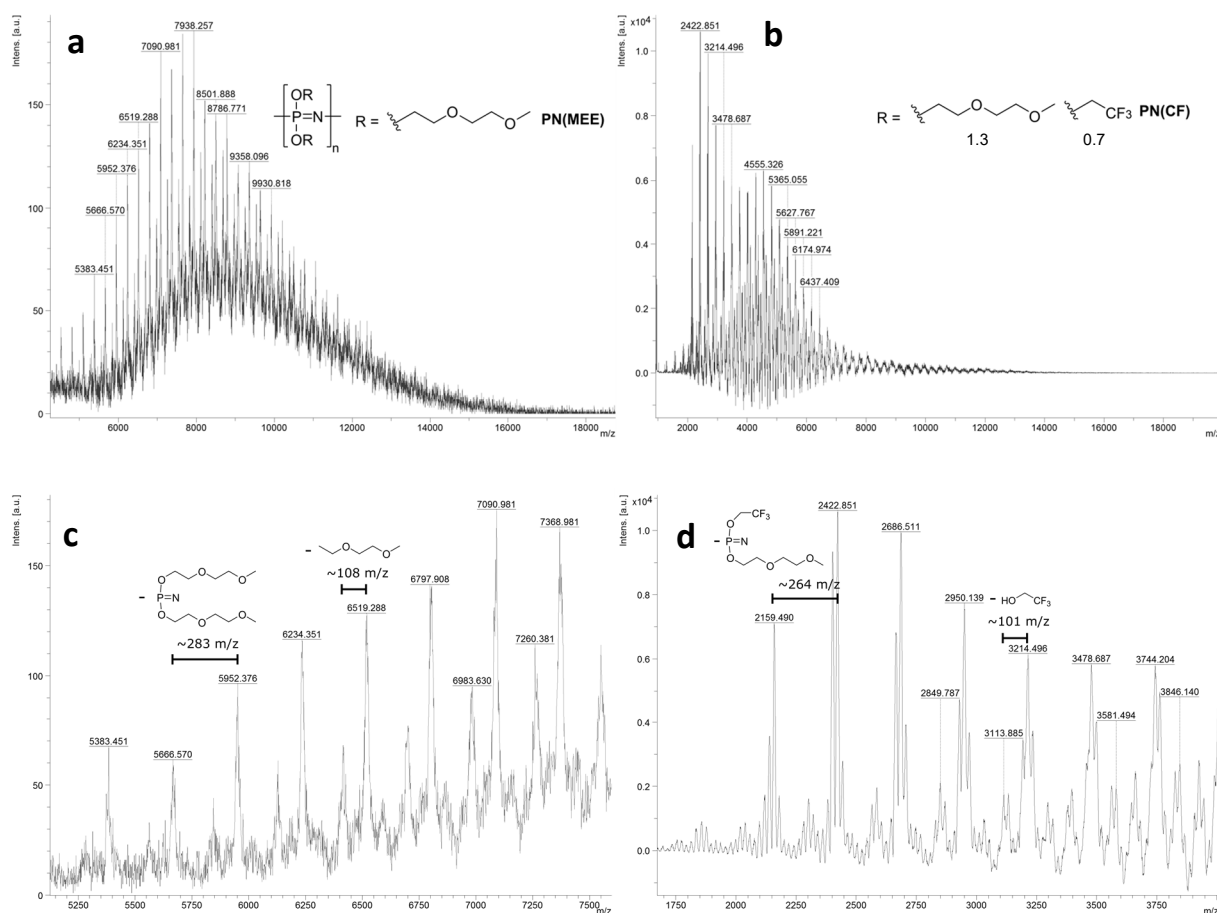


Figure 5.7: MALDI TOF mass spectra of a) PN(MEE) and b) PN(CF) with zoomed in excerpts of the respective spectra in c) and d) showing the fragmentation pattern and corresponding phosphazene fragments.

The major fragments detected from PN(MEE) (Figure 5.7c) are 283 m/z apart which corresponds to the mass of a disubstituted methoxy(ethoxy)ethoxy phosphazene unit. Minor steps of a difference of 108 m/z match the weight of one side-group. The PN(CF) substitution pattern in Figure 5.7d, shows a pattern with peaks 264 m/z apart matching the non-geminal substituted phosphazene with one of each side groups, the polyether and trifluoroethoxide. This is likely due to the steric demands of the alkoxy ether in the first substitution step as one would usually expect a geminal substitution pattern for phosphazenes substituted with alkoxides due to electronic factors. The minor peaks, with a weight difference of 101 m/z correspond to the loss of trifluoroethanol. At higher m/z ratios, the substitution pattern is inconclusive (Figure 5.7b), indicating a mix of phosphazenes substituted with different amounts of the two side-groups that have broad m/z ranges.

5.2.2 Coating Process onto the Thin-Film Electrode

Freshly prepared 10 wt% polymer solutions in toluene, with 2 wt% benzophenone used as a cross-linking reagent, were spin-coated onto 100 nm silicon thin-film electrodes on nickel-

coated copper substrates and subsequently cross-linked (copper substrate: CR Cu, see section 3.2.2.2, page 48 and section 3.2.5.1, page 59 for the comparison to the alternative GG Cu substrate). A photograph and SEM micrographs of the polymer-coated anode are shown in Figure 5.8.

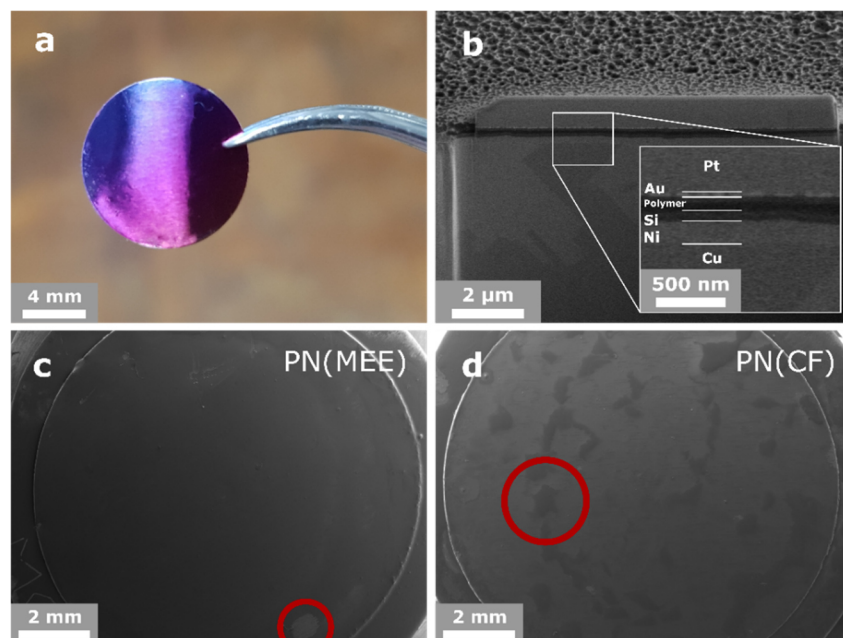
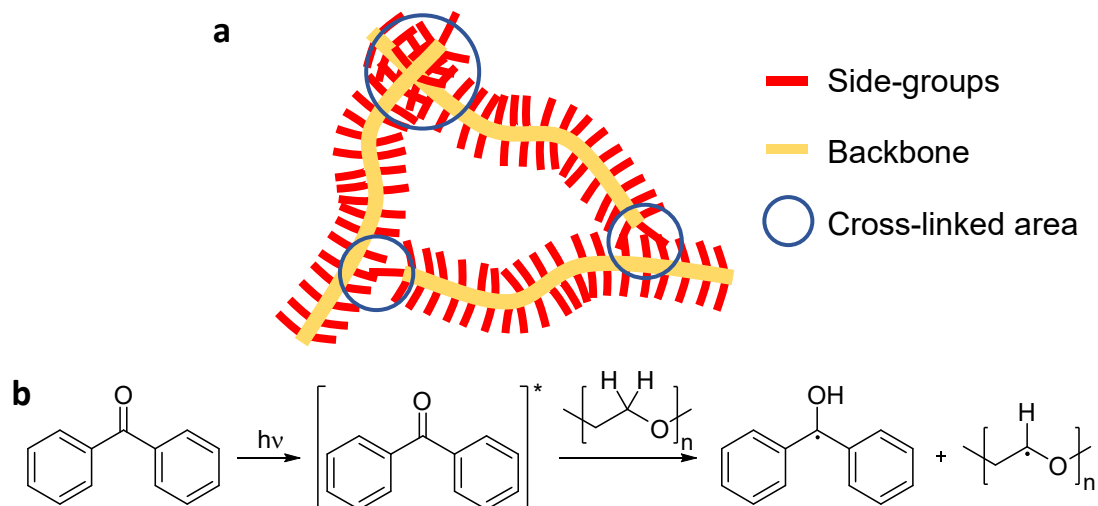


Figure 5.8: Photograph and SEM images of 100 nm *a*-Si thin-film anodes on Ni-coated CR Cu coated with PN(MEE) and PN(CF). a) Photograph of the glossy, polymer-coated electrode. b) FIB SEM cross section of the PN(MEE)-coated electrode that was sputter-coated with gold followed by the deposition of a platinum bar. c) PN(MEE)-coated electrode. The area with missing coating is circled. d) PN(CF)-coated electrode. The area with high contrast due to compositional variance is circled.

The polymer coating is transparent and evenly covers the anode with an apparent thickness of 100–200 nm in the FIB cross section (Figure 5.8b). However, since topological features from the copper substrate are filled with the polymer, the thickness of the coating varies across the anode. Nevertheless, there are very few defects in the PN(MEE) coating that would expose the electrode surface, any defects that are present are close to the edge of the anode (Figure 5.8c). The PN(CF) coating, on-the-other-hand, shows areas of different contrast in Figure 5.8d. These are believed to form during the drying process, as polymers with different side-groups phase segregate with the darker areas resembling the PN(MEE) coating.

Cross-linking of the linear polymer was achieved through a radical-initiated mechanism.^[208] The procedure is similar to that described by Wiemhöfer *et al.* for their poly(phosphazene) gel electrolytes.^[121,122] Coated electrodes were exposed to UV radiation (low pressure Hg, 450 W) for 15 minutes. During the exposure, benzophenone, through an excited state, abstracts a proton

from the methoxy(ethoxy)ethoxy side chain and creates a radical. The carbon radicals can then recombine to form carbon-carbon bonds between the poly(phosphazenes) side-groups. A scheme of the cross-linked product and the radical formation mechanism are shown in Scheme 5.2.



Scheme 5.2: a) Depiction of the assumed structure of the cross-linked polymers; b) mechanism of the UV induced radical formation of the ethylene glycol side-chains with benzophenone.^[209]

Coated and cross-linked anodes were left in a vacuum oven at 100°C for a couple of hours to remove any remaining solvent or water. However, while benzophenone has a low melting point, it also has a low vapour pressure both as a solid and liquid and therefore it is likely to remain in the polymer after the drying process.^[210] As a redox active molecule, it may add irreversible capacity during discharge and be incorporated into the SEI, however, no measures were taken to remove the material due to the small total amount expected to be present in the final material.

Anodes coated with the polymers show a significant difference in wettability (Figure 5.9). The PN(MEE) coating shows a larger water contact angle (WCA) of 85.2° than the pristine thin-film with a contact angle of 68.3°, while the PN(CF) coating appears almost hydrophilic with a much smaller WCA of 12.0°.

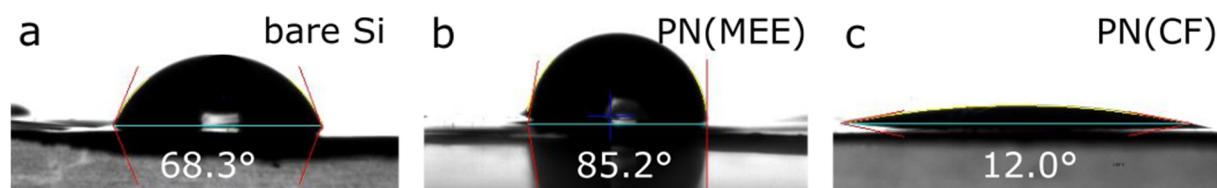


Figure 5.9: Water contact angles measured for the a) bare, b) PN(MEE)-coated and c) PN(CF)-coated silicon thin-film anodes.

One would expect the fluorinated polymer to show a larger WCA. The observed angles may not be due to the chemical composition but the degree of cross-linking as the PN(CF) coating is still sticky to the touch after UV radiation. Cross-linking appears to be more efficient for the polymer with pure poly-ether side-groups, which may reflect the availability of C-H bonds, to react with the radical, present in the polymer.

5.2.3 Electrochemical Performance

The coated anodes were deployed in lithium half-cells with LP30. Cells were cycled galvanostatically to a 100 mV cut-off voltage at a rate of $\sim C/5$. Figure 5.10 shows the electrochemical performance of the coated electrodes and the bare electrode.

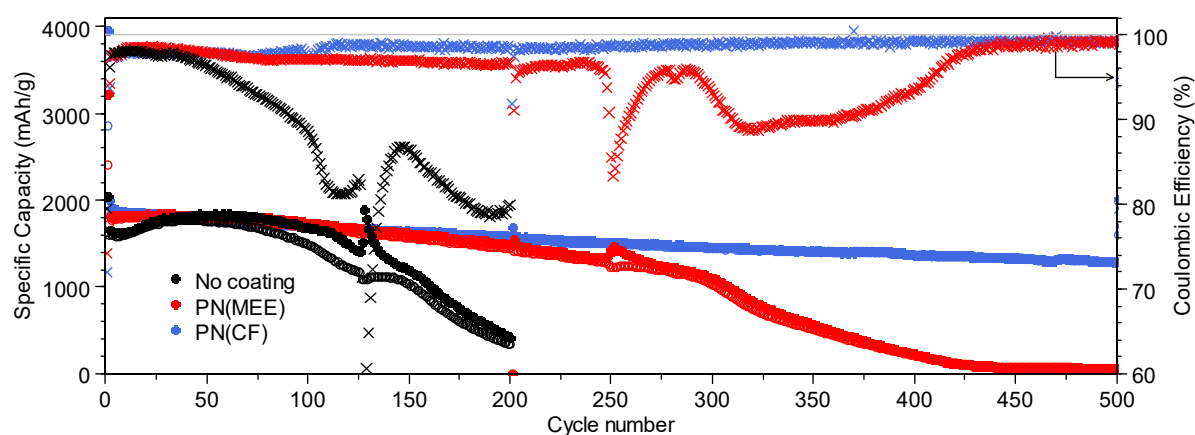


Figure 5.10: Electrochemical performance over 500 cycles of 100 nm *a*-Si thin-film anodes on Ni-coated CR Cu bare, and coated with PN(MEE) or PN(CF). The cells containing a polymer coating were restarted after 200 cycles. Filled symbols: lithiation; empty symbols: delithiation; **x**: Coulombic efficiency; rate: 1st C/30, 2nd+ C/5; cut-off voltage: 1st 5 mV, 2nd+ 100 mV.

The polymer coatings elongate the cycle life of the electrode greatly. While the untreated electrode shows poor performance and quickly degrades just after 100 cycles, the lifetime is more than doubled by the deposition of a PN(MEE) coating and further extended by using PN(CF), achieving more than 500 cycles without failing. The key values of each electrodes' electrochemistry are listed in Table 5.2.

Table 5.2: Figures from the cycling data of the 100 nm *a*-Si thin-film electrode on Ni-coated CR Cu without a coating and coated with PN(MEE) and PN(CF).

Cycle	1 st			2 nd		100 th			300 th		
	Charge mAhg ⁻¹	Discharge mAhg ⁻¹	CE %	Charge mAhg ⁻¹	CE %	Charge mAhg ⁻¹	CE %	Ret* %	Charge mAhg ⁻¹	CE %	Ret* %
-	1625	2045	79.4	1595	96.2	1491	88.6	93.5	-	-	-
PN(MEE)	2396	3229	74.3	1717	94.3	1689	97.1	98.4	1028	93.1	59.6
PN(CF)	2853	3961	72.0	1875	93.7	1682	97.6	89.7	1446	98.9	77.2

*Capacity retention relative to the second cycle

The cycling data shows that all films experience a very high irreversible capacity loss (ICL) in the first cycle but it must be noted that the polymer layers induce larger ICLs, as they may contain benzophenone and solvent impurities, such as water, that can decompose during the first cycle.

In addition, the data shows that the CE is lowest for the PN(CF)-coated electrode, and highest for the PN(MEE)-coated electrode during the first 50 cycles. The efficiency then decreases quickly for the uncoated sample, while the PN(MEE) sample reaches 97.1% and PN(CF) reaches 97.6% by the 100th cycle. From the 300th cycle onwards, the PN(CF)-coated electrode shows CE of 99% and above, exceeding the maximum values achieved for the other electrodes.

Regarding capacity, the control sample without a coating shows an increase in capacity over the first 60 cycles, where it reaches a maximum before subsequently decreasing (see earlier discussion in Chapter 2). The PN(MEE)-coated electrode shows a similar trend with a slight increase in capacity, reaching a maximum at cycle 75. However, the PN(CF)-coated electrodes show a slow and steady decrease in capacity from the second cycle onwards. Nonetheless, capacity retention is similar over the first 200 cycles for the coated electrodes but before the “dip” in capacity for the PN(MEE)-coated electrode that occurs on the 300th cycle, PN(CF) shows a ~17% higher capacity retention.

Figure 5.11 shows the voltage profiles and differential plots for the 1st, 10th and 100th cycle of the three electrodes.

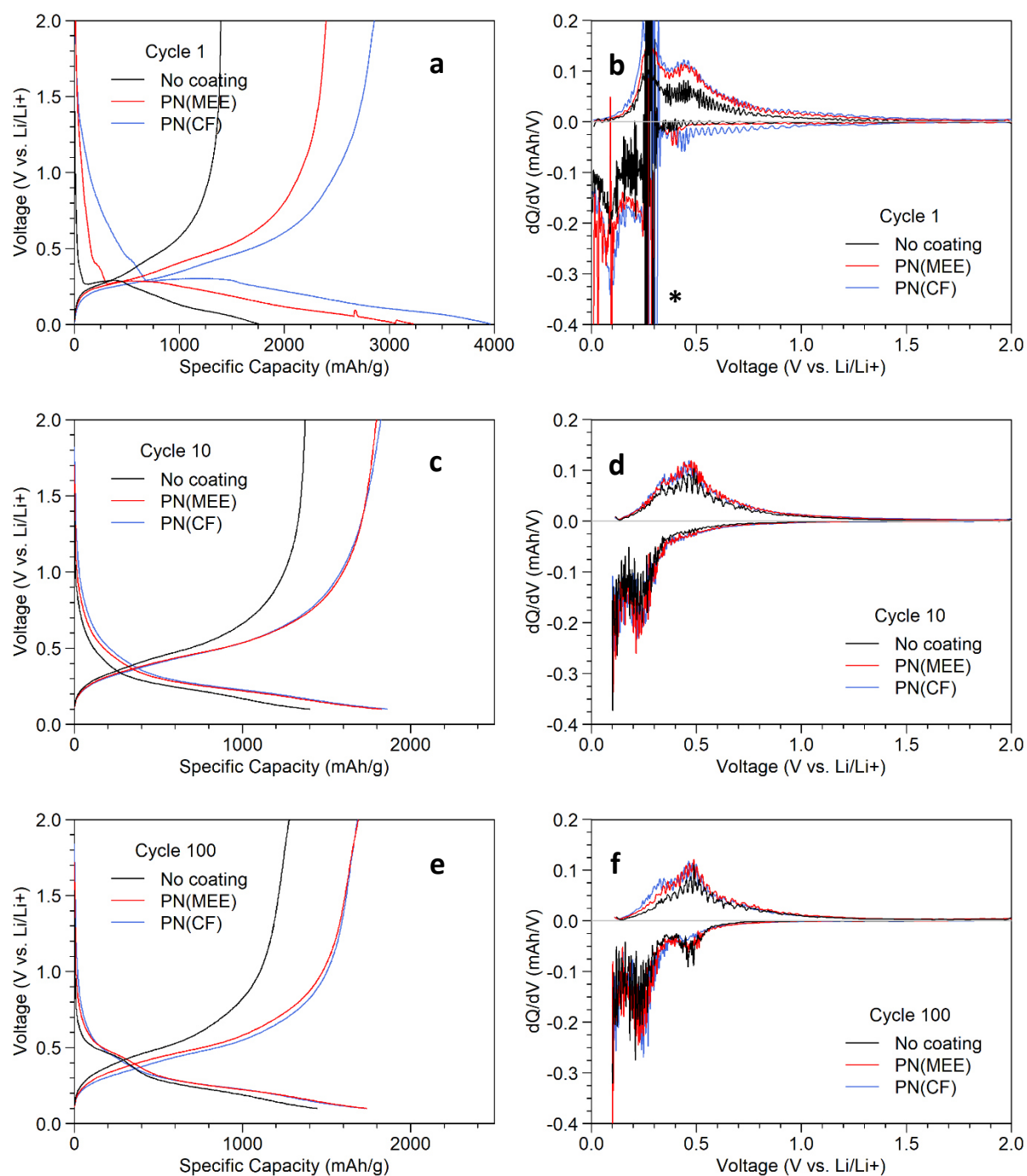


Figure 5.11: Voltage profiles (a, c, e) and differential plots (b, d, f) of 100 nm *a*-Si thin-film anodes on Ni-coated CR Cu without a coating, and PN(MEE) and PN(CF) coatings. a-b) 1st cycle, c-d) 10th cycle and e-f) 100th cycle. Rate: 1st C/30, 2nd+ C/10; cut-off voltage: 1st 5 mV, 2nd+ 100 mV. *The electrochemical process showing a positive sloping during the discharge process in the 1st cycle obstructs parts of the dQ/dV charge plot. The significant features are still visible.

In the first cycle the PN(CF)-coated electrode shows the most electrochemical activity of the samples at higher voltages >0.5 V and distinct process at ~ 0.45 V which relate to SEI formation and other surface reactions. All cells show the typical plateau at 0.3 V as discussed in Chapter 3 on page 47. Deducting the capacity going into the processes before reaching the pseudo-plateau, both polymer-coated electrodes show equal capacity in the silicide formation.

The voltage profiles of the 10th cycle (Figure 5.11c-d), look alike for the polymer-coated electrodes. The reference lacks in capacity at this point. On the 100th cycle, the cycling profile and differential plots appear similar for the reference and PN(MEE)-coated electrodes, indicating similar reactivity of the material. We see less of the surface-specific electrochemical process at ~ 0.45 V for the PN(CF)-coated electrode (Figure 5.11f), suggesting a more passivating effect of the coating.

In addition, it was observed that decreasing the cut-off voltage to 40 mV for the PN(CF)-coated electrode after 500 cycles led to an increase in capacity. However, restarting the cell cycling after 500 cycles led to an increase in capacity. However, restarting the cell cycling after 50 cycles at the new cut off voltage after a rest of 3 days, showed the typical degradation profile after a further 15 cycles (Figure 5.12).

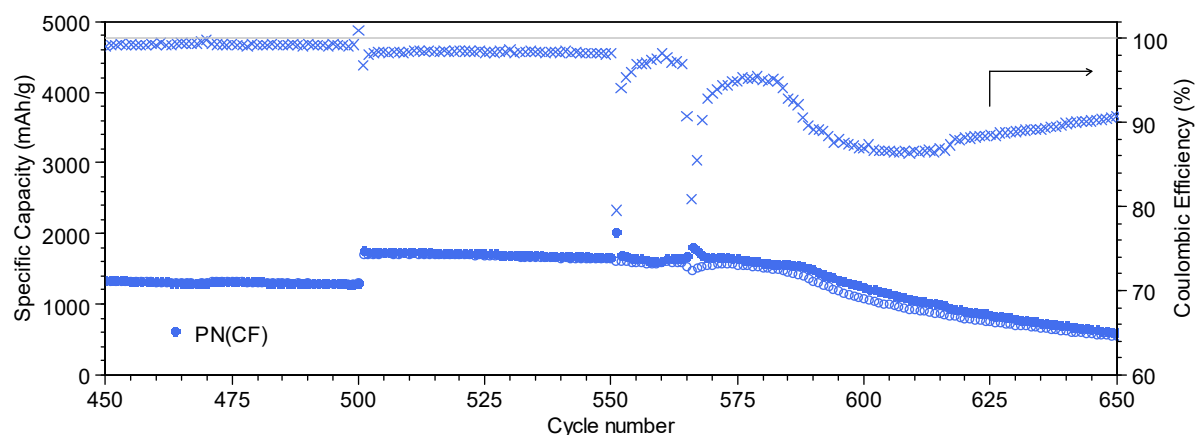


Figure 5.12: Electrochemical performance of the PN(CF)-coated 100 nm *a*-Si thin-film electrode on Ni-coated CR Cu after lowering the cut-off voltage from 100 mV to 40 mV on the 500th cycle and restarting after resting on the 550th cycle for 3 days. Filled symbols: lithiation; empty symbols: delithiation; x: Coulombic efficiency; rate: C/5; cut-off voltage: 100 mV, 500th+ 40 mV.

It appears, that the lower cut-off voltage and resting disturbs the system in a way that the anode loses its ability to cycle reversibly. The CE decreases from 99% to 98% after lowering the cut-off voltage and the characteristic “dip” in efficiency is seen from the 560th cycle, indicating delamination and loss of electrical contact. The peaks found in the dQ/dV spectra of the polymer-coated electrodes are shown in Figure 5.13 over the lifetime of the cell.

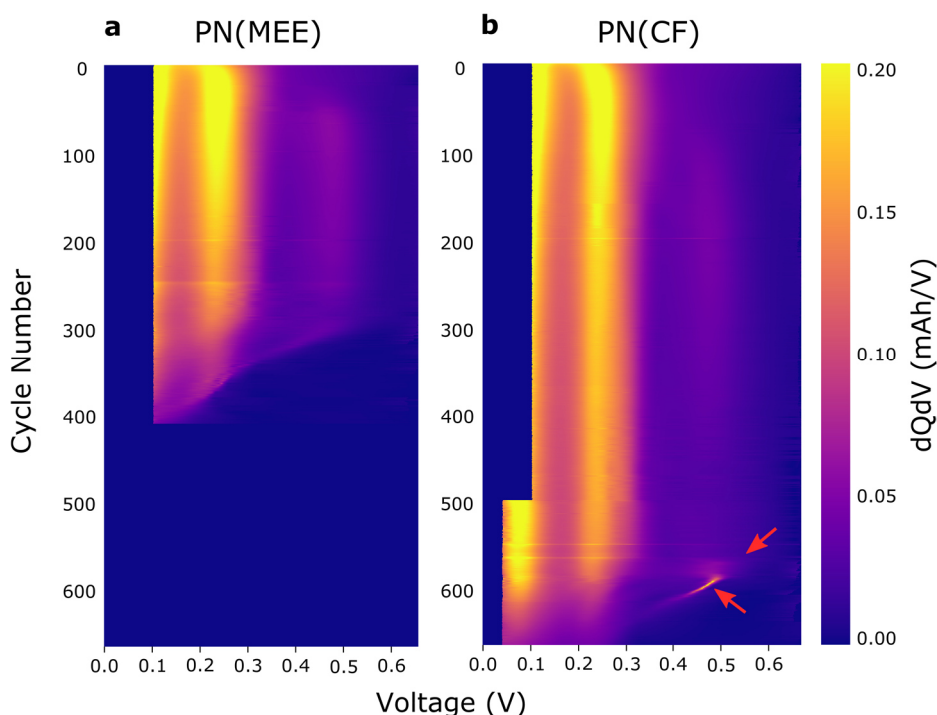


Figure 5.13: Maps of the intensities of the electrochemical processes observed in the dQ/dV discharge plots below 650 mV for the 100 nm *a*-Si thin-film anodes on Ni-coated CR Cu coated with a) PN(MEE) (400 cycles) and b) PN(CF) (650 cycles).

The Li_2Si formation is seen at ~ 0.25 V and $\text{Li}_{3.5}\text{Si}$ at ~ 0.1 V in Figure 5.13. Both processes decrease in intensity with an increasing number of cycles, fading towards the end of the anodes' lifetimes. In Figure 5.13b, the Li_2Si peak appears particularly stable between the 200th and 500th cycle until the cut-off voltage is changed. The peak broadens as the $\text{Li}_{3.5}\text{Si}$ phase is accessed.

The process at ~ 0.45 V is visible in Figure 5.13a after 50 cycles and stays and fades towards the end. In Figure 5.13b, the process only appears after 100 cycles and decreases in intensity towards the 500th cycle. Marked by the red arrows in Figure 5.13b, restarting after a 3 d rest on the 550th cycle, the process increases in capacity and, the process becomes sharper and shifts towards lower voltages on the “dip”, while both the Li_2Si and $\text{Li}_{3.5}\text{Si}$ peaks fade.

Figure 5.14 shows the changes in voltage and height of the first lithiation peak and the small peak at ~ 0.45 V over the duration of cycling, highlighting the changes around “dips” in CE.

The reference sample has been discussed in section 3.2.2.2 on page 73. We have observed a slow increase in capacity and voltage of the Li_2Si peak in the early cycles followed by both values dropping until reaching the characteristic “dip”, after which both values will decrease. The second significant decrease in CE observed in the sample in pure LP30 (process ‘iv’, see section 3.2.2.2), is not observed for the polymer-coated electrodes.

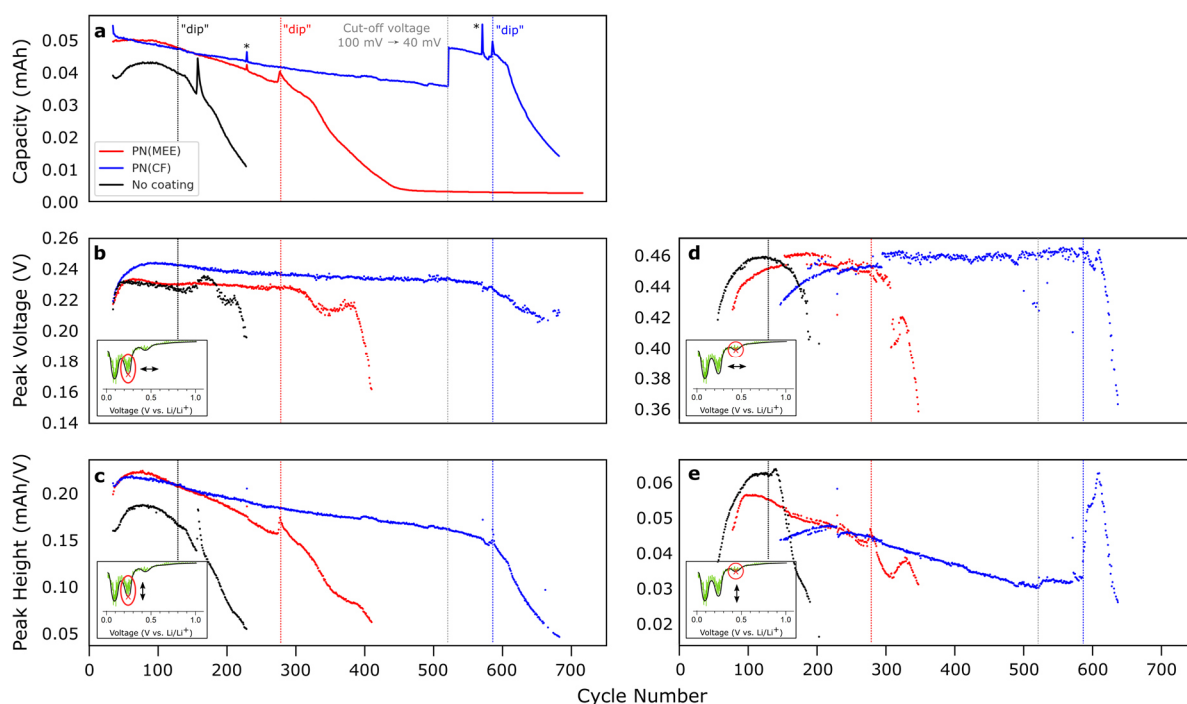


Figure 5.14: Capacity (a) and voltage and height of the Li_2Si (b-c) and electrochemical process at ~ 0.45 V (d-e) dQ/dV peaks of the cells cycled with and without PN(MEE) or PN(CF). The vertical lines mark the characteristic “dips” in efficiency. The insets show the peak positions in a typical dQ/dV plot for clarity.

The PN(MEE) coating shows a similar rise in Li_2Si peak potential and intensity which decreases PN more slowly. During the “dip” we see the expected increase in capacity, the voltage however does not change until 25 cycles later, when both the voltage and capacity drop.

The PN(CF)-coated anode shows a much earlier onset of lithiation, at voltages above 0.24 V which is above all other reported values in this thesis, including the samples cycled with VC and FEC (see section 4.2.2.1, Figure 4.8 on page 96). The peak height shows a much flatter decay and increases less during the first few cycles (Figure 5.14c).

The process discussed as being surface-specific in section 3.2.3 on page 55, shows a maximum voltage of 0.46 V for all three electrodes in Figure 5.14d. We can think of the process as an indicator of the exposed silicon surface area to the electrolyte. Hence, the voltage increases depending on how the samples crack and structurally evolve to expose more silicon surface. It will then decrease after the “dip” when delamination leads to the freshly-exposed surface being covered in SEI, hindering electron transfer for further lithiation and electrolyte degradation.

The bare anode shows a large peak height of the process at 0.46 V that quickly fades after the “dip” similar to its peak voltage. The PN(MEE)-coated electrode shows a similar, sharp, but delayed rise of the process. It then fades more slowly than observed for the reference.

PN(CF) is unique in the trends observed. We detect the process later and observe that it slowly increases in peak height and fades to very low values. Upon changing the voltage cut-off, the processes peak height is increased. We observe a decrease in the CE during these cycles. Upon resting for three days and restarting the cell, the peak height shoots up. This clearly indicates that a large area of silicon surface is now exposed to the electrolyte. The peak is very sharp (as seen in Figure 5.13), meaning that the process is occurring almost unhindered.

Lastly, we investigate the irreversible capacity loss over time as a measure of irreversible reactions with the lithium ions in Figure 5.15

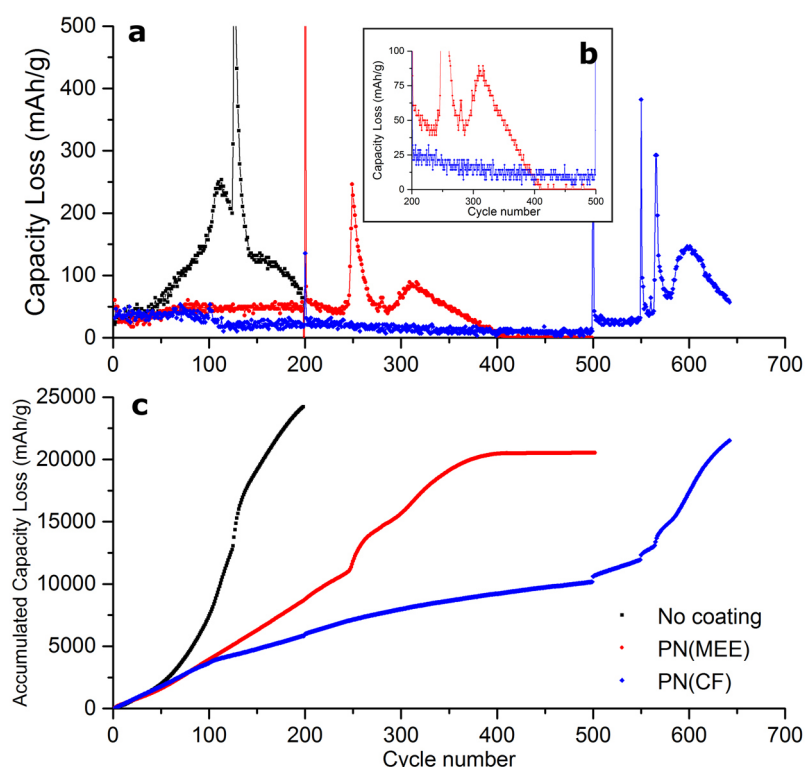


Figure 5.15: a) Capacity loss per cycle for cells with 100 nm *a*-Si thin-film anodes on Ni-coated CR Cu without a coating and PN(MEE) and PN(CF) coatings. b) Inset showing the capacity loss between the 200th and 500th cycle. c) Accumulated capacity loss over 700 cycles.

The cell bearing the silicon thin-film anode reaches incredibly high losses by the 200th cycle of 23932 mAhg⁻¹. The largest increases are observed after the “dip” (Figure 5.15b). The polymer coatings will show similar increases after the individual “dips” in efficiency. The PN(MEE)-coated electrode shows a constant consumption of lithium with ~50 mAhg⁻¹ being lost per cycle before the dip. The PN(CF)-coated electrode shows to consume the least amount of lithium with an accumulated loss of only 10171 mAhg⁻¹ before decreasing the voltage cut-off on the 500th cycle. After 100 cycles, as seen in the CE, lithium is consumed less.

5.2.4 Electron Microscopy and Energy-Dispersive X-ray Spectroscopy

SEM micrographs of the PN(MEE)- and PN(CF)-coated electrodes after 500 and 525 cycles, respectively, are shown in Figure 5.16 in comparison to the bare electrode after 200 cycles.

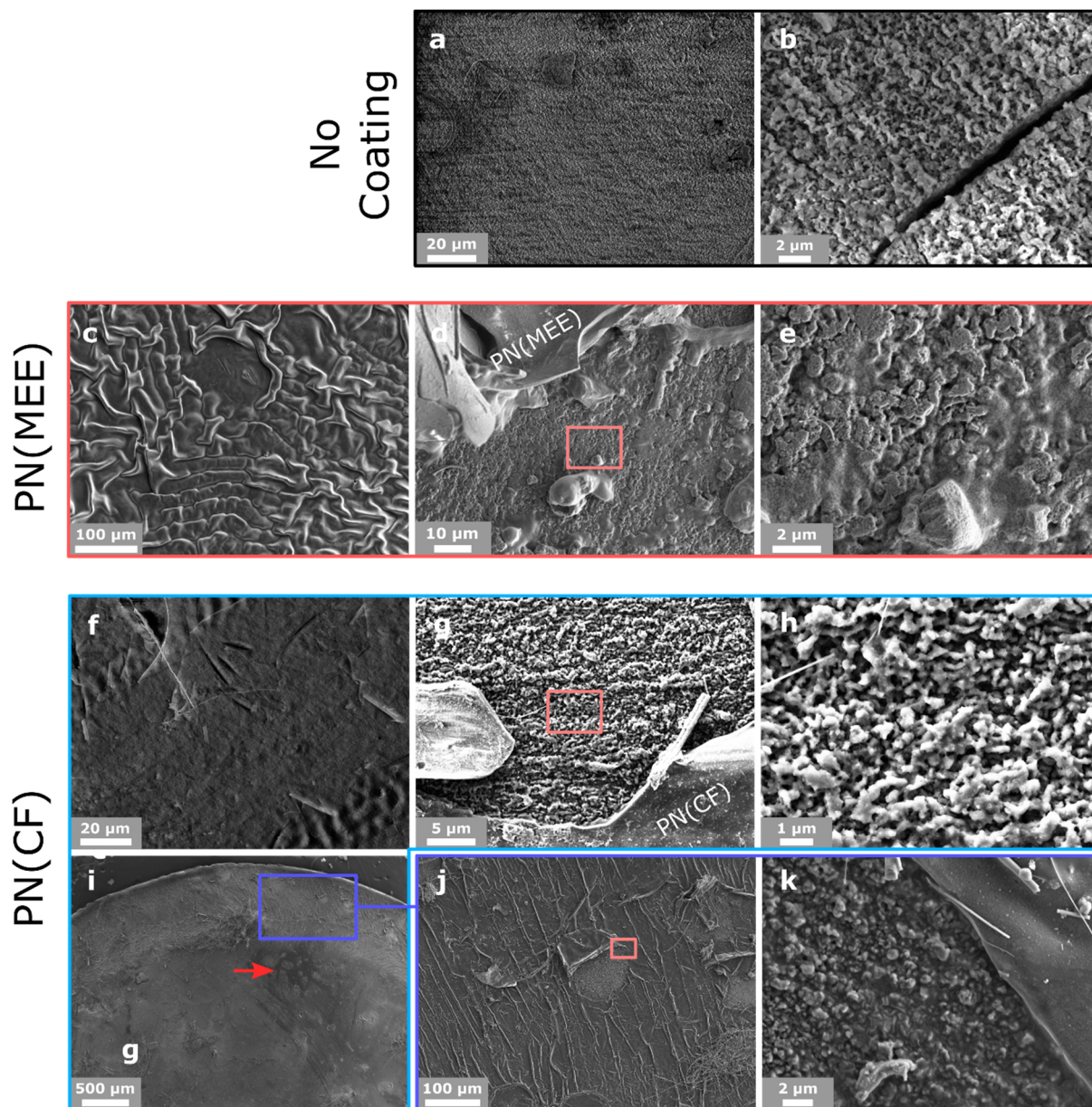


Figure 5.16: SEM micrographs of the cycled 100 nm *a*-Si thin-film anodes on Ni-coated CR Cu with and without poly(phosphazene) coatings. a-b) Electrode without a coating after 200 cycles. c-e) Surface, peeled of area and the Si/SEI material of the PN(MEE)-coated electrode (500 cycles). f-h) Surface, peeled of area and the Si/SEI material of the PN(CF)-coated electrode (525 cycles) i-k) Overview, peeled of area and the Si/SEI material near the edge of the PN(CF)-coated electrode. The arrow marks an area of different contrast. The magnified areas e), h) and k) are highlighted in d), g) and j), respectively.

At the time of disassembly for SEM analysis, the anode coated with PN(CF) was still functional after 525 cycles with a capacity retention of >70%, while the other samples were at the end of their cycle life.

The cycled bare electrode shows a microscopically flat surface of the Si/SEI material that adopts the microscopic features of the current collector and shows a grainy nanostructure (Figure 5.16a-b) which was discussed in more detail in section 3.2.2.3. In contrast, the PN(MEE) coating appears wrinkled after cycling (Figure 5.16c) and in areas where the polymer was peeled off, an amorphous Si/SEI material is seen (Figure 5.16d-e) that is structurally distinct to the one observed in Figure 5.16b. The morphology showed larger, flatter, grainy agglomerates partially covered by a space-filling substance. In a similar manner, the PN(CF) coating after cycling appears even flatter (Figure 5.16f) than that observed for PN(MEE) and moreover, the underlying Si/SEI material shows much finer grain-sizes and even distinct pin holes in the material. Areas near the edge of the electrode appear wrinkled with a flattened Si/SEI structure underneath (Figure 5.16i-k). This could be caused by a marginally thicker coating near the edge from the spin-coating process or from seeping of the electrolyte into the electrode from the uncoated edges. The other major region is assigned to those of a different contrast, previously shown in Figure 5.8d that remain after cycling.

Figure 5.17 shows the blade-cut cross section of the coated and cycled anodes.

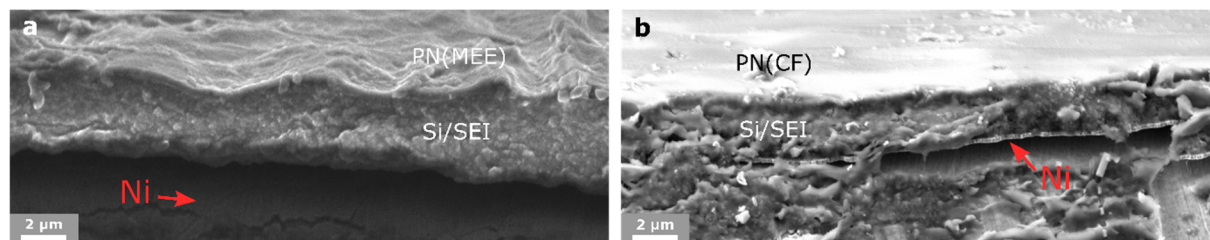


Figure 5.17: SEM micrographs of the blade-cut cross section of the 100 nm *a*-Si thin-film anodes on Ni-coated CR Cu coated with a) PN(MEE) after 500 cycles and b) PN(CF) after 525 cycles.

The cross section of the PN(MEE) electrode (Figure 5.17a) shows a Si/SEI mix about twice as thick as that underneath the PN(CF) coating (Figure 5.17b). Moreover, the nickel layer is physically bent down with the copper substrate, away from the Si/SEI material in Figure 5.17a, while in Figure 5.17b it remains connected to the Si/SEI material and peels off from the copper substrate. SEM micrographs of the FIB cross sections of the electrodes are shown in Figure 5.18.

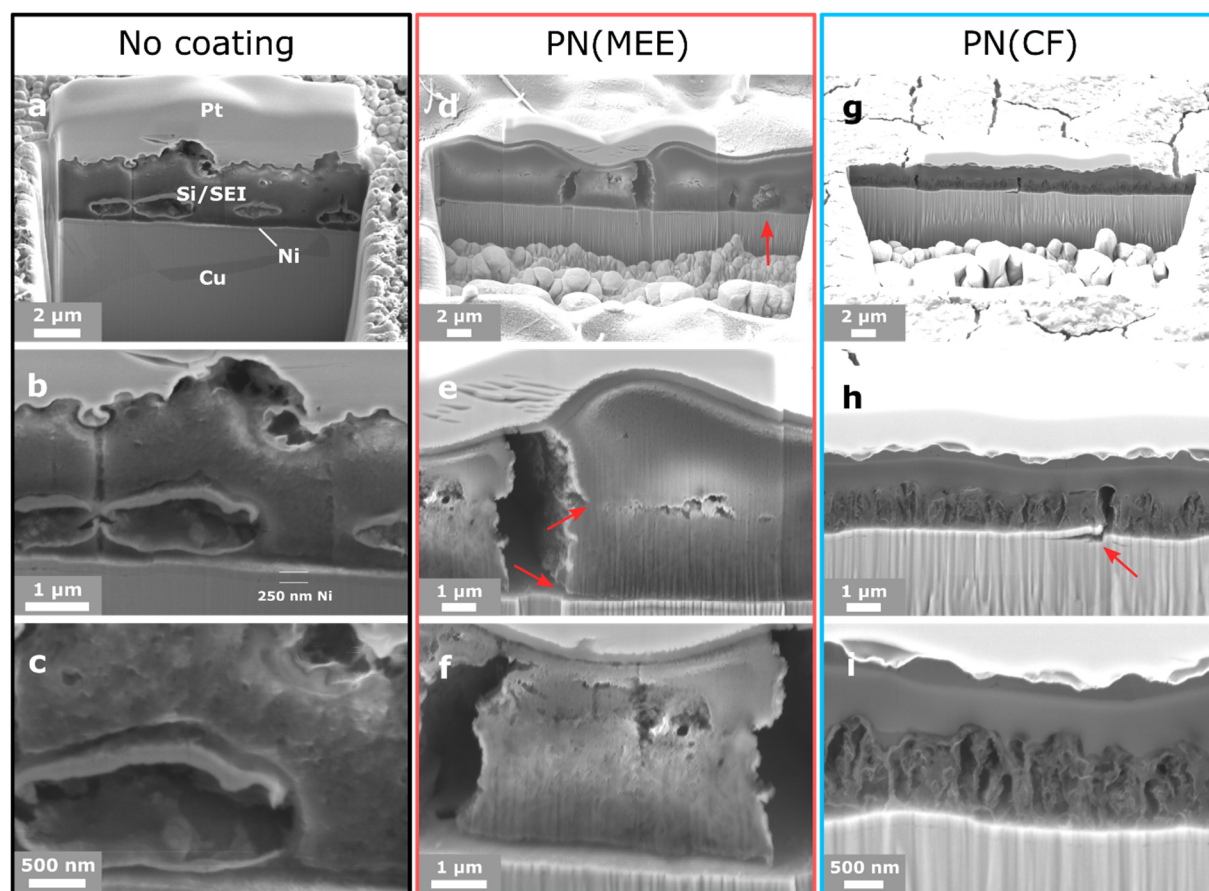


Figure 5.18: SEM micrographs (10 kV) of the FIB cross section of the 100 nm *a*-Si thin-film anodes on Ni-coated CR Cu with and without poly(phosphazene) coatings. a-c) Electrode without a coating after 200 cycles. The individual layers observed for the cross sections are labelled in a). d-f) PN(MEE)-coated electrode after 500 cycles showing a thin polymer coating on a thick SEI on the Si/SEI material. The arrow in d) shows a pocket where electrolyte was presumably trapped. The arrows in e) show the change in texture between the top SEI layer and the Si/SEI material and the delamination from the nickel interlayer. g-h) PN(CF)coated electrode after 525 cycles showing silicon strands covered by a smooth polymer/SEI layer. The arrow in h) shows the nickel interlayer staying attached to the Si material, delaminating from the current collector. The surfaces were coated with gold and a platinum bar was deposited on the FIB milling site. Images were recorded at an angle of 53°.

The bare and PN(MEE)-coated electrodes have accumulated significant amounts of SEI (Figure 5.18a-f) and show delamination from the current collector upon exposure to the electron beam. Similar to the findings in the blade-cut cross sections, the healthy PN(CF)-coated electrode stays attached to the nickel interlayer which delaminates instead from the current collector, highlighted in Figure 5.18h.

The Si/SEI material formed from the bare electrode appears grainy but similar over the entire cross section. Large pockets of electrolyte entrapped by the amorphous Si/SEI material can be observed in Figure 5.18b and are also found in the PN(MEE)-coated Si/SEI material (highlighted in Figure 5.18d).

The PN(MEE) coating shows to have swollen slightly into a 200–300 nm thick layer that covers an undulating 1–4 μm layer of additional SEI that is distinguishable from the 2 μm Si/SEI material on the current collector. The interphase between the material and excess SEI is relatively consistent over the cross section in Figure 5.18d and appears to charge from the electron beam more than the rest of the material. The behaviour is similar to the charging observed in the upper region of the material formed on the bare electrode in Figure 5.18a. As the material dries out under the electron beam, the large gaps in the material (Figure 5.18f) are observed to widen.

The PN(CF) polymer appears to have merged into a <1 μm thin SEI layer covering a 1 μm thick silicon layer. The top layer has cracked after the sputter coating with gold showing large cracks of high contrast on the surface. Beneath, the silicon appears as strands stretched between the nickel base layer and the polymer/SEI material (Figure 5.18i). The strands are less than 100 nm wide in parts but appear to be interconnected. It further appears, that a rough material is located on the polymer surface, potentially SEI or electrolyte that escapes the polymer layer upon drying.

To connect the observed morphology with the chemical composition of the individual regions, Figure 5.19 shows the EDS element mapping for the cross sections. Only the area in between platinum or gold and the nickel interlayer is analysed, for reasons discussed in section 3.2.5.3, page 64. The spectra for the LP30 sample have been discussed in more detail in the same section in regard to Figure 3.17 from page 57 onwards.

The PN(MEE) coating covers a layer of oxygen, carbon and fluorine-rich SEI, which is clearly separated from silicon-rich Si/SEI material underneath it (Figure 5.19b). The bulk shows high electron counts for phosphorus, indistinguishable from the polymer. This is likely to arise from the decomposition of the hexafluorophosphate anion present in LP30 given the low atomic percentage of phosphorus in the polymer, itself.

The PN(CF) coated electrode (Figure 5.19c) shows similar elemental distributions, with silicon being located closer to the current collector, found in higher concentration where the micrographs show the lacy silicon structure. However, due to the intensity of the nickel signal, the mapping of the lighter elements closer to the current collector is difficult. The micrographs show a very high phosphorus concentration in the top-layer which may again be a combination of the polymer and hexafluorophosphate decomposition products.

Nickel is seen best where the lacy Si structure in Figure 5.19c allows the penetration of the electron beam. The material in Figure 5.19b appears to block the beam most.

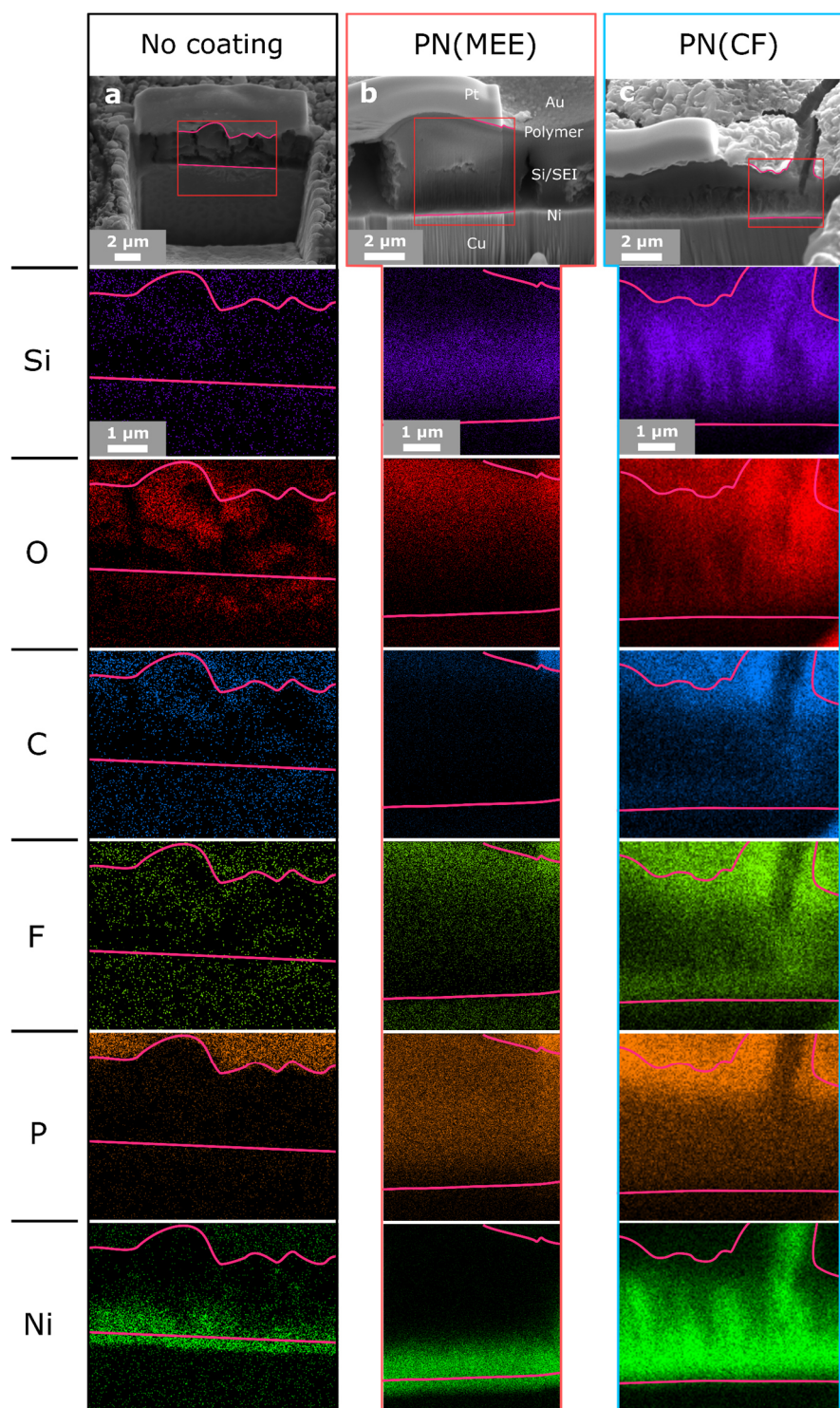


Figure 5.19: SEM micrographs and EDS element maps (15 kV) of the FIB cross section of the 100 nm *a*-Si thin-film anodes on Ni-coated CR Cu without and with poly(phosphazene) coatings. a) Electrode without a coating after 200 cycles. b) PN(MEE) coating after 500 cycles. c) PN(CF) coating after 525 cycles. The surface was coated with Au and Pt was deposited on the site for FIB milling. The highlighted areas in the micrographs correspond to the EDS element maps with marked borders enclosing the area between the platinum bar and the nickel interlayer. Micrographs were recorded at an angle of 53°.

5.2.5 Synergies of the PN(MEE) Coating with Electrolyte Additives

As the polymer is permeable to the liquid electrolyte, additives that have been reported to improve the cyclability of the thin-film electrode, FEC and VC, were tested in cells containing silicon thin-film electrodes coated with PN(MEE) for their synergistic effects. Unfortunately, the better-performing PN(CF) coating had not been developed at the point of testing and is not part of the analysis. The electrochemical performance of the cells is presented in Figure 5.20.

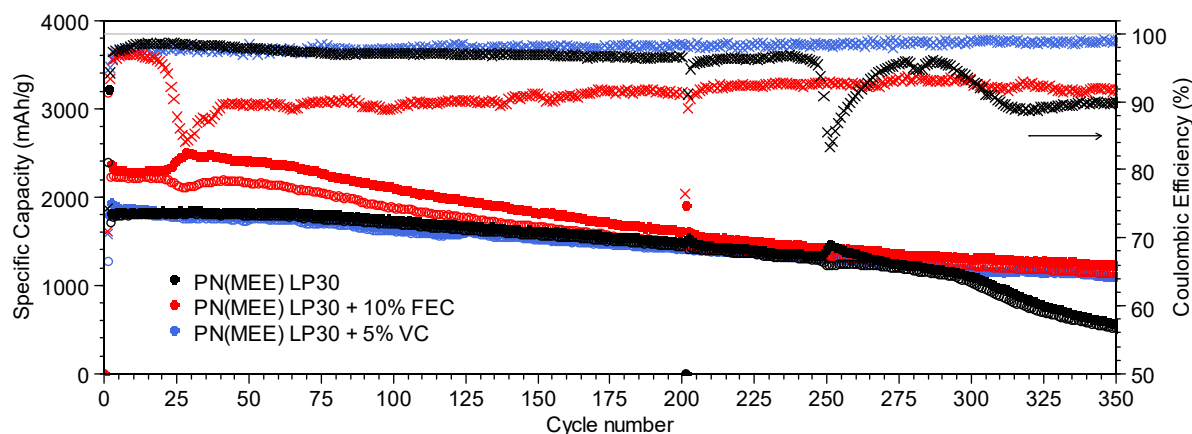


Figure 5.20: Electrochemical performance over 350 cycles of the 100 nm *a*-Si thin-film anodes on Ni-coated CR Cu coated with PN(MEE) with different electrolytes: pure LP30, LP30 + 10% FEC, LP 30 + 5% VC. Cycling was restarted after 1 d rest at 200 cycles. Filled symbols: lithiation; empty symbols: delithiation; x: Coulombic efficiency; rate: 1st C/30, 2nd+ C/10; Cut-off voltage: 1st 5 mV, 2nd+ 100 mV.

Unsurprisingly, both additives extend the cycle-life compared to the cell with pure LP30. However, adding FEC causes a “dip” in CE to below 90% after only 20 cycles which recovers to only 92% after 200 cycles. Moreover, the cell shows a significant capacity fade that plateaus after 250 cycles. The cells actual specific capacity may not be higher than that of the other samples for reasons discussed in Chapter 3, section 3.2.1. The capacity retention when adding FEC over 300 cycles is the poorest of the three cells.

The addition of VC yields an extended cycle life compared to the electrode cycled in pure LP30 whilst showing similar electrochemical behaviour. The CE is slightly worse over the first 60 cycles when compared to the control, but the VC sample reaches 99% by the 300th cycle. The system without the polymer in Chapter 4 (see Figure 4.5), shows better performance, but consisted of an electrode on a different substrate under different cycling conditions. One noticeable difference is that we do not observe the efficiency “dips” present in the absence of a polymer layer.

The capacity loss over time is shown in Figure 5.21. The irreversible capacity loss for FEC is largest from the start, seen in Figure 5.21b, and increases at a highly accelerated rate after 25 cycles. By the 400th cycle a total irreversible capacity loss of 58054 mA_hg⁻¹ has accumulated, more than twice the 20461 mA_hg⁻¹ observed at this point for the coated anode cycled with pure LP30. The cell with 5% VC in the electrolyte initially starts off at higher lithium consumption than that with pure LP30 but will only have consumed 9218 mA_hg⁻¹ by the 375th cycle.

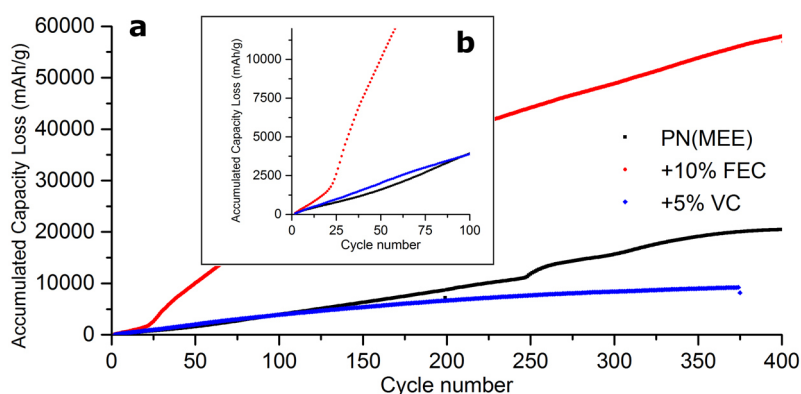


Figure 5.21: a) Accumulated capacity loss in cells with PN(MEE)-coated with 100 nm *a*-Si thin-film anodes on Ni-coated CR Cu cycled in pure LP30, LP30 +10% FEC and LP30 + 5% VC electrolytes. b) Inset showing the accumulated capacity loss over the first 100 cycles.

Similar to the electrodes studied with additives in the absence of a polymer coating in Chapter 4, the cells were analysed and disassembled before reaching the point of failure. Electron micrographs of the electrode surfaces after cycling are shown in Figure 5.22.

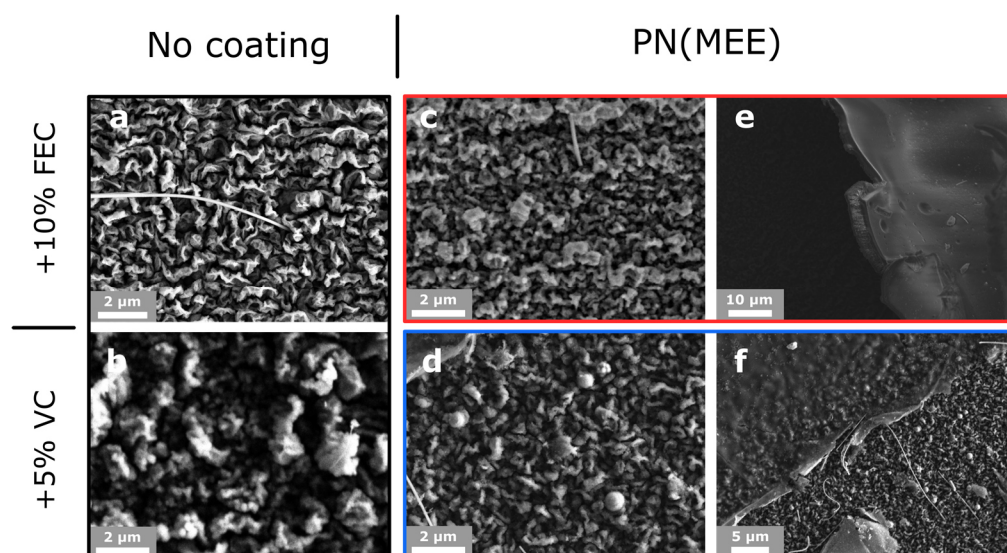


Figure 5.22: SEM micrographs of cycled 100 nm *a*-Si thin-film anodes on Ni-coated CR Cu in LP30 and a) 10% FEC (200 cycles), b) 5% VC (200 cycles), c) 10% FEC underneath the PN(MEE) coating (400 cycles), d) 5% VC underneath a PN(MEE) coating (375 cycles). e) Peeled-off PN(MEE) (10% FEC sample), f) partially peeled-off PN(MEE) (5% VC sample).

The structures observed in Figure 5.22c-d are similar to the surfaces formed without a polymer coating. Addition of FEC causes the formation of a lamellar anode structure with more diffuse edges, compared to the uncoated sample. However, with VC, the surface under the polymer appears less grainy with finer cracks in a more porous surface. This is not dissimilar from the surface observed for the PN(CF)-coated electrode. We do not observe separated, large silicon islands that were present on the anode cycled with VC but without the polymer coating (section 4.2.2.2 in Figure 4.11 and Figure 4.12, found on page 98 onwards).

Peeling off the coating in the VC sample reveals a thin polymer layer overlaying the porous fine-structure (Figure 5.22f) while in the FEC sample, in Figure 5.22e, there is a $\sim 2 \mu\text{m}$ thick layer of amorphous material stuck to the polymer. EDS element maps of the area on the coated electrode cycled with FEC are shown in Figure 5.23.

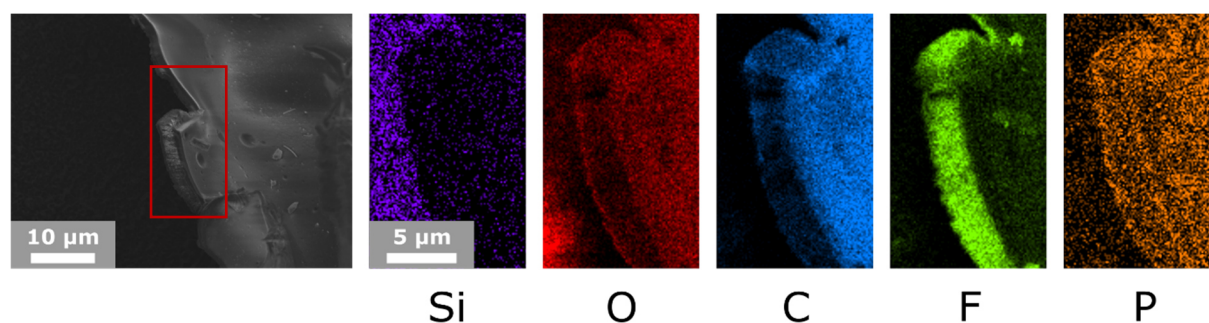


Figure 5.23: SEM micrograph and EDS element maps of the peeled-off PN(MEE) coating for the cell cycled with LP30 + 10% FEC.

In the EDS element map, silicon is only detected in the background but is not present in the polymer or the material attached to it. The PN(MEE) coating shows mostly carbon, oxygen and phosphorus, while the material attached to it bears significant amounts of fluorine, some oxygen, carbon and phosphorus.

Adding FEC to the thin-film electrode, it will transform into the high surface area silicon nanostructures as expected for FEC (Figure 5.22a). The SEI that forms will however show better adhesion to the polymer. During delithiation it will stay attached to it allowing a fresh SEI to form every cycle on the freshly expose Si surface. Given the instability of FEC, CE of only 92% are reached. We assume that the cell will cycle stable until all of the FEC is consumed, similar to the FEC consumption observed on other silicon electrodes.^[178]

5.3 Silicon Anode Stabilisation with Phosphazene Coatings

Two different mechanisms of stabilisation are observed for the different polymers. A comparison of the electrodes coated with the two different poly(phosphazenes) is shown in Figure 5.24.

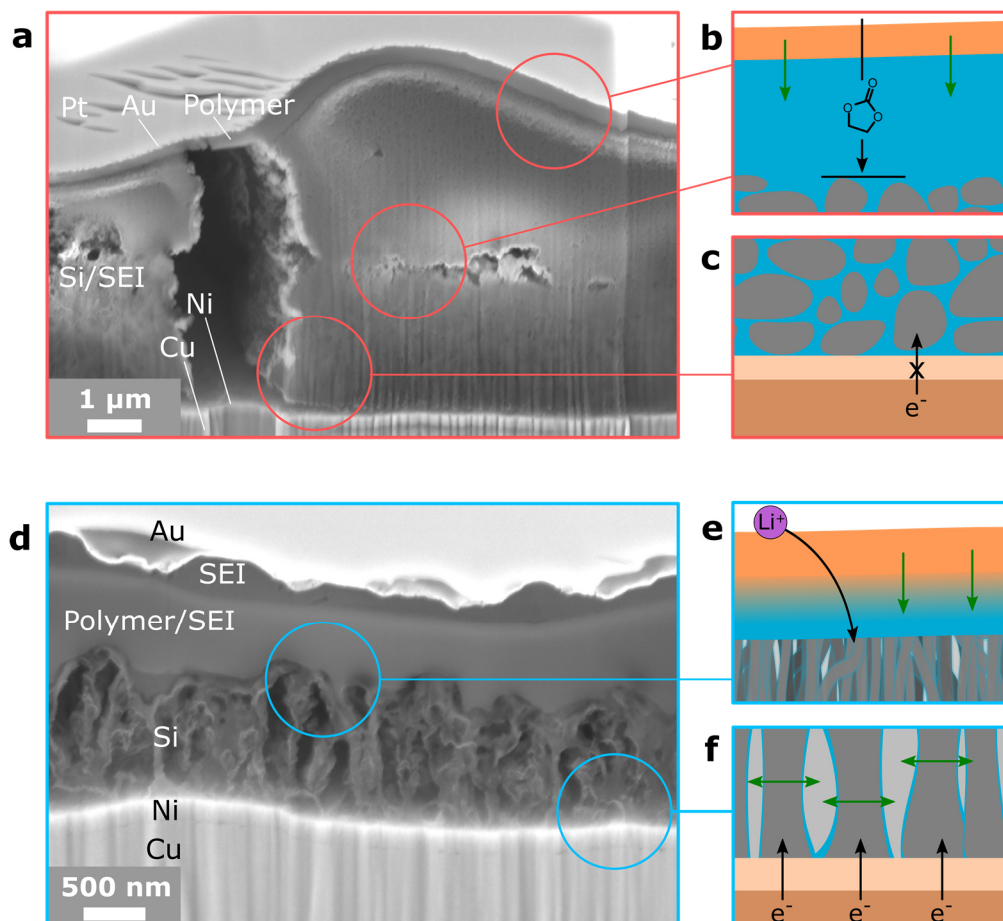


Figure 5.24: FIB SEM images of the cycled, poly(phosphazene)-coated Si thin-film electrodes showing the different components and proposed stabilisation mechanisms thereof. a) FIB SEM image of the PN(MEE)-coated electrode after 500 cycles showing distinct features: b) a polymer layer on a fine layer of SEI, clearly separated from the Si/SEI material, maintaining the volume expansion but allowing electrolyte to permeate and continuously form additional SEI and c) the Si/SEI material phase formed upon continuous cycling resembles the structure of the electrode obtained from LP30 without the coating showing delamination from the current collector breaking electron conduction pathways. d) FIB SEM image of the PN(CF)-coated electrode after 525 cycles showing distinct features: e) a merged polymer/SEI layer that is permeable to lithium ions covering a nanoporous network of silicon strands and evenly applies positive pressure on the material, controlling the volume expansion and f) silicon strands that may expand into the void space observed during lithiation maintaining electronic conduction pathways to the current collector.

The FIB SEM cross section of the cycled and failed PN(MEE)-coated electrode shows three significant features (Figure 5.24a): A distinct boundary between the polymer and accumulated

SEI, the separation thereof from the Si/SEI material (Figure 5.24b), and the delamination of the material from the current collector (Figure 5.24c). Volume expansion of the silicon material is contained between the polymer (and underlying SEI formed during cycling) and the current collector (Figure 5.24a). These mechanical forces keep the formed Si/SEI material in place and are likely responsible for the extended lifetime of the cell as delamination is slowed down. The polymer itself is largely unaffected by the electrochemistry and, whilst it swells slightly due to the electrolyte, it does not show strong interactions with the silicon material.

As electrolyte seeps through the coating, SEI accumulates on the silicon surface. This continuous formation of the SEI can be seen in the low CE observed in Figure 5.10 and the irreversible capacity loss quantified in Figure 5.15. Further analysis of the cell's electrochemical performance from Figure 5.12 and Figure 5.14 suggest that the processes occurring are similar to those observed on the bare electrode i.e. that the Si/SEI material delaminates from the current collector when the cell degrades which breaks the electron conduction pathways (Figure 5.24c). We do not observe a shift in voltage for the Li_2Si peak towards higher voltages around the “dip”. Referring back to the discussion in Chapter 2, a stress-potential coupling may be the reason for this, as the Si/SEI must be under constant mechanical stress from the polymer coating and attachment to the current collector, in contrast to material that can freely peel off.

Similarly, PN(CF) provides mechanical stability but now the polymer also appears to be integrated in the SEI formed on top of the silicon electrode (Figure 5.24 e). During cycling, maintaining electrical contact to the current collector, the silicon material cracks vertically forming strand-like nanostructures which can receive lithium ions through the polymer/SEI material and electrons from the connection to the nickel base. The finer polymer/SEI layer with PN(CF) appears to effectively limit the diffusion of the electrolyte to the anode so that excellent CEs (Figure 5.10) are observed. Moreover, there are fewer reactions occurring on the silicon surface observed in the lack of intensity of the process at ~ 0.45 V (Figure 5.14).

However, the silicon structure that is formed *in situ* is very delicate: changes in the cycling conditions may destroy the structure (see Figure 5.12). The silicon structure formed at a voltage cut-off of 100 mV may accommodate a lower amount of lithium than initially intended but attempting to store more lithium through an even lower cut-off voltage causes the void spaces in the structure to be exhausted. The cascade of subsequent structural changes ultimately leads to the familiar “dip” in the electrochemical profile that sees a sharp increase of reactions on the silicon surface with the process at 0.46 V being extremely high. We assume, that the protective

layer has given in at this point, exposing the huge surface area of fine silicon strands to the electrolyte. What follows is the expected degradation that is observed in the absence of a coating.

Judging from the physical appearance of the films from before and after cycling, a polymer film with a lower degree of cross-linking would offer more possibilities to adapt to the stresses during cycling and to be incorporated into a functional passivating layer on the surface of the electrode. Moreover, the chemical functionalities on the polymer will affect the interactions with the electrolyte, silicon surface and lithium ions.

An example of such can be seen in the PN(MEE) coating which was shown to be affected by the electrolyte formulation in section 5.2.5 with different affinities of the SEIs formed to the silicon and polymer layers. The sample with added VC may have benefited from the increased mechanical stability as the “dips” in CE that have occurred in the uncoated sample with VC (see section 4.2.2.1, Figure 4.5 on page 92) were not observed. The delamination of the VC-stabilised islands may be inhibited.

Strictly speaking, from the observations in this chapter, the polymer layers as deposited are not an artificial SEI but a gel electrolyte that provides a scaffolding for the formation of a surface coating in combination with degradation products from the liquid electrolyte as seen in is the case of PN(CF). PN(MEE) acts rather as a simple physical barrier, that distributes the mechanical stress over the surface area and slows down the delamination of the anode. The extra weight added to the system from the polymer technically lowers the specific capacity of the anode. If we may utilise it as an electrolyte or a separator, it’s inclusion may decrease the need for additional components and therefore can further decrease the weight of the cell.

5.4 Conclusions

The work in this chapter shows a synthetic pathway to stabilise the silicon thin-film anode through poly(phosphazene) coatings that show high versatility. The coatings increase the lifetime of the silicon thin-film anodes significantly.

The synthetic pathway facilitates the design of the product for its intended application need. The “living” cationic polymerisation provides control over the chain length, influencing the physical properties of the product, allowing the formation of a polymer that shows low viscosity and good solubility in organic solvents. MALDI TOF spectra confirm that a step-wise substitution with different alkoxide side-groups yields a non-geminal substitution pattern. Polymer coatings were applied from solution by spin-coating onto Si thin-film electrodes and

were cross-linked under UV radiation with a radical initiator. The solution-based approach is more versatile than PVD (e.g. LiPON) while providing similar stabilisation.^[83]

The lifetime of the thin-film electrode increases by more than 100% when depositing a PN(MEE) coating and is further extended when using a PN(CF) coating. The PN(CF)-coated electrode has shown stable cycling over 500 cycles but is sensitive to changes in lithiation depth. The two polymers have shown to stabilise and increase the cyclability of the electrode differently as summarised in Figure 5.25.

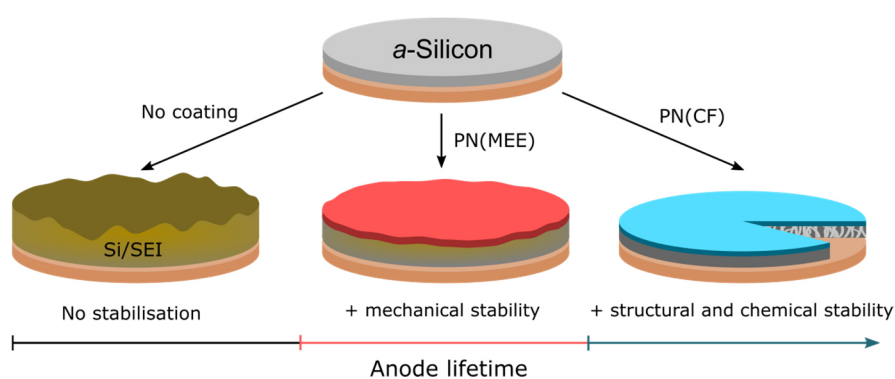


Figure 5.25: Summary of the impact found of the different polymer coatings on the long-term cyclability of the silicon thin-film electrode.

PN(MEE) acts as a physical barrier, extending the lifetime by distributing stress during the expansion and delaying the delamination of the Si/SEI material, which appears similar in morphology to that formed without a coating. The PN(CF) coating forms a functional SEI that effectively prevents electrolyte from permeating to the electrode while granting ion conductivity. The silicon electrode underneath the PN(CF) coating forms a lacey, porous network that provides void space for the volume expansion during lithiation. The combination with electrolyte additives shows both constructive and destructive synergies and needs to be investigated further with the softer PN(CF) polymer.

Overall, the technique holds incredible potential to further increase the lifetime of silicon anodes and may be applied to other battery component surfaces not solely limited to be applied in LIBs.

5.5 Experimental

5.5.1 Materials

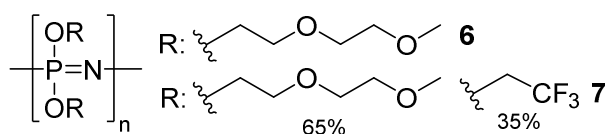
Phosphorus trichloride and sulfuryl chloride were obtained from Sigma Aldrich and distilled under nitrogen atmosphere prior to use. 2-(2-Methoxyethoxy) ethanol (99%) and hexamethyldisilazane (99%) were obtained from Sigma Aldrich. Trifluoroethanol (99.8%, ultra-pure) was obtained from Acros Organics. Solvents used were dried over a suitable drying reagent and distilled before use.^[129]

5.5.2 Experimental Details

5.5.2.1 Synthesis of Trichloro(trimethylsilyl)phosphoranimine **D**

$$\begin{array}{c} \text{Cl} \\ | \\ \text{Cl}-\text{P}=\text{N}-\text{SiMe}_3 \\ | \\ \text{Cl} \\ \mathbf{D} \end{array}$$
 The monomeric phosphazene precursor was synthesised following the improved procedure described by Manners *et al.*^[206] To a total volume of 200 mL *n*-butyl lithium solution (0.8 M in hexanes, 160 mmol, 1.0 eq.) was added a solution of hexamethyldisilazane (33.5 mL, 160 mmol, 1.0 eq.) in 50 mL *n*-hexane (abs.) slowly at 0°C over the course of 2 h. The reaction mixture was slowly warmed to room temperature and left to stir for 18 h. All volatiles were removed under reduced pressure to yield crystalline lithium hexamethyldisilazide (**E**). The solid was dissolved in 300 mL diethylether (abs.) and cooled to 0°C. Phosphorus trichloride (14 mL, 160 mmol, 1.0 eq.) was added slowly over 30 min. The mixture was allowed to warm to room temperature and stirred for another 2 h. The mixture was again cooled to 0°C and sulfuryl dichloride (12.9 mL, 160 mmol, 1.0 eq.) was added slowly *via* syringe over 30 min. After stirring for another 2 h at room temperature, all solids were filtered off over Celite and volatiles were removed under reduced pressure, cooling the reaction vessel to 0°C at all times. The liquid was distilled (23°C, 1.3 x 10⁻¹ mbar) to yield colourless trichloro(trimethylsilyl)phosphoranimine (**D**) (24.0 g, 92 mmol, 76%).

³¹P{¹H} NMR (162.0 MHz, Et₂O): δ = -58.8 ppm (Lit. δ = -53.0 ppm in CDCl₃).^[206]

5.5.2.2 Synthesis of the Poly(phosphazenes) PN(MEE) **5** and PN(CF) **6**

Trichloro(trimethylsilyl)phosphoranimine **D** (2.3 g, 1.0 eq., 10.2 mmol) was added to a phosphorus pentachloride (12 mg, 0.01 eq.,

57.6 μmol) solution in 45 mL toluene (abs.). The solution turned opaque after an hour and was left to stir for 2 days until clear. At this stage the $^{31}\text{P}\{^1\text{H}\}$ NMR spectrum showed complete conversion to the product **B**. The solvent was removed, and the crude product was slowly added to a solution of freshly prepared sodium alkoxide solution sodium hydride and the appropriate alcohol; i.e., 2.2 eq. sodium methoxy(ethoxy)ethoxide to form PN(MEE) (**6**); 1.2 eq. methoxy(ethoxy)ethoxide followed by excess sodium trifluoroethoxide to form PN(CF) (**7**) in THF (abs.) at 0°C . After 5 days the reactions were complete, the organic solvent was removed *in vacuo* and the residue was dissolved in deionised water. The product was purified by dialysis over 5 days in deionised water, changing the water multiple times each day. After removing the solvent, the polymers were received as highly viscous yellow liquids.

PN(MEE): 2.2 g, 76%.

$^{31}\text{P}\{^1\text{H}\}$ NMR (162.0 MHz, THF- d_8): $\delta = -8.01$ ppm.

^1H NMR (399.6 MHz, THF- d_8): $\delta = 4.11$ (bm, 2 H), 3.67 (bm, 2 H), 3.62 (bm, 2 H), 3.48 (bm, 2 H), 3.30 (s, 3 H) ppm.

$^{13}\text{C}\{^1\text{H}\}$ NMR (100.5 MHz, THF- d_8): $\delta = 72.0, 70.4, 70.2, 65.0, 58.0$ (CH_3) ppm.

PN(CF): 2.4 g, 80%.

$^{31}\text{P}\{^1\text{H}\}$ NMR (162.0 MHz, THF- d_8): $\delta = -6.74$ (b, 25%), $-7.7 - -9.0$ (b, 75%) ppm.

^1H NMR (399.6 MHz, THF- d_8): $\delta = 4.45$ (b, 2 CH_2OCF_3), 4.14 (b, 2 H), 3.65 (b, 2 H), 3.59 (b, 2 H), 3.46 (bm, 2 H), 3.28 (s, 3 H) ppm.

$^{13}\text{C}\{^1\text{H}\}$ NMR (100.5 MHz, THF- d_8): $\delta = 71.9, 70.2, 70.0$ (b), 65.5 (b), 62.3 (q, CH_2OCF_3 , $^3J_{\text{C-F}} = 34$ Hz), 57.9 (CH_3) ppm.

^{19}F NMR (376.0 MHz, THF- d_8): $\delta = -76.0$ (m) ppm.

5.5.3 Methods

Detailed descriptions of the techniques and instruments used can be found in Chapter 2 Methods. Measurements were performed under standard operating conditions.

5.5.3.1 Electrodes

All 100 nm Si anodes used were prepared in the CCR sputter coater by deposition onto nickel-coated (250 nm) current collectors. Both cold-rolled copper (CR Cu) and copper for graphene growth (GG Cu) discs were used.

5.5.3.2 Spin Coating

In a typical coating process, the polymer (10 wt%) and benzophenone (2 wt%) were dissolved in toluene and sonicated until clear. Polymer solution (0.1 mL) was dropped onto electrode discs mounted on a Delta 10 TT spin-coater (SUESS MicroTec Lithography GmbH). The discs were spun at 300 rpm for 30 s, followed by 2500 rpm for 120 s and left to dry for a few hours before cross-linking using a UV lamp (low pressure Hg, 450 W) for 10 min. The electrodes were dried in a vacuum oven at 100°C before being deployed in coin cells.

5.5.3.3 Coin Cells

Polymer-coated anode discs and 0.1 mL of LP30 electrolyte with and without additives were used for the coin cell. Additives were mixed with the electrolyte prior to adding them to the cell (FEC: 10 vol%, VC: 5 vol%).

5.5.3.4 Galvanostatic Cycling

Cells were cycled on a LANDT potentiostat at C/30 to 5 mV for the first cycle, followed by C/n for consecutive cycles (n=2, 5, 10) to different voltage cut-offs (100 mV, 40 mV), depending on the experiment.

5.5.3.5 Electron Microscopy

Coin cells were disassembled at full charge (2 V) and the anodes were rinsed with DMC. The electrodes were analysed in the TESCAN MIRA3 FEG-SEM and exposed to air during the transfer. Samples were coated with gold, using a sputter coater for FIB-SEM analysis on a Zeiss Cross-beam 540. EDS spectra and maps were recorded using the Oxford Instruments Aztec Energy X-maxN 80 EDS system on the TESCAN MIRA3 FEG-SEM.

Chapter 6 Preliminary Work Towards Poly(phosphazene) Silicon Surface Grafts

The real-world application of Si anodes in LIBs will require that the current work can be applied in the far more difficult area of silicon nanoparticles. Si nanoparticles have been used successfully when part of slurry anodes.^[52,79] Their small diameter proves to support the stresses occurring during repeated cycling and, with the right combination of binders and conductive material, may provide decent capacity retention. This section of the chapter describes ongoing studies of the poly(phosphazene) coating of silicon nanoparticles. Although electrochemical studies in this area have not yet been undertaken, the work presented serves to show how the previously described studies on silicon thin-films will be developed towards working batteries.

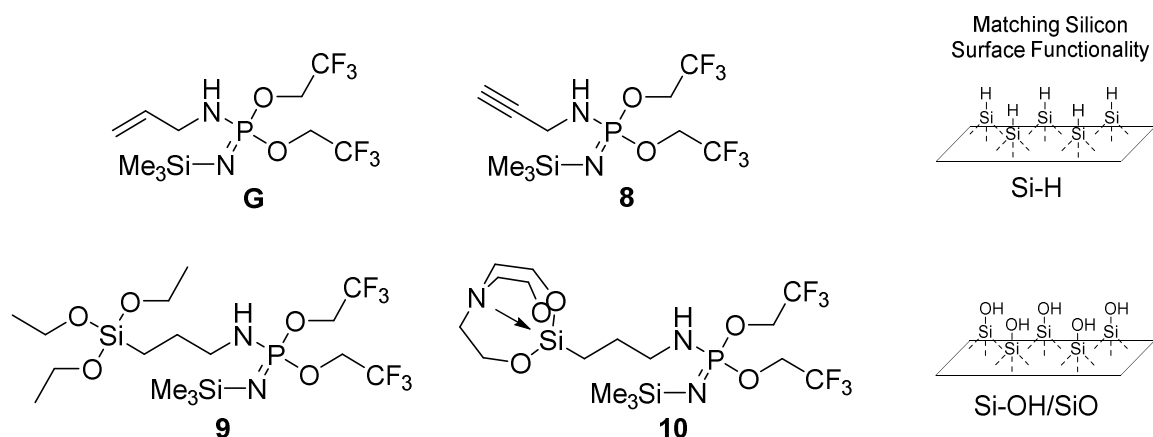
An ideal SEI should be ionically conductive, yet electronically insulating. LiPON layers for example have been shown to have a certain thickness threshold where electronic conductivity ceases and where they then start to act as an artificial SEI, stopping an SEI from electrolyte decomposition from forming.^[67,68]

As recent reports have shown, surface grafts with short-chain organic molecules and polymers may improve the performance of nanoparticle and thin-film Si anodes, respectively. The strategies, outlined in section 1.5, Figure 1.15 on page 20, developed by Gao *et al.* and Shen *et al.*, use the reactivity of specific molecules towards the silicon surface to design layers that aid the formation of a beneficial SEI during cycling.^[94,95]

In order to gain control of the polymer thickness on silicon surfaces, we are taking a similar approach by exploring the possibility of phosphazene surface grafts, based on alkenes, alkynes and silanes. Preliminary results in this chapter present amino phosphoranimines that can be attached to the silicon surface and may form a starting point for poly(phosphazenes) to be formed *via* the “living” cationic polymerisation pathway used in Chapter 5.

6.1.1 Synthesis

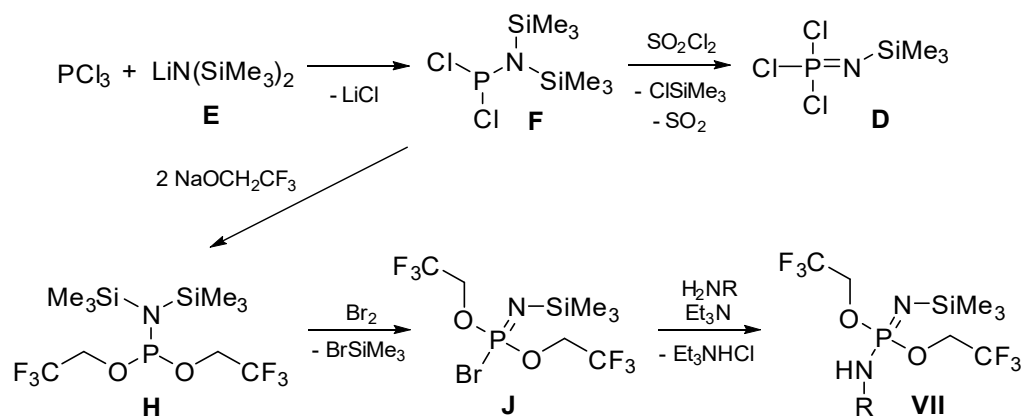
Four molecules have been successfully synthesised (Scheme 6.1) to match common silicon surface functionalities, i.e., silanes and silica or silanols.



Scheme 6.1: Amino phosphoranimes with different linkers, that match the reactivity of common silicon surface functionalities.

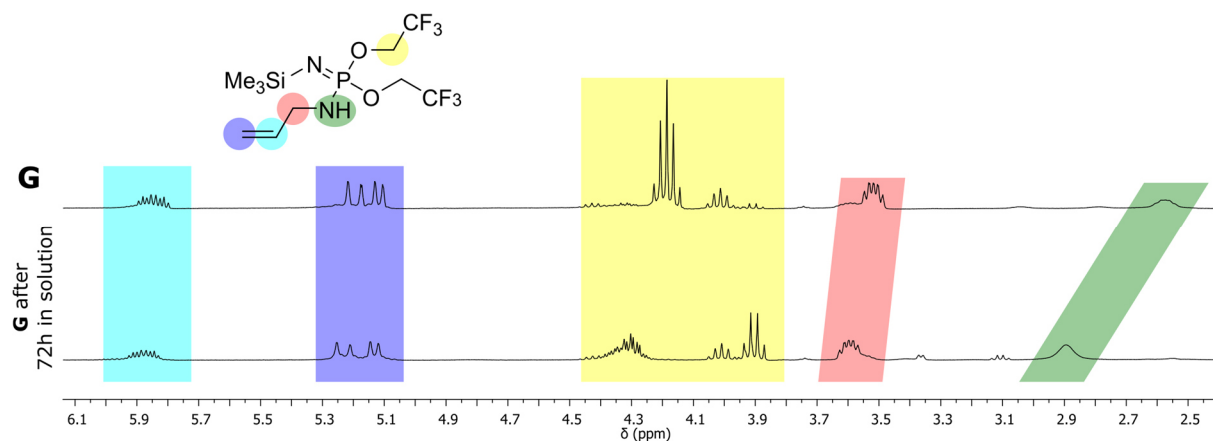
Allcock *et al.* have presented the alkene-substituted phosphoranimine, **G** (Scheme 6.1), and have studied its polymerisation with **D** and substitution pattern of the polymer observed after the reaction with alkoxides.^[211] Trifluoroethoxide substituents on the phosphorous atoms are common in the field, as they react well with the P-Cl bond but are not sterically hindered. The alkene **G** and alkyne **8** (Scheme 6.1) provide the possibility of functionalising a silicon surface where there are Si-H bonds present. This can be achieved by UV-irradiation or with a TM-catalyst. Compounds **9** and **10** (Scheme 6.1) are based on silanes. The (3-aminopropyl)triethoxysilane group in **9**, is a common surface graft for silicon oxides and TM-oxide surfaces, usually forming a Si-O-Si bonds with the elimination of ethanol.^[212–215] APTES-functionalised molecules may react with themselves when exposed to moisture to form films or particles.^[216,217] The silatrane present in **10**, is a derivative of APTES, where the nitrogen atom of the triethoxy amine coordinates to the silicon atom, providing stabilisation. Surface layers formed by such a linker have been reported to be thinner than those formed from APTES.^[74,215] The silatrane was synthesised from the reaction of APTES with triethanolamine. The reaction is usually performed in a solvent but works just as well without. The product was obtained in high yields and purity after removing the ethanol by-product.

The synthesis of the amino phosphoranimes was carried out following the procedure presented by Allcock *et al.* and is shown in Scheme 6.2 (see Experimental section).^[211] The chlorine substituents of the P(III)-species **F** were substituted for trifluoroethoxide side-groups forming the phosphoranimine **H**, followed by the oxidation with bromine to form the bromo phosphoranimine **J**. Next, **J** was reacted with the respective amine and triethylamine to form the desired linker. The synthetic pathway has been used previously to synthesise novel phosphazenes as well as branched polymers and co-polymers.^[218–220]

Scheme 6.2: Synthetic pathway to amino phosphoranimes **VII**.

The identities of the intermediates and products were confirmed by NMR spectroscopy and MS analysis. Compounds **G** and **8** contained some impurities due to difficulties in purifying the small amount of material produced. Both **9** and **10** were obtained in good purity and yield.

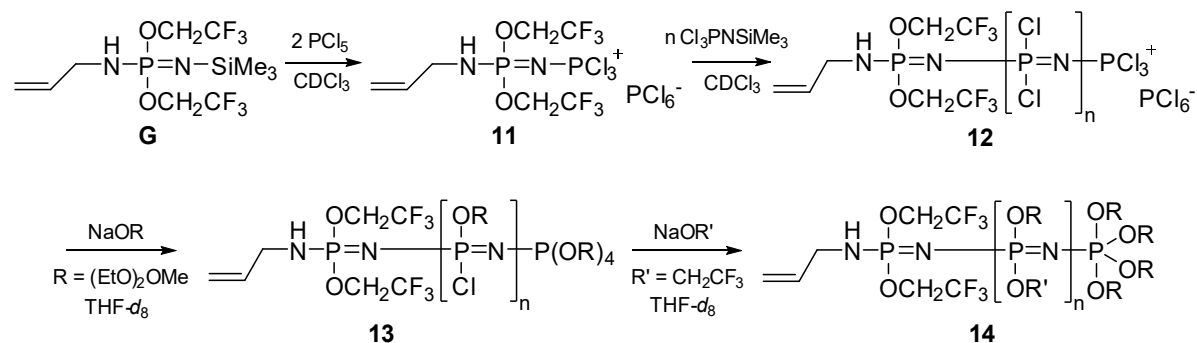
For compound **G**, some of the impurities present could be identified by ^1H NMR spectroscopy as the decomposition products, likely formed during its hydrolysis. As seen in Figure 6.1, when **G** is dissolved in spectroscopic grade CDCl_3 , at least one of the trifluoroethoxide groups (shown in yellow, quintet in the top spectrum) is hydrolytically cleaved, producing trifluoroethanol (seen as a quartet at ~ 3.9 ppm in the bottom spectrum). At the same time a resonance at 15.7 ppm also grows in in the ^{31}P NMR spectrum, which we assign to a $\text{P}=\text{O}$ phosphorus atom (compared to -1.75 ppm for **G**).

Figure 6.1: ^1H NMR spectra of **G** before (top) and after 72 h (bottom) in non-dried CDCl_3 .

6.1.2 Attempted Functionalisation of Si-H Wafer and Nanoparticle Surfaces

Attempts to coat Si-H surface functionalised nanoparticles and wafers have been made using **G** as the polymer precursor. The polymerisation strategy followed the same route presented in

Chapter 5 on page 116. The reaction is shown in Scheme 6.3. First, two equivalents of PCl_5 are added to create the reactive species **11**.



Scheme 6.3: Synthesis of a poly(phosphazene) from the allylamino phosphoranimine **G** via the “living” cationic polymerisation.

After ca. 15 minutes all PCl_5 has been consumed and the reactive $-\text{PCl}_3^+$ species **11** is formed. Adding 10 eq. of **D** initiates the polymerisation. The process was followed by $^{31}\text{P}\{^1\text{H}\}$ NMR spectroscopy which showed that the reaction was complete after three hours, with the disappearance of the signal at -53.8 ppm for the monomer **D** (Figure 6.2). The NMR spectroscopic data is similar to that observed by Allcock *et al.*^[211] The polymerisation was followed by the attempted chloride substitution with 2 equivalents of the sterically demanding sodium methoxy[(ethoxy)ethoxy] ethoxide per PCl_2 unit which formed partially substituted **13**. Full substitution was achieved by adding sodium trifluoroethoxide, forming **14**.

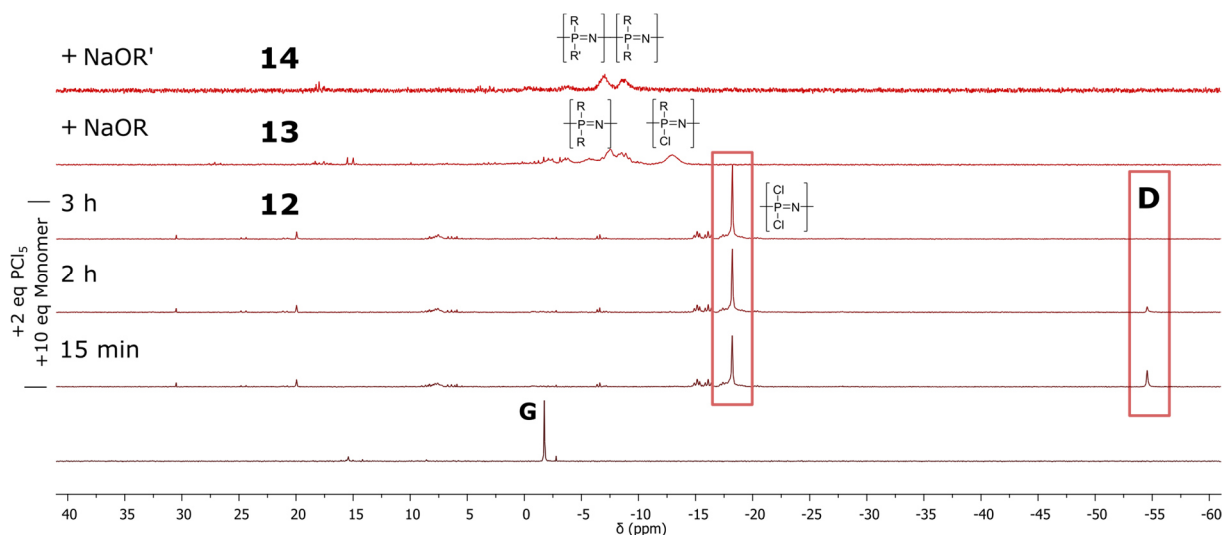


Figure 6.2: $^{31}\text{P}\{^1\text{H}\}$ NMR spectra of the stages of polymerisation from the allylamino phosphoranimine **G**. Two equivalents of PCl_5 are added in DCM (abs.) followed by 10 equivalents of the monomer **D**. The poly(chlorophosphazene) **12** is fully formed after 3 h with the disappearance of the signal for **D**. The polymer is then partially substituted with an alkoxy ether in THF first, forming **13**, followed by trifluoroethoxide to form fully substituted **14**.

Silane terminated nanoparticles are best obtained from CVD processes and, although commercially available, are expensive. Unfortunately, attempts to etch the oxide layer off the surface of silicon nanoparticles using hydrofluoric acid failed, only forming large agglomerates that were still covered in large amounts of silicon oxide, rather than discrete silane (Si-H) terminated particles. Under these circumstances the polymer could not be grafted onto the silicon surface using prolonged UV radiation. Further attempts to obtain a coating on etched silicon wafers were also unsuccessful.

6.1.3 Functionalisation of Oxide-covered Silicon Wafers

More chemically stable and easily accessible are silicon materials that have a native oxide layer, which consists of Si-O bonds and terminal silanols. The surface chemistry matches that of the phosphoranimines functionalised with APTES **9** and the corresponding silatrane **10**. To test their ability to graft onto the surface, preliminary studies on their deposition onto silicon wafers have commenced. Silicon wafers were etched with Piranha solution (sulfuric acid and hydrogen peroxide, 5:1, v/v) and exposed to a 1 vol% solution of the grafts in dry toluene at 70°C for 1 h. The wafers were washed with a mixture of acetonitrile and ethanol and tested for their wettability. Additionally, reference wafers were treated in exactly the same way with an APTES solution and toluene only as references. The contact angles of each surface are shown in Figure 6.3.



Figure 6.3: Contact angles measured for the Piranha treated silicon wafers after 1 h at 70°C in a) toluene, b) 1 vol% APTES on toluene, c) 1 vol% **9** in toluene and d) 1 vol% **10** in toluene.

The wafer in Figure 6.3b shows a large reduction in the WCA after the treatment with APTES. Both of the fluorinated phosphoranimine grafts show an increase in the WCA, with the APTES-based grafts introducing higher hydrophobicity with a WCA of 91.0° in **9** and 85.9° in **10** (Figure 6.3c-d). This behaviour is expected for molecules containing trifluoroethoxy side-groups. The smaller angle observed for the silatrane **10** may be due to steric hinderance and the resulting poorer coverage of the silicon surface.

X-ray photoelectron spectroscopy (XPS) was attempted on the phosphoranimine-coated and reference wafers but may have been affected by the sample being exposed to air and moisture for 3 weeks prior to the measurements (Figure 6.4).

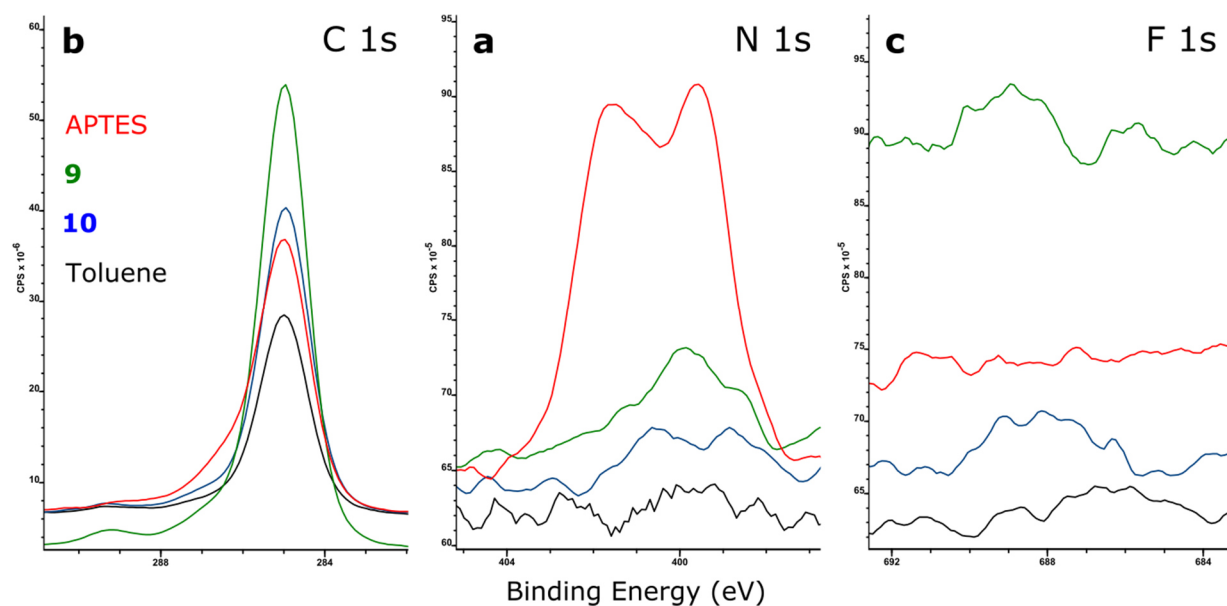


Figure 6.4: C 1s, N 1s and F 1s XPS scans of the silicon wafers treated with toluene and 1 vol% solutions of APTES (red), **9** (green), and **10** (blue) in toluene (reference: black).

An increase in the intensity of the C 1s peak is observed for all three grafts (APTES, **9** and **10**) with the largest increase in **9**. The APTES functionalised surface shows a significant peak in the N 1s scan. The two peaks observed suggest the presence of NH_2 (399.5 eV) and NH_3^+ or hydrogen bonded NH_2 (401.6 eV).^[221,222] Compounds **9** and **10** show traces of nitrogen and almost no sign of F 1s peaks. The intensities for all elements observed for compound **10** appear lower, hence it may form thinner films.

We intend to test the treated wafers avoiding exposure to air and moisture in the future. Furthermore, EDS and electron energy loss spectroscopy (EELS) may be used to gain further information about this system.

6.1.4 Direct Polymer Growth from Si Nanoparticles

We have further attempted to grow a polymer surface layer directly from the silicon nanoparticles oxide layers. Silicon nanoparticles (100 mg, average diameter of 100 nm obtained from Alfa Aesar) were dried and suspended in 20 mL of a 1 vol% solution of **9** in DCM. The solution was stirred, then left to stand overnight, and the solvent was decanted. The process was repeated three times. A solution of 20 mg PCl_5 in DCM was added and the mixture stirred. Again, three times, the solution was left to stand and the solvent decanted. Monomer **D** was added, and the solution was stirred for 3 days. Following the reaction by $^{31}\text{P}\{^1\text{H}\}$ NMR was attempted, but the nanoparticles in the solution made shimming difficult. The solvent and any

unreacted **D** were removed *in vacuo* and the particles were examined by transmission electron microscopy.

Figure 6.5 shows the appearance of the pristine silicon nanoparticles and the nanoparticles from the polymerisation procedure suspended in THF.

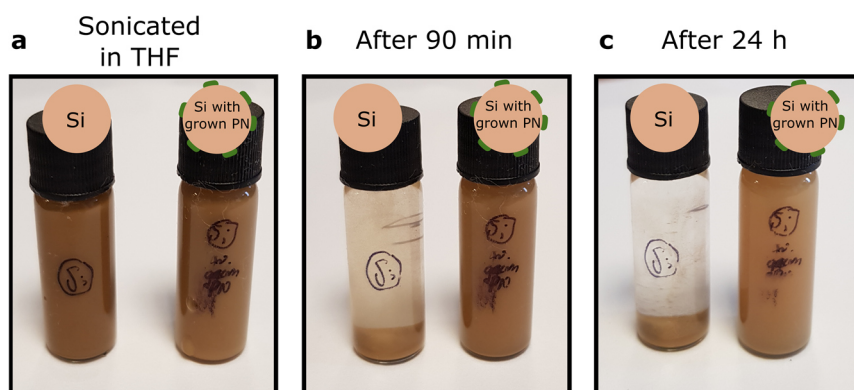


Figure 6.5: Vials containing 10 mg of pristine silicon nanoparticles and silicon nanoparticles from the polymer growth experiment in THF directly after sonicating (a), after 90 min (b) and after 24 h (c).

After sonicating the vials, both particles form an even suspension with the solvent. Most of the pristine particles sediment after 1.5 h and a clear supernatant is observed after 24 h. The surface covered nanoparticles appear mostly suspended after 1.5 h, and even after 24 h, some particles remain in suspension, suggesting stronger interactions between the grafted particles and the solvent. After removing the suspension, a thin layer of the phosphazene covered nanoparticles remains attached to the glass walls, indicating that the poly(chlorophosphazene) may react with the glass-surface.

TEM micrographs and EDS analysis of the covered particles in Figure 6.6a show the presence of phosphorus and chlorine containing substance on and between the nanoparticles in low concentrations, as the spectrum in Figure 6.6b confirms.

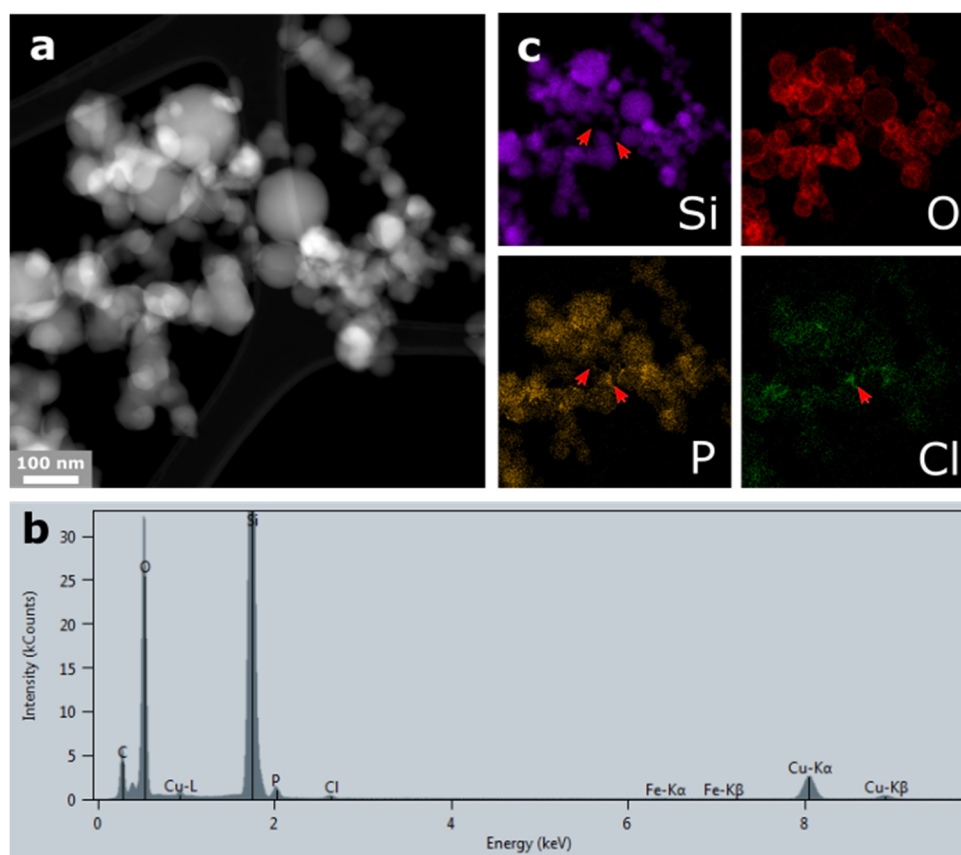


Figure 6.6: TEM micrograph (a) and EDS spectrum (b) and element maps (c) of the silicon nanoparticles after the attempted growth of a poly(phosphazene) from the surface.

The element maps in Figure 6.6c show that the polymer is found in larger concentrations in between the particles and in agglomerates. The arrows in the figure show areas where no silicon is detected, but in which both phosphorus and chlorine are. In these areas it is likely, that polymer that has been formed in solution has dried in between the particles. While no increased concentration of phosphorus is detected on the edges of the nanoparticles, the diffuse phosphorus map appears to extend beyond the areas of the particles (where silicon is detected), suggesting that the phosphorus signal not only arises due to the underlying silicon material and that the particles have been coated with the poly(phosphazene).

Overall, the results obtained so far in this area show plenty of promise for the future extension of the polymer methodology to silicon nanoparticles and this work will form the basis for future studies in this area.

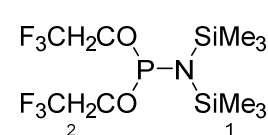
6.2 Experimental

6.2.1 Materials

Undoped silicon wafers were obtained from University Wafers. APTES (98%), triethanolamine (98%+) and plasma-synthesised, crystalline silicon nanoparticles were obtained from Alfa Aesar (average particle size ~100 nm, 99%). Trifluoroethanol (99.8%, extra pure) was obtained from Acros Organics. 2-(2-methoxyethoxy)ethoxy ethanol (98%) was obtained from Sigma Aldrich. Solvents used were dried over a suitable drying reagent and distilled before use.^[129]

6.2.2 Phosphoranimine and Polymer Syntheses

6.2.2.1 Difluoroethoxy-*N,N*-bis(trimethylsilyl) phosphanamine **H**

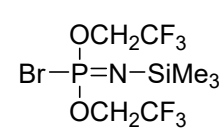


A stirred suspension of sodium hydride (purity 95%, 1.75 g, 69.3 mmol, 2.0 eq.) in THF (20 mL) was cooled to 0°C and trifluoroethanol (8.23 g, 72.1 mmol, 2.1 eq.) was slowly added. After strong evolution of H₂, a clear solution was obtained. The solution was warmed to room temperature and stirred for an additional two hours. A solution of freshly prepared **F** (34.2 mmol, 1.0 eq.) in THF (20 mL) was slowly added to the reaction mixture and a colourless precipitate formed. The suspension was filtered over Celite[®] and the solvent was removed *in vacuo*. The product was purified by vacuum distillation (0.1 mmHg, 47°C). Difluoroethoxy-*N,N*-bis(trimethylsilyl) phosphanamine **H** was isolated as a colourless liquid (5.80 g, 14.9 mmol, 44%).

³¹P{¹H} NMR (162.0 MHz, CDCl₃): δ = 172.6 ppm.

¹H NMR (399.6 MHz, CDCl₃): δ = 4.01 ('2', m, 4H), 0.27 ('1', d, *J* = 1.4 Hz, 18H) ppm.

6.2.2.2 Bromotrifluoroethoxy phosphoranimine **J**

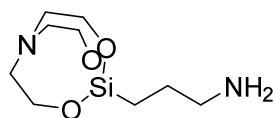


A solution of **H** (2.27 g, 5.83 mmol, 1.0 eq.) in DCM (15 mL) was cooled to -78°C and Br₂ (0.62 g, 7.76 mmol, 1.3 eq.) in DCM (10 mL) was added dropwise as a white precipitate formed. The reaction mixture was stirred overnight, and the precipitate was filtered off. The solvent and volatile by-products were removed *in vacuo*, and the product was purified by fractioned vacuum distillation (0.1 mmHg, 42°C). Bromotrifluoroethoxy phosphoranimine **J** was obtained as a colourless liquid (1.12 g, 2.83 mmol, 49%).

³¹P{¹H} NMR (162.0 MHz, CDCl₃): δ = -34.17 ppm.

^1H NMR (399.6 MHz, CDCl_3): $\delta = 4.34$ (m, 4H, OCH_2CF_3), 0.12 (d, $J = 0.7$ Hz, 9H) ppm.

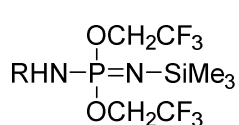
6.2.2.3 1-(3-Aminopropyl)silatrane



To stirred APTES (10.0 g, 45.2 mmol, 1.0 eq.) under a nitrogen atmosphere was added triethanolamine (6.54 g, 43.8 mmol, 1.0 eq.) dropwise. The solution was left to stir over night during which most of the mixture crystallised. Liquid components were removed *in vacuo* and 1-(3-Aminopropyl)silatrane was received as a colourless, crystalline solid (10.3 g, 60.7 mmol, 98%) and directly used for the reaction with **10**.

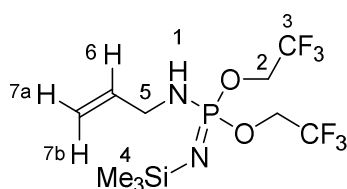
^1H NMR (399.6 MHz, CDCl_3): $\delta = 3.75$ (t, $J = 5.8$ Hz, 6H), 2.79 (t, $J = 5.8$ Hz, 6H), 2.61 t, $J = 7.0$ Hz, 2H), 1.61 – 1.43 (m, 2H), 1.21 (s, b, 2H), 0.48 – 0.31 (m, 2H).

6.2.2.4 Surface Grafts from **J**



To the stirred solution of an amine (1.89 mmol, 1.5 eq.) in THF (10 mL) was added triethylamine (192 mg, 1.89 mmol, 1.5 eq.). Bromide **J** (500 mg, 1.26 mmol, 1.0 eq.) was added slowly resulting in the precipitation of a colourless solid. The solution was decanted with a filter cannula and the solvent was removed *in vacuo* to yield a clear liquid.

Allylamino phosphoranimine **G**: colourless liquid, 370 mg, 0.99 mmol, 79% (~80% pure).

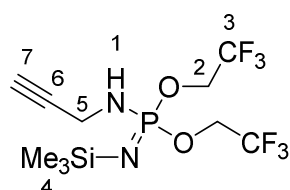


TOF MS ASAP+ (MeCN, 100°C): $m/z = 373.0948$ (calc. 373.0936, EH^+).

$^{31}\text{P}\{^1\text{H}\}$ NMR (162.0 MHz, CDCl_3): $\delta = -1.75$ ppm.

^1H NMR (399.6 MHz, CDCl_3): $\delta = 6.06 - 5.60$ ('6', m, 1H), 5.22 – 5.10 ('7a', '7b', m, 2H), 4.19 ('2', quintet, $J = 8.3$ Hz, 4H), 3.52 ('5', m, 2H), 2.57 ('1', m, 1H), 0.04 ('4', s, 9H).

Propargylamino phosphoranimine **8**: yellow liquid, 450 mg, 1.21 mmol, 96% (~75% pure).

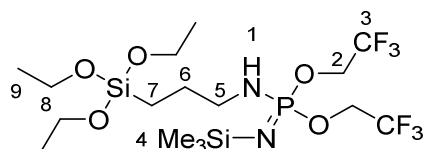


TOF MS ASAP+ (MeCN, 100°C): $m/z = 371.0780$ (calc. 371.0779, $8H^+$).

$^{31}P\{^1H\}$ NMR (162.0 MHz, $CDCl_3$): $\delta = -3.67$ ppm.

1H NMR (399.6 MHz, $CDCl_3$): $\delta = 4.29 - 4.12$ ('2', m, 4H), 3.75 – 3.61 ('5', m, 2H), 2.94 – 2.71 ('7', m, 1H), 2.26 ('1', t, $J = 2.4$ Hz, 1H), 0.06 ('4', s, 9H).

Aminopropylsilane phosphoranimine **9**: clear liquid, 7.1 g, 13.05 mmol, 80%.



TOF MS ASAP+ (MeCN, 100°C): $m/z = 537.1810$ (calc. 537.1805, $9H^+$).

$^{31}P\{^1H\}$ NMR (162.0 MHz, $CDCl_3$): $\delta = -0.90$ ppm.

1H NMR (399.6 MHz, $CDCl_3$): $\delta = 4.17$ ('2', quintet, $J = 8.3$ Hz, 4H), 3.75 ('8', q, $J = 5.8$ Hz, 6H), 2.89 ('5', m, $J = 13.8, 6.9$ Hz, 2H), 2.81 – 2.64 ('1', m, 1H), 1.70 – 1.45 ('6', m, 2H), 1.22 ('6', t, $J = 7.0$ Hz, 9H), 0.71 – 0.51 ('7', m, 2H), 0.03 ('4', s, 9H).

Aminopropylsilatrane phosphoranimine **10**: clear, viscous liquid, 7.6 g, 13.9 mmol, 79%.

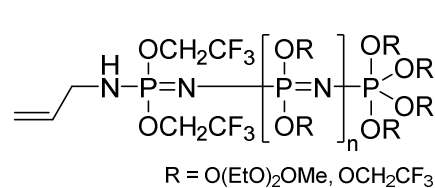


TOF MS ASAP+ (MeCN, 100°C): $m/z = 548.1608$ (calc. 548.1601, $10H^+$).

$^{31}P\{^1H\}$ NMR (162.0 MHz, $CDCl_3$): $\delta = -0.33$ ppm.

1H NMR (399.6 MHz, $CDCl_3$): $\delta = 4.17$ ('2', quintet, $J = 8.3$ Hz, 4H), 3.75 ('8', t, $J = 5.8$ Hz, 6H), 2.99 ('1', m, $J = 12.4, 6.4$ Hz, 1H), 2.92 – 2.72 ('5' & '9', m, 8H), 1.58 ('6', dd, $J = 14.8, 7.3$ Hz, 2H), 0.48 – 0.33 ('7', m, 2H), 0.02 ('4', s, 9H).

6.2.2.5 Living Cationic Polymerisation of **D**



PCl_5 (25 mg, 0.126 mmol, 1.8 eq.) and **D** (25 mg, 0.067 mmol, 1 eq.) were dissolved in dry $CDCl_3$ (0.6 mL). The mixture was shaken until the PCl_5 was dissolved. To this mixture **7** (150 mg, 0.671 mmol, 10 eq.) was added quickly and the mixture was agitated. The reaction was monitored by $^{31}P\{^1H\}$ NMR spectroscopy. Full conversion was observed after three hours. The solvent was removed *in*

vacuo and a freshly prepared mixture of the ethoxide formed from NaH (30 mg, 1.25 mmol, 18.6 eq.) and 2-(2-methoxyethoxy)ethoxy ethanol (152 mg, 1.27 mmol, 18.8 eq.) in THF-*d*₈ (0.6 mL) was added quickly to form a viscous, colourless suspension. After 18 hours no full conversion was observed. Trifluoroethoxide (~1 mmol) was added in THF (1 mL) and the solution was agitated for another hour and full conversion was detected. The polymer was taken up in water, decanted, then taken up in hexane and decanted again to remove impurities.

6.2.2.6 Living Cationic Polymerisation of **D**

To a suspension of 200 mg silicon nanoparticles in 20 mL DCM (abs.) was added **9** (0.2 mL) and the mixture was stirred for 6 h. Stirring was stopped, and the nanoparticles were left to sediment overnight. The solvent was decanted, and 20 mL of fresh DCM (abs.) was added and the process repeated twice, after which the particles were dried *in vacuo*. A solution of PCl₅ (20 mg) in DCM was added to the particles and after 6 h of stirring, the above process was repeated for three times in total. The solvent was removed, and the particles were dried *in vacuo*.

6.2.3 Methods

6.2.3.1 Silicon Wafer Preparation

Undoped silicon wafers (100) were cut into small 3 x 2 cm pieces and washed with acetone and deionised water before being etched with a 10% HF solution. The pieces were washed with Milli-Q® water and dried under a dry argon stream. Wafers were used as etched for experiment with compound **G**.

Cleaned wafers for grafting of **9** and **10** were then submerged in Piranha acid (sulphuric acid and hydrogen peroxide, 5:1) and left to stand for 3 h with occasional swirling to remove the bubbles formed on the wafer surface. The wafers were rinsed with Milli-Q® water and dried under a dry nitrogen stream.

6.2.3.2 X-ray Photoelectron Spectroscopy (XPS)

XPS measurements were carried out at the Harwell XPS facility at the Diamond Light Source in Didcot, UK, by local staff.

6.2.3.3 Transmission Electron Microscopy (TEM) and EDS

TEM micrographs were recorded on a Thermo Scientific (FEI) Talos F200X G2 TEM using HAADF and BF STEM detectors. EDS spectra were obtained using a Super-X EDS detector system.

Chapter 7 Summary and Conclusion

This thesis presents a detailed study of the silicon thin-film as a model electrode for LIBs. Its general electrochemistry and degradation of these thin-films are discussed and their potential for studies regarding electrolyte additives and artificial SEIs is demonstrated. The work provides a better understanding of the degradation of silicon as an anode material for LIBs and presents potential solutions to overcome the challenges found in the volume expansion and continuous SEI formation which are major road-blocks in the real-world applications of silicon as an anode in LIBs. These insights may help in accessing silicon's high gravimetric capacity which could largely increase the overall capacity of LIBs.

The detailed degradation study presented in Chapter 3 has provided an excellent insight into the impact of material parameters and cycling conditions on the lifetime and changes in the electrode structure expected for thin-film silicon electrodes. The evolution of electrode fracturing has been explored in great detail by results obtained through electron microscopy. Limiting the thickness plays a major role in mitigating lithiation-induced stress, with 100 nm thin-films performing better than thicker films. It is confirmed that a freshly deposited metal interlayer on top of the current collector, in the form of a 250 nm nickel layer, improves the silicon anodes performance. This is attributed to better silicon-metal interactions and is (in part) assumed to be an effect of the absence of a significant oxide layer between silicon and current collector. The surface structure of the current collector also plays a role in how the anode degrades, but mainly affects the appearance of the electrodes structure. The conditions under which samples are prepared for further analysis post-cycling are crucial for consistency in the results. Cautious washing and drying under inert conditions are best to maintain the integrity of the cycled anodes, since their surface structure and the SEI that is formed can be severely compromised by fast drying or oxidation.

The electrochemical cycling conditions affect the lifetime, accessible capacity and resulting structure of the electrode significantly. Increasing the charging rate leads to a decrease in capacity through kinetic limitations at rates of 1C, whereas slower rates (C/5 and C/10, for example) show similar performance. The electrodes cycled at lower rates form a smooth surface structure compared to the sharp edges characteristic of faster rates. Lowering the cut-off voltage yields more accessible capacity while significantly decreasing the lifetime of the electrode. This is associated to the enhanced volume expansion due to the larger amount of lithium being inserted. Overall, this study has provided a coherent account of the relevant factors that need to

be considered when using silicon thin-film electrodes as a model system and have implications for future studies of bulk silicon anodes.

Further insights are obtained using electrolyte additives for the work presented in Chapter 4. The synthesis of ^{13}C -labeled FEC has enabled advanced NMR spectroscopic studies by Yanting Jin on the composition of the SEI formed on silicon from the electrolyte additive. In her work crucial fragments of the SEI on silicon nanowires have been identified in the form of cross-linked polymeric species that show different chemical structures depending on the electrolyte composition. Following on from this, in a detailed study of the fully characterised silicon thin-film anodes in the current work, has shown that the additives FEC and VCs have specific structural impacts on SEI formation on silicon thin-film anodes. It has been shown that the initially flat electrode can continuously crack into smaller fragments until reaching a limiting size where the Si/SEI composite formed may cycle stably for more than 350 cycles (compared to ~ 100 cycles without electrolyte additives) without significant structural changes or capacity loss thereafter. The structures observed are different, depending on the additive used. For FEC, a lamellar microstructure is observed, composed of fine composite, nano-structures of Si/SEI. These nanoscopic features of the SEI are approximately 200 nm wide with larger features at the base which maintain electrical contact with the current collector. For VC, however, larger islands of Si/SEI are formed. These micron-sized Si/SEI islands are attached to the current collector by connections that are between 160 and 300 nm in width. In the process of forming the SEI for FEC, a large capacity loss is observed. It is assumed that the capacity loss stops when a sufficiently stable SEI is formed. At this point, the SEI formed from FEC appears to be superior to that formed from VC. These findings shed light on the problem of FEC consumption in LIBs with silicon as part of their active material. They show that the continuous structural change which exposes fresh silicon surfaces, will lead to FEC depletion.

In Chapter 5, poly(phosphazenes) were successfully synthesised and applied to the silicon thin-film anode as artificial SEIs, increasing cycling life. Two poly(phosphazenes) were prepared: a purely glycol ether substituted polymer **6** and a partially trifluoro ethoxy substituted polymer **7**. By spin-coating and cross-linking the polymers onto the anodes from a toluene solution, very thin (100–200 nm) polymer coatings were formed. Post cycling analysis of the cells shows that the coatings swell with the electrolyte and stabilise the anode differently. A coating of **6** allows stabilisation by containing the Si/SEI composite, which appears similar to that formed without a coating. The coating leads to prolonged physical contact to the current collector, leading to an increase in lifetime of more than 100%. Further SEI is still being formed with every cycle and eventually the electrode will show similar characteristics in its degradation

to the uncoated samples. Coating the electrode with 7, which contains trifluoroethoxy sidegroups, leads to the formation of an improved SEI. The coating appears to less efficiently crosslink but form a surface layer with the electrolyte that effectively stabilises the anode. The silicon anode degrades differently, forming a lacy structure that is supported by the polymer based SEI on top and that maintains electrical contact with the current collector at the base. The results show great opportunities for future studies. Given the ability to change polymer chain length, type of substituents and their substitution pattern within the polymer, the application of polyphosphazenes may not be limited to silicon anodes in LIBs, but other active materials for battery applications in which volume expansion and SEI formation are fundamental roadblocks.

The transition towards real-life applications has commenced in Chapter 6 with progress being made towards the design of thin phosphazene layers through grafting onto bulk silicon surfaces. Four phosphoranimines, bearing suitable linkers that are compatible with various surface functionalities, have been synthesised and the growth of short-chain polymers from them has been investigated. Results indicate that it will be possible to transfer the concept of thin phosphazene layers onto any silicon material in the near future, making it possible to coat nanoparticles, for example, that are much more suitable for the manufacturing of high energy density anode materials.

Silicon is a challenging anode material for long-term cycling. However, due to its enormous benefits (particularly its high capacity), there is considerable interest in this material in academia and industry. In this thesis a model thin-film silicon anode has been explored in a great deal of detail, providing fundamental insights regarding the mechanisms of degradation which may be expected using bulk silicon anodes. A particular area of interest for the future in this regard are the studies of artificial SEIs which could be of value for the stabilisation of bulk silicon during cycling. Surface coatings based on poly(phosphazenes) may extend the life-time of bulk silicon anodes, making the ultimate goal of developing viable LIBs based in silicon possible. Furthermore, this technology could lead to an advance in other promising future battery technologies in which volume expansion of the electrodes is a major problem.

References

- [1] IEA, *Global Energy and CO2 Status Report 2018*, **2019**.
- [2] IPCC, *Summary for Policymakers*, **2018**.
- [3] J. Rogelj, D. Shindell, K. Jiang, S. Fifita, P. Forster, V. Ginzburg, C. Handa, H. Khashgi, S. Kobayashi, E. Kriegler, et al., in *IPCC Spec. Rep. Glob. Warm. 1.5 °C*, Pallav Purohit, **2018**, 82.
- [4] “What happens when it’s really windy? — 10:10 Climate Action,” can be found under <https://1010uk.org/talk-about-wind/too-windy>, **2019**.
- [5] G. L. Soloveichik, *Annu. Rev. Chem. Biomol. Eng.* **2011**, 2, 503–527.
- [6] B. Dunn, H. Kamath, J. M. Tarascon, *Electrical Energy Storage for the Grid: A Battery of Choices*, **2011**.
- [7] T. M. Gür, *Energy Environ. Sci.* **2018**, 11, 2696–2767.
- [8] “A Behind the Scenes Take on Lithium-ion Battery Prices | BloombergNEF,” can be found under <https://about.bnef.com/blog/behind-scenes-take-lithium-ion-battery-prices/>, **2019**.
- [9] R. Service, “Giant batteries and cheap solar power are shoving fossil fuels off the grid,” DOI 10.1126/science.aay7094 can be found under <https://www.sciencemag.org/news/2019/07/giant-batteries-and-cheap-solar-power-are-shoving-fossil-fuels-grid>, **2019**.
- [10] O. Babacan, A. Abdulla, R. Hanna, J. Kleissl, D. G. Victor, *Environ. Sci. Technol.* **2018**, 52, 13600–13608.
- [11] Bloomberg New Energy Finance, “Electric Vehicle Outlook 2018 | Bloomberg NEF,” can be found under <https://about.bnef.com/electric-vehicle-outlook/#toc-download>, **2018**.
- [12] C. Buchal, H.-D. Karl, H.-W. Sinn, *Kohle motoren, Windmotoren Und Dieselmotoren: Was Zeigt Die CO2-Bilanz?*, **2019**.
- [13] EEA, *Trends and Projections in Europe 2015: Tracking Progress towards Europe’s Climate and Energy Targets*, **2015**.
- [14] Q. Dai, J. C. Kelly, L. Gaines, M. Wang, *Batteries* **2019**, 5, 2–15.

- [15] M. Winter, B. Barnett, K. Xu, *Chem. Rev.* **2018**, *118*, 11433–11456.
- [16] The Royal Swedish Academy of Sciences, *Press Release: The Nobel Prize in Chemistry 2019*, **2019**.
- [17] B. Dunn, H. Kamath, J. M. Tarascon, *Science* **2011**, *334*, 928–935.
- [18] F. Shi, Z. Song, P. N. Ross, G. A. Somorjai, R. O. Ritchie, K. Komvopoulos, Failure Mechanisms of Single-Crystal Silicon Electrodes in Lithium-Ion Batteries, **2016**.
- [19] F. Shi, Z. Song, P. N. Ross, G. A. Somorjai, R. O. Ritchie, K. Komvopoulos, *Nat. Commun.* **2016**, *7*, 11886.
- [20] G. Girishkumar, B. McCloskey, A. C. Luntz, S. Swanson, W. Wilcke, *J. Phys. Chem. Lett.* **2010**, *1*, 2193–2203.
- [21] Y. Wang, E. Sahadeo, G. Rubloff, C. F. Lin, S. B. Lee, *J. Mater. Sci.* **2019**, *54*, 3671–3693.
- [22] M. R. Palacín, *Chem. Soc. Rev.* **2009**, *38*, 2565–2575.
- [23] Z. Chen, I. Belharouak, Y. K. Sun, K. Amine, *Adv. Funct. Mater.* **2013**, *23*, 959–969.
- [24] G. N. Zhu, Y. G. Wang, Y. Y. Xia, *Energy Environ. Sci.* **2012**, *5*, 6652–6667.
- [25] J. Cabana, L. Monconduit, D. Larcher, M. R. Palacín, *Adv. Mater.* **2010**, *22*, E170–E192.
- [26] S. H. Yu, X. Feng, N. Zhang, J. Seok, H. D. Abruña, *Acc. Chem. Res.* **2018**, *51*, 273–281.
- [27] S. Muench, A. Wild, C. Friebe, B. Häupler, T. Janoschka, U. S. Schubert, *Chem. Rev.* **2016**, *116*, 9438–9484.
- [28] W. Liu, P. Oh, X. Liu, M. J. Lee, W. Cho, S. Chae, Y. Kim, J. Cho, *Angew. Chemie - Int. Ed.* **2015**, *54*, 4440–4457.
- [29] A. Purwanto, C. S. Yudha, U. Ubaidillah, H. Widiyandari, T. Ogi, H. Haerudin, *Mater. Res. Express* **2018**, *5*, 122001.
- [30] N. Nitta, F. Wu, J. T. Lee, G. Yushin, *Mater. Today* **2015**, *18*, 252–264.
- [31] F. Zheng, M. Kotobuki, S. Song, M. O. Lai, L. Lu, *J. Power Sources* **2018**, *389*, 198–213.
- [32] G. E. Blomgren, *Liquid Electrolytes for Lithium and Lithium-Ion Batteries*, **2003**.

- [33] R. Younesi, G. M. Veith, P. Johansson, K. Edström, T. Vegge, *Energy Environ. Sci.* **2015**, *8*, 1905–1922.
- [34] D. M. Seo, S. Reininger, M. Kutcher, K. Redmond, W. B. Euler, B. L. Lucht, *J. Phys. Chem. C* **2015**, *119*, 14038–14046.
- [35] H. Ashassi-Sorkhabi, A. Kazempour, P. Salehi-Abar, *Ionics* **2019**, 1–9.
- [36] S. S. Zhang, *J. Power Sources* **2006**, *162*, 1379–1394.
- [37] E. Foreman, W. Zakri, M. Hossein Sanatimoghaddam, A. Modjtahedi, S. Pathak, A. G. Kashkooli, N. G. Garafolo, S. Farhad, *Adv. Sustain. Syst.* **2017**, *1*, 1700061.
- [38] D. Bresser, D. Buchholz, A. Moretti, A. Varzi, S. Passerini, *Energy Environ. Sci.* **2018**, *11*, 3096–3127.
- [39] C. C. Nguyen, T. Yoon, D. M. Seo, P. Guduru, B. L. Lucht, *ACS Appl. Mater. Interfaces* **2016**, *8*, 12211–12220.
- [40] K. K. Jana, S. J. Lue, A. Huang, J. F. Soesanto, K.-L. Tung, *ChemBioEng Rev.* **2018**, *5*, 346–371.
- [41] E. Peled, S. Menkin, *J. Electrochem. Soc.* **2017**, *164*, A1703–A1719.
- [42] A. Wang, S. Kadam, H. Li, S. Shi, Y. Qi, *npj Comput. Mater.* **2018**, *4*, 15.
- [43] E. Peled, D. Golodnitsky, G. Ardel, *J. Electrochem. Soc.* **1997**, *144*, L208.
- [44] S. Shi, P. Lu, Z. Liu, Y. Qi, L. G. Hector, H. Li, S. J. Harris, *J. Am. Chem. Soc.* **2012**, *134*, 15476–15487.
- [45] E. Peled, *J. Electrochem. Soc.* **1979**, *126*, 2047–2051.
- [46] L. Xing, O. Borodin, G. D. Smith, W. Li, *J. Phys. Chem. A* **2011**, *115*, 13896–13905.
- [47] T. Li, P. B. Balbuena, *Chem. Phys. Lett.* **2000**, *317*, 421–429.
- [48] X. Zhang, J. K. Pugh, P. N. Ross, *J. Electrochem. Soc.* **2001**, *148*, E183.
- [49] M. N. Obrovac, L. Christensen, *Electrochem. Solid-State Lett.* **2004**, *7*, A93.
- [50] F. Wang, L. Wu, B. Key, X. Q. Yang, C. P. Grey, Y. Zhu, J. Graetz, *Adv. Energy Mater.* **2013**, *3*, 1324–1331.
- [51] A. L. Michan, G. Divitini, A. J. Pell, M. Leskes, C. Ducati, C. P. Grey, *J. Am. Chem. Soc.* **2016**, *138*, 7918–7931.

- [52] J. R. Szczech, S. Jin, *Energy Environ. Sci.* **2011**, *4*, 56–72.
- [53] A. Mukanova, A. Jetybayeva, S. T. Myung, S. S. Kim, Z. Bakenov, *Mater. Today Energy* **2018**, *9*, 49–66.
- [54] M. Salah, P. Murphy, C. Hall, C. Francis, R. Kerr, M. Fabretto, *J. Power Sources* **2019**, *414*, 48–67.
- [55] M. Gu, Y. He, J. Zheng, C. Wang, *Nano Energy* **2015**, *17*, 366–383.
- [56] M. Ko, S. Chae, J. Cho, *ChemElectroChem* **2015**, *2*, 1645–1651.
- [57] Y. X. Yin, L. J. Wan, Y. G. Guo, *Chinese Sci. Bull.* **2012**, *57*, 4104–4110.
- [58] A. Franco Gonzalez, N. H. Yang, R. S. Liu, *J. Phys. Chem. C* **2017**, *121*, 27775–27787.
- [59] H. S. Lee, B. J. Lee, *Met. Mater. Int.* **2014**, *20*, 1003–1009.
- [60] N. Ding, J. Xu, Y. Yao, G. Wegner, I. Lieberwirth, C. Chen, *J. Power Sources* **2009**, *192*, 644–651.
- [61] X. H. Liu, L. Zhong, S. Huang, S. X. Mao, T. Zhu, J. Y. Huang, *ACS Nano* **2012**, *6*, 1522–1531.
- [62] I. Ryu, J. W. Choi, Y. Cui, W. D. Nix, *J. Mech. Phys. Solids* **2011**, *59*, 1717–1730.
- [63] T. D. Hatchard, J. R. Dahn, *J. Electrochem. Soc.* **2004**, *151*, A838.
- [64] L. Y. Beaulieu, K. W. Eberman, R. L. Turner, L. J. Krause, J. R. Dahn, *Electrochem. Solid-State Lett.* **2001**, *4*, A137.
- [65] Y. Sun, K. Liu, Y. Zhu, *J. Nanomater.* **2017**, *2017*, 1–15.
- [66] H. Tao, L. Z. Fan, W. L. Song, M. Wu, X. He, X. Qu, *Nanoscale* **2014**, *6*, 3138–3142.
- [67] J. Li, N. J. Dudney, J. Nanda, C. Liang, *ACS Appl. Mater. Interfaces* **2014**, *6*, 10083–10088.
- [68] Y. Hamedí Jouybari, F. Berkemeier, *Electrochim. Acta* **2016**, *217*, 171–180.
- [69] D. S. M. Iaboni, M. N. Obrovac, *J. Electrochem. Soc.* **2016**, *163*, A255–A261.
- [70] K. Ogata, E. Salager, C. J. Kerr, A. E. Fraser, C. Ducati, A. J. Morris, S. Hofmann, C. P. Grey, *Nat. Commun.* **2014**, *5*, 3217.
- [71] B. Key, R. Bhattacharyya, M. Morcrette, V. Seznéc, J. M. Tarascon, C. P. Grey, *J. Am. Chem. Soc.* **2009**, *131*, 9239–9249.

- [72] B. Key, M. Morcrette, J. M. Tarascon, C. P. Grey, *J. Am. Chem. Soc.* **2011**, *133*, 503–512.
- [73] J. W. Wang, Y. He, F. Fan, X. H. Liu, S. Xia, Y. Liu, C. T. Harris, H. Li, J. Y. Huang, S. X. Mao, et al., *Nano Lett.* **2013**, *13*, 709–715.
- [74] B. J. Brennan, A. E. Keirstead, P. A. Liddell, S. A. Vail, T. A. Moore, A. L. Moore, D. Gust, *Nanotechnology* **2009**, *20*, 505203.
- [75] R. Nesper, *Prog. Solid State Chem.* **1990**, *20*, 1–45.
- [76] P. Limthongkul, Y. Il Jang, N. J. Dudney, Y. M. Chiang, *J. Power Sources* **2003**, *119–121*, 604–609.
- [77] C. J. Wen, R. A. Huggins, *J. Solid State Chem.* **1981**, *37*, 271–278.
- [78] A. Bordes, E. De Vito, C. Haon, C. Secouard, A. Montani, P. Marcus, *ACS Appl. Mater. Interfaces* **2015**, *7*, 27853–27862.
- [79] M. Ashuri, Q. He, L. L. Shaw, *Nanoscale* **2016**, *8*, 74–103.
- [80] M. Haruta, Y. Kijima, R. Hioki, T. Doi, M. Inaba, *Nanoscale* **2018**, *10*, 17257–17264.
- [81] N. Liu, H. Wu, M. T. McDowell, Y. Yao, C. Wang, Y. Cui, *Nano Lett.* **2012**, *12*, 3315–3321.
- [82] Y. Yang, Z. Wang, R. Zhou, H. Guo, X. Li, *Mater. Lett.* **2016**, *184*, 65–68.
- [83] A. Reyes Jiménez, R. Nölle, R. Wagner, J. Hüsker, M. Kolek, R. Schmuch, M. Winter, T. Placke, *Nanoscale* **2018**, *10*, 2128–2137.
- [84] Y. Kim, G. M. Veith, J. Nanda, R. R. Unocic, M. Chi, N. J. Dudney, *Electrochim. Acta* **2011**, *56*, 6573–6580.
- [85] Y. Liu, K. Xie, Y. Pan, Y. Li, H. Wang, W. Lu, C. Zheng, *Ionics* **2018**, *24*, 723–734.
- [86] X. H. Liu, L. Q. Zhang, L. Zhong, Y. Liu, H. Zheng, J. W. Wang, J. H. Cho, S. A. Dayeh, S. T. Picraux, J. P. Sullivan, et al., *Nano Lett.* **2011**, *11*, 2251–2258.
- [87] H. Kim, M. Seo, M. H. Park, J. Cho, *Angew. Chemie - Int. Ed.* **2010**, *49*, 2146–2149.
- [88] B. Hertzberg, A. Alexeev, G. Yushin, *J. Am. Chem. Soc.* **2010**, *132*, 8548–8549.
- [89] C. Zhang, A. Song, P. Yuan, Q. Wang, P. Wang, S. Zhang, G. Cao, J. H. Hu, *Mater. Lett.* **2016**, *171*, 63–67.

- [90] N. Liu, Z. Lu, J. Zhao, M. T. McDowell, H. W. Lee, W. Zhao, Y. Cui, *Nat. Nanotechnol.* **2014**, *9*, 187–192.
- [91] N. Liu, H. Wu, M. T. McDowell, Y. Yao, C. Wang, Y. Cui, *Nano Lett.* **2012**, *12*, 3315–3321.
- [92] N. Liu, Z. Lu, J. Zhao, M. T. McDowell, H. W. Lee, W. Zhao, Y. Cui, *Nat. Nanotechnol.* **2014**, *9*, 187–192.
- [93] M. Haruta, Y. Kijima, R. Hioki, T. Doi, M. Inaba, *Nanoscale* **2018**, *10*, 17257–17264.
- [94] Y. Gao, R. Yi, Y. C. Li, J. Song, S. Chen, Q. Huang, T. E. Mallouk, D. Wang, *J. Am. Chem. Soc.* **2017**, *139*, 17359–17367.
- [95] B. H. Shen, G. M. Veith, W. E. Tenhaeff, *Sci. Rep.* **2018**, *8*, 11549.
- [96] J. H. Gladstone, J. D. Holmes, *J. Chem. Soc.* **1864**, *17*, 225–237.
- [97] R. M. Glover, *Lancet* **1853**, *61*, 34.
- [98] H. R. Allcock, *J. Inorg. Organomet. Polym.* **1992**, *2*, 197–211.
- [99] H. R. Allcock, *Chem. Rev.* **1972**, *72*, 315–356.
- [100] H. R. Allcock, *Soft Matter* **2012**, *8*, 7521–7532.
- [101] H. R. Allcock, *Appl. Organomet. Chem.* **2013**, *27*, 620–629.
- [102] I. Teasdale, O. Brüggemann, *Polymers* **2013**, *5*, 161–187.
- [103] C. W. Allen, *J. Fire Sci.* **1993**, *11*, 320–328.
- [104] S. T. Fei, H. R. Allcock, *Mater. Res. Soc. Symp. Proc.* **2008**, *1127*, 50–55.
- [105] A. K. Andrianov, H. R. Allcock, *Polyphosphazenes in Biomedicine, Engineering, and Pioneering Synthesis*, American Chemical Society, Washington, DC, **2018**.
- [106] A. Wilson, D. F. Carroll, *J. Chem. Soc.* **1960**, 2548.
- [107] G. J. Bullen, *J. Chem. Soc. A Inorganic, Phys. Theor. Chem.* **1971**, 1450–1453.
- [108] H. R. Allcock, *Phosphorus-Nitrogen Compounds*, Academic Press, **1972**, 385–395.
- [109] Y. Chatani, K. Yatsuyanagi, *Macromolecules* **1987**, *20*, 1042–1045.
- [110] H. R. Allcock, *Phosphorus-Nitrogen Compounds*, Academic Press, **1972**, 16–35.
- [111] L. Kapička, P. Kubáček, P. Holub, *J. Mol. Struct. THEOCHEM* **2007**, *820*, 148–158.

- [112] A. B. Chaplin, J. A. Harrison, P. J. Dyson, *Inorg. Chem.* **2005**, *44*, 8407–8417.
- [113] A. S. Elayan, C. W. Allen, E. S. Peterson, *J. Inorg. Organomet. Polym. Mater.* **2017**, *27*, 119–123.
- [114] H. R. Allcock, C. A. Crane, C. T. Morrissey, J. M. Nelson, S. D. Reeves, C. H. Honeyman, I. Manners, *Macromolecules* **1996**, *29*, 7740–7747.
- [115] K. Ono, K. Saito, *Chemistry and Applications of 4,5-Diazafluorenes*, Wiley, **2008**.
- [116] C. W. Allen, *Coord. Chem. Rev.* **1994**, *130*, 137–173.
- [117] H. R. Allcock, *Synthesis, Structures, and Emerging Uses for Poly(Organophosphazenes)*, **2018**.
- [118] G. A. Nazri, D. M. MacArthur, J. F. O’Gara, *Am. Chem. Soc. Polym. Prepr. Div. Polym. Chem.* **1989**, *30*, 430–431.
- [119] H. R. Allcock, N. J. Sunderland, R. Ravikiran, J. M. Nelson, *Macromolecules* **1998**, *31*, 8026–8035.
- [120] N. Kaskhedikar, M. Burjanadze, Y. Karatas, H. D. Wiemhöfer, *Solid State Ionics* **2006**, *177*, 3129–3134.
- [121] S. Jankowsky, M. M. Hiller, O. Fromm, M. Winter, H. D. Wiemhöfer, *Electrochim. Acta* **2015**, *155*, 364–371.
- [122] S. Jankowsky, M. M. Hiller, H. D. Wiemhöfer, *J. Power Sources* **2014**, *253*, 256–262.
- [123] S. Schmohl, X. He, H. D. Wiemhöfer, *Polymers* **2018**, *10*, 1350.
- [124] M. Burjanadze, Y. Karatas, N. Kaskhedikar, L. M. Kogel, S. Kloss, A. C. Gentschev, M. M. Hiller, R. A. Müller, R. Stolina, P. Vettikuzha, et al., *Zeitschrift für Phys. Chemie* **2010**, *224*, 1439–1473.
- [125] X. He, S. Schmohl, H. D. Wiemhöfer, *ChemElectroChem* **2019**, *6*, 1166–1176.
- [126] A. J. Smith, J. C. Burns, X. Zhao, D. Xiong, J. R. Dahn, *J. Electrochem. Soc.* **2011**, *158*, A447.
- [127] A. J. Smith, J. C. Burns, D. Xiong, J. R. Dahn, *J. Electrochem. Soc.* **2011**, *158*, A1136.
- [128] H. N. Southworth, *Scanning Electron Microscopy and Microanalysis*, Springer US, **1975**.

- [129] W. L. F. Armarego, C. Chai, *Purification of Laboratory Chemicals*, Elsevier Science, New York, **2009**.
- [130] G. R. Fulmer, A. J. M. Miller, N. H. Sherden, H. E. Gottlieb, A. Nudelman, B. M. Stoltz, J. E. Bercaw, K. I. Goldberg, *Organometallics* **2010**, *29*, 2176–2179.
- [131] S. F. Macha, P. A. Limbach, *Curr. Opin. Solid State Mater. Sci.* **2002**, *6*, 213–220.
- [132] K. Schroder, J. Alvarado, T. A. Yersak, J. Li, N. Dudney, L. J. Webb, Y. S. Meng, K. J. Stevenson, *Chem. Mater.* **2015**, *27*, 5531–5542.
- [133] Q. Wu, B. Shi, J. Bareño, Y. Liu, V. A. Maroni, D. Zhai, D. W. Dees, W. Lu, *ACS Appl. Mater. Interfaces* **2018**, *10*, 3487–3494.
- [134] B. A. Boukamp, G. C. Lesh, R. A. Huggins, *J. Electrochem. Soc.* **1981**, *128*, 725–729.
- [135] J. P. Maranchi, A. F. Hepp, A. G. Evans, N. T. Nuhfer, P. N. Kumta, *J. Electrochem. Soc.* **2006**, *153*, A1246.
- [136] V. A. Sethuraman, M. J. Chon, M. Shimshak, V. Srinivasan, P. R. Guduru, *J. Power Sources* **2010**, *195*, 5062–5066.
- [137] V. A. Sethuraman, V. Srinivasan, A. F. Bower, P. R. Guduru, *J. Electrochem. Soc.* **2010**, *157*, A1253.
- [138] J. Yin, M. Wada, K. Yamamoto, Y. Kitano, S. Tanase, T. Sakai, *J. Electrochem. Soc.* **2006**, *153*, A472.
- [139] J. Li, A. K. Dozier, Y. Li, F. Yang, Y. T. Cheng, *J. Electrochem. Soc.* **2011**, *158*, A689.
- [140] H. B. Chew, B. Hou, X. Wang, S. Xia, *Int. J. Solids Struct.* **2014**, *51*, 4176–4187.
- [141] W. Xu, N. L. Canfield, D. Wang, J. Xiao, Z. Nie, X. S. Li, W. D. Bennett, C. C. Bonham, J. G. Zhang, *J. Electrochem. Soc.* **2010**, *157*, A765.
- [142] K. L. Lee, J. Y. Jung, S. W. Lee, H. S. Moon, J. W. Park, *J. Power Sources* **2004**, *129*, 270–274.
- [143] M. T. Demirkan, L. Trahey, T. Karabacak, *J. Power Sources* **2015**, *273*, 52–61.
- [144] R. S. Weatherup, L. D’Arsié, A. Cabrero-Vilatela, S. Caneva, R. Blume, J. Robertson, R. Schloegl, S. Hofmann, *J. Am. Chem. Soc.* **2015**, *137*, 14358–14366.
- [145] Z. Jia, W. K. Liu, *Appl. Phys. Lett.* **2016**, *109*, 163903.

- [146] F. Farmakis, C. Elmasides, P. Fanz, M. Hagen, N. Georgoulas, *J. Power Sources* **2015**, *293*, 301–305.
- [147] M. T. McDowell, S. W. Lee, J. T. Harris, B. A. Korgel, C. Wang, W. D. Nix, Y. Cui, *Nano Lett.* **2013**, *13*, 758–764.
- [148] A. Ulvestad, J. P. Maehlen, M. Kirkengen, *ECS Trans.* **2015**, *64*, 107–111.
- [149] X. Xiao, P. Liu, M. W. Verbrugge, H. Haftbaradaran, H. Gao, *J. Power Sources* **2011**, *196*, 1409–1416.
- [150] H. Jung, M. Park, Y. G. Yoon, G. B. Kim, S. K. Joo, *J. Power Sources* **2003**, *115*, 346–351.
- [151] “RSC- Periodic Table,” can be found under <http://www.rsc.org/periodic-table/history>, **2019**.
- [152] G. Ji, Y. Ma, J. Y. Lee, *J. Mater. Chem.* **2011**, *21*, 9819–9824.
- [153] W. S. Chang, C. M. Park, J. H. Kim, Y. U. Kim, G. Jeong, H. J. Sohn, *Energy Environ. Sci.* **2012**, *5*, 6895–6899.
- [154] K. Kitada, O. Pecher, P. C. M. M. Magusin, M. F. Groh, R. S. Weatherup, C. P. Grey, *J. Am. Chem. Soc.* **2019**, *141*, 7014–7027.
- [155] R. S. Weatherup, L. D’Arsié, A. Cabrero-Vilatela, S. Caneva, R. Blume, J. Robertson, R. Schloegl, S. Hofmann, *J. Am. Chem. Soc.* **2015**, *137*, 14358–14366.
- [156] J. P. Maranchi, A. F. Hepp, A. G. Evans, N. T. Nuhfer, P. N. Kumta, *J. Electrochem. Soc.* **2006**, *153*, A1246.
- [157] Z. Du, T. D. Hatchard, R. A. Dunlap, M. N. Obrovac, *J. Electrochem. Soc.* **2015**, *162*, A1858–A1863.
- [158] Z. Du, T. D. Hatchard, P. Bissonnette, R. A. Dunlap, M. N. Obrovac, *J. Electrochem. Soc.* **2016**, *163*, A2456–A2460.
- [159] Y. N. Zhou, W. J. Li, H. J. Chen, C. Liu, L. Zhang, Z. Fu, *Electrochem. commun.* **2011**, *13*, 546–549.
- [160] M. S. Park, Y. J. Lee, S. Rajendran, M. S. Song, H. S. Kim, J. Y. Lee, *Electrochim. Acta* **2005**, *50*, 5561–5567.
- [161] M. Miyachi, H. Yamamoto, H. Kawai, *J. Electrochem. Soc.* **2007**, *154*, A376.

- [162] A. Palmieri, T. Wang, J. Zhang, N. Spinner, M. Liu, W. E. Mustain, *J. Electrochem. Soc.* **2017**, *164*, A867–A873.
- [163] Y. M. Kang, K. T. Kim, J. H. Kim, H. S. Kim, P. S. Lee, J. Y. Lee, H. K. Liu, S. X. Dou, *J. Power Sources* **2004**, *133*, 252–259.
- [164] I. N. Lund, J. H. Lee, H. Efstathiadis, P. Haldar, R. E. Geer, *J. Power Sources* **2014**, *246*, 117–123.
- [165] L. Luo, P. Zhao, H. Yang, B. Liu, J. G. Zhang, Y. Cui, G. Yu, S. Zhang, C. M. Wang, *Nano Lett.* **2015**, *15*, 7016–7022.
- [166] M. Ulldemolins, F. Le Cras, B. Pecquenard, V. P. Phan, L. Martin, H. Martinez, *J. Power Sources* **2012**, *206*, 245–252.
- [167] M. T. Demirkan, L. Trahey, T. Karabacak, *Thin Solid Films* **2016**, *600*, 126–130.
- [168] J. Graetz, C. C. Ahn, R. Yazami, B. Fultz, *Electrochem. Solid-State Lett.* **2003**, *6*, DOI 10.1149/1.1596917.
- [169] N. S. Choi, K. H. Yew, K. Y. Lee, M. Sung, H. Kim, S. S. Kim, *J. Power Sources* **2006**, *161*, 1254–1259.
- [170] G. G. Eshetu, E. Figgemeier, *ChemSusChem* **2019**, *12*, 2515–2539.
- [171] Y. Jin, N.-J. H. Kneusels, P. C. M. M. Magusin, G. Kim, E. Castillo-Martínez, L. E. Marbella, R. N. Kerber, D. J. Howe, S. Paul, T. Liu, et al., *J. Am. Chem. Soc.* **2017**, *139*, 14992–15004.
- [172] Y. Jin, N.-J. H. Kneusels, L. E. Marbella, E. Castillo-Martínez, P. C. M. M. Magusin, R. S. Weatherup, E. Jónsson, T. Liu, S. Paul, C. P. Grey, *J. Am. Chem. Soc.* **2018**, *140*, 9854–9867.
- [173] A. L. Michan, M. Leskes, C. P. Grey, *Chem. Mater.* **2016**, *28*, 385–398.
- [174] A. L. Michan, B. S. Parimalam, M. Leskes, R. N. Kerber, T. Yoon, C. P. Grey, B. L. Lucht, *Chem. Mater.* **2016**, *28*, 8149–8159.
- [175] V. Etacheri, O. Haik, Y. Goffer, G. A. Roberts, I. C. Stefan, R. Fasching, D. Aurbach, *Langmuir* **2012**, *28*, 965–976.
- [176] H. Nakai, T. Kubota, A. Kita, A. Kawashima, *J. Electrochem. Soc.* **2011**, *158*, A798.

- [177] E. Markevich, K. Fridman, R. Sharabi, R. Elazari, G. Salitra, H. E. Gottlieb, G. Gershinsky, A. Garsuch, G. Semrau, M. A. Schmidt, et al., *J. Electrochem. Soc.* **2013**, *160*, A1824–A1833.
- [178] R. Jung, M. Metzger, D. Haering, S. Solchenbach, C. Marino, N. Tsiouvaras, C. Stinner, H. A. Gasteiger, *J. Electrochem. Soc.* **2016**, *163*, A1705–A1716.
- [179] I. A. Shkrob, J. F. Wishart, D. P. Abraham, *J. Phys. Chem. C* **2015**, *119*, 14954–14964.
- [180] K. Leung, S. B. Rempe, M. E. Foster, Y. Ma, J. M. M. Del La Hoz, N. Sai, P. B. Balbuenab, *J. Electrochem. Soc.* **2014**, *161*, A213–A221.
- [181] H. Ota, Y. Sakata, A. Inoue, S. Yamaguchi, *J. Electrochem. Soc.* **2004**, *151*, A1659.
- [182] L. El Ouatani, R. Dedryvère, C. Siret, P. Biensan, S. Reynaud, P. Iraçabal, D. Gonbeau, *J. Electrochem. Soc.* **2009**, *156*, A103.
- [183] L. Chen, K. Wang, X. Xie, J. Xie, *Electrochem. Solid-State Lett.* **2006**, *9*, A512.
- [184] M. L. Daroux, P. W. Faguy, E. Yeager, *J. Electrochem. Soc.* **1987**, *134*, 1611–1620.
- [185] L. Gireaud, S. Grugeon, S. Pilard, P. Guenot, J. M. Tarascon, S. Laruelle, *Anal. Chem.* **2006**, *78*, 3688–3698.
- [186] D. Aurbach, A. Zaban, A. Schechter, Y. Ein-Eli, E. Zinigrad, B. Markovsky, *J. Electrochem. Soc.* **1995**, *142*, 2873–2882.
- [187] K. Xu, G. V. Zhuang, J. L. Allen, U. Lee, S. S. Zhang, P. N. Ross, T. R. Jow, *J. Phys. Chem. B* **2006**, *110*, 7708–7719.
- [188] N. S. Choi, K. H. Yew, H. Kim, S. S. Kim, W. U. Choi, *J. Power Sources* **2007**, *172*, 404–409.
- [189] J. Zhang, X. Yang, R. Wang, W. Dong, W. Lu, X. Wu, X. Wang, H. Li, L. Chen, *J. Phys. Chem. C* **2014**, *118*, 20756–20762.
- [190] Y. G. Ryu, S. Lee, S. Mah, D. J. Lee, K. Kwon, S. Hwang, S. Doo, *J. Electrochem. Soc.* **2008**, *155*, A583.
- [191] G. M. Veith, M. Doucet, R. L. Sacci, B. Vacaliuc, J. K. Baldwin, J. F. Browning, *Sci. Rep.* **2017**, *7*, 1–15.
- [192] M. Sina, J. Alvarado, H. Shobukawa, C. Alexander, V. Manichev, L. Feldman, T. Gustafsson, K. J. Stevenson, Y. S. Meng, *Adv. Mater. Interfaces* **2016**, *3*, 1600438.

- [193] Y. Domi, H. Usui, M. Shimizu, K. ichi Miwa, H. Sakaguchi, *Int. J. Electrochem. Sci.* **2015**, *10*, 9678–9686.
- [194] A. Reyes Jiménez, R. Klöpsch, R. Wagner, U. C. Rodehorst, M. Kolek, R. Nölle, M. Winter, T. Placke, *ACS Nano* **2017**, *11*, 4731–4744.
- [195] G. Yao, Z. Duan, *Jingxi Huagong* **2012**, *29*, 394–397.
- [196] L. J. Krause, T. Brandt, V. L. Chevrier, L. D. Jensen, *J. Electrochem. Soc.* **2017**, *164*, A2277–A2282.
- [197] N. L. Wu, Y. T. Weng, F. S. Li, N. H. Yang, C. L. Kuo, D. S. Li, *Prog. Nat. Sci. Mater. Int.* **2015**, *25*, 563–571.
- [198] E. J. Dufek, J. R. Klaehn, J. S. McNally, H. W. Rollins, D. K. Jamison, *Electrochim. Acta* **2016**, *209*, 36–43.
- [199] S. Ganapathiappan, K. Chen, D. F. Shriver, *J. Am. Chem. Soc.* **1989**, *111*, 4091–4095.
- [200] J. Sun, Z. Yu, X. Wang, D. Wu, *ACS Sustain. Chem. Eng.* **2014**, *2*, 231–238.
- [201] M. Otsuki, T. Ogino, K. Amine, in *ECS Trans.*, ECS, **2006**, 13–19.
- [202] D. J. Wang, Q. L. Mou, S. G. Wan, X. J. Song, D. T. Tian, *Phosphorus, Sulfur Silicon Relat. Elem.* **2012**, *187*, 944–951.
- [203] S. Jankowsky, M. M. Hiller, R. Stolina, H. D. Wiemhöfer, *J. Power Sources* **2015**, *273*, 574–579.
- [204] J. Paulsdorf, N. Kaskhedikar, M. Burjanadze, S. Obeidi, N. A. Stolwijk, D. Wilmer, H. D. Wiemhöfer, *Chem. Mater.* **2006**, *18*, 1281–1288.
- [205] B. Wang, *Macromolecules* **2005**, *38*, 643–645.
- [206] B. Wang, E. Rivard, I. Manners, *Inorg. Chem.* **2002**, *41*, 1690–1691.
- [207] C. H. Honeyman, I. Manners, C. T. Morrissey, H. R. Allcock, *J. Am. Chem. Soc.* **1995**, *117*, 7035–7036.
- [208] C. J. Nelson, W. D. Coggio, H. R. Allcock, *Chem. Mater.* **1991**, *3*, 786–787.
- [209] M. Doytcheva, R. Stamenova, V. Zvetkov, C. B. Tsvetanov, *Polymer (Guildf)*. **1998**, *39*, 6715–6721.
- [210] C. G. d. Kruif, J. C. va. Miltenburg, J. G. Blok, *J. Chem. Thermodyn.* **1983**, *15*, 129–136.

- [211] H. R. Allcock, J. M. Nelson, R. Prange, C. A. Crane, C. R. De Denus, *Macromolecules* **1999**, *32*, 5736–5743.
- [212] E. T. Vandenberg, L. Bertilsson, B. Liedberg, K. Uvdal, R. Erlandsson, H. Elwing, I. Lundström, *J. Colloid Interface Sci.* **1991**, *147*, 103–118.
- [213] R. M. Pasternack, S. R. Amy, Y. J. Chabal, *Langmuir* **2008**, *24*, 12963–12971.
- [214] N. Majoul, S. Aouida, B. Bessaïs, *Appl. Surf. Sci.* **2015**, *331*, 388–391.
- [215] S. Hsieh, W. J. Chao, C. W. Hsieh, *J. Nanosci. Nanotechnol.* **2009**, *9*, 2894–2901.
- [216] J. Kim, *ACS Symp. Ser.* **2011**, *1062*, 141–165.
- [217] J. Wang, D. X. Ye, G. H. Liang, J. Chang, J. L. Kong, J. Y. Chen, *J. Mater. Chem. B* **2014**, *2*, 4338–4345.
- [218] J. M. Nelson, H. R. Allcock, *Macromolecules* **1997**, *30*, 1854–1856.
- [219] H. R. Allcock, Y. C. Song, L. B. Steely, *Macromolecules* **2006**, *39*, 8334–8338.
- [220] T. J. Taylor, A. P. Soto, K. Huynh, A. J. Lough, A. C. Swain, N. C. Norman, C. A. Russell, I. Manners, *Macromolecules* **2010**, *43*, 7446–7452.
- [221] R. G. Acres, A. V. Ellis, J. Alvino, C. E. Lenahan, D. A. Khodakov, G. F. Metha, G. G. Andersson, *J. Phys. Chem. C* **2012**, *116*, 6289–6297.
- [222] D. Meroni, L. Lo Presti, G. Di Liberto, M. Ceotto, R. G. Acres, K. C. Prince, R. Bellani, G. Soliveri, S. Ardizzone, *J. Phys. Chem. C* **2017**, *121*, 430–440.